



UNIVERSITÀ
DI TRENTO

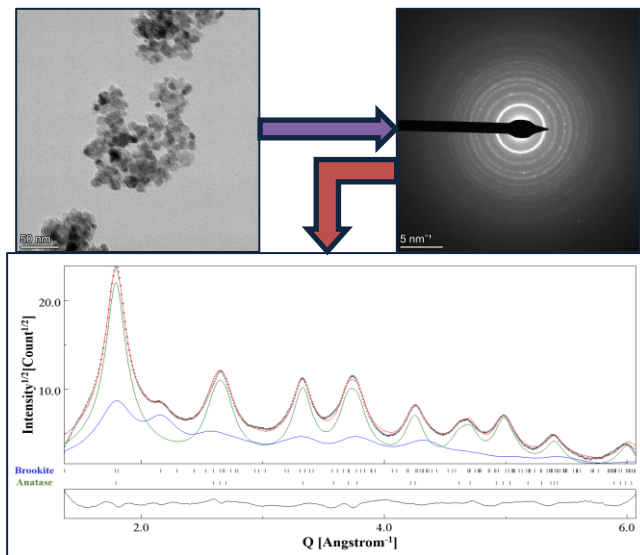
Department of
Industrial Engineering

Doctoral School in Materials, Mechatronics
and Systems Engineering

XXXV cycle

Ultrafine particulate matter and nanostructured materials: A comprehensive transmission electron microscopy approach

Ankur Sinha



July 2023

**ULTRAFINE PARTICULATE MATTER AND NANOSTRUCTURED
MATERIALS: A COMPREHENSIVE TRANSMISSION ELECTRON
MICROSCOPY APPROACH**

Ankur Sinha

E-mail: ankur.sinha@unitn.it

Approved by:

Prof. Stefano Gialanella, Advisor
Department of Industrial Engineering
University of Trento, Italy.

Prof. Luca Lutterotti, Advisor,
Department of Industrial Engineering
University of Trento, Italy.

Ph.D. Commission:

Dr. Priyadarshini Jayashree,
Department of Industrial Engineering
University of Trento, Italy.

Prof. Stefano Frabboni,
Department of Physics, Computer
Science and Mathematics
*University of Modena and Reggio
Emilia, Italy.*

Prof. Enrico Mugnaioli,
Department of Earth Sciences
University of Pisa, Italy.

University of Trento,
Department of Industrial Engineering

July 2023

University of Trento - Department of Industrial Engineering

Doctoral Thesis

Ankur Sinha- July, 2023

Published in Trento (Italy) – by University of Trento

*Dedicated to all Doctors, Nurses, Researchers, and other Medical Staff
who worked tirelessly and selflessly during peak COVID-19 times.*

Table of contents

Abstract	1
Chapter I: Introduction	4
I.1 Nanostructured materials	4
I.2 Characterization of nanostructured materials.....	7
I.2.1 Imaging (SEM and S/TEM) and spectroscopy (EDXS)	9
I.2.2 Other microscopy and spectroscopy techniques.....	15
I.2.3 Diffraction: X-Ray powder diffraction (XRPD), neutron powder diffraction (NPD), electron powder diffraction (EPD) and analysis	18
Chapter II: Basic concepts	23
II.1 A brief history of TEM	23
II.2 Transmission electron microscopy and diffraction	24
II.2.1 Magnetic lenses.....	24
II.2.2 Imaging: Bright field and Dark field	26
II.2.3 Electron diffraction.....	29
II.2.3.1 Electron diffraction: Kinematic and Dynamical diffraction formulae	
34	
II.2.4 Selected area electron diffraction (SAED) and its types	36
II.3 Energy dispersive spectroscopy.....	38
II.3.1 Fluorescence Yield	40
II.4 Line Profile Analyses:	41
II.5 The Rietveld method	42
II.5.1 Rietveld method applied to EPD ring patterns	45
II.5.2 Peak shape function	46
II.5.3 Phase analysis using EPD	48
II.5.4 Le Bail method:.....	50
II.6 Material Analysis Using Diffraction (MAUD).....	52
II.7 ThermoFisher TALOS F200S S/TEM.....	53
Chapter III: TEM sample preparation	55
III.1 Introduction.....	55
III.2 Sample preparation techniques.....	55
III.2.1 PM from disc brake systems	55
III.2.1.1 Introduction	55
III.2.1.2 Methodology	57

III.2.1.3 Validation of methodology	58
III.2.2 Nanostructured materials	62
III.3 Highlights of the chapter	62
Chapter IV: Rietveld method applied to electron powder diffraction patterns- Methodology	64
IV.1 Introduction	64
IV.2 Material and methodology	65
IV.3 Results and discussion	73
IV.3.1 Camera length calibration	73
IV.3.2 Instrumental broadening function	78
IV.3.3 Microstructure determination from EPD	81
IV.4 Highlights of the chapter	87
Chapter V: Rietveld method applied to electron powder diffraction patterns: Application to microstructural analysis	89
V.1 Introduction	89
V.2 Material sample description	89
V.3 Rietveld method: Key points	91
V.4 Results and discussion	93
V.4.1 nc- Yttrium oxide	93
V.4.2 Nanocrystalline Silicon (nc-Si)	96
V.4.3 Nanocrystalline titanium dioxide (nc- TiO ₂)	100
V.4.4 Particulate matter from a disc brake	104
V.4.5 Hematite from heat treatment of natural Goethite	106
V.5 Highlights of the chapter	109
Chapter VI: Combined electron powder diffraction and energy dispersive spectroscopy study	111
VI.1 Introduction	111
VI.2 Material: Nanocrystalline cobalt iron oxide	112
VI.3 Results and discussion	113
VI.4 Highlights of the chapter	121
Chapter VII: Final comments and scope for further development	122
VII.1 Accomplishments of the project	122
VII.2 Limitations of the proposed methodologies	125
VII.3 Further development	126
Appendix A1	127
Appendix A2	127

References	145
Publications	164
Conferences, Workshops, and Schools attended.....	166
Acknowledgment.....	167

Abbreviations

TEM: Transmission electron microscopy

SEM: Scanning electron microscopy

EPD: Electron powder diffraction

SAED: Selected Area Electron Diffraction

XRPD: X-ray powder diffraction

EDXS: Energy dispersive X-ray spectroscopy

NC: Nanocrystalline

UFG: Ultrafine grain

PM: Particulate Matter

DF: Dark Field

BF: Bright Field

MAUD: Material Analysis Using Diffraction

HWHM: Half width at half maximum

FWHM: Full width at half maximum

WSS: Weighted Sum of Squares

Rwp: Weighted reliability factor

Rwp_{no_bkg}: Weighted reliability factor without background

Abstract

The twenty-first century may be termed the “nano-century,” as nano-structured materials have become deep-rooted in our everyday life. Cosmetics, pharmaceuticals, textiles, electronics, food packaging, automobile, and many more industries directly or indirectly consume or produce nano-crystalline powders, or in general nanomaterials, in large quantities. The incredible growth in their production has challenged the conventional characterization tools available to researchers. Characterization of nanoparticles is a prerequisite before their possible usage in any field, however, it becomes indispensable for nanostructured materials of environmental concerns and unlike for chemical toxicants, the characterization of such materials is not limited only to purity and chemical composition.

A transmission electron microscope (TEM) is a robust characterization tool providing imaging, diffraction, and spectroscopic techniques possibly at the atomic resolution in one single instrument. This PhD thesis aims to combine the three methodologies to yield the best possible route for quantitative characterization of the nanostructured assemblies. In this context, the Rietveld refinement of selected area electron diffraction (SAED) patterns, which encodes structural information in the form of the diffracted electron intensities, has capabilities to yield phase composition and microstructure from material volumes many orders of magnitude lesser than in complementary techniques such as X-ray diffraction (XRD) and neutron diffraction (ND). This unique superiority of TEM is crucial in the study of nanostructured materials as local quantitative characterization may not be adequately performed by XRD and ND. Moreover, TEM readily permits the attainment of elemental composition from the same region of interest using energy dispersive x-ray spectroscopy (EDXS) or electron energy loss spectroscopy (EELS) to further support the diffraction-based studies.

This thesis has been divided into four parts, as shown in the schematic below. After introductory topics, Part 1 (Chapter III) focuses on the development of a sample preparation technique for particulate matter collected using environmental sampling systems to be analyzed using electron microscopy tools, i.e., scanning electron microscopy (SEM) and TEM. The method based on extraction replica, has been applied to wear debris collected on aluminium substrates during dynamometer studies of disc brakes. Especially concerning the TEM analysis, the technique is useful since

the collected particles cannot be directly observed on the substrates. As for SEM, the accurate quantification of Al, which is usually present in the brake wear debris, is difficult if the analysis is performed directly on the Al filter. Moreover, the development of the technique was crucial since it gave the opportunity to extend the methodology of electron powder diffraction (EPD) based microstructure characterization also to complex samples, like those related to environmental research.

The first step forward to the proposed methodology to study nanostructured materials concerns establishing a calibration method to separate the instrumental effects from the physical broadening caused by the microstructure of the analyzed samples. To fulfil this very important criterion, in Part 2 (Chapter IV), a standard nanocrystalline CeO₂ powder has been used and calibration for camera lengths and instrumental broadening function has been performed in correlation with the microstructural data obtained from XRD results of the same material. In this approach, a total of twelve diffraction patterns were collected using three SAED apertures- 800, 200, and 40 μm , and four camera lengths- 1360, 1080, 844, and 658 mm. The instrumental broadening function determined through Rietveld refinement-based characterization of these diffraction patterns yielded an interesting trend, wherein for a particular SAED aperture, the instrumental broadening function decreased with the increase in camera length. A dedicated procedure for the Rietveld refinement of SAED patterns of nanostructured materials has been developed using *MAUD* (Material Analysis Using Diffraction) software.

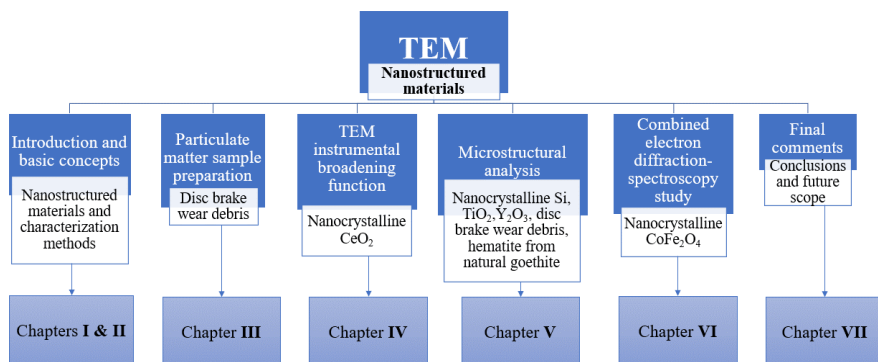
In the field of nanostructured materials, new compounds/phases are being synthesized at a rapid pace, with high-output techniques that can yield many variants within a single experiment. Such techniques find usage in a variety of fields, such as drug delivery, catalysis, and semiconductors. The physical and chemical properties of these newly designed materials are not a function only of their structural form, but in the case of multiphase materials, also depend on the relative amounts of the components. In line with the crucial role of phase identification and consequently determination, Part 3 (Chapter V) demonstrates the capabilities and limits of EPD to study the microstructure of homogeneous and complex multi-phase systems, also for the sampled particulate matter discussed in Part 1 (Chapter III). These include nanocrystalline silicon, yttrium oxide, titanium dioxide, wear debris from disc brake

wear, and hematite obtained from the heat treatment of natural goethite, each displaying microstructural parameters that needed to be tackled with the proposed methodology. These case studies with different complexities were appropriately selected and studied.

In Part 4 (Chapter VI), the limitations of relying only on electron diffraction, wherein significant changes in the structural information of a particular phase could be easily overlooked, have been demonstrated for a mixed oxide and countered by combining SAED with EDXS in one Rietveld fitting. For this analysis, cobalt iron oxide featuring impurities with a chemical composition of Na, Mg, Ca, Ti, and Mn was studied, with its modelled EDX spectrum coupled with the diffractogram. The developed technique, although at a nascent stage with scope for further development, allows determining in addition to the microstructure, the degree of substitution of the parent elements- Fe and Co, by the impurity atoms.

Thus, although the mathematics of electron diffraction is critical from the view of electron-matter interaction, the current work rather delves more into the development of suitable methodologies and their application to fill the existing gap in the literature by extending the approach of the Rietveld refinement to SAED patterns for studying mainly the microstructure, also combined with other characterization techniques such as XRD and EDXS, for solving problems of scientific interest in the area of nanostructured materials.

Schematic of the organization of the thesis



Chapter I: Introduction

1.1 Nanostructured materials

The growth in the field of nanostructured materials can be credited to a large degree to the seminal work by Gleiter and co-authors [1]. The present very broad field of nanostructured materials can be divided into three categories [2]: nanocrystalline materials, nanoparticles, and nano devices. It is hard to give a specific definition for a nanostructured material. Moreover, in many cases, the terms “nanomaterials,” “nanophase materials,” and “nanocrystalline materials” have been used interchangeably. Nanomaterials have at least one dimension in the range of 1-100 nm and show a direction-dependent phenomenon [3]. Nanomaterial is either a manufactured, incidental, or naturally existing material having particles in the unbound, aggregated, or agglomerated states, wherein for at least 50 % of the particles in the number size distribution, the external dimensions are in the 1-100 nm size range [4]. Nanostructured materials essentially display three features: The atomic domains, i.e., the grains or phases are spatially confined to a dimension less than 100 nm; a significant amount of these atomic domains are associated with the interfacial environments; there exist interactions between the domains [5].

For a particular nanostructured material, depending on the dimensions in which its length scale is nanometers, the classification can be done into i) nanoparticles (0-D), ii) lamellar structures (1-D), iii) filamentary structured (2-D), iv) bulk nanostructured materials (3-D). Nanoparticles can be termed as atomic clusters. A layered/lamellar structure refers to a nanostructure having the magnitude of length and width much greater than the thickness that has dimensions of a few nanometers. A 2D nanostructure can be visualized as filamentary, having a length substantially greater than the width/diameter, which are in nanometer dimensions. The 3-D nanostructures are the most common and are equiaxed, i.e., having all the three dimensions in the nanometer size range and termed nanostructure crystallites. However, nanostructured materials may be composed of different types of phases- crystalline, quasicrystalline, or amorphous, and could belong to a variety of materials- polymers, metals, intermetallics, semiconductors, ceramics, or composites. In such a scenario, if the grains are composed of crystals, then the material is termed as nanocrystalline. Fig. I-1 shows the four types of nanocrystalline materials through a schematic, adapted from Siegel [5].

Fig. I-2 shows a two-dimensional schematic of a nanostructured material, adapted from Gleiter [6]. As shown in the schematic, a nanostructured material composed of building blocks (mostly crystallites) in the nanometer size range can be microstructurally heterogeneous. The heterogeneity arises from the fact that the crystallites can have coherent/ incoherent interfaces (e.g., grain boundaries)

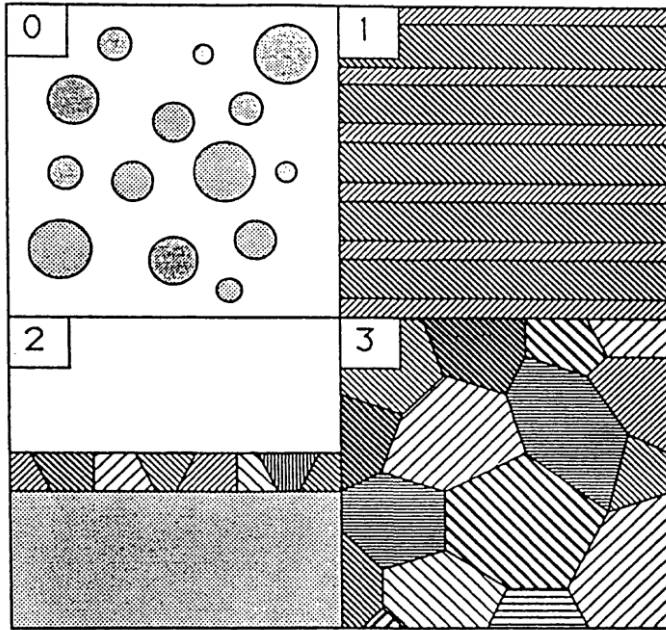


Figure I- 1 Schematic representation of four types of nanocrystalline materials [5].

depending on different atomic structures, chemical composition, and orientation. Thus, nanocrystalline materials can be said to constitute two structural components: crystallites having long-range order with different crystallographic orientations, thus forming the 'crystalline component'; and inter-crystalline regions that are structurally inconsistent from one region to another, termed as the 'interfacial region'. Depending on the type of chemical bonds between the atoms, the density of the interfacial regions could be 10-30 % less than that of the crystalline part [7]. Lu. [8] has predicted for grains of spherical or cubical shapes the volume fraction of the interfacial regions as 50 % for grains with a size of 5 nm, 30 % for 10 nm grains, and, 3 % for with a dimension of 100 nm. In particular, a nanocrystalline metal could contain a substantial number of atoms at these interfaces with random relationships.

From a very strict definition, nanocrystalline materials display microstructure with a characteristic length scale up to a few tens of nanometers. As for those materials that have extended range up to a few hundred of nanometers, those can be termed as 'ultrafine grained' or 'submicron' materials [9,10]. Kumar et al. [11] have classified materials having grain sizes smaller than 100 nm as nanocrystalline, while those materials having grain sizes in the 100-1000 nm range as ultrafine-grained materials.

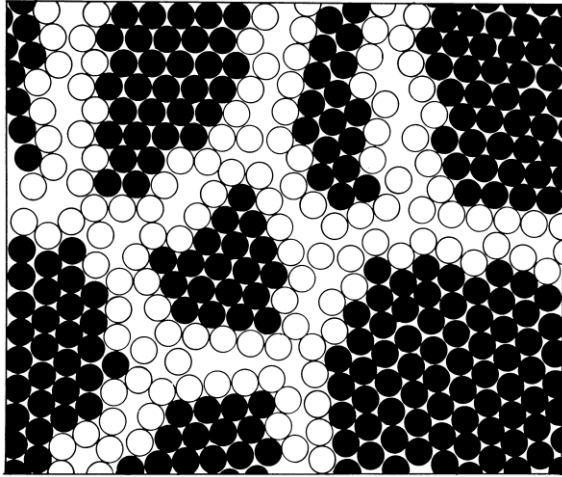


Figure I- 2 Schematic representation of equiaxed nanocrystalline metal distinguishing between atoms associated with the individual grains (black circles) and those constituting grain boundary network (white circles) [5].

Nanomaterials have gained prominence since they have tuneable physical, chemical, and biological properties that have been reported to be superior or different from those of the conventional grain sized ($>1 \mu\text{m}$) single crystals or polycrystalline materials having the same chemical composition. In several cases, bulk nanocrystalline materials and thin films of such materials have been shown to demonstrate high values of hardness [12,13], strength [14,15], and fatigue resistance [16,17]. Although there is the constraint that a very high value of hardness may actually lead to a decrease in the ductility, thereby limiting the practical utility for any particular field of application, some researchers have demonstrated that in certain materials simultaneous high values of these two properties is possible [18–20]. Another interesting feature of these materials, in the case of selected ceramics and metallic alloys, is the existence of superplasticity at lower temperatures and these demonstrate the property of superplasticity [21,22], and anomalously fast diffusion [23,24]. The combination of these properties, especially the existence of high strength and ductility, suggests the possible usage of nanocrystalline materials for structural and functional applications.

Fig. I-3 shows the variation of the yield stress with the grain size for three types of material microstructure- nanocrystalline (NC), ultrafine-grained (UFG), and coarse-grained (micrometer-sized grains). When the grain size is reduced from the micrometer size, then a linear the Hall-Petch [25] relationship is observed. The reduction in the grain size enhances the grain boundary regions that act as dislocation

barriers, leading to dislocation pile-up and an increase in strength. However, if the grain size is further refined below a size of approximately 10 nm, an inverse Hall-Petch effect is seen, leading to a lower value of yield stress [26,27].

Thus, nanocrystalline materials present an excellent opportunity to study the structure-property relation of materials right down to the nano regime and use them for technological advancements. In this regard, it is essential to study the microstructure, which can be termed as the deviation from the 'ideal structure', of these materials, including the evaluation of the compositions of the phases, in view of their specific application.

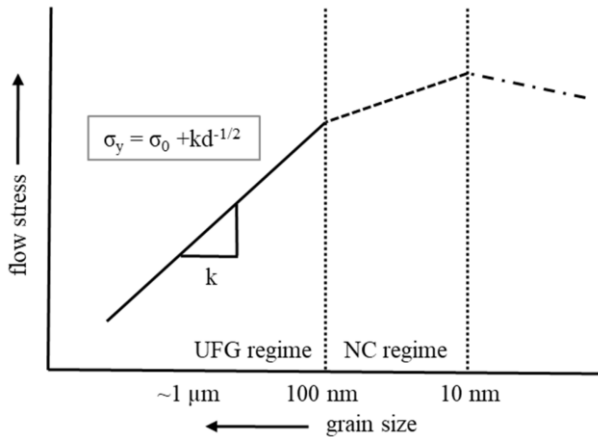


Figure I- 3 Schematic showing the variation of flow stress for different types of materials with grain size [28]. UFG- ultrafine grained; NC- nanocrystalline

1.2 Characterization of nanostructured materials

As mentioned before, the properties of nanocrystalline materials are inherently different and, in many cases, superior to their conventional-grained counterparts. It is thus essential to study the microstructure of these special materials to understand the variation of the structure with the decreasing crystallite sizes since this is the dominant parameter governing the material properties. Thus, microstructural investigations are primarily essential to elucidate the inherent underlying mechanisms. Even so for the materials of environmental concerns, microstructural investigations become important for the relevant toxicological studies.

Characterization of nanostructured materials may be performed at different levels. Some of the characterization methods aim to determine the morphological aspects—shape and size of the nanostructures, while others characterize the detailed structural information [29]. The structure of these materials can be studied at different levels, requiring varying sophistication of the instrumentation—molecular structure, atom level structure, electronic structure, microstructure, and crystal structure. For routine purposes, XRD and ND-based Rietveld analyses are used extensively for crystal structure studies. These are additionally supported by the morphological information from the microscopy techniques, usually SEM and TEM [30].

In the framework of this thesis, we have focused mainly on the microstructural features of polycrystalline nanostructured materials. In this regard, crystallites (also referred to as ‘coherent domains’) are three-dimensional entities that propagate the incident radiation in a coherent manner without the loss in phase. A grain (refer to Fig. I-4) that could be observed directly under a microscope is composed either of a single crystallite or many crystallites. A polycrystal is thus an ensemble of many crystallites.

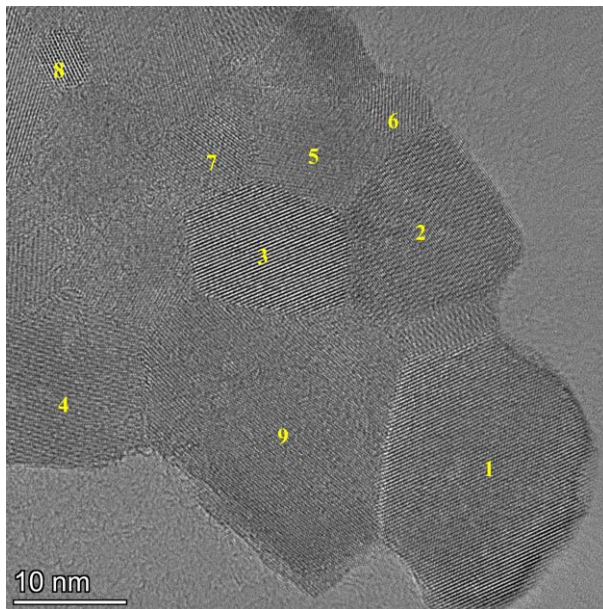


Figure I- 4 Numbered grains of nanocrystalline Y₂O₃ that could indeed compose many crystallites, which are coherently scattering domains.

1.2.1 Imaging (SEM and S/TEM) and spectroscopy (EDXS)

Morphology is an important feature to distinctly characterize the properties of nanostructured materials. Unlike for the bulk materials, the shape strongly governs the properties of nanostructured materials [31]. A particle is generally three-dimensional and could have many possible shapes. "Particle size" is a one-dimensional scalar value to represent the three-dimensional particle [32].

In scanning electron microscopy a high-energy narrow focused electron beam is scanned across the surface of a specimen to record the image generated using the electrons scattered from the surface [33]. The electrons do not penetrate to a greater depth since the acceleration of the electron in the column is lesser as compared to the TEM, providing essential surface information through secondary and backscattered electrons. In an SEM analysis, the interaction volume and the spot size may be greater than the interatomic distances, and hence the resolution of the SEM is lesser as compared to the TEM, rendering the imaging of the individual atoms not possible. Still, depending on the instrument, the resolution of the SEM can be anywhere between lesser than 1 nm and 20 nm [29].

However, the distinct advantage is that a larger area of the specimen can be imaged, yielding average characteristics of the nanostructured systems. Moreover, sample preparation is often easier than for TEM and relatively thicker samples can be studied. SEM images have a great depth of field and a unique characteristic of giving a three-dimensional appearance of the particles, useful for understanding their morphology [34]. One of the challenges in nanoscience and nanotechnology is the synthesis of nanoparticles with specific sizes and shapes, as desired for a particular field of application [35,36]. Concerning the last point, SEM-based studies have been helpful in determining the morphologies of the particles. During the synthesis, depending on the parameters of the reaction, the morphology of the particles can vary from spherical to cauliflower-like, as demonstrated for ZnO nanoparticles by Moghri Moazzen et al. [30]. Chen et al. [34] observed that varying the reaction conditions in the hydrothermal technique can vary the particle morphology of Fe₃O₄ from spherical to biscuit-like. Siddiqui et al. [37] synthesized nanocrystalline ZrO₂ using sol-gel technique and observed very different morphologies depending on the type of precursor used. These variations in the particle morphology of course have an impact also on the average crystallite size. In addition to these microstructural evaluations, the chemical composition of the particles can be determined with the incorporation of spectroscopy (SEM-EDXS) [38,39].

EDXS is mainly used for the chemical characterization of the particles and is an important portion of the work done in this thesis work. The technique relies on the fact that different elements have their unique structure of the electron orbitals involved in the emission of the X-ray characteristic lines. In an EDXS system, the incident high-voltage electron beam knocks out an electron from the inner shell of the material,

causing the formation of an electron hole in the electronic structure. To fill the electron hole, the transition of an electron from the outer shell with a higher energy state occurs, and the difference in the energy between the higher and lower shells is released as a characteristic X-ray [40]. EDXS systems can be incorporated both in SEM and TEM.

Fig. I-5 shows the morphology of the particles emitted from the disc brake systems studied in this project work. These particles were collected on an impactor used for environmental monitoring purposes (refer to chapter III). The variation in the shape of the particles from spherical, plate-like, to needle-shaped, is compliant with the observations made in other studies involving emissions from disc brake systems [41]. The elemental compositions determined from these particles are crucial in the determination and possible quantification of the phases constituting them. The elemental compositions from three particle clusters marked in Fig. I-5 b) are listed in Table I-1.

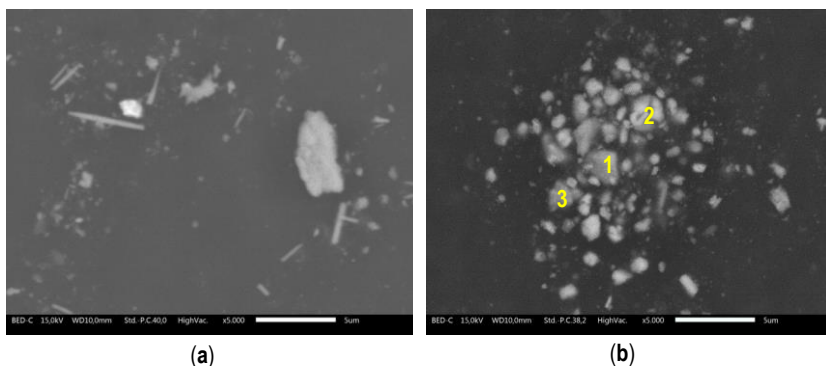


Figure I- 5 Different particle morphology using SEM obtained for disc brake wear debris

The demand for a higher resolution is fulfilled by including TEM in the study of the nanostructured systems, although the representativeness of the whole material under observation remains an issue to be tackled [42]. In a TEM, a highly accelerated (80–300 keV) electron beam is allowed to transmit through a thin sample, and mainly the electrons scattered in the forward direction give rise to the formation of the images. In a modern TEM, it is possible to obtain a spatial resolution lesser than 1 angstrom [29]. TEM is the ultimate standard for the characterization of nanostructured materials. TEM can provide a high spatial resolution covering the entire nanometric size range of 1-100 nm. The image analysis of the 2D projections can be used to determine the physical characteristics- size, shape, and surface morphology of individual nano-sized entities [43,44]. The agglomerates/aggregates of the particles may also be studied and

to some extent, the primary particles constituting them can be identified [45,46]. Apart from the conventional bright field and dark field imaging modes, the imaging techniques also include high-resolution TEM, STEM imaging [47], and 3D electron tomography [48].

Table I- 1 EDXS results from three clusters marked in Fig. I-5 b). The elemental compositions suggest that these constitute different phases.

Element	Area 1 Wt. %	Area 2 Wt. %	Area 3 Wt. %
Oxygen	16.2	24.5	24.1
Magnesium	1.7	2.7	2.0
Aluminum	0.8	2.3	1.1
Silicon	1.6	2.4	1.3
Sulfur	1.9	2.2	2.1
Chromium	0.6	0.9	-
Iron	66.6	36.5	58.9
Copper	4.9	17.2	3.1
Zinc	2.7	6.4	4.7
Tin	-	-	2.7
Zirconium	0.5	1.6	-
Antimony	2.1	3.4	-

The inclusion of spectroscopic methods, EDXS and EELS, permits the user to attain knowledge of the elemental composition of localized regions which is very helpful for the overall characterization theme in the case of multi-phase components [29,49]. The diffraction techniques including selected area electron diffraction (SAED) [50,51], convergent beam electron diffraction (CBED) [52,53], and nanobeam electron diffraction (NBED) [54,55] can disclose the crystallographic structure of nano-objects. However, images include the phases, i.e., it is a more complete information compared to diffraction and can be directly interpreted up to a certain resolution. Moreover, imaging does not require a crystalline sample and is more convenient for analyzing the local structure in polycrystalline samples, around grain boundaries and defects.

High-resolution EM(HREM) images use phase contrast based on the coherent interaction of many-electron beams to depict the lattice fringes and atomic structure of the materials. Fig. I-6 shows one such example of a nanocrystalline yttrium oxide sample studied in this thesis. Such direct observations can provide clear indications of the morphologies of the nanometer-sized crystallites demarcated by the boundaries.

Such images can also be used to determine the crystallite sizes in different crystallographic directions.

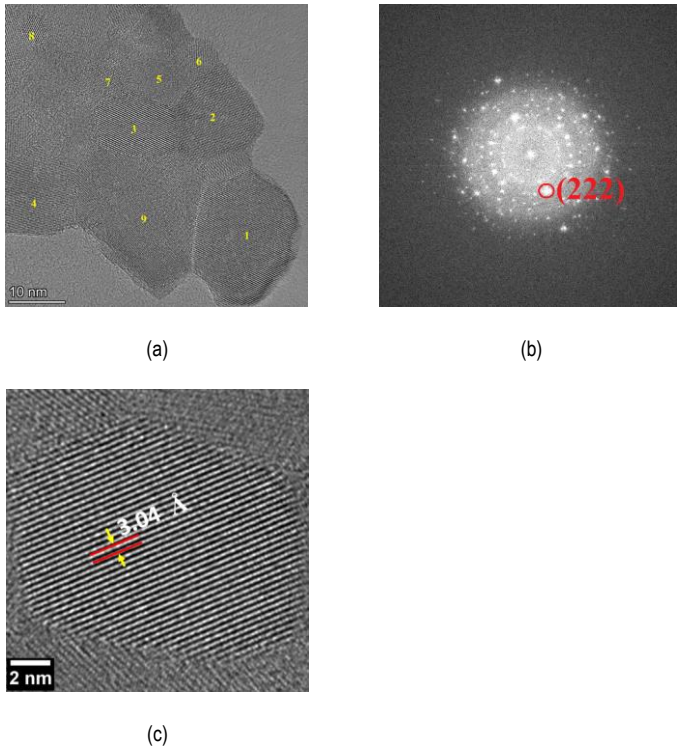


Figure I- 6 (a) Individual crystallites of Y_2O_3 in a high-magnification image, with (b) its FFT. (c): An enlarged area of the crystallite marked '3' in panel (a), used to determine the interplanar spacing of the (222) planes as 3.04 Å.

TEM-EDXS information collected at a high resolution is helpful also for phase determination. Fig. I-7 shows the TEM BF image of particle clusters analyzed in this thesis work [56]. The three different regions marked in the image were found to be composed of different types of particles. Table I-2 lists the elemental composition of these particle clusters. Based on some prior knowledge of the friction composite, it could be concluded that the region marked '1' comprised graphite particles, '2' was a silicon carbide particle cluster, whereas '3' was rich in the elements that constituted the *friction layer*. El-Nahhal et al. [57] studied the microstructure constituting core-shell

and chemical composition of silica and functionalized silica coated zinc oxide nanoparticles using TEM-EDXS. Similar study on core-shell multifunctional magnetic nanoparticles constituting cobalt ferrite based nanoparticles coated by a double silica/titania shell has been done by Greene et al.[58].

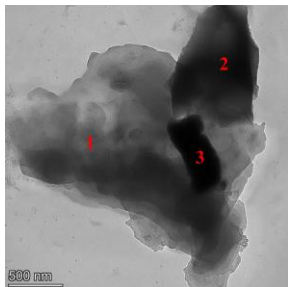


Figure I- 7 TEM BF image of a disc brake wear debris showing three different particle clusters. The EDXS results from these clusters are listed in Table I-2

Table I- 2 EDXS results from three clusters marked in Fig. I-7. The elemental compositions suggest that these constitute different phases.

Element	Area 1 Mass %	Area 2 Mass %	Area 3 Mass %
Carbon	99	23	62
Oxygen	1	26	6
Silicon	-	52	3
Iron	-	0.1	25
Chromium	-	-	3
Tin	-	-	1

If suitable attachments are available, a TEM can also be used in the *scanning mode (STEM)*, like an SEM. One very big advantage of STEM is that lenses are not used in the formation of the images, so the lens aberrations do not hamper the resolution of the collected data. In the STEM mode of operation, a focused sub-nanometer-sized probe scans over the specimen. A very high resolution, down to 0.1 nm for high-resolution STEM, depending on the nanosized illuminating probe can be obtained [59]. Various signals- secondary electrons, transmitted electrons, backscattered electrons,

and X-rays, are produced in the specimen due to the electron scattering, capable of providing accurate physical and chemical characteristics of the specimen.

In an STEM unit, multiple detectors are available that can be used simultaneously to obtain different yet complementary information from the specimen. The bright field (BF) detector intercepts the direct beam while the annular dark field (ADF) detector surrounds the direct beam to collect the electrons that are scattered. Thus, the forward scattered electrons on-axis electrons are collected by the BF detector and the electrons that are scattered in the forward direction through small angles ($< 3^\circ$) are collected on the ADF detector [60]. Those electrons that are scattered to even higher angles, enhancing the atomic number dependence of the contrast in the image, are detected by the high-angle annular dark field (HAADF) detector.

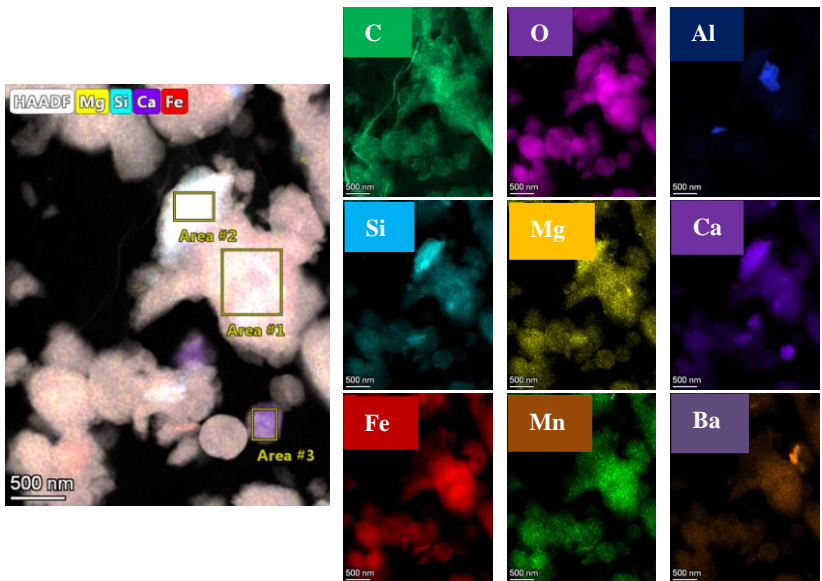


Figure I- 8 STEM HAADF image with selected overlapped wear debris constituents and X-ray maps. The three areas from which the compositional data are given in Table I-3 have been indicated.

The high-angle incoherent scattering is dependent on the scattering by atomic nuclei, yielding an intensity that is proportional roughly to the squared atomic number ($I \sim Z^{1.6-2}$) [61], as expected based on the Rutherford scattering maximization and limiting diffraction contrast effects. This type of imaging is thus referred to as Z-contrast

imaging and one of its advantages is that specimen features with different chemical compositions can be identified.

EDXS elemental mapping combines the high spatial resolution of the STEM mode with the X-ray signals from the entire predefined scanning area, to construct the elemental distribution of the detected elements. With modern STEMs, it is possible to record the EDXS spectrum at every data point, permitting to extract distribution map of any element. These elemental distributions can be superimposed on the STEM images. An example of this is shown in Fig I-8 for a disc bake wear debris sample studied in this thesis work. The fine-scale intermixing of the constituents and the local relative compositions are seen through the semi-quantitative distribution of the different elements. Along with the maps, quantitative EDXS data were obtained from the three marked regions identified on the HAADF image, listed in Table I-3.

Table I- 3 EDXS results from three areas marked in Fig. I-8.

Element	Area 1 Mass %	Area 2 Mass %	Area 3 Mass %
O	30.8	38.1	44.0
Mg	0.9	3.2	0.7
Al	1.7	3.3	0.2
Si	3.8	14.2	1.0
S	1.2	1.0	0.4
Ca	5.9	19.6	36.0
Mn	0.9	0.7	0.4
Fe	51.3	18.0	16.3
Ba	3.6	1.9	1.1

1.2.2 Other microscopy and spectroscopy techniques

In laser *scanning confocal microscopy*, a narrow and focused convergent beam is rastered across a specimen like in an SEM. Using ultraviolet light (UV) that has a shorter wavelength instead of the visible light spectrum gives a better resolution and depth of field. In laser confocal scanning microscopy, the light that does not originate from the focal plane is rejected, permitting the user to perform optical slicing [62], i.e., serially produce images of thin sections across planes of different orientations. The three-dimensional representations give a realistic view of the specimen studied, and the sharp quality of the image with quantitative imaging analysis can provide vital structural information at the mesoscale [63]. Zhang and Monteiro-Riviere[64] used the technique in the application of drug delivery involving the penetration of nanoparticles

through the skin and the detection of single nanoparticles. Germann and Davis[65] applied the technique for the detection of a single fluorescent nanoparticle in a solution. An extension of laser confocal scanning microscopy is the generation of the Raman spectrum from the scanning laser beam [66].

Atomic force microscopy (AFM) is a type of scanning probe microscopy that is used for studying and imaging surface profiles [67]. The technique can provide a resolution comparable to TEM and higher than SEM. In AFM, an extremely sharp tip of a few microns in length and diameter lesser than 100 Å, is made to come in close proximity or contact with the specimen being imaged. The tip is located at the free end of a cantilever that is 100-200 µm long, and the deflections caused due to contact force on the tip are recorded and processed to image the topographical representation of the specimen. Unlike SEM, surface features without any obstructions can be revealed as no coating is required. As compared to TEM, the main advantage in some cases is that a complicated sample preparation procedure is not required and much more surface information than 2D TEM images can be obtained. Rao et al. [68] studied TiO₂, ZrO₂, and Al₂O₃ nanoparticles/agglomerates, with visualizations of the nanoparticles in the three dimensions. Similar size measurements of nanoparticles have been studied by other researchers[69].

Scanning tunneling microscopy (STM) is a characterization tool for visualization of the surfaces of conducting samples and analyzing their electronic properties at the atomic level [67]. When a metallic tip is brought near a conducting or a semiconducting a bias voltage applied between the tip and the material surface allows the electrons to tunnel either from the tip to the surface or from the surface to the tip through the vacuum between them. To start the tunneling procedure, the STM tip is brought within several angstroms distance from the surface of the sample. Variations in the tunnelling currents as the probe passes over the specimen, which are functions of the local density of states at the Fermi level [29], are transformed into an image. Walton et al. [70] studied through STM the variations in morphologies of single-layer MoS₂ during catalysis, highlighting the crucial role of the technique in investigating the structure at the atomic level of catalytically active nanoparticles.

X-ray photoelectron spectroscopy (XPS) is a surface-sensitive analytical technique that is capable of measuring elemental composition, and chemical and electronic states of the elements in a nanostructured material [71]. X-rays are bombarded on the surface of a material in an ultrahigh vacuum, and the number of emitted electrons from the top 1-10 nm and their kinetic energies are simultaneously measured [72]. Zhang et al.[73] used XPS coupled with other techniques to determine the oxidation state of cerium ions in ceria nanoparticles. Alwin et al. [74] elucidated the structure of graphitic carbon nitride nanomaterials comprehensively through XPS and XRD. Since the

accurate description of the internal structure of a nanostructured material is essential for understanding its properties, XPS is a valuable technique.

Photoluminescence spectroscopy (PLS) is a technique suitable for studying the electronic structure of both extrinsic and intrinsic semiconducting nanomaterials [71]. Photoluminescence is the process in which a photon transfers its energy to an electron, thereby exciting it from its ground state to an excited state within a femtosecond timescale [75]. If there exist multiple excited states in the material, then the higher states excited electrons rapidly relax to the lowest excited states non-radiatively. However, if the return of the electron to the equilibrium state is through a radiative process, then the excess energy between the two states is released in the form of a photon, and the process is termed photoluminescence. For a semiconductor bombarded with a light source having the energy of the photons greater in magnitude than the band gap energy of the material, transfer of electrons to the conduction band is possible with the generation of holes. The recombination of the electron-hole pair leads to the emission of a photon having a characteristic wavelength of the material. Peng et al.[76] studied the PL spectra at different time intervals after the growth of the synthesized CdSe nanocrystals. The authors concluded that PL spectra can be converted to a size distribution curve assuming a particular δ function emission (refer to [76]) for every single size of nanocrystals and the same emission efficiency for the different sizes. PLS has been used for the characterization of other nanocrystals- ZnO [77], La-doped TiO₂ [78], and Si [79].

Raman Spectroscopy is based on the inelastic scattering of incident photons by the vibrating molecules in a sample. The technique can be implemented to study the structure of liquids, gases, and of amorphous and crystalline solids [80]. For a crystalline solid, the Raman effect is dependent on the space group symmetry. Transitions that can be rotational, electronic, or vibrational are induced by the incident radiations on the atoms or molecules present in the scattering medium. Usually, a Raman plot indicates inelastically scattered light intensity as a function of the radiation shift in wavenumber. A wide range of material characteristics- interatomic/ intermolecular bond strengths, crystallinity, mechanical strain, and effects of temperature and pressure can be estimated [81]. In the characterization of a nanostructured material, the different vibrational modes will correspond to the peaks in the spectrum. Raman spectroscopy is amongst the most precise techniques for characterizing carbon nanostructures since carbon can exist in a variety of different physical forms [82]. Viera et al. [83] performed a detailed structural characterization of amorphous silicon and nanocrystalline silicon thin films that were grown in radio-frequency plasma using Raman spectroscopy. Choi et al.[84] studied the size effects of TiO₂ nanoparticles in Raman spectra and observed that decreasing the particle diameter caused the broadening and shifts of the Raman bands.

1.2.3 Diffraction: X-Ray powder diffraction (XRPD), neutron powder diffraction (NPD), electron powder diffraction (EPD) and analysis

Although electron microscopy and scanning probes can provide information at the atomic resolution, much detailed information about the 3D arrangements of the atoms in the crystals and symmetry requires diffraction-based methods. Nanostructured materials may also display morphology at a much larger scale due to the combination of nanoscale entities, crystallization nucleation [85], aggregation, and agglomeration [86]. High-resolution imaging requires a higher electron dose compared to diffraction, both in TEM and STEM modes, causing a fast deterioration of the sample. At the same time, resolution in diffraction is higher, because lens aberrations are less important; it is much easier to get 3D information in diffraction compared to tomographic imaging. Moreover, depending on the diffraction contrast, using dark field mode analysis may not be able to produce high-resolution images of individual crystallites of different phases if there is interference between the diffraction signals from these phases.

In such cases, the diffraction-based approach is helpful, which is although an indirect method for the crystallite size evaluation, but still can provide reliable size-related information. Thus, present-day investigations of the atomic structure of the materials, and determination of the distribution of the atoms inside the crystals and molecules rely mainly on the diffraction methods, in which the diffraction patterns are analyzed [87]. A diffraction pattern is a spectrum of real space periodicities in a material [88].

At the same time, TEM- assisted structural and microstructural characterization at the nanoscale under quasi-kinematical conditions has also been attained through *precession techniques* [89], such as: electron diffraction tomography [90,91], orientation mapping [92], automated crystal orientation and phase mapping [93], and zone-axis precession electron diffraction [94].

The similarity between the three radiations used for the structure analysis- neutrons, X-rays, and electrons is that since the problem is geometric in nature, any of these can be used for determining the coordinates of the centres of gravity of the atoms present in a crystal. The dissimilarities between the three approaches arise mainly from the differences in the interaction of the given radiation and the specimen. The radiation from the X-ray tube consists of a continuous spectrum of energies along with the characteristics lines since electrons from the source may either lose their energy in a series of collisions with the target atoms or a single collision may knock off an inner shell electron, leaving the atom in an excited state [95]. The latter, i.e., the characteristics lines are mostly used in crystal structure studies and contain an appreciable fraction of the total X-ray energy from the X-ray tube.

In electron diffraction studies, a monochromatic beam of electrons is generated by the direct acceleration of the charged particles through electric potentials of 30-300 keV. As far as the interaction with matter is concerned, electrons are scattered by both electrons and nuclei in a material, whereas the X-rays are scattered due to the interaction between the negatively charged electrons and the incoming X-rays electromagnetic fields [60]. The distribution of electrons is over the atomic volume having a linear extent of around 1 Å, which is approximately the wavelength of the X-ray signals used. Thus, pronounced interference effects are observed because of scattering by individual atoms. The Fourier treatment of the X-ray diffraction data provides a picture of how electron density is distributed within the crystal, wherein the peaks correspond to the atoms. However, if the incoming radiation is an electron, then the nuclear scattering is not negligible in comparison with the electronic scattering. Consequently, electron density distributions in crystals are detected by the X-rays whereas electrostatic potential distribution in crystals is detected by the electrons [96]. The Fourier treatment of the electron diffraction data gives a picture of the distribution of the electrostatic potential in the lattice, with the maxima corresponding to the atoms (nuclei) [87].

The ratio between the coherently scattered radiation to the incident radiation on the specimen dictates the absolute magnitude of the scattering amplitude, and hence the extent of interaction occurring between the specimen and the radiation. However, both for electrons and X-rays, the scattering amplitude is found to decrease as a function of $\sin \theta / \lambda$, based on the *form factor* that is more prominent for the electrons. In contrast, the scattering amplitude for neutrons is found to be isotropic since the interaction of the neutrons is mainly with the nucleus, and nucleus-electron interaction is minimal. This has been shown schematically in Fig. I-9 for scattering of different radiations by Cu atoms, adapted from [97]. Moreover, the wavelength of the neutron is of the order of 10^{-8} cm , which is much larger than the size of the nucleus, typically of the order of 10^{-13} cm [97]. The form factor for the X-rays and the electrons are representative of the scattering amplitude generated by an atom to that caused by a single-bound electron. Thus, knowing the scattering amplitude of a single electron, the theoretical value of the scattering amplitude for X-rays and electrons can be calculated. For a particular nanopowder studied in this thesis- CeO_2 , the plot of structure factor, i.e., scattering from a unit cell for the two types of radiations- X-ray and electron, has been also plotted in Fig. I- 10. The difference in these values has a direct consequence on the calculated intensities in the powder diffraction patterns (equation 14, chapter II).

Next, it has been found that the scattering cross sections are proportional to the squared values of the scattering amplitudes. For neutrons and X-rays, the scattering cross sections are of the same order of magnitude as the scattering amplitudes, but for electrons, these vary by factors of few millions.

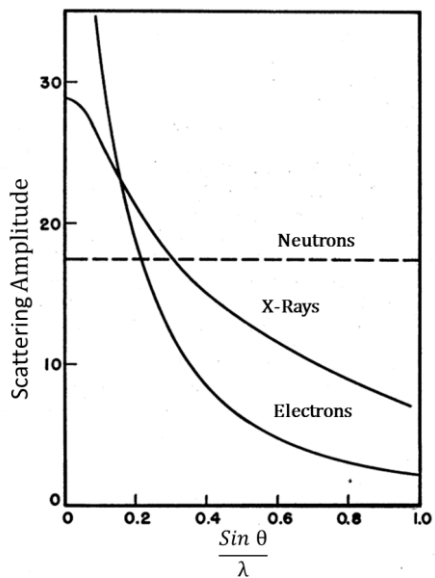


Figure I- 9 The amplitude of scattering by copper atoms for different radiations [97].

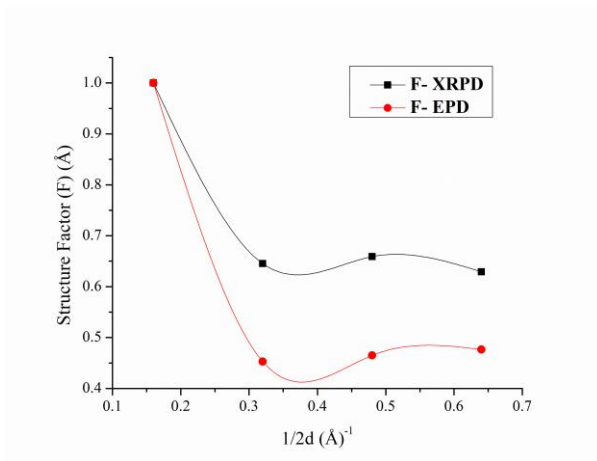


Figure I- 10 The amplitude of scattering by CeO_2 nanopowder for X-ray and electron radiations. Note: The values have been normalized.

For a comparative study, the average absolute value of the atomic amplitude of scattering for X-rays, electrons, and neutrons are 10^{-11} cm, 10^{-8} cm, and 10^{-12} cm, respectively [87]. Since the intensity of scattering is proportional to the square of the scattering amplitude, the corresponding scattering intensities for X-rays, electrons, and neutrons will bear the ratio $1:10^6:10^{-2}$ by a single atom. Thus, in order to get approximately the same measure of the intensity of scattering, the thickness (size) of the specimens must be varied depending on the type of radiation. An approximate value of the linear dimensions is 1 mm for X-rays, $10^{-5} - 10^{-4}$ mm for electrons, and several millimeters for neutrons. A direct consequence of the large variation in the scattering intensities is the difference in the necessary exposure time required for recording the diffraction patterns photographically. For X-rays, the duration could be up to several hours, while electron diffraction patterns could be collected within seconds.

Diffraction line profile analysis is considered to be a versatile and non-destructive method to characterize the microstructure of a material. Ideally, the intensity plot from an infinite crystal should comprise diffraction lines without width at some discrete diffraction angles [98]. However, both the instrument and the specimen under observation cause a broadening of the diffraction lines. The imperfect crystalline structure of the specimen is deduced from the broadened diffraction lines in terms of the effective crystallite (domain) size, macro and microstrain. The origin of these parameters is attributed to the finite size of the crystallites, micro-twins, stacking faults, dislocations, stresses, etc [99]. In this regard, the coherent domain size is considered as the size of a coherently diffracting region inside a grain that represents a fault-free region between dislocations.

However, there are some disadvantages of EPD as compared to single crystal diffraction: information is reduced to 1D, and peak overlapping may be critical for materials with long cell parameters, pseudo-symmetries and/or for polyphasic samples.

There are two basic techniques through which the diffraction-based line profile analysis is performed: i) Fourier deconvolution method adapted by Stokes [100] in which Fourier analysis forms an integral part; ii) real space techniques, such as integral breadth [101], variance method [102], and peak fitting techniques [103].

The development of the field started when Scherrer [104] in 1918 proposed that the broadening of the diffraction lines is due to the small crystallites.

The average grain size representative of the whole sample can be obtained using diffraction patterns approximated based on the half width at half maximum (HWHM) of the line profile using the Scherrer equation [105]: $d_{hkl} = \frac{k\lambda}{\beta_{hkl} \cos\theta_{hkl}}$; where d_{hkl} is the average grain size along the crystallographic orientation (hkl), i.e., in the direction

perpendicular to the crystal lattice planes with Miller indices (hkl) of the cubic crystallite ; k the crystallite shape factor that depends not only on the crystallite shape, but also on the definition of the average crystallite size [106]; β_{hkl} is the HWHM of the line (hkl) in radians after accounting for the instrumental effects; θ is the Bragg angle.

Uvarov and Popov [107] calculated the crystallite size of nc-TiO₂ having a narrow crystallite size distribution using the Scherrer method applied to XRPD data and also using direct measurement based on the TEM imaging. The Authors noted a very close match between the results obtained up to a crystallite size of 35 nm. He et al.[108] demonstrated that the size determined from the Scherrer equation refers to the grain height that is normal to the crystal plane, and the upper possible detection limit of crystal grain size as 137 nm for Si (100). However, although the Scherrer formula has helped researchers for decades to get a rough estimate of the crystallite size, it neglects the importance of microstrains and its implications on the powder diffraction pattern. Moreover, there are problems associated with the incorrect incorporation of instrumental broadening and overlapping peaks [108,109].

After Scherrer's formula, the next advancement in the field occurred when Stokes and Wilson [110] in 1944 developed a more complex and exact theory for the line broadening and also included lattice strain as a broadening source. Stokes [100] proposed a Fourier-deconvolution technique to extract the physical broadening from the observed patterns. Further development of the method of Stokes [100] was made by Bertaut [111] and Warren and Averbach [112], and a more detailed description of the complete line profile shape was possible. The authors observed that the order of diffraction (i.e. contribution from a particular crystallographic plane) had a key role in the determination of the microstrain. Hall [25], similar to Stokes and Wilson [110], demonstrated that crystallite size as well as stress effects cause the broadening of the diffraction profiles. The Williamson-Hall equation [113] attributes the size and strain to the integral breadth determined from each reflecting plane through a convolution of the Scherrer crystallite size and Stokes-Wilson strain broadening.

The major drawback of deconvolution method of line profile analysis is that in the case of large peak overlapping and weak physical broadening, the Stokes method cannot be applied without significant errors. Moreover, the mathematical process involved in the analysis could be cumbersome. Thus, with the development of Rietveld refinement [114] and subsequently of other full powder pattern fitting techniques [115,116], the major focus in the last decades has been on the integral breadth methods.

Rietveld refinement [114], based on the least squares approach is carried out on the whole diffraction pattern to obtain the best fit between the measured and calculated diffraction profiles. The Rietveld method applied to the EPD is a major topic in this thesis and has been discussed in Chapters II, IV, V, and VI.

Chapter II: Basic concepts

II.1 A brief history of TEM

The wave-like nature of the electron, with a wavelength substantially smaller than visible light, was first theorized by the scientist Louis de Broglie in 1925 [117]. Not long after this and with confirmation of the wave nature of electrons by different research groups using electron diffraction, the invention of the powerful material characterization tool is credited to the scientists Ernst Ruska and Max Knoll. The two scientists laid the foundation of how electron lenses may be used for the collection of electron images in their paper "Das Elektronenmikroskop" [118], published in the year 1932. The revolutionary invention overcame the problem of lower resolution associated with visible light, and since then resolution has defined the progress of the technology of the associated field. Microscopes with theoretical resolutions of 10 nm were developed by the 1930s and these were further reduced to 2 nm by 1944 [119].

The first commercial TEM was developed by Siemens company in the year 1939, around the same time when the theory of electron optics was being studied by Otto Scherzer [120]. After the second world war, majorly two companies- JEOL in Japan and Philips in Europe made the tool available commercially, leading to a growth in its usage both in the field of biology and material science. The usage of TEM to study thin metal specimens prepared using the electrolytic method was pioneered by Robert Heidenreich [121]. The study of defect structures in the metals that still remains a strong hold of TEM was studied in aluminium by Hirsch et al.[122] and in stainless steel by Bollmann [123] in the mid-1950's. Around the same time, Vainshtein [124] in 1956 developed the concept of oblique-texture electron diffraction (OTED), which facilitates the illumination of a large amount of slightly disoriented flat crystals, emphasizing the mosaicity of the sample [125]. Although sample preparation may be complex for OTED and analysis of single nanocrystal cannot be performed, OTED analysis involves reduced dynamical effects and allowed the structure solution and refinement of a number of organic and inorganic phases [126]. In line with the innovations in the field, direct lattice images of thin films of materials became an area of interest- copper and platinum phthalocyanine by Menter and Bowden [127] in 1956; gold by Komoda [128] in 1964; graphite by Heidenreich et al. [129] in 1968.

The next landmark achievement of the field happened in the 1970's when commercial STEM became available. Although a formal development of the instrument had been done by Manfred von Ardenne in 1938 [130], it was the work of Albert Crewe and co-workers in the 1960s that established STEM as a practical technique by employing a field emission gun providing a coherent source of electrons [131]. Around the same time, energy dispersive X-ray spectroscopy (EDXS) was also developed, and by mid-1970 became an option on many TEM, opening the pathway for the knowledge of the

elemental composition of the materials. The quantitative measurements were possible with the detector calibration based on the Cliff and Lorimer method [132,133]. Modern TEMs now offer a unique combination of structure analysis through electron diffraction and HREM with elemental analysis using EDXS and EELS.

By mid-1990 it was realized that the resolution could be further improved only if the chromatic and spherical aberrations were compensated. The advancement in this direction was provided by Haider et al. [134] with the development of the first spherical aberration-free TEM, providing a resolution of the order of 0.1 nm. At the same time, precession electron diffraction techniques for structural studies under quasi-kinematical conditions became popular due to the pioneering work of Vincent & Midgley [89]. Since the year 2000, there has been a rise in the 3D ED techniques with new protocols for the collection of diffraction patterns [135], and all of them essentially aim to increase the number of observed reflections, reducing dynamical effects and decreasing data acquisition time as compared to classical oriented patterns [136–138].

II.2 Transmission electron microscopy and diffraction

II.2.1 Magnetic lenses

The electron gun is mounted at the top of the TEM column and the generated electrons are accelerated against an accelerating voltage in the range of 100-300 keV. To generate the electron beam, materials with low work functions for the emission of electrons are employed as the source. In a thermionic type of electron gun, the filament made of tungsten fibre or LaB₆ crystal is heated using an electric current that supplies the required energy for the emission of the electrons. In this case, an intense beam with a large energy spread is produced. In modern TEMs, field emission guns (FEG) are used in which the electrons are emitted from a tungsten needle with a very sharp pointed tip by applying an electric field. In this case, a beam with higher coherence is generated that can be focussed to a very tiny spot.

The TEM works on many of the same principles of optics as the light microscope. Instead of using a convex lens, a magnetic lens, which consists of a coil of Cu wire inside an iron cylinder as shown in Fig. II-1, is used. The passage of electric current through the coils creates a magnetic field that is essentially inhomogeneous, being weaker at the center of the lens and increasingly stronger towards the bore of the cylinder. The net effect of this magnetic field is that a parallel beam of electrons is focussed into a spot (crossover), owing to electrons moving closer to the lens center being less deflected as compared to those passing far from the center. For an electron with a charge q ($=-e$), passing through a magnetic field of strength \mathbf{B} and electric field

of strength E , a Lorentz force F is experienced, which is given by the following expression:

$$\mathbf{F} = -e(\mathbf{E} + \mathbf{v} * \mathbf{B})$$

The focussing effects of these magnetic lenses can be varied by changing the magnetic field B that the electrons are subjected to. As clear from the expression of the Lorentz force, the force F being a vector product is perpendicular to both velocity and the magnetic field, causing helical trajectories for an electron motion inside the lens and thereby leading to an image rotation. The magnetic lenses fulfil two crucial tasks in a modern TEM:

- They generate an electron beam having certain characteristics. Those lenses that are part of the condenser lens system, form either a parallel beam of electrons as required for TEM-based studies or a focussed beam for analysis in the scanning mode.
- They form the images- objective lens; and magnify them- intermediate lenses.

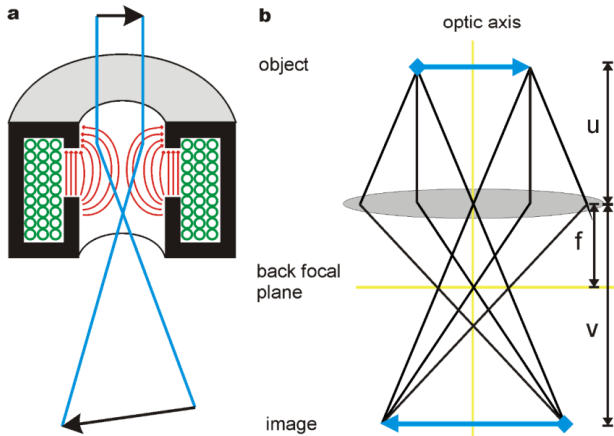


Figure II-1 (a) Schematic showing cross-section of a magnetic lens. The copper wire shown in green is coiled inside an iron cylinder (black). The rotationally symmetric but radially non-homogeneous magnetic field (red) focuses the electron beam (blue). Analogously with a convex glass lens (b), a magnified image of an object appears in the image plane but is rotated w.r.t. to the object (magnetic rotation) [139].

However, these magnetic lenses are notoriously poor in their working abilities and suffer from different types of aberrations that need to be corrected for obtaining high-quality TEM data. A common analogy used to describe the inefficiency of electromagnetic lenses is to compare them with the bottom part of a coca-cola bottle being used as a magnifying glass. The main aberrations present in these lenses include spherical aberration, chromatic aberration, and astigmatism.

Spherical aberration (Cs) in electron lenses exists because the off-axis electrons are deflected more strongly by the magnetic field than those close to the optic axis. The overall effect of this error is that an enlarged image of a point is created in the image plane. Hence, the smallest image of the object is formed just in front of the imaging plane of the lens and is termed the spherical aberration disc of least confusion.

In visible light microscopy, an appropriate concave lens is used to compensate for the spherical aberration of a convex lens. However, in the electromagnetic lens system, a carefully designed aberration corrector system is used to perform a function similar to that of the concave lens.

Chromatic aberration: In electron microscopes, the ideal scenario would be to have the electron beam of a single wavelength or a monochromatic beam. However, there are fluctuations associated with the spread in the energy of electrons emitted by the electron gun. The actual value of the energy spread depends on the type of source that is being used, and it could be up to ~0.3 eV for cold FEG; ~1 eV for LaB₆; ~3 eV for tungsten hairpin filaments. In addition, especially for the thicker samples, a range of energies and corresponding wavelengths are generated due to the interaction of the electron beam with the sample. Since the objective lens bends the electrons with lower energy more strongly, there is again a blurry disk formation at the image plane for a corresponding point in the object plane.

Astigmatism: This error in electron lenses arises when the electrons encounter a non-homogeneous magnetic field. This happens because of the machinability constraint in manufacturing soft iron pole pieces that are perfectly cylindrically symmetrical. In addition, inhomogeneity in the microstructure of the pole pieces, contributions due to the dirty apertures and lack of their proper centering upon their insertion, and asymmetry in the windings plays a role in the increase in the astigmatism error. Astigmatism is corrected with the help of stigmators, devices that apply weak supplementary magnetic fields to compensate for the non-homogeneous magnetic field.

II.2.2 Imaging: Bright field and Dark field

Fig.II-2 shows the TEM column with the arrangement and positions of different lenses and apertures below the specimen stage. The TEM may be operated to form the diffraction pattern from a selected region of the specimen or one of the several types of images. Henceforth, the qualitative or quantitative information of the material microstructure is correlated between the imaging and the diffraction data.

The objective lens system positioned below the sample is the heart of the TEM imaging system since it forms the first image and the diffraction pattern, and the resolution of the entire microscope depends on the quality of the data produced by the objective lens. Images and diffraction patterns are simultaneously formed by the objective lens, and a magnified image of either of these may be focused on the viewing screen. The magnification of the diffraction patterns is expressed in terms of the effective camera length. This is possible because the first projector lens (diffraction lens/intermediate lens) system situated below can be switched between the two settings, i.e., focused

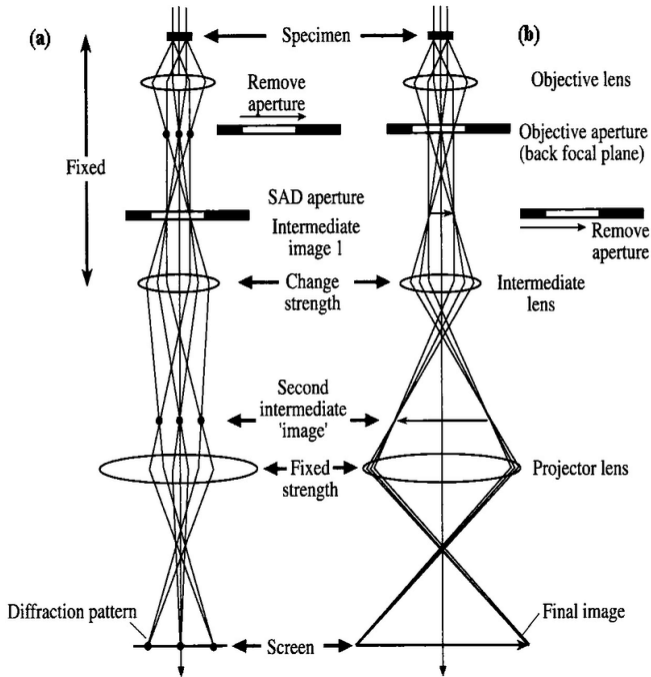


Figure II-2 The two basic operations of the TEM imaging system involve (a) diffraction mode: projecting the diffraction pattern (DP) onto the viewing screen and (b) image mode: projecting the image onto the screen. In each case, the intermediate lens selects either the back focal plane (BFP) (A) or the image plane (B) of the objective lens as its object [60].

either on the image (a) or the diffraction pattern (b). The thin TEM sample is placed in front of the objective lens. The diffraction pattern is formed at the back focal plane of the objective lens and with the recombination of the diffracted beams, the image of the object is formed in the image plane. The diffraction, intermediate, and projector lens

systems below the objective lens perform the function of either focussing or magnifying the diffraction pattern or the image on the fluorescent screen, which is used to convert the electron intensities into visible light signals.

The objective aperture essentially controls the angular range of the electrons scattered by different mechanisms that can pass down the length of the microscope column for the formation of the image. If the objective aperture is centered as shown in Fig. II-3 a), i.e., about the optical axis, then in the absence of the specimen, a bright background would be visible on the screen. An image acquired in this scenario is termed a bright field image. Those regions of the sample that diffract strongly, i.e., through angular range such the diffracted beams do not pass through the aperture because of their high density or thicker regions, will appear darker in such an image. In fact, this effect is called the mass-thickness contrast and is utilized by microscopists in several studies of different materials, whether amorphous or crystalline, biological or inorganic. The usage of the objective aperture provides contrast in the images, since if the objective aperture is not inserted, then virtually all the electrons will contribute to the formation of the image.

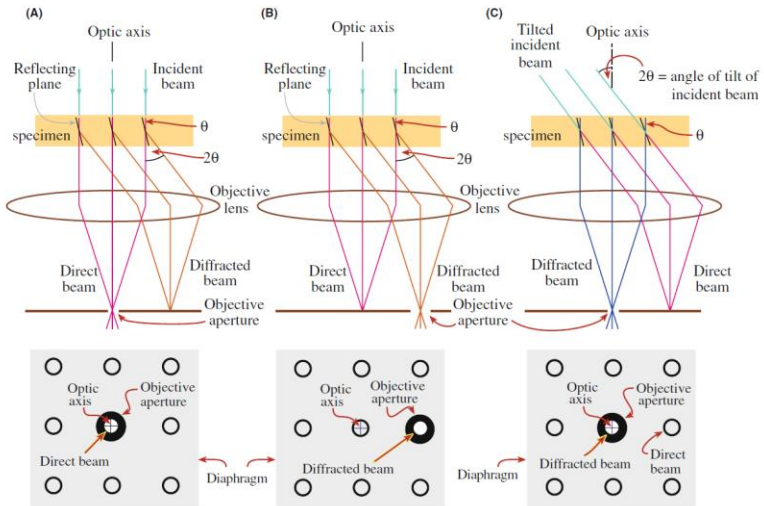


Figure II-3 Ray diagrams showing how the objective lens and objective aperture are used in combination to produce (A) a bright field (BF) image formed from the direct electron beam, (B) a displaced-aperture dark field (DF) image formed with a specific off-axis scattered beam, and (C) a centered dark field (CDF) image where the incident beam is tilted so that the scattered beam emerges on the optic axis [60].

Moreover, an objective aperture can be inserted in the back focal plane in the diffraction mode to select a particular beam to form an image. This approach based on the diffraction contrast is referred to as dark field imaging since in the absence of the specimen the background appears dark. It is often used to study the defect structures in the specimen. In fact, any material feature that alters the planes giving rise to the Bragg reflections, including changes in the composition for the multi-component systems can change the structure factor, which influences the diffracted intensity.

However, if the objective aperture is displaced from the optical axis such that the transmitted beam is intercepted and a diffracted beam contributes to the formation of the image, a dark field image of poor quality is produced (Fig. II-3 b). This happens because of the additional spherical aberration and astigmatism effects encountered when the electron beam path is not close to the optical axis. This problem can be countered by following a better method, wherein the incident electron beam is tilted so that the chosen diffracted beam travels along the optical axis and then passes through the centered objective aperture. The image formed using this technique is called as the centered dark field (Fig. II-3c).

II.2.3 Electron diffraction

The electron beam that has passed through the sample consists of two components: elastically and inelastically scattered electrons. The diffraction pattern can provide crucial crystallographic information. The two parameters of particular importance concerning electron diffraction are the intensity of the scattering and their angular distribution. The well-known Bragg's law has significance in the study of materials with electron diffraction, just as in the case of X-ray and neutron diffraction. The following is a brief description of electron diffraction essential for setting the tone for further topics, adapted from Williams and Carter [60] and Goodhew et al. [40].

Fig. II-4 a) shows the wave vectors or k-vectors incident on (k_I) and scattered by a plane of atoms (k_D), corresponding to the incident and scattered plane wavefronts W_I and W_D (Fig. II-4b), respectively.

The vector K shown in Fig. II-4 a) is the change in k due to diffraction. It can be shown that the magnitude of these k-vectors is equal for an elastic scattering, bearing the relation:

$$|k_I| = |k_D| = |k| = \frac{1}{\lambda} \quad (1)$$

Based on simple trigonometry, it can be seen that:

$$|K| = \frac{2 \sin\theta}{\lambda} \quad (2)$$

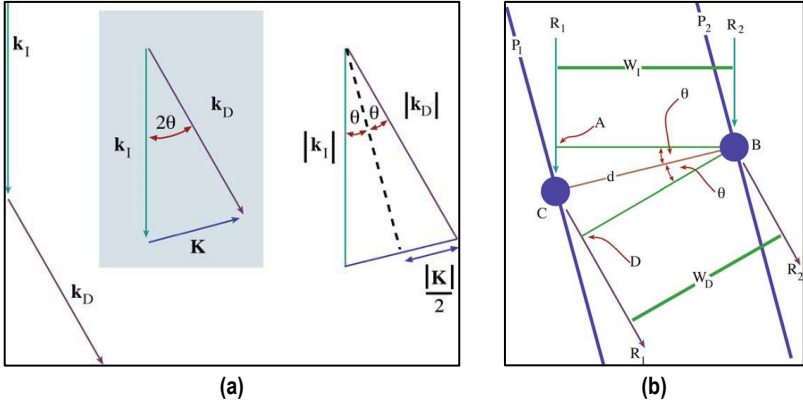


Figure II-4 Definition of the scattering vectors: (a) the incident wavefront normal is k_I , the diffracted wave normal is k_D , K is the difference vector ($=k_D - k_I$); (b) $\sin \theta$ is defined as $K/2k_I$ [60]

Fig. II-4 b) shows the interference between two waves diffracted by two atoms on the planes P_1 and P_2 , normal to the vector CB . The distance travelled by ray R_1 is greater than the distance travelled by R_2 by $AC + CD$. Based on simple geometry, we can see that: $AC + CD = 2d \sin \theta$

For the two waves to interfere constructively, the angle θ equals the Bragg angle θ_B . Then equation 2 can be written as:

$$|K| = \frac{2 \sin \theta_B}{\lambda} \quad (3)$$

The path difference between the two waves in this case, $AC + CD$, is equal to $n\lambda$, where n is an integer. Thus, $n\lambda = 2d \sin \theta$, which is the Bragg's law. For a first order reflection and in combination with equation 1, we can determine a unique value for the wave vector K as K_B :

$$|K_B| = \frac{1}{d} = g \quad (4)$$

where Bragg reflection g may also be represented as a reciprocal lattice vector and is perpendicular to a set of planes.

However, although Bragg law is a necessary condition for a diffracted maximum, it is not a sufficient condition. For a non-zero diffracted amplitude, it is also necessary that the extinction conditions are satisfied for the type of unit cell in question, i.e., the amplitude of scattering by one unit cell (equation 15), determining the structure amplitude, is also non-zero [140].

The relationship between the reciprocal lattice points shown in Fig. II-5a) and the diffraction pattern can be better understood on the basis of Ewald sphere construction, shown in Fig. II-5b). In this construction, the diffracting crystal instead of real space is represented by its reciprocal lattice. The electron beam is represented by a vector of magnitude $1/\lambda$, terminating at the origin of the reciprocal lattice (C). Finally, a sphere with a radius $1/\lambda$ is drawn about C. The sphere is generally shown in two dimensions through a circle, together with a two-dimensional section across the reciprocal lattice. Based on this construction, diffraction occurs if the sphere passes through the reciprocal points. In other words, the Bragg diffraction conditions are satisfied if the Ewald sphere touches the reciprocal lattice points. The radius of the Ewald sphere is very large (270 nm^{-1} for 100 keV electron beam) as compared to the reciprocal lattice vectors (typically 5 nm^{-1}). For small angles of diffraction as encountered in the TEM, the Ewald sphere may be considered a plane.

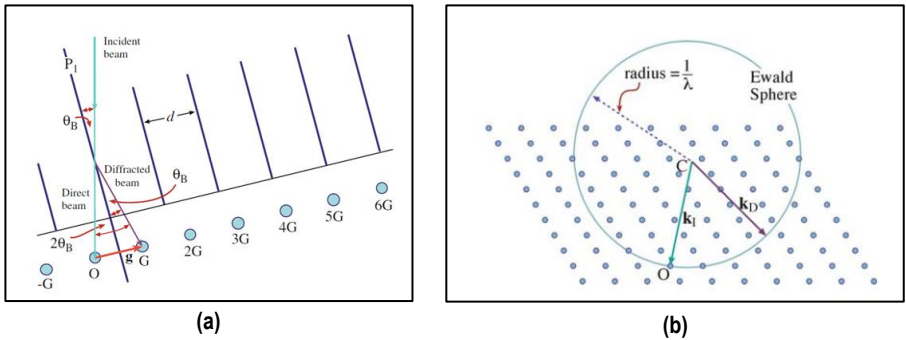


Figure II-5 (a) Diffraction from a set of planes a distance d apart. The planes have been oriented to be in the Bragg diffracting condition (θ_B is the incident angle). Note that the planes are not parallel to the incident beam. The resultant diffraction spots (reciprocal-lattice points) are labeled G , $2G$, etc.; (b) The Ewald sphere of reflection is shown intersecting anon-cubic array of reciprocal-lattice points. The vector CO represents k_i , the wave vector of the incident wave, and O is the origin of the reciprocal lattice. k_D is any radius vector. When the radius of the sphere is similar to the spacing between the points in the reciprocal lattice, as is the case for Xrays, the sphere can only intersect a few points. When λ is much smaller, as for 100-keV electrons, the radius is much larger, the sphere is flatter, and it intersects many more points [60]

The diffraction rings shown in Fig. II-6 in the transmission geometry are formed where the cone of the beams of the diffracted electron beams by the specimen intersects the Ewald sphere. The rings are then projected onto a planar detector by varying the projector lens settings for the purpose of recording the pattern and further analysis. The radius of these rings is related to the Bragg angle of diffraction and the camera length by the expression:

$$R = L \tan 2\theta_B \quad (5)$$

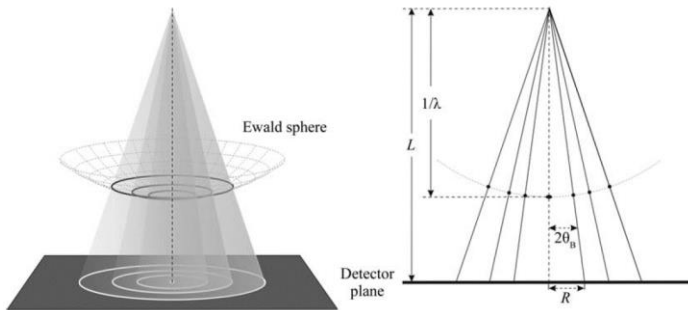


Figure II-6 Schematic diagram of the Ewald sphere construction and the geometry for recording electron diffraction patterns [141]

However, as is often encountered, the crystal may not be oriented exactly at the Bragg angle. In such a scenario, the Ewald sphere could miss a reciprocal lattice point by a vector s (Fig. II-7 a). As proposed earlier, this should be a condition wherein there is no diffraction from the crystal planes, yielding no diffraction intensity. However, in the case of real crystals, the condition for Bragg diffraction is modified, resulting in substantial diffraction intensity even if the condition of the Ewald sphere passing exactly through the reciprocal lattice points is not satisfied.

The above phenomenon maybe explained by considering the penetration of an electron beam through a material of thickness t as shown in Fig. II-7 b) divided into different slices of equal thickness.

The passage of the electron beam through each of these slices induces changes in the phase and amplitude scattering of the electron scattering. The total intensity of the scattering I_g is determined by adding the scattering from all the slices, taking into consideration the phase differences induced. It can be shown that the diffracted intensity is given by:

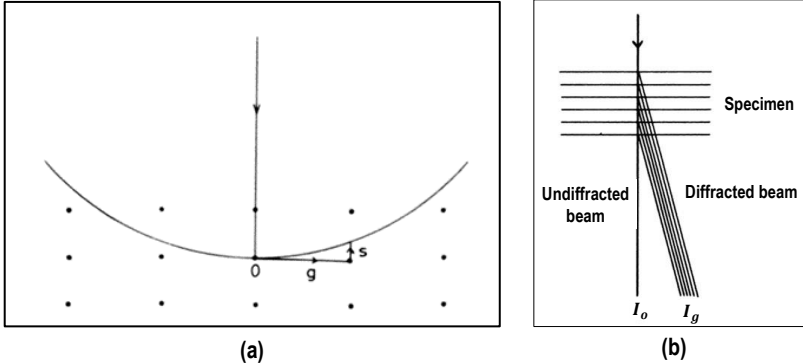


Figure II-7 (a) The Ewald sphere diagram for a crystal oriented such that the reciprocal lattice misses the reflecting sphere by a vector s ; (b) Schematic diagram showing the path differences between electrons scattered at different depths in a crystal [40].

$$I_g = \left(\frac{\pi}{\xi_g} \right)^2 \frac{\sin^2(\pi t s)}{(\pi s)^2} \quad (6)$$

ξ_g is a constant for a material for a fixed value of \mathbf{g} , and is known as the extinction distance. It is given by the equation:

$$\xi_g = \frac{\pi V_c \cos \theta_B}{\lambda F_g} \quad (7)$$

In the above expression, F_g is the structure factor and V_c is the volume of the unit cell.

Fig. II-8 a) represents graphically the variation of diffracted intensity I of the electron beam with variation in the diffraction angle from the Bragg diffraction ($\theta_B, s = 0$). The graph clearly shows that although the diffracted intensity would be maximum at the Bragg angle, there is still diffraction occurring when s is not equal to zero. The width of the main central peak at half of its height is $1/t$, suggesting that the thinner the crystal, the greater the chances of diffraction occurring even when there is a variation in the angle from the Bragg angle of diffraction.

The corresponding relaxation in terms of the Ewald sphere construction may be represented by enlarging the reciprocal lattice points in a direction normal to the specimen, such that we have rods in Fig. II-8 b) (usually referred to as rel rods) instead of points, providing greater chances of the passage of the Ewald sphere through these. Again, since the lengths of rel rods are inversely proportional to the material thickness, a thinner specimen will produce a greater number of diffraction spots.

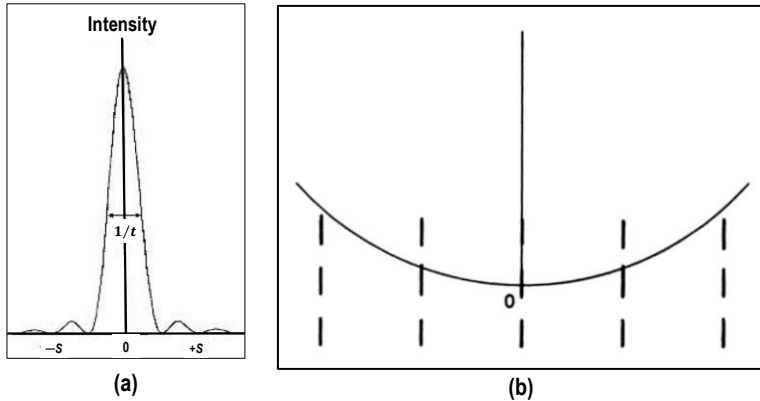


Figure II-8 (a) The variation of diffracted intensity with deviation from the Bragg angle for a crystal of thickness t . (b) The Ewald sphere construction for a thin crystal [40]

II.2.3.1 Electron diffraction: Kinematic and Dynamical diffraction formulae

The elementary assumption of the kinematical theory of diffraction may be stated as follows: if the radiation (X-rays, neutrons, or, electrons) is incident on a limited number of scattering centers (atoms), then the absolute magnitude of the amplitudes of scattering of the radiation and correspondingly the intensities of the scattered beams will be smaller compared to the intensity of the primary beam [87]. Under this assumption, it is permitted to ignore the energy lost by the primary beam during the interactions resulting in the formation of coherently scattered radiations. At the same time, the coherent scattering of the secondary beams, which in their turn also act as primary beams, gives rise to new diffracted beams, is also neglected. As the volume (i.e., the number of scattering centers) giving rise to the coherent scattering increases, the intensities of the secondary beams would also increase, and then the description of the process must be rather based on the dynamical theory of scattering. In this theory, the secondary scattered beams are not neglected and they are qualitatively equivalent to the primary beam.

Electron diffraction patterns can be obtained for amorphous or nanocrystalline materials. Since electrons have a very short wavelength, it is possible to observe the powder diffraction rings having a large range of S ($=\sin \theta/\lambda$). Both X-ray diffraction and electron diffraction use atomic scattering and interference of the waves for probing the

atomic structure of the material. However, a major difference is that since the electrons are charged particles and hence the interaction with the material is very strong. Consequently, electrons are influenced by the electrostatic potential distribution, whereas for X-rays the scattering function is electron density distribution, and both of these peak similarly at the atomic sites. Thus, much smaller crystals of the range 10^3 nm^3 can be studied using electron diffraction [96].

The most commonly used energy ranges of high energy electrons is 100-400 keV and the corresponding wavelengths of electrons for these are roughly fifty times smaller than those for the X-rays. The scattering angles for the electrons are extremely smaller and fall in the order of 0.01 radians and to a useful approximation, the diffraction pattern represents a planar section of the reciprocal space [142]. The fact that the elastic scattering of the incoming electron beam is several magnitudes higher than that for the X-ray has an impact on the structural/microstructural analysis using electrons as a possible radiation. A favourable consequence is that electron diffraction patterns can be obtained from small single crystal regions having very small thickness equal to a few layers of atoms. A serious drawback of the strong scattering is that the otherwise simple kinematical approximation, based on which the X-ray scattering phenomenon is analyzed is not suitable for electron diffraction except for very thin crystals constituting light atom materials. It has been observed that strong dynamical effects may be observed for crystals that are as small as 100 Å, or even lesser for materials having heavy atoms.

The method of structure analysis based on the kinematical approximation relies on the fact that the electron diffraction intensity is directly proportional to the squared values of the structure factor amplitudes [143]. The Blackman two-beam correction model provides the intensities of the reflections in terms of the crystal thickness and electron wavelength [144]. In MAUD program, it is possible to include the corrections of the Blackman model with the usual approximations in the refinement [145]. The dynamic diffracted intensity I_d in terms of the F_{hkl} can be expressed as follows [141]:

$$I_d \propto |F_{hkl}| \int_0^{A_{hkl}} J_0(2x) dx \quad (8)$$

Here, $A_{hkl} \sim \frac{\gamma \lambda |F_{hkl}| t}{V_c}$, the upper limit of the integral. In these expressions, γ is the relativistic constant for the electron; λ is the wavelength of the electron; $J_0(2x)$ refers to a zeroth order Bessel function; t refers to the thickness of crystallites along the beam direction; V_c is the cell volume. It has been proposed that when the value of A_{hkl} is small and the corresponding value of the Bessel function is equal to 1, the dynamic diffracted intensity approaches the value determined by the kinematic approximation [146]. The diffracted intensity based on the kinematical approximation is given by the following expression [147]:

$$I_k \sim \frac{I_0}{4\pi L} \frac{\lambda d_{hkl}^2 m_{hkl} V_{sample}}{V_c^2} |F_{hkl}|^2 \quad (9)$$

However, if the value of A_{hkl} is relatively larger, the integral of the Bessel function approaches a value of 1/2. In such a case, the diffracted intensity is found to be proportional not to the squared value of the structure factor, as predicted by the kinematical approximation. Then, the expression for the dynamical intensity is given by:

$$I_d = \frac{I_0}{4\pi L} \frac{d_{hkl}^2 m_{hkl} V_{sample}}{V_c \gamma t} |F_{hkl}| \int_0^{A_{hkl}} J_0(2x) dx \quad (10)$$

where, L is the camera length; d_{hkl} is the interplanar spacing; m_{hkl} is the multiplicity of the reflection; V_{sample} is the sample volume.

In this regard, it is important to highlight the contribution of Palatinus et al. [148], wherein the authors used the precession electron diffraction technique for structural refinements using electron diffraction patterns, and obtained better results for the full dynamical refinement, as compared with refinement using kinematical and two-beam approximations. However, the focus of thesis work is rather on microstructural evaluation, using ring SAED patterns, which can at best be analyzed under the two-beam dynamical approximation.

II.2.4 Selected area electron diffraction (SAED) and its types

It is often useful to form the diffraction patterns from only selected areas of interest of the specimen. There are two fundamental techniques for performing this task. In the first method, which is the major area of this thesis work, using an aperture called the selected area electron diffraction (SAED) aperture, only a smaller portion of the total illuminated area is selected. In an alternative method, the beam is condensed in the form of a small spot and the diffraction pattern is then collected from the whole of the small illuminated region. This latter technique is referred to as convergent beam diffraction and the diameter of the beam at the specimen stage is controlled by the condenser lens system.

The EPD formed using the technique shown in Fig. II-2a) refers to SAED. The pattern is formed through the electrons that are scattered from a limited region of the sample, described by the size of the selected area (SA) aperture. Using different-sized SA apertures, specific material features may be studied. The size of the SA apertures used in this thesis were: 800 μm , 200 μm , 40 μm , and 10 μm . The formed SAED patterns can be magnified using different camera lengths. The major interesting feature of a SAED pattern is that illumination of a large area of the specimen is possible, particularly useful for recording the diffraction patterns for polycrystalline

materials (for instance, nanoparticles). It is also suitable for radiation-sensitive specimens like organic thin films since low-dosage electron diffraction can be achieved.

The physical appearance of the SAED patterns can provide information regarding the crystalline or amorphous nature of the material under observation (Fig. II-9). The diffraction pattern from an amorphous material will constitute fuzzy (diffused) rings or halos due to the lack of any regular spacing of atoms in the structure of the material. For crystalline materials in particular, the number of grains contributing towards the formation of the diffraction pattern can influence its appearance. A single crystal, oriented in such a manner that a selected number of families of crystallographic planes contribute towards the diffraction pattern (those satisfying Bragg's law conditions), will yield a regular array of spots. Diffraction data obtained from several crystals (Fig. b) that are oriented in different directions will generate a rather complicated pattern as the final pattern collected will be the summation of the contributions from all the selected crystals. The diffraction spots fall on rings that have a constant value of r , and are not randomly distributed but only selected spots along a particular radius of the ring are observed. If the number of randomly oriented crystals selected is still further increased, then the diffracted spots on the rings become hard to discern and the collected pattern is said to be a continuous ring pattern. Such ring patterns have been studied in this thesis. In conventional TEM-based structural or microstructural investigations of nanostructured materials, ring diffraction patterns are of primary importance.

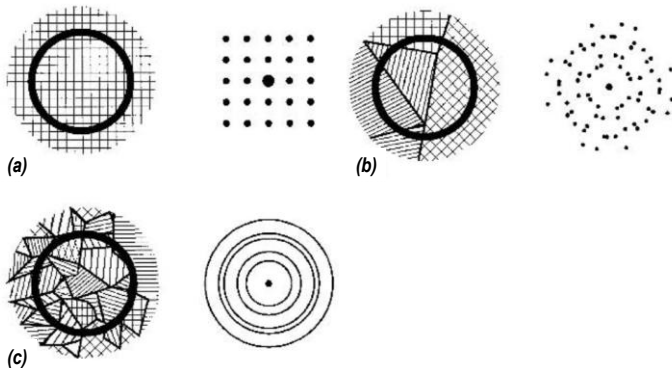


Figure II-9 Types of diffraction patterns that arise from different specimen microstructures. (a) A single perfect crystal. (b) A small number of grains - notice that even with five grains the spots begin to form circles. (c) Many randomly oriented grains - the spots have now merged into rings [40].

II.3 Energy dispersive spectroscopy

Whenever a specimen is bombarded with high-energy electrons in an electron microscope, X-rays representative of the atoms present in the material (characteristic X-rays) is produced. X-ray microanalysis refers to using X-rays for analyzing specimens, down to the micro or nanoscale. Concerning the microanalysis, the study could be performed qualitatively or quantitatively. The measurement of the wavelengths (or energies) of each characteristic X-ray can help us in determining the elements present in the specimen. On the other hand, calculating how many X-rays of any kind are emitted every second can give an idea of the concentration of the element present in the specimen. If a crystal spectrometer fitted having a diffracting crystal is used to detect the X-rays based on the wavelengths, then the technique is termed wavelength dispersive X-ray spectroscopy (WDXS). Contrarily, if an energy dispersive spectrometer is used, then the technique is called energy dispersive X-ray spectroscopy (EDXS).

EDXS finds large-scale applications in electronics, physical and chemical sciences, and forensic-related investigations. However, the usage of the technique in materials science and engineering is unparalleled. EDXS helps in the identification of the phases, structure, presence of impurities, and verification of the quality standards.

The spatial resolution in the X-ray analysis in SEM is limited by the size of the sampling volume which is of the order of $1 \mu\text{m}^3$. This resolution is smaller than that is usually obtained in electron microscopy images and many material features are indeed smaller than $1 \mu\text{m}^3$, requiring higher resolution. A reasonable method to counter the problem is preparing thin samples, like those used for TEM-based studies.

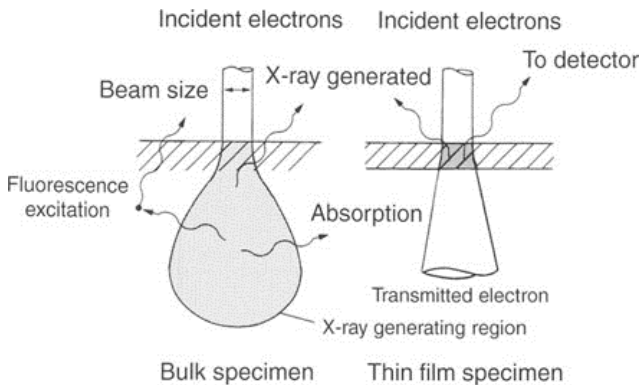


Figure II-10 Broadening of the incident electron beam in a specimen [149]

Although the lateral spread of the beam increases with penetration depth and the shape of the interaction volume depends on the energy of the electron beam, the average atomic number of the specimen material, for a sufficiently thin specimen the spread of the beam is much smaller. This has been highlighted in Fig. II-10. For best results in TEM-EDXS analysis of thin films, the electron beam must impinge on an area to be studied using a finely focused probe. Since the number of X-rays emitted from a thin film is many times smaller than from bulk material, the detector must be positioned at a suitable inclination very close to the specimen.

To quantitatively determine the concentration of an element present in a bulk specimen under study, we calculate the number of characteristic X-ray counts in a fixed time interval from the specimen (N_{spec}) and compare it with the number of characteristic X-ray counts from a standard material (N_{std}). Then the concentration of the specific element in the specimen (C_{spec}) is given by:

$$C_{spec} = \frac{N_{spec}}{N_{std}} \times C_{std} \quad (11)$$

In the above expression, C_{std} is the accurately known composition of the element in the standard material. N is the peak count once the background has been subtracted. Of course, the determination of a correct background is a prerequisite for accurate quantification and many modelling and filtering routines are adopted.

The problem associated with the above technique is that the specimen constituting several elements under observation is compared with a series of standard elements, that are essentially pure elements. Consequently, corrections are required in equation (11) in terms of atomic number (Z), absorption (A), and fluorescence (F) because of differences in the properties such as density and the atomic number of the standard and the specimen. The correction is commonly referred to as ZAF correction and computer programs usually produce satisfactory results, especially for the elements that are present in abundance in the specimen.

As far as thin films are concerned, under certain scenarios, the quantitative analysis may be easier than the bulk materials. This is mainly because the absorption and fluorescence corrections may be neglected since the path lengths traversed by the X-rays in thin films are extremely short. It has been noted by Cliff and Lorimer [132,133]:

$$\frac{C_A}{C_B} = k_{AB} \times \frac{N_A}{N_B} \quad (12)$$

In the above equation, N_A and N_B refer to the measured characteristic X-ray intensities of any two elements A and B, respectively; C_A and C_B are their respective weight fractions in the specimen. The scaling factor k_{AB} depends not only on the two elements but also on the operating conditions and the detector. Usually, to avoid the

determination of k for all possible combinations of elements, it is preferred to calculate it for all the elements required in terms of a single element, usually Si. So, if k_{ASi} and k_{BSi} have been determined using alloys or minerals of known compositions, then k_{AB} can be expressed as k_{ASi}/k_{BSi} .

II.3.1 Fluorescence Yield

The elementary process leading to the determination of the chemical composition of the specimen either in a qualitative or quantitative manner is the ionization of the inner shells of atoms of any of the elements present by the fast-moving electrons. The process of ionization causes the atom to become unstable, leading to de-excitation occurring within a time span of 10^{-14} s after the ionization [150]. The first process of de-excitation involves a single electron, which transfers its state from a less-bound outer shell to a more-bound inner shell that has been emptied by the ionization. During this radiative transition, the difference in energy between the initial and final states is emitted in the form of an X-ray photon.

However, an alternative mechanism of de-excitation involving a two-electron process is also possible. During this process, the energy of the ejected electron (Auger electron) is equal to the energy difference between the original excitation energy and the binding energy associated with the outer shell from which the electron is ejected [60]. In this regard, the probability of the emission of an X-ray photon in contrast with the emission of an Auger electron is determined through fluorescence yield, ω , given by the ratio of the X-ray emissions to the inner shell ionizations. The fluorescence yield, ω , is found to be strongly dependent on the atomic number [60], and determined for different elements using the expression:

$$\omega = \frac{Z^4}{a + Z^4}$$

Where, a is a constant, with a value $\sim 10^6$ for the K shell.

Less bound electrons, typically associated with outer shells of light elements, are more prone to emit Auger electron than X-ray photon, leading to problems in EDXS analysis of light elements.

In the framework of this thesis, the emphasis was on integrating the EDX spectrum with the EPD pattern of a nanostructured material. The approach could be beneficial firstly in speeding up the process of the detection of the phases present in an unknown sample. Moreover, in many cases, the diffraction pattern is found to be not sensitive enough for detecting the phases that are present in extremely small amounts but are interesting to be quantified nevertheless. Even for a single-phase material, there are possibilities of substitutional atoms in the form of impurities or dopants being present

at the lattice points. The Rietveld fitting of the EDXS profile in form of a combined analysis with EPD is interesting in these regards and has been discussed in Chapter VI.

II.4 Line Profile Analyses:

The powder diffraction pattern contains information in a strongly integrated form that is in fact a convolution of several sample-related and instrumental effects, further complicated by the presence of overlapped reflections and background, and often with multiple spectral components. Fig. II-11 shows the extensive information content of a powder diffraction pattern [151,152]. Thus, while decoding the different contributions to the experimental pattern, if we perform the analysis in a limited angular range, which is totally attributed to a single reflection (single-peak analysis), the procedure becomes difficult and rather subjective. The study related to the effects causing the shape and width of the diffraction profiles suffers from this serious limitation when using classical methods based on [153]: integral breadths- Scherrer formula [104,105] or Williamson Hall plot [113]; or numerical Fourier analysis- Warren-Averbach method [112]. These were discussed briefly in Chapter I.

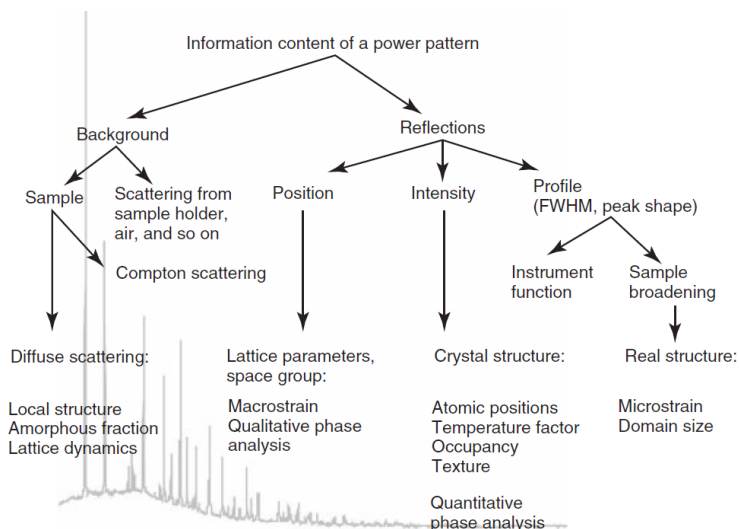


Figure II-11 Schematic picture of the information content of a powder pattern [151,152]

Consequently, there has been an increase in the usage of profile-fitting techniques in the last decades. Most proposed algorithms follow one of the two strategies- i) pattern decomposition, i.e., separation of the pattern into single diffraction profiles; and ii) pattern modeling, i.e., modeling of the entire experimental pattern or a large part of it. In the pattern decomposition techniques, the various identified reflections are fitted using analytical functions, and the background is represented by a suitable polynomial function, with no conditions on the fitting parameters pertaining to the structural and microstructural constraints. For instance, the integrated peak intensity in the pattern decomposition methods is not related to the structure factors and the peak width and shape parameters of the profiles do not depend on the domain size and lattice defects [154].

Pattern decomposition can be performed quickly using most of the available line profile analysis software, and it provides critical information to be used in the subsequent analysis in terms of peak intensity, position, width, and shape. The drawback is that pattern decomposition methods can be rather arbitrary in the definition of the starting parameters used in the fitting routine and the actual number of reflections considered. Thus, it is difficult to assess the uniqueness of the solution and the reliability of the error estimates. Hence, although pattern decomposition techniques offer flexibility, they can turn into ill-conditioned problems [155]. An improvement over the technique considers using a structural constraint to the peak position (See Le-Bail method, Section II.5.4).

The problems associated with the pattern decomposition methods can be rectified using the approach of pattern modelling, in which all the reflections in a powder pattern are modelled based on the parameters describing the physical properties of the specimen. The most renowned and successful technique based on this philosophy is Rietveld refinement (Section II.5). In pattern modelling too analytical functions are used to describe the diffraction profiles, but the important difference is that peak positions and intensities are strongly constrained by a structural model [151]. At the same time, peak width and shape are also constrained by using suitable parametric expressions to account for their change with the diffraction angle [156].

II.5 The Rietveld method

The Rietveld method is called so in honour of its inventor Dr. Hugo M. Rietveld. Dr. Rietveld worked on computer-based techniques in line with the extraction of complete information from the powder diffraction and published two seminal papers on the topic [114,157], afterward making his computer code freely available. The least-square methods developed prior to the Rietveld method worked only on the individual peaks by minimizing the differences between the observed and the calculated intensities.

However, the Rietveld method optimizes the fitting of the entire powder diffraction pattern at the same time.

The approach of the Rietveld refinement is in stark contrast to the single-crystal refinement methods, wherein the structural parameters are fitted against the 'observed' structural factors. Thus, the algorithm requires additional parameters that consider the correct determination of the peak shapes and positions, in addition to the peak intensities determined from the structural parameters. The position of the peaks is influenced by the lattice parameters, plus one or more parameters, depending on the type of instrument used. The shape of the peaks on the other hand depends on many factors, such as broadening due to the crystallites and crystal defects, and instrumental broadening. The Rietveld refinement must model all the Bragg reflections, and the non-Bragg scattering originating due to air scattering (depending on the instrument), instrumental imperfections, and the background. These factors induce complexity in the model [151].

A critical issue in the powder diffraction pattern is that the intensity measurements are usually less accurate as compared to the single crystal methods. One reason behind this is the possible peak overlapping occurring in the polycrystalline samples in contrast to the single crystals. Secondly, the background contribution in the powder method is larger and less separable. Still, the powder diffraction methods have their own significance in structural studies. Firstly, for many materials, only the polycrystalline state can be synthesized. Moreover, the single crystals available may actually not be genuine representatives of the bulk state. Secondly, and which is the area explored in this thesis work, the additional parameters determined through the Rietveld refinement of the powder diffraction pattern provide an indirect measurement of the sample features, such as texture, lattice constant, crystallite size, and microstrain.

In the Rietveld method, the best fit between the entire observed powder diffraction pattern and the whole calculated pattern is obtained based on the method of the minimization of the least squares, by refining simultaneously the models for associated parameters, such as the sample characteristics (crystallite size, r.m.s. microstrain, etc.), instrumental functions, and crystal structure(s) [151].

The powder diffraction pattern recorded in the digitized format has numerical intensity values, y_i , spanning over thousands of i in the pattern, comprises the observed/experimental data. The best fit is sought through the least-squares fitting of all y_i 's simultaneously. The quantity minimized during the process is the residual S_y :

$$S_y = \sum_i w_i (y_i - y_{ci})^2 \quad (13)$$

where, y_i is the experimental intensity at the i^{th} step and y_{ci} is the corresponding calculated intensity, respectively; and $w_i = 1/y_i$, is the relevant weight.

A powder diffraction pattern obtained from a crystalline material may be thought to consist of many individual reflection profiles, each having its peak position, height, breadth, and tails that decay gradually from the peak position. The integrated peak intensity is directly proportional to the diffracted Bragg intensity I_K , where K is the set of relevant Miller indices, (hkl).

A major concern in the Rietveld method is that no efforts are made initially for allocating the experimental intensities to particular Bragg reflections and neither to the resolved overlapping reflections. Hence, we need a reasonably good starting model, it mainly being a structure refinement method and not a structure solution method.

The calculated intensities y_{ci} are obtained using the $|F_K|^2$ values determined through the structural model by summing the total contributions of Bragg reflections from within a specified range using the computed structure factors F_K and the background value [15].

$$y_{ci} = s \sum_K L_K |F_K|^2 \phi(2\theta_i - 2\theta_K) P_K A + y_{bi} \quad (14)$$

In the above equation, s is the scaling factor; for a particular Bragg reflection, K ; L_K combines Lorentz, polarization, and multiplicity factors; ϕ represents the reflection profile function that takes into account both instrumental features and possibly the specimen features- broadening due to crystallite size and r.m.s. microstrain, specimen displacement, differences due to absorption; P_K represents the preferred orientation function; A is the absorption factor; $|F_K|$ represents the structure factor for a specified K^{th} Bragg reflection. The atomic scattering factors are to be corrected for electron diffraction.; y_{bi} is the background intensity value at the i^{th} step.

The structure factor F_K can be determined from the equation (15):

$$F_K = \sum_j N_j f_j \exp[2\pi i(hx_j + ky_j + lz_j)] \exp[-M_j] \quad (15)$$

In the above equation, (hkl) are the Miller indices of the diffracting planes; x_j , y_j , and z_j are the position coordinates of the j^{th} atom in the unit cell.

$$M_j = 8\pi^2 u_s^2 \sin^2 \theta / \lambda^2 \quad (16)$$

u_s^2 is the r.m.s. thermal displacement factor for the j^{th} atom and N_j is its site occupancy multiplier.

Observation of above equations indicates that the major difference encountered in the application of the Rietveld refinement to neutron, X-ray, and electron diffraction lies in the atomic scattering factor f_j in equation 15.

II.5.1 Rietveld method applied to EPD ring patterns

Rietveld method has been applied to the EPD patterns of different nanostructured systems in Chapters IV and V. There are two major challenges to the application of the method for EPD that has been conventionally used for XRPD and neutron diffraction data. Firstly, since the EPD is collected from a confined region of the specimen, the average statistics of the data may be really poor as compared to X-ray diffraction experiments. This aspect has been discussed in section IV.3.1 in Chapter IV. Nevertheless, EPD from thin films or small sample areas can reveal material features that are difficult to obtain using bulk characterization methods [145,158]. Secondly, the presence of the dynamical effects in the EPD data renders the quantitative estimation of the scattered intensities very difficult. In fact, the latter is one of the main reasons for the lack of crystallographic studies based on EPD, in contrast to XRPD and neutron diffraction.

EPD patterns are collected on area detectors, such as CCD cameras, imaging plates, or photographic films. For the application of Rietveld refinement on the EPD pattern, the 2D image first needs to be converted to a 1D intensity profile. The experimental conditions to be considered are the optical illumination of the specimen, setting the specimen at the eucentric height of the stage, camera length calibration, and the projector lens focusing. The intensity integration essentially requires four steps: i) identifying the regions of the diffraction pattern for the integration. The beam stopper shadow covering the portions of the diffraction pattern can be manually removed in the latest version (V 2.996) of the MAUD software. ii) Centering of the diffraction pattern. The diffraction pattern usually suffers from centering errors. The magnitude of this error can rise if the transmitted beam is not focussed correctly or if diffraction astigmatism is not corrected to the right extent. iii) Distortion correction. The diffraction pattern in many cases may appear elliptical because of the detector tilting, i.e., the detector not being perpendicular to the electron beam. iv) Finally, for a constant angle, integrating the diffracted intensities. The diffraction pattern is integrated in fine discrete steps of increasing scattering angle, having a fixed interval spacing. All the diffraction pixels falling with a sector (i.e., between two radii) are summed. Some previous MAUD based works on EPD ring patterns Rietveld refinement have been cited [145,158]

All the necessary steps have been discussed in detail in Appendix A1.

Unlike the XRPD, the inelastic scattering in EPD does not produce only a negligible background. The inelastic scattering has also a contribution from the supporting film, if present on the TEM grid. The background of the 1D intensity plot is fitted with a polynomial function. If an amorphous supporting film made of carbon is used, then diffused halos giving rise to broadened peaks are observed [159]. These hamper the profile fitting and may even give the false impression of additional peaks in the powder

diffraction pattern. To counter this critical issue, the diffraction pattern from a naked grid can be collected and fitted separately. The peak intensities and shape configurations obtained then need to be implemented in the Rietveld refinement of the EPD patterns of the real materials.

The unit cell parameters determined from the Rietveld refinement of the EPD are usually subjected to errors due to inaccurate camera length calibration. Although there have been reporting of up to 0.3 % accuracy in the camera length calibration, in most cases a maximum accuracy of around 2 % can be obtained [60]. The microstructure of the analyzed material in terms of the crystallite and microstrain can also be determined. The observed intensity profile is a convolution of the sample-related broadening and the instrumental effects. In terms of the scattering angle, the width of the peaks of the EPD profile is smaller than that of XRPD. However, the coherence length of the electrons is much smaller than that of X-rays [141]. As a consequence, if both EPD and XRPD are collected for the same material, the effective peak width of the EPD is larger [160].

The separation of the instrumental effects from the overall peak broadening is difficult for EPD. This issue has been discussed in Chapter V. Consequently, the microstructural features determined from the Rietveld refinement of the EPD could be subjected to errors, especially for a material with large crystallites. Thus, the average diffraction domain size determined using EPD should be cross-checked with those determined from TEM images.

In summary, although electron diffraction is a very old area of research, Rietveld refinement of the EPD is relatively new. Results obtained for the Rietveld refinement applied to EPD of nanostructured materials are interesting, and these will be highlighted in great depth in Chapters IV and V. The incorporation of two beam dynamical correction helps to counter the research gap existing in the literature of Rietveld refinement of EPD patterns, in contrast to the abundant literature of XRPD and neutron diffraction. The issue of instrumental broadening function determination and its effects on microstructural determination has special significance.

The focus of this thesis is mainly on the microstructure evaluation of nanocrystalline materials through Rietveld refinement of the EPD. However, structure determination of different unknown crystals has also been attempted: Al-Fe alloys [161], metal-cluster compounds [162], and zeolites [163]. The most widely used programs for EPD-based Rietveld refinement are *MAUD* [164,165] and *FullProf* [166].

II.5.2 Peak shape function

The accurate description of the peak shapes of a powder diffraction pattern is essential for obtaining reliable information from the Rietveld refinement. The profile peaks are

influenced by the sample (crystal defects, crystallite size, stress/strain) and the instrument (source of radiation, geometry, holder, etc.), varying continuously as a function of the scattering angle. The profile shape may also vary with the (hkl) Miller indices. The description of these variations using a single peak shape function is difficult [167]. Of the analytical functions available, the most frequently used for X-ray and neutron diffraction data is the pseudo-Voigt approximation [168]. Even in the selected cases where Rietveld refinement has been applied to EPD, pseudo-Voigt is the most common choice [50,169,170]. However, some researchers have also used the Pearson VII function [159,171].

Once the diffraction peaks have been corrected for all the non-Bragg components, for instance, the background and the instrumental effects, microstructural parameters in terms of r.m.s. microstrain and crystallite size may be extracted. Warren [172] demonstrated that the Gaussian function is capable of modelling the strain-related distribution reasonably well. However, a Gaussian function shows discrepancies in modelling the size-related broadening, especially for the small coherent domain sizes [173]. It has been found that particle size effects give rise to a Lorentzian (Cauchy) component towards the peak profile shape [103]. Thus, the best possible candidate for modelling the peak profile shapes is a convolution of the Cauchy and Gaussian function [174], commonly called the "Voigt" function. Improvements in the Voigt function have been made through modifications (Pearson VII and pseudo-Voigt functions) using which, the Voigt function can be varied between the limits of the Gaussian and Cauchy functions. In particular, the pseudo-Voigt function being a linear combination of the Cauchy and Gaussian functions based on the mixing parameter η in the ratio $\eta / (1 - \eta)$, has been found to model the Voigt function with a higher degree of accuracy [175].

Before the refinement of the structural/microstructural or the profile parameters can be initiated, the positions of the experimental and calculated peaks must match closely. In this regard, for 2D EPD images, a calibration procedure using a standard material is required for determining the corrected camera lengths, as discussed in Chapter IV. Larger variations in these calibrated values may lead to the determination of unit cell parameters with large errors.

Just as for the XRPD, it is possible to refine the atomic displacement factors using the Rietveld fitting of EPD. However, it may not always be possible to explain the results straightforwardly. This is primarily because of all the refined parameters, atomic coordinates and displacement factors (Debye-Waller factor) are extremely sensitive to the dynamical scattering in the EPD data. The impact of dynamical scattering on the atomic displacement factors has been discussed in Chapter V, section V.3.2 taking nc-Si as an example. There are multiple reasons for an increased value of the Debye-Waller factor. Firstly, for nanocrystalline materials, local heating of an increased

number of near-surface atoms during the electron beam illumination may lead to a higher value. Secondly, if the acceleration voltage of the electron beam exceeds the material-specific threshold value, then there are chances of rearrangements of atoms in the material [141]. The defects generated as a result of this rearrangement may further lead to an increased value, and this is a dynamical process. Consequently, to reduce complexity, throughout this thesis work whenever the isotropic Debye-Waller factor has been refined, a single refined value has been associated with all the atoms even for multiphase systems.

II.5.3 Phase analysis using EPD

The mathematics for the procedure of quantitative phase analysis is well established. However, due to a significant number of mostly experimental factors, the accuracy of the method is seriously reduced [176]. The geometry of the instrument and the data collection conditions determine features, such as accurate and precise measurement of the peak positions and their intensities, counting statistics, and the resolution of the overlapping peaks. At the same time, specimen features such as i) large broadening due to the crystallites and microstrain causing increased peak width and overlap; ii) preferred orientation of the grain along certain crystallographic directions leading to distorted observed relative intensities in contrast to a nanopowder with randomly oriented grains; iii) the grain size effect, i.e., diffraction data obtained from too few crystallites such that the specimen representative diffraction data is unavailable; iv) micro-absorption, owing to which a selected phase may absorb strongly the incident and the diffracted beams, as compared to the other phases, leading to its underestimation.

Quantification from the powder diffraction methods relies on the precise determination of the contributions from the concerned phases toward the final pattern. The powder diffraction methods can be divided into two groups: i) Single peak methods, where the abundance of any phase in the mixture is related to the intensity measurement of an individual or a group of peaks of that particular phase. However, the technique suffers from the flaws, such as peak overlap, preferred orientations, and microabsorption. ii) Whole pattern powder diffraction methods on the other hand rely on the direct comparison of the experimental diffraction data over a large diffraction angular range with a calculated pattern determined from the summation and scaling of all the phase components based on the crystal structure information in a least square minimization technique [177–179]. Thereafter, the weight fractions are calculated by solving the simultaneous equations considering the scaling factors of the individual phases, and the mass absorption coefficients that are determined from the elemental composition of each phase. The whole pattern fitting method can be applied to complex samples containing disordered materials, wherein the overlapping of the peaks means that the individual peak intensities cannot be measured.

Phase analysis of crystalline materials using the EPD is possible if the structural information of the components is available beforehand. It is a two-step procedure. In the first step, the potential candidate structures must be shortlisted that may be present in the sample. In this regard, the chemical information available from the spectroscopic techniques-EDXS and EELS is helpful in reducing the number of possible candidates (crystalline structures) [150,180]. The identification of the phases present in the specimen is done based on the fingerprinting of the diffraction pattern. However, a semi-quantitative/quantitative analysis validates the existence of the identified phases, and provides additional information like phase fractions and texture.

Nanostructured materials yield ring diffraction patterns. The first step is to convert the ring pattern into a 1D plot of diffracted intensities. For fingerprinting, the minimum information needed is the position of the diffracted peaks, especially those corresponding to the largest d values/ least scattering angles. However, these are not always available in the X-ray diffraction dedicated databases [181]. In any case, the use of the diffraction peak intensities of the EPD for the purpose of fingerprinting suffers from low validity as these could be affected by the texture in the sample and the lack of conformity for the EPD to kinematic diffraction formalism. Thus, phase identification can be ascertained only if one set of the model structure, out of several potential phases, matches the observed intensities based on the best fit. For quantitative modelling, information on the atomic positions of different elements in the unit cell is required. These are usually available in the crystallographic information file (CIF) and can be downloaded from sources, such as COD [182] and AMCDS [183]. The atomic coordinates are not available in the older PDF-2 database [184], but for many of the phases, the information can be obtained from the updated PDF-4+ database [185].

For electrons, the atomic scattering factor is available in International Tables for Crystallography, Vol. C (2004) [186]. In the MAUD software used in this thesis work, electron atomic scattering factors have been included from Peng et al.[187].

The volume fraction of the individual phases is determined at the final refinement cycle of the algorithm. It is assumed that for every pixel of the 2D EPD pattern, the net intensity is a linear combination of the contributions from the individual phases. The following is a brief description of the volume fraction determination using powder pattern fitting adapted from Zuo et al. [141].

The number of equations of the least square minimization procedure is reduced keeping the information of all the equations intact by forming a matrix **A** as:

$$a_{ij} = \sum_k \text{Model}_k(i) \text{Model}_k(j), \quad (17)$$

In the above expression, the summation is conducted for every pixel k for the models chosen for the i^{th} and j^{th} phases, and the vector \mathbf{b} with the background linkage as follows:

$$b_i = \sum_k (\text{Measured}_k - \text{Background}_k) \text{Model}_k(i) \quad (18)$$

Thereafter, using the matrix inversion technique, the vector \mathbf{x} is determined from the equation $\mathbf{Ax} = \mathbf{b}$.

The coefficients of the linear combination, $[x(i)]$, refer to the intensities of the peaks of the phase i on the absolute scale. $I_{max}(i)$ on the absolute scale represents the intensity determined for the strongest peak of the phase i , providing diffracted intensity distribution by one unit cell. Based on these formulations for the phase i , $x(i)/I_{max}(i)$ can yield the number of unit cells in the analyzed volume. Thus, the volume occupied by the phase i in the total volume under consideration could be given by: $V(i)x(i)/I_{max}(i)$, where for the phase i , $V(i)$ represents the volume of the unit cell. Finally, the volume fraction of the phase i , represented by f_i , may be determined as:

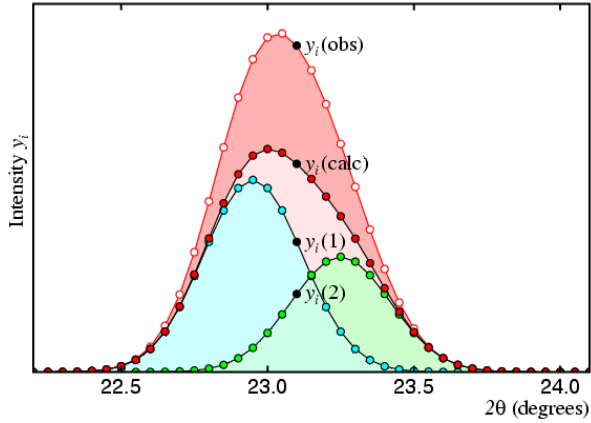
$$f_i = \frac{V(i)x(i)}{I_{max}(i)} / \sum_i \frac{V(i)x(i)}{I_{max}(i)} \quad (19)$$

Lábár et al.[188] observed that the content of the major constituent phases in a mixture can be detected with an accuracy of 10-15 %. The detection limit of course depends on the scattering power of the concerned phase.

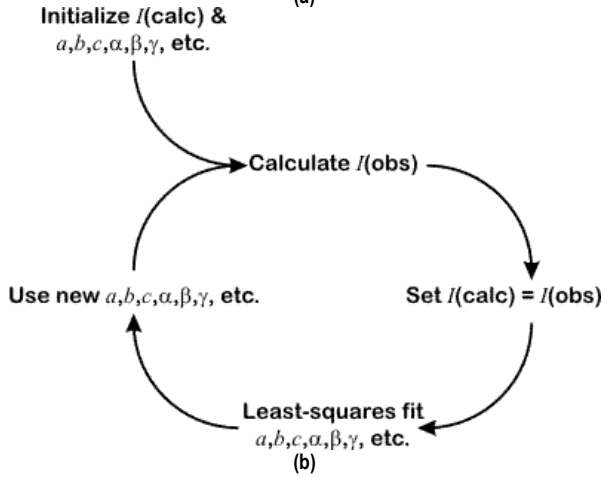
II.5.4 Le Bail method:

The Le-Bail method [189] is a clever adaptation of the Rietveld algorithm. The Le-Bail algorithm proceeds to the determination of the observed intensities of the peaks in an unconventional manner. The unique feature is that the model can work even in the absence of structure factors. Firstly, the calculated pattern is determined by setting arbitrarily all F_K values to unity [190]. Correspondingly, a set of $F_{K,I}$ values that are independent of the structural model are obtained. With these $F_{K,I}$ values, $F_{obs,K}$ are calculated and thereafter the algorithm is iterated at each step by replacing the F_K value with the newly determined $F_{obs,K}$ value. The replacement at successive stages leads to a quick decrement in the differences between the observed and the simulated patterns. The Le-Bail method also treats the intensities of the reflections as arbitrary values, apportioning intensities based on the relative multiplicities in the case of overlapped reflections.

Initially, the peak intensities are set to some arbitrary value e.g., 1000. These arbitrary values are treated as “calculated” values, as if they have been determined from a structure model [191]. In Fig. II-12 a), the observed profile has been highlighted with a red line having white dots and the calculated profile is shown with a black line having red dots. The observed intensity of the peak 1 is given by:



(a)



(b)

Figure II-12 Le-Bail method implementation: a) The calculated and observed peaks; b) the sequence of steps followed in the algorithm.

$$I_{obs}(1) = \sum_i y_i(obs) * y_i(1)/y_i(cal)$$

Similarly, the peak intensity of 2 (in green) is determined as:

$$I_{obs}(2) = \sum_i y_i(obs) * y_i(2)/y_i(cal)$$

Where, $y_i (cal) = y_i (1) + y_i (2)$. The summation in the above equations are taken over all profile points that contribute towards the peak intensity.

The “observed” intensity values determined in this manner will be biased, as depending on the initial $I(calc)$, but will still closely imitate the true observed $I(hkl)$ than any set arbitrary value. The procedure followed in the algorithm is shown in Fig. II-12b)

The Le-Bail method has valuable usage to model an impurity phase, where the unit cell information of the impurity may be known but its structure is unknown. It has also significance if a particular phase is highly textured or insufficient number of grains to provide reliable intensities. For the impurity phase, the peaks are attributed arbitrary intensities. The method also contributes to determine the initial estimates of the non-structural parameters, such as lattice constants, background, and peak shapes in a crystallographic fitting. Moreover, for structural fittings, these non-structural parameters can be fixed at the values of their initial estimates, which helps to speed up the structural fitting process.

In the context of this thesis, Le-Bail method served to characterize the standard nanocrystalline CeO₂ sample where only the peak broadening term was desired with a good match of the peak intensities for the determination of the instrumental broadening function.

II.6 Material Analysis Using Diffraction (MAUD)

MAUD has been extensively in this thesis for Rietveld fitting of data- XRPD, EPD, and EDXS. The program has been developed by Prof. Luca Lutterotti at the Department of Industrial Engineering, University of Trento. It can be downloaded freely from the website: <http://nanoair.dii.unitn.it:8080/maud/> [192]. The main features of the program are as follows:

- MAUD has been written in Java and can run on Windows, Linux, MacOSX, Unix.
- The most interesting feature of the software is that it can be used for neutrons [193,194], TOF [195,196], X-rays [197,198], synchrotrons [164, 199], electrons [169,165], and combined analysis [145,200].
- Quantitative phase analysis with the simultaneous refinements of the crystal structure and texture analysis can be performed. The software has an in-built ‘Quantitative phase analysis wizard’ for the benefit of the user that can perform quantitative analysis sequentially.
- Microstructure analysis in terms of size-strain broadening, anisotropy, defects, and turbostratic disorders are included.
- Combined analysis using MAUD is possible since it is possible to work with multiple spectra from different techniques/instruments. Recently, the option

of analyzing the fluorescence spectra from XRF has been implemented. The valuable addition gave the possibility of exploring the role of chemical information in supplementing the diffraction data from XRD. On similar lines, the possible role of EDXS in supporting SAED for studying localized material characteristics has been attempted in this thesis work, albeit with limitations.

- CIF files can be directly imported into the software. Moreover, in the library of the software, almost all major crystal structures are present for the benefit of the user.
- A special feature, especially concerning this thesis work, is that the program supports working with images collected on 2D detectors (CCD, imaging plates, that are curved or flat). Multiple datafile formats can be directly fed to the program.
- The program supports different optimization algorithms, such as least squares, evolutionary, and simplex. Le-Bail and Pawley fittings are supported by the software.

II.7 ThermoFisher TALOS F200S S/TEM

All TEM data that have been presented in this work were collected on ThermoFisher TALOS F 200S S/TEM at the Department of Industrial Engineering, University of Trento, Italy. Listed below are the essential features of this microscope, and a figure showing it exteriors (Fig. II-13 a) and interiors (Fig. II-13b).

ThermoFisher TALOS F200S S/TEM	
S-FEG	High temporal and spatial coherency; High total beam current
STEM unit	Up to 4x 4kx4k, simultaneous BF/A(D)F/DF/HAADF imaging Segmented DF4 detector for Differential Phase Contrast imaging
X-Twin objective lens system	Constant power providing swift mode switches (Low mag to high mag, TEM ↔ STEM, changing HTs) >5 mm gap, space for more; <i>in-situ</i> and 3D experiments
Total beam current FEG	> 150 nA
Probe current	0.6 nA @ 1 nm probe (200 kV)
TEM Information limit	0.12 nm
STEM HAADF resolution	0.16 nm
STEM magnification range	290 – 330M×
TEM magnification range	25 – 1.50M×
Super-X detector	2 in-column windowless SDDs, LN2 dewar lasts 4 days, 60 mm ² active area giving 0.4 srad solid angle 100.000 spectra/sec; Cleanest spectra
CETA 16M	4kx4k, large field of view

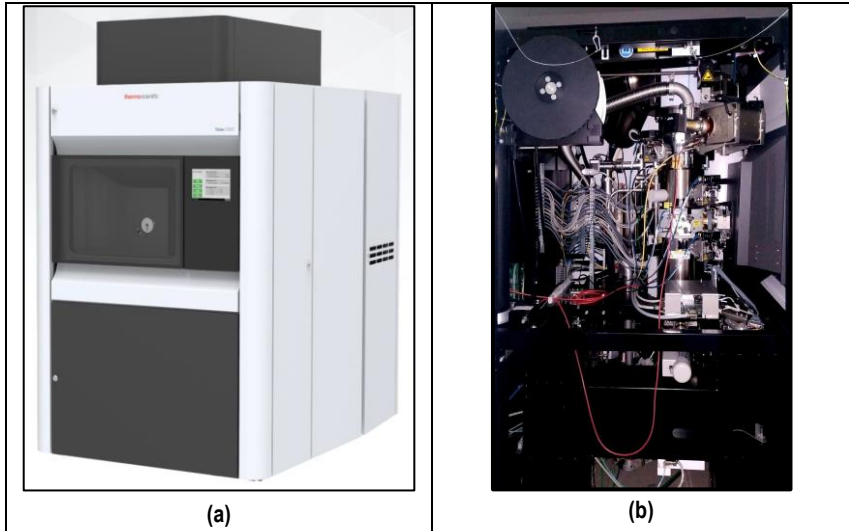


Figure II-13 ThermoFisher TALOS F200S S/TEM instrument at the Department of Industrial Engineering, University of Trento showing a part of exteriors (a) and interiors (b)

Chapter III: TEM sample preparation

III.1 Introduction

Operating TEM involves high costs. Moreover, since the sampling volumes are extremely small, it is prescribed that, if possible, the sample should first be investigated using other techniques like visible light microscopy and scanning electron microscopy. Once a decision has been taken that TEM data are essential, it is of paramount importance that the results justify the resources that have been utilized to procure them. A major hindrance in the collection of high-quality and valuable data is the low-quality specimen.

TEM sample preparation is a vast topic and there are books dedicated to only this issue [201,202]. The primary requirement to be fulfilled during this step is that the produced specimens should be representative of the original material, i.e., the pristine and genuine material features should be preserved. Moreover, it is usually not preferred to have a series of preparatory steps [203], although literature shows that they become necessary in many cases. These may include freezing or drying of the specimens to maintain the particle characteristics and stability in the high vacuum conditions of the microscope [204], the application of a conductive coating of elements like carbon or gold to avoid the charging effects [205], and in some special cases the substrate containing the particles may have to dissolved in a suitable solvent, which are thereafter collected on another substrate that better suits its imaging [206]. Lastly, although still very relevant, the sample preparation should be feasible also in terms of time, so that enough thin samples may be prepared for a reliable statistical reconstruction.

As specified in the previous two chapters, this thesis work concerns the ultrafine fraction of particulate matter and nanostructured materials only. In this regard, we have specified in this chapter two sample preparation techniques- one concerning the particulate matter (PM) collected during dynamometer bench tests [207,208], and the other based on the solution drop method/ drop casting technique [209]. The former has been applied on the PM collected in the form of disc brake wear debris on aluminium substrate. The latter was applied to the other nanostructured materials- CeO_2 , Y_2O_3 , Si, $\text{Fe}_2\text{O}_3/\text{FeOOH}$.

III.2 Sample preparation techniques

III.2.1 PM from disc brake systems

III.2.1.1 Introduction

A major component of ambient air pollution is airborne particulate matter (PM) [210].

PM is a very complex and heterogeneous air-suspended mixture of solid and liquid particles, whose physical and chemical characteristics vary continuously by location [211]. Airborne particulate matter has been classified based on the average aerodynamic diameter, D as: $2.5 \mu\text{m} < D < 10 \mu\text{m}$ are coarse particles, PM_{10} ; $0.1 \mu\text{m} < D < 2.5 \mu\text{m}$ pertain to fine particles, $\text{PM}_{2.5}$; $D < 0.1 \mu\text{m}$ are ultrafine particles (UFP), $\text{PM}_{0.1}$. The size of these particles as well as their chemical composition influences the toxicity, and UFPs having high specific surface area are in certain aspects most dangerous for the environment [212–214]. Thus, the characterization tools to study these particles should possess adequate spatial resolution and the means to identify and quantify the constituents of the particles.

There are different anthropogenic sources of PM causing its presence at a hazardous level, such as cooking using solid fuels, smoking, construction and demolition of buildings, aircraft and ships, hydrothermal and other power plants, and vehicular emissions (exhaust and non-exhaust contributions) [215]. A disc brake unit consists of two brake pads that constitute a complex friction material, and a disc that is conventionally made up of cast iron. Emissions from the wear of disc brakes, ranging from PM_{10} to $\text{PM}_{0.1}$, and with a wide range of organic and inorganic chemical species, have received a lot of interest from different environmental protection agencies [216–218]. The emissions from disc brakes also have a dominant share in the resuspended particles, not only in the vicinity of release spots but even over large distances, especially as concerns ultrafine fraction. Investigations specific to the emissions from automobile disc brakes have been conducted through two methods: laboratory and field tests. Although these latter are interesting for assessing the brake emission behavior under real driving conditions [219,220], they present a critical limitation in the difficulty of creating an enclosure around the brake assembly, capable to avoid PM leakages. In this respect, laboratory tests turn out to be certainly more effective. The detailed design of the collection strategies of PM can be referred to from other works [208]. Here, we will focus only on the sample preparation technique, once the PM has been collected on the substrate.

Fig. III-1 shows the PM collected on aluminum substrates used for capturing airborne PM using a DEKATI ELPI plus impactor. The aluminum substrates are usually sprayed with a siliconic vacuum grease (DEKATI DS515) to provide adhesion on the substrate surface for effective trapping of the incoming PM. Two aerodynamic particle size ranges $1.6\text{-}2.5 \mu\text{m}$ (Sample A, Fig. III- 1a), and $108\text{-}170 \text{ nm}$ (Sample B, Fig. III-1b) have been considered in this study. The biggest challenge is to work with the finer fraction of the particles. These particles are in a very limited amount and have low surface density.

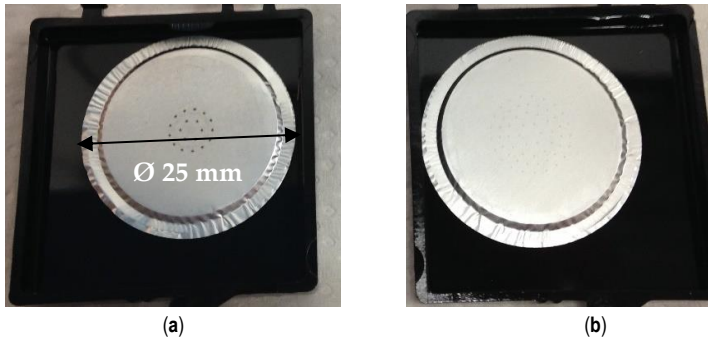


Figure III- 1 Aluminum substrates used to collect PM from disc brake materials dyno-tested (a) Sample A having particles in the aerodynamic diameter range 1.6-2.5 μm ; (b) Sample B collecting PM with an average aerodynamic diameter of 108-170 nm.

III.2.1.2 Methodology

For extracting the particles from the substrates, extraction replicas in the form of acetate foils of 200 μm thickness were used. Fig. III-2 shows through a schematic the steps to be followed in the proposed sample preparation methodology, starting with the collection of the PM onto the aluminium substrates (Step 1). In Step 2, a portion of the substrate containing a sufficient amount of particles is carefully cut from the original substrate. If it suits, it is better to carry out this operation with the aid of a light microscope. Then, on the cut sector of the aluminium substrate, just a few drops of acetone are dropped exactly on the location of the PM pile-up regions that are to be extracted. The acetate foil is then carefully positioned onto the cut sector, taking care that there is no bubble formation. The setup should be left untouched for roughly twenty minutes. During this stage, the particles on the Al substrate get embedded on the acetate foil and when the acetone dries, the acetate foil is detached from the Al substrate stripping away the particles. The process is capable to extract all the particles originally present on the Al substrate, without leaving behind any possible phase present in the original PM.

With the particles now on the acetate foil, at this stage SEM analysis can be performed if required. However, since the acetate foil is non-conductive, the deposition of a conductive carbon coating using a high vacuum carbon coater may help the observations by countering the beam charging effects (Step 3). Carbon coating is in any case required as a further step of the present TEM sample preparation protocol. Two contradicting aspects have to be considered concerning the thickness of the carbon coating. The coating should be thick enough to have the required strength to retain the embedded particles. On the other hand, an upper limit on the thickness is

required so that any original features of the particles are not masked, especially those requiring high-resolution images. In view of these two points, it is proposed that the thickness of the carbon coating should be in the range of 20-50 nm.

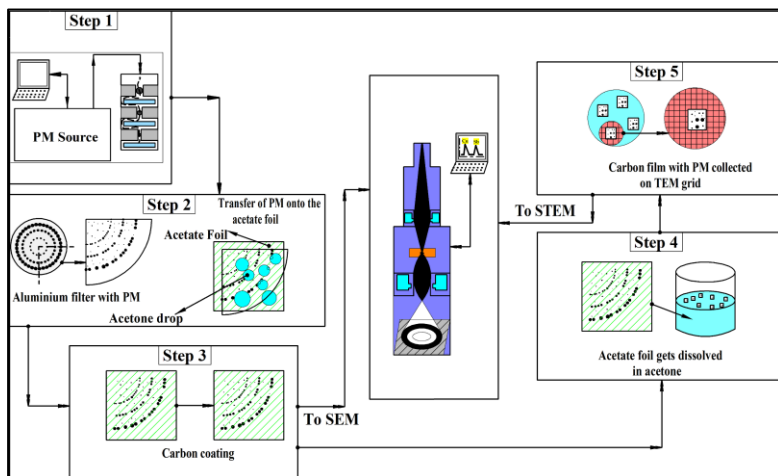


Figure III- 2 Schematic of the main steps involved with the present sample preparation protocol.

Contrarily, if the PM are originally collected on polymeric substrates, for instance, polycarbonate, we can skip the PM extraction step using the acetate film. In Step 4, the acetate film or the polycarbonate substrate is then dissolved in suitable solvents- acetone for acetate and chloroform for polycarbonate. The carbon film fragments containing the PM and floating in the solvent are then collected using suitable TEM grids. The choice of the grid material should be such that it does not interfere with the X-ray lines of the PM constituents so that reliable spectroscopy investigations can be performed (Step 5). In this investigation, Au TEM grids with a pitch size of 100 μm have been used.

III.2.1.3 Validation of methodology

The PM transfer methodology is particularly beneficial when dealing with the ultrafine fraction of the wear debris, as shown in Fig. III-1b). The morphology of the particles belonging to samples A and B are shown in Figs. III-3a) and b), respectively. The EDXS spectrum obtained from the field of view of Fig. III-3b) provides an average composition of the finer fraction of the particles and is listed in Table III-1. It is important to mention the presence of a significant fraction of aluminium in these

particles, present in the form of aluminium oxide, the determination of which would have been inaccurate if the SEM investigations were performed directly on the Al substrate.

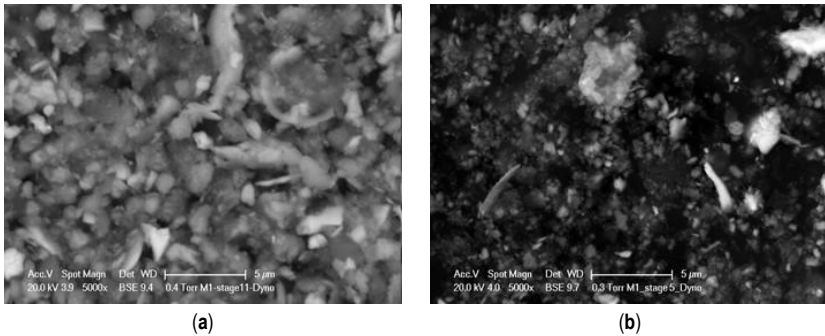


Figure III- 3 a) a general view of a spot of particles from sample A, collecting the PM in the aerodynamic diameter range 1.6-2.5 µm (see Fig. III-1 a). The heterogeneous morphologies are typical of debris coming from the composite brake pad mix, intermixed with iron-rich particles, mainly oxides, from the cast-iron disc. b) finer PM from sample B.

Table III- 1 Composition of the PM from sample B, as evaluated from EDXS data acquired from the field of view in Fig. III-3b). Please note: oxygen and carbon have not been included in the quantification calculation.

wt.%	(a)
Mg	16.0
Al	13.0
Si	6.4
S	7.0
Ca	4.1
Cr	0.9
Mn	0.9
Fe	31.6
Cu	5.2
Zn	4.0
Zr	3.7
Sn	7.3

The need for higher resolution, especially concerning the finer fraction of PM, renders TEM-based techniques suitable for the analysis. In this regard, the collected PM have been studied through TEM high magnification images, microstructural characterization has been performed using SAED, and chemical composition was determined through EDXS. Simultaneously, the study in scanning mode (STEM), has been particularly useful in the elucidation of the local distribution of the elements semi-quantitatively using elemental maps and phase identification across particle clusters.

The STEM mode operation allows demonstrating the very fine mixing between the constituents of the disc (mainly Fe and O) with those of the brake pads (other mapped elements), as shown in Fig. III-4 for particles belonging to Sample B. The high-angle annular dark field image (on the left) has the required high spatial resolution to demonstrate the core-shell structure of the iron particles, being covered by iron oxide. This confirms the tribo-oxidation mechanism wear debris generation from the cast iron disc, discussed in detail elsewhere [221,222].

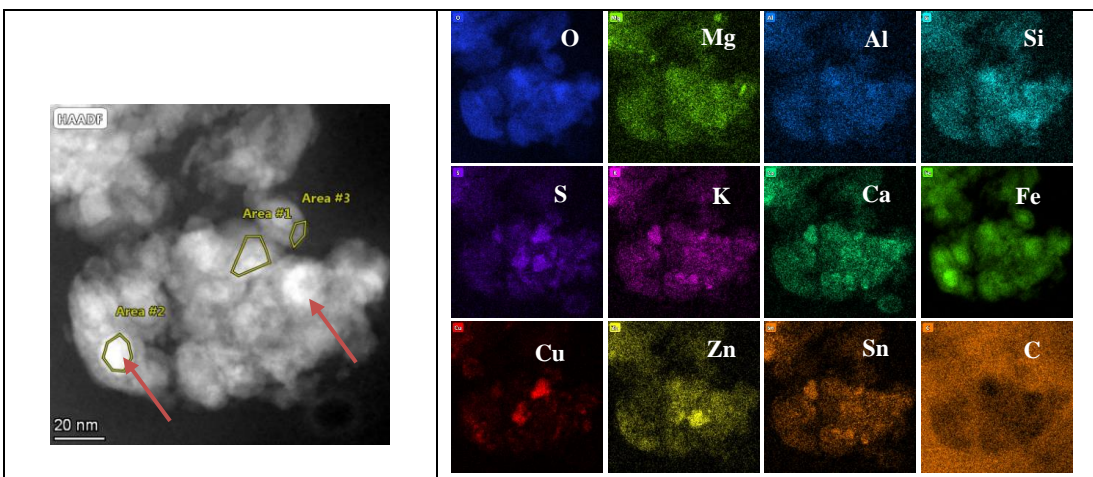


Figure III- 4 STEM HAADF image of a cluster of PM from sample B and a set of X-ray maps. The arrows in the STEM image show some of the core-shell structure of oxidized iron particles. The three areas from which the compositional data are given in Table III-2 have been indicated.

Additionally, it is possible to study very localized variations in the composition of the particles, as done for the three marked areas in the HAADF image. These compositions are shown in Table III- 2. All three regions exhibit large concentrations of iron, arising mainly due to the abrasion and tribo-oxidation of the brake disc [223].

Table III- 2 Composition of the PM from sample B, as evaluated from EDXS data acquired from the three areas marked in Fig. III-4. Please note: carbon, although detected (see relevant map in Fig. III-4) has not been quantified, since coming not only from the particles but also from the coating present on the TEM grid.

wt.%	Area 1	Area 2	Area 3
O	22.6	12.9	35.4
Mg	0.7	0.4	1.0
Al	0.2	0.1	0.5
Si	1.3	0.6	0.9
S	7.7	0.5	1.1
K	-	0.1	0.3
Ca	0.6	0.3	0.4
Fe	34.1	76.1	49.3
Cu	24.7	5.7	5.1
Zn	2.8	1.5	1.9
Sn	5.3	1.8	4.0

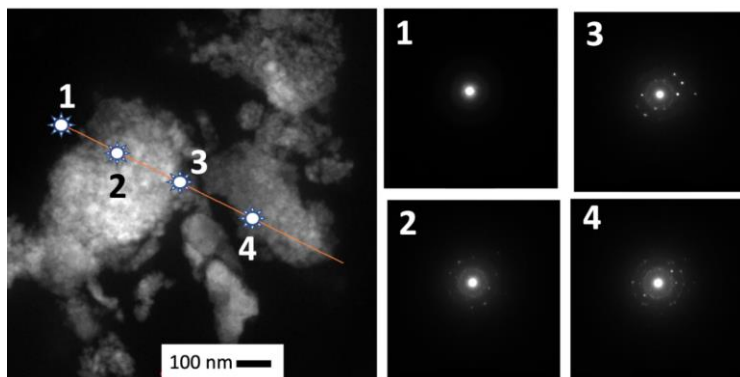


Figure III- 5 STEM microdiffraction patterns acquired in the four marked spots (1-4) of a cluster of PM grains from sample B. The following phases have been identified in the different areas: 1) amorphous (carbon film on the TEM grid); 2) Fe_3O_4 ; 3) and 4): $\alpha\text{-Fe}$ and Fe_3O_4

Still, thanks to the high-resolution STEM-EDXS, it is possible to differentiate between regions displaying high iron particle content (Area 2) from those that are rich in iron

oxide (Area 1 and 2). The presence of other elements are compliant with the compositions of the brake pad materials reported in literature [224].

Certainly, the methodology can be further supported with the introduction of electron diffraction-based analysis. This has been demonstrated in Fig III-5, where in the DF STEM mode, selected regions of a cluster have been analyzed for their structural characteristics. The diffraction patterns obtained from the four regions highlight the presence of different phases: 1-amorphous (carbon film present on the TEM Au grid); 2- iron oxide (Fe_3O_4); 3 & 4- iron and iron oxide ($\alpha\text{-Fe}$ and Fe_3O_4).

III.2.2 Nanostructured materials

The specimens of inorganic nanopowders studied in this thesis- CeO_2 , Y_2O_3 , Si, TiO_2 , and $\text{Fe}_2\text{O}_3/\text{FeOOH}$, CoFe_2O_4 were prepared by the solution drop technique. The method has also been referred to as the drop-casting technique in the literature [209]. A measured quantity of the nanopowder, in the range of 0.015-0.02 g, was dispersed in 7-8 mL ethanol. The standard requirement of this procedure is to achieve a dilution ratio such that a monolayer of nanoparticles is visible on the TEM grid when viewed under the microscope. Too much particle overlap, unlike in the case of a monolayer, prevents accurately viewing the particle edges for measurement [225]. Once the dilution ratio is decided, sonication of the solution could help in breaking the aggregates. Thus, the duration of the ultrasonic mixing was kept at 15 min. 30 μL of the solution was immediately transferred using a pipette onto the carbon coated TEM grid. Cu grid was used for all but CoFe_2O_4 specimen, for which Au grid was used. The suspension on the grid was left to dry in the air.

There has been ample criticism of this procedure as aggregates may form during drying, especially at the perimeter of the perimeter of the dried droplet [209]. This leads to ambiguity in terms of differentiating the formed aggregates from the true aggregates present in the specimen. There may also be loss of particles if there is poor adhesion with the TEM grid. However, the procedure is relatively simple, fast, and requires minimal equipment. At the same time, it can be extended to range of nanomaterials- nanoparticles, nanotubes, and nanowires.

III.3 Highlights of the chapter

- The scope of removing the particles from the substrates has a direct implication on the compositional analysis. Getting rid of the elements like Al and Si (from SiO_2 and silicic grease) is essential so that they do not interfere with the detection and quantification of the original constituents of the particles.

- Heterogeneity in the sampling efficiency of the environmental monitoring systems can be studied since the methodology can be applied to extract particles separately from different regions of the sampling substrates. In this regard, it is paramount that the sample preparation protocol is not leaving behind any PM on the substrates.
- The successful preparation of TEM samples for the sub-micrometric particles has utility with respect to the characterization of PM emitted from systems generating ultrafine particles, interesting for their implications on the environment and requiring adequate resolution not only for microstructural but also for chemical and crystallographic studies.
- The high-resolution information obtained from different sample regions through STEM coupled with EDXS can be further used in the source apportionment studies and to identify the resuspension effects of the finer fraction of the atmospheric PM, down to the nanoscale.
- A thorough crystallographic analysis is possible thanks to the possibility of collecting relevant electron diffraction patterns supported by EDXS analysis. Not only from the point of phase determination but microstructural characterization can be inferred based on the Rietveld-based fitting of the diffraction patterns, as discussed in Chapter V.

Chapter IV: Rietveld method applied to electron powder diffraction patterns- Methodology

IV.1 Introduction

In the previous chapters, we have deduced that TEM is a multi-analytical tool having the capability to perform quantitative characterization of nanostructured materials. The morphological information and phase contrast of the nanoparticles from high magnification images, elemental composition from the spectroscopic techniques-EDXS and EELS, and phase identification and microstructural elucidation using SAED are strong points in favour of TEM for characterizing nanostructured materials. EPD facilitates probing extremely small volumes with the sensitivity to detect changes in the structure due to short-range ordering, distorted lattices, the presence of defects, or secondary phases.

Consequently, microstructural and structural characterization of nanostructured materials based on Rietveld refinement of SAED has been attempted by researchers: TiO₂ [171,50,145]; ZnS and ZnO [158]; hydroxyapatite [226,160]; MnFe₂O₄ [159]; Mn₃O₄ [145]; Al and α - MnS [169]. Horstmann & Meyer [227] determined that the component of dynamical scattering is less than 10% for ED patterns of polycrystalline Al crystals that are smaller than 9 nm for electron-beam energies in the range of 20–50 keV. Weirich et al. [50] observed weak dynamical interactions for a 120 keV energy-filtered powder diffraction pattern collected on texture-free nanocrystalline TiO₂ (anatase) having average crystallite size of 7 nm. Kim et al. [159] studied polycrystalline MnFe₂O₄ with 11 nm average crystal size and observed that for a 120 kV electron beam, the ratio of the kinematical to dynamical contributions towards the structure factor was approximately 1:1.5. Luo et al. [228] concluded in their study of Au₃Fe_{1-x} alloy that a less than 3 % correction for the dynamical scattering could improve the long-range order parameter estimated value. Thus, it is favorable to analyze the EPD patterns not under the kinematical approximation but by implementing the two-beam dynamical correction that calculates the intensities of the reflections as a function of the electron wavelength and crystal thickness.

However, a prerequisite for the line profile analysis, for determining the microstructural, structural, or textural features of the material under observation, is to have precise knowledge of the line broadening caused by the instrument. If the contribution of the instrument in the overall broadening of the reflections is not considered, then it may lead to the determination of erroneous sample characteristics. As an example, Weidenthaler, 2011[42] observed a 25 % error in the crystallite size of a nanocrystalline Cr₂O₃ sample if the instrumental effects were neglected. The very important standard procedure to separate instrumental broadening from physical broadening has already been studied extensively for the complementary X-ray

diffraction technique [229–231]. Although electron diffraction-based crystallographic analysis has gained prominence in recent years, there exists a gap in the literature concerning a standard protocol to calibrate a transmission electron microscope for its instrumental broadening function [145]. The purpose of this chapter is to elaborate on the methodology that has been used for its determination. This chapter also serves as the base for the next chapter in which different application examples of nanocrystalline materials for microstructural analyses have been considered.

IV.2 Material and methodology

An ideal material for the determination of instrumental broadening function is one that itself does not contribute substantially to the overall line broadening. In such a scenario, the entire broadening of the line profile can be attributed to the instrument. A material that is suitable for the determination of the instrumental broadening of an XRD instrument is not appropriate for TEM. For XRD, a preferred sample is one that is so well crystallized that the broadening caused because of the finite size of the crystallites and microstrain is negligible. This is possible in the case of sufficiently large crystallites with low defect concentrations, leading to almost zero microstrains.

However, such a material with large crystallites is not appropriate for the determination of the instrumental broadening function of a TEM. Firstly, a material with large crystallites causes a discontinuous and grainy electron diffraction ring pattern. Secondly, TEM analysis is a direct function of the material thickness, and the thinner the specimen better are the results. The specimen should be thin enough to guarantee electron transparency, such that a part of the incoming electron beam is transmitted to form the relevant EPD, instead of being completely backscattered or absorbed.

A cerium oxide (Alfa Aesar, 99.5% pure, minimum rare earth oxide (REO), 15–30 nm) nanopowder was used as a standard for the instrumental broadening function determination. The choice of this material is justified since cerium oxide has a simple crystal geometry- cubic, space group: Fm-3m, and well-defined physical and chemical properties. At the same time, this particular CeO₂ sample has a narrow crystallite size distribution and grains that are oriented randomly, i.e., not textured. The latter property renders it more suitable for EPD-based Rietveld analysis since the dynamical effects are minimized.

The broadening of the Bragg reflection lines occurs due to both sample (**f**) and instrumental (**g**) effects. The broadening caused by the sample is an indirect measure of its microstructural parameters- size and microstrains. The former is limited not only to the coherently/ incoherently diffracting domains but may also include the subgrain structures (for example small-angle boundaries) and the effects generated due to the stacking and twin faults [232]. The latter is generated due to the crystal defects-

dislocations and point defects [233]. The overall observed diffraction profile broadening (\mathbf{h}) is a convolution product of \mathbf{f} and \mathbf{g} , to which a background term (\mathbf{b}) is added. Mathematically, it is represented as [234,235]: $\mathbf{h} = \mathbf{f} \otimes \mathbf{g} + \mathbf{b}$. The instrumental broadening parameter is a mathematical convolution of the emission profile of the concerned radiation used, coupled with all the instrumental aberrations that could be physical or geometric [236].

The implementation of the methodology was conducted in coordination with the microstructural parameters of the standard CeO₂ sample obtained from XRPD. However, firstly there was also the need to correctly determine the instrumental broadening function of the XRD instrument. The instrument used was an Italstructures IPD3000 diffractometer, operated in reflection mode. The diffractometer was equipped with a Cu source anode coupled with a multilayer monochromator. The diffraction patterns were acquired on a 4096-channel Inel CPS120 curved position sensitive detector, covering 120° 2θ angular range, with an approximate channel resolution of 0.03°. The acquisition time was 30 min. The calibration standard material used for the purpose was an isotropic Y₂O₃ from Sigma Aldrich (99.99% trace metals basis) after calcination at 1573 K for 24 hours, to remove any possible microstrain. The peak broadening of the collected pattern was attributed to the instrumental effects, by setting to zero the size-strain contribution of the standard and refining the instrumental function for the XRD instrument, $\mathbf{g}_{XR}(x)$, using the Caglioti function.

Thereafter, the same instrument was used for the complete microstructural characterization ($\mathbf{f}_{XR}(x)$) of the TEM standard sample, CeO₂, as follows:

$$\mathbf{h}_{XR}(x) = \mathbf{f}_{XR}(x) \otimes \mathbf{g}_{XR}(x) + \mathbf{b}_{XR}(x) \quad (1)$$

This complete output in the form of sample characteristics was taken as an input parameter for the EPD analysis, ultimately leading to the determination of the instrumental broadening function of the TEM, $\mathbf{g}_{TEM}(x)$. Of course, during this latter analysis, the sample characteristics $\mathbf{f}_{XR}(x)$ was kept fixed and not refined.

$$\mathbf{h}_{TEM}(x) = \mathbf{f}_{XR}(x) \otimes \mathbf{g}_{TEM}(x) + \mathbf{b}_{TEM}(x) \quad (2)$$

Since we are using the method of profile fitting and not of deconvolution [100], the broadened profile \mathbf{h} needs to be approximated with some analytical function, although in the literature some non-analytical and 'learned' functions have been cited [237]. The most common functions used are Gaussian and Lorentzian (Cauchy). For the Gaussian function, the integral breadth β using the convolution integral may be expressed as:

$$\beta_{hc}(x) = \beta_{gc}(x) + \beta_{fc}(x) \quad (3)$$

For the Gaussian function, the following expression holds:

$$\beta_{hG}^2(x) = \beta_{gG}^2(x) + \beta_{fG}^2(x) \quad (4)$$

However, just as for the XRD line profiles that cannot be best approximated using only either of the above two functions [238], also for the EPD we have used the combination of the two in the form of pseudo-Voigt function. In the Rietveld refinement methodology of refining the crystal structures using powder diffraction, the crystal structures and the profile shape functions are refined simultaneously following the least squares procedure. The incapability of the profile shape function to model correctly the observed intensities of the Bragg reflections leads to distortion in the results obtained for the structural and microstructural parameters.

Multiple SAED patterns were collected for a reliable calibration protocol. For this, we used three selected area (SA) apertures: 800, 200, and 40 μm . Corresponding to each of the SA apertures, we varied the camera length (CL) as 1360 mm, 1080 mm, 844 mm, and 658 mm. Thus, in total twelve different diffraction patterns were analyzed. In addition, the C2 lens current was kept constant while varying the camera lengths for a particular SA aperture. Interesting observations were made while collecting the patterns under these conditions.

For a particular CL of 844 mm, Fig. IV-1 shows the diffraction patterns Figs. a-c) corresponding to the largest to the smallest SA apertures, respectively, from the field of view shown in Figs. d-f). A marked difference in the appearance of the diffraction patterns can be seen. The diffraction pattern collected with the largest SA aperture of 800 μm (Fig. a) displays a smooth variation of the intensity along the rings with only a selected number of brighter spots, in contrast to the diffraction pattern corresponding to the 40 μm SA aperture (Fig. c) where comparatively a greater number of these isolated spots are visible. This is an expected result that the selection of a larger or smaller number of crystallite domains will have on the physical appearance of the appearance and their respective analyses.

The diffraction patterns were imported in MAUD using the ImageJ (<https://imagej.nih.gov/ij/>) plugin. The rings of each pattern were segmented into sectors 10 ° wide, i.e., this process could yield thirty-six individual patterns. However, as shown in Fig. IV-2 the azimuthal segmentation of the rings generated thirty-four diffractograms, excluding the zero signal region corresponding to the beam stopper. These multiple diffractograms were used as the dataset and can be stored separately using the program. These were thereafter integrated to yield the final 1D plot that served as the starting reference for any diffraction pattern to initiate the process of Rietveld refinement. Using this process, we can preserve the positions of the original coordinates of the points, and transform the intensities present in a 2D image to a 1D

plot with a low textural signature [164,239]. The complete procedure to be followed for performing this operation has been demonstrated in Appendix A1.

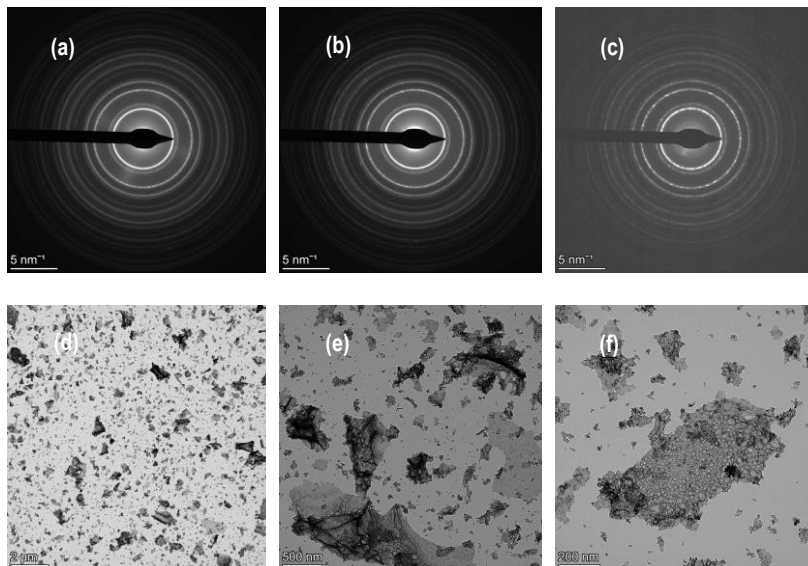


Figure IV- 1 Diffraction patterns of the CeO₂ standard sample, corresponding to CL 844 mm acquired using a) 800 μm SA aperture; b) 200 μm SA aperture; c) 40 μm SA aperture from the field of view in (d), (e), and (f), respectively.

The background is an important parameter to be fitted for any reliable quantification of the microstructure. This is especially true for the EPD since the background has a higher value as compared to the XRPD or neutron diffraction. The high background value is generated due to the following main terms- inelastic scattering, incoherent scattering, and also the scattering due to the amorphous carbon film present on the TEM grid, if any [240,60]. As in most cases, the fitting of the background was performed using a polynomial function of the fourth degree. Additionally, specifically in the case of electron diffraction, the transmitted beam causes a sharp increase in the background values at low angles. Thus, an additional gaussian peak was used for a better fitting.

The analyzed particles were supported on the Cu grid having an amorphous carbon film. Thus, the collected diffraction pattern also had the contribution of diffused scattering intensity originating due to the C film [159].

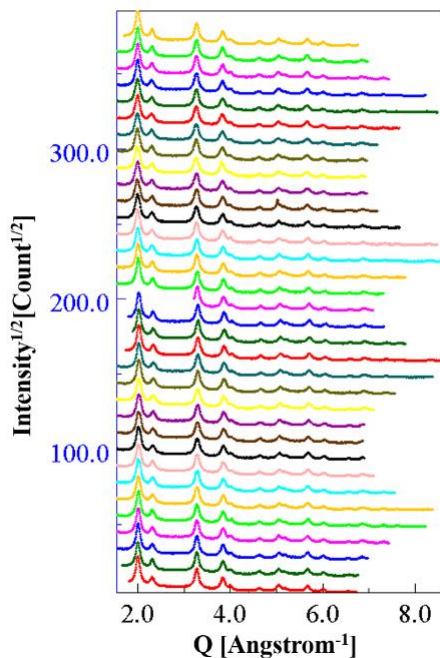


Figure IV- 2 Diffractograms obtained from the azimuthal segmentation (10° sectors) of the SAED pattern. These were then integrated to obtain the 1-D ED pattern. Please note: the data refer to the SA aperture 200 μm - CL 1080 mm combination.

The two halos superimposed on the amorphous diffraction profile are shown in Fig. IV-3. There could obviously be a difference between the experimental and calculated profiles due to these additional scattering, leading to an incorrect determination of the microstructure. To account for this effect, the amorphous diffraction pattern from the naked Cu grid was fitted separately. The intensities of the two halos, along with their shape configurations were added manually during the refinement of CeO_2 EPD patterns.

The atomic scattering factor depends on the type of radiation used, as discussed in Chapter 1. In MAUD-based analysis, the electron atomic factors prescribed by Peng et al.[187] are used. A pseudo-Voigt function was used for the modeling of the Bragg reflections since this function being a linear combination of the gaussian and Lorentzian terms can provide a close match between the experimental and calculated intensities [50,241]. The continuous variation in the line profile being closely measured

can lead to a better determination of the crystallite and microstrain line broadening contribution [174].

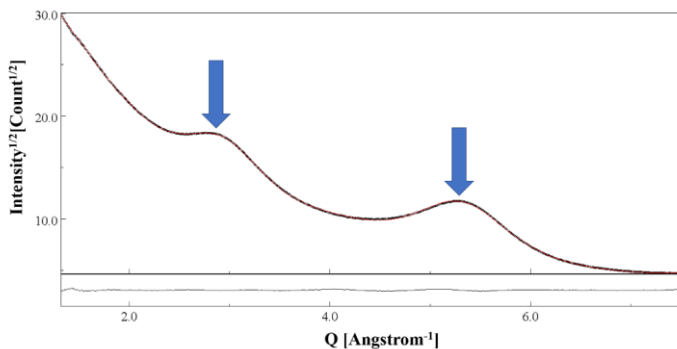
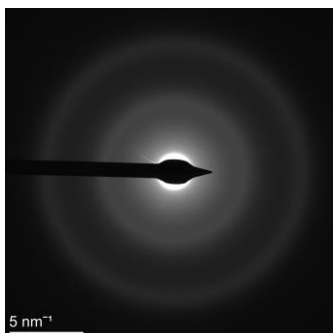


Figure IV- 3 Diffraction pattern from the naked Cu grid having the supporting C film (a). Intensity profile from the C-supporting film with halos marked by two arrows (b). Please note: The data refer to the SA aperture 200 μm -CL 1080 mm combination. Y-axis: sqrt. (Intensity); X-axis: Q (\AA^{-1})

The starting refinement cycles are performed for fitting the background, and the intensity scale factor is also set to refined. Subsequently, the errors associated with centering of the original 2D diffraction pattern, and the tilting errors, i.e., the error originating due to the detector not being perpendicular to the incoming electron beam are refined. This step is required to transform the coordinates of the image, i.e., the experimental data into the correct Q values. This has been demonstrated in Fig IV-4. wherein, the errors initially visible in Fig. IV-4 a) are reduced in Fig. IV-4 b).

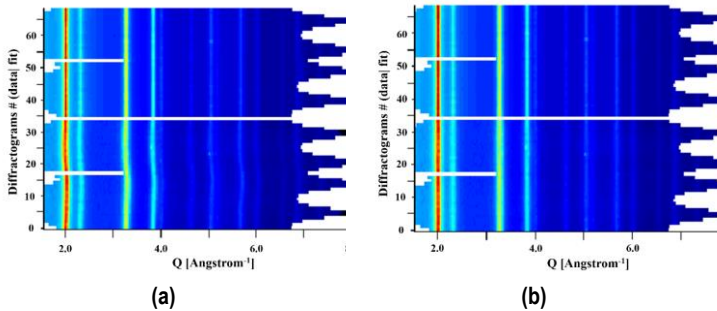


Figure IV- 4 Two dimensional multiplot of the calculated (upper part) and experimental (bottom part) profiles are displayed. In (a) we see an offset between the data and the fit, as well as 'waviness' in the experimental profile, which is corrected in (b) by accounting for both centering and elliptical errors. Please note: (b) has been plotted just after implementing the corrections and these refer to the SA aperture 200 μm - CL 1080 mm combination.

TEM diffraction patterns can be collected at different camera lengths (CLs) that are provided by the manufacturers. However, there could be up to 10 % error in the instrumental nominal values [60,242]. If the correct value of the CLs is not determined, then there would be large variations in the positions of the diffracted and calculate peak profiles. The variation in the camera lengths occurs majorly due to the following reasons: magnetic hysteresis in the electron lenses of the TEM, specimen position present within the objective lens, the electron beam convergence based on the settings of the condenser lens system, and the focus conditions [141]. For determining the correct value of a particular CL, a possible method might be to collect multiple diffraction patterns using different SA apertures, and calibrate the concerned CL each time, since CL does not depend on the size of the SA aperture used. If the errors in the obtained values are within the specified limits, we can say that the correct value has been approached.

At the time of the acquisition of the diffraction pattern, the standard sample used must be set at the eucentric height of the stage, the focus of the objective lens should be set to its standard value, and a representative region of the specimen should be selected avoiding any possible interference of the sustaining metallic grid. The C2 current intensity also has an impact on the calibrated CL value. However, in our experience, if the eucentric height of the sample is maintained correctly, astigmatism errors of the condenser and objective lenses have been corrected, the image focus is

cross-checked with its FFT, diffraction astigmatism if encountered has also been compensated, then we should not need to change the C2 current intensity for collecting diffraction patterns at multiple camera lengths for a particular SA aperture setting. Any further adjustment in the focus conditions required upon changing the CL can be fulfilled by just using the diffraction focus.

Thereafter, using the equation $Rd = \lambda L$, the corrected CL value can be determined. In this equation, R is the radius of the rings generated by the crystallite domains, d is the interplanar spacing for a particular set of planes for the standard material, λ is the wavelength of the electron beam at the acceleration voltage used, and L is the corrected camera length.

MAUD offers the simple 'Delft' and 'Popa LB' models [103] for describing the line broadening due to the microstructural features. For the XRPD data, the Delft model provided an average crystallite size value of 124.9 (4) Å whereas the value of the same parameter calculated using the 'Popa LB' model was 98 Å. Since the value associated with the Delft model had a lesser deviation from the average value of 128 Å determined using the bright field image of the crystallites shown in Fig. IV-5 d), the Delft model was used for all subsequent calculations. The simple Delft model associates Lorentzian broadening for the finite-sized crystallites whereas Gaussian broadening is assumed for microstrain related broadening [164]. To study the shape and size variations of the crystallites depending on the chosen (hkl) planes, the Popa model [243] was considered. As per the Popa model, for the Laue class $m\bar{3}m$ the average crystallite size $\langle R_{hkl} \rangle$ for a crystallite of anisotropic shape is given by:

$$\langle R_{hkl} \rangle = R_0 + R_1 K_4^1(x, \varphi) + R_2 K_6^1(x, \varphi) + \dots \quad (5)$$

For the different R_i coefficients of the above harmonic series, R_0 corresponds to the average value of the isotropic crystallite; Here, $x = \cos \phi$, where ϕ is the polar angle and φ corresponds to the azimuthal angle in an orthogonal coordinate system. Since CeO_2 has a cubic crystal structure, we can use the term '[hkl] direction' for referring to the dimension of a crystallite that is perpendicular to the (hkl) plane.

Le-Bail method (discussed in Chapter II) is based on the 'pattern decomposition' technique that necessarily does not need a structural model and involves the allotment of all the observed intensities to the individual Bragg reflections [189]. The Le-Bail fit gives an indication of the best profile fitting of the experimental data points and the values of the reliability factors (Rwp value) for the Rietveld fitting where the structure factors are taken into consideration, should approach those obtained using the Le-Bail fitting [167]. Le-Bail fitting was used for the determination of the $g_{TEM}(x)$.

As a next step, there was a need to validate the consistency of the adopted methodology. In this stage of the methodology, we kept the instrumental broadening function parameters obtained in the previous step, $g_{TEM}(x)$, fixed and evaluated the sample microstructural parameters using EPD, $f_{TEM}(x)$.

This step provided the requisite opportunity to compare the sample characteristics determined through XRPD, $f_{XR}(x)$, with those obtained using EPD, $f_{TEM}(x)$. In this two-step calibration methodology, we analyzed the EPD patterns under three different modes- The Le-Bail method, Kinematical approximation, and the Blackman two-wave dynamic correction [144].

IV.3 Results and discussion

IV.3.1 Camera length calibration

The diffraction patterns collected on the standard CeO₂ sample displayed a uniform and continuous distribution of the diffracted intensities along the rings (see Fig. IV-1). This indicates the absence of any preferred orientations (texture) in the analyzed sample, as also confirmed through the Rietveld refinement of the XRPD and EPD data. Indeed, a good fit could be obtained without the inclusion of any texture models, although available in the software package [169]. This further proves the adequacy of the chosen material for the purpose of calibration.

Since we have repeatedly emphasized in Chapter 1 that crystallite size is an important parameter that influences the material properties, its evaluation through different techniques was adopted. For a comparative study, Fig. IV-5 a) and b) respectively show the BF and DF images of a particle cluster. Fig. IV-5 c shows the *ImageJ* analyzed DF image in Fig. b, and the histogram (Fig. d) corresponds to the size distribution of the crystallites that yielded an average value of 135 Å. The average value of the crystallites was also determined using a high-resolution image shown in Fig. IV-5 e), giving a value of 128 Å.

With reference to the Rietveld fitting of the XRPD and EPD data shown in Fig. IV-6, the experimental data points (black dots) and the calculated profiles (red line) along with the residual curve have been plotted. From the refined XRPD data shown in Fig. IV-6 a), an average crystallite size of 124.9 (4) Å was determined after taking shape anisotropy into account. The results from this analysis, are listed in Table IV-1. The Rietveld fitting of the EPD pattern collected with the SA aperture 200 μm corresponding to the 1080 mm camera length is shown in Fig. IV-6 b).

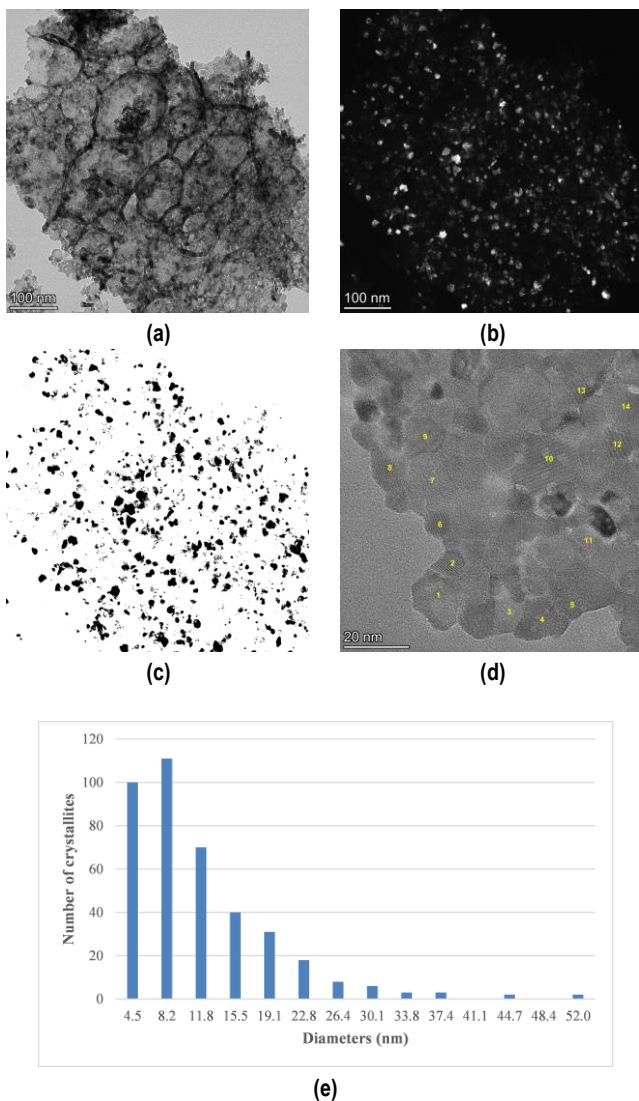


Figure IV- 5 a) BF micrograph of CeO₂ nanoparticles aggregate; b) Corresponding DF micrograph; c) Threshold of Dark Field micrograph shown in (b); d) Histogram of the size distribution of crystallites, used to determine an average size of 135 Å; e) High magnification image with fourteen marked crystallite domains that were clearly visible. These were used to estimate the average crystallite size.

Throughout this thesis work, for all the physical parameters determined through the Rietveld refinement, we have adopted the standard criteria of reporting the decimal digits up to the value provided by the algorithm for estimated standard deviation (e.s.d.).

Table IV- 1 XRPD profile fitting: Reliability factors, cell-parameter, crystallite size refinement s obtained from the analyses of CeO₂ nanopowder.

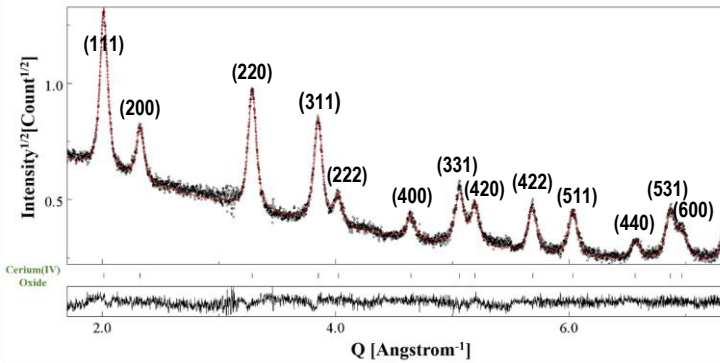
Method	R _{wp} %	R _{Bragg} %	a (Å)	Average Crystallite size (Å)
XRD	13.41	8.79	5.4101(3)	124.9(4)

The camera lengths estimated based on the twelve diffraction patterns acquired under different operating conditions are listed in Table IV-2. There is no substantial difference in the calibrated values, as also shown in Fig. IV-7.

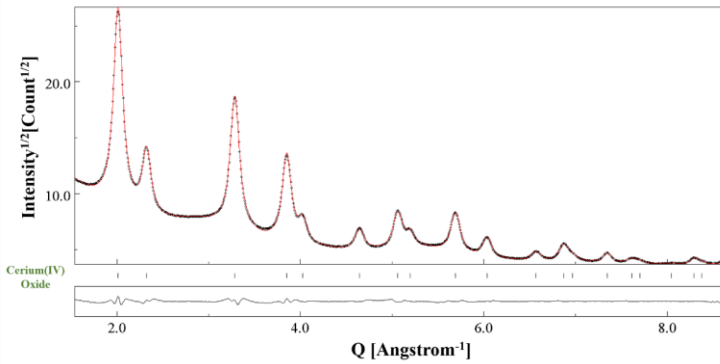
This is an expected result since the calibrated value of a particular camera length anyway does not depend on the size of the SA aperture used, although every time the SA aperture was changed, a corresponding focus adjustment in the diffraction pattern using the C2 current intensity was required. The maximum variation in the calibrated values was seen for the largest camera length of 1360 mm, whereas the least deviation amongst the calibrated values was observed for the smallest camera length of 658 mm.

It is essential to synthesize the instrumental profile at any angle of interest since the reflection lines of the standard reference sample and sample under observation do not coincide. Therefore, the characteristic features of the standard's line profile shapes must be modelled analytically. Although equation 6 [156] was derived for neutron diffraction and then confirmed for satisfactorily modelling the angular variation of the symmetric part of the XRD line profile width, we aim to apply here the same for the EPD.

Also, as indicated in Table IV-2, we have used the weighted reliability factor without background ($R_{wp_{no_bkg}}$) as the reliability factor to gauge the accuracy of the fitting. It is to be noted that we have a high background value for EPD (see Fig. IV-6b)). Thus relying on the R_{wp} could be misleading as it is easier to fit a slowly varying background as compared to accurately fitting the Bragg reflections [151]. Additionally, we also note that the $R_{wp_{no_bkg}}$ values for the EPD patterns collected with different CLs combinations of SA aperture 40 μm display higher values of $R_{wp_{no_bkg}}$.



(a)



(b)

Figure IV- 6 Results of the combined analysis of CeO_2 nanopowders for (a) XRPD patterns considered to extract $f_{XR}(x)$, (b) EPD fitted with input from (a) using a pattern-matching mode (Le Bail). Please note: Fig. b) refers to the SA aperture 200 μm -CL 1080 mm combination. Dot line: Experimental intensity profile; red line: calculated profile.

This is just because of the poor statistics of these diffraction patterns (see Fig. IV-1c) due to the contribution from a limited number of crystallite domains. For a particular case of SA aperture 40 μm -CL 1080 mm combination, Fig. IV-8 shows the Rietveld fitting of the EPD, showing the effects of collecting the diffraction pattern from a small region of the sample corresponding to the 40 μm SA aperture.

Table IV- 2 Calibrated camera lengths for different SA apertures: 800 μm , 200 μm , and 40 μm . The reliability factor, Rwp_{no_bkg} , has also been tabulated for each profile fitting.

Camera length, mm (instrument)	SA 800 μm		SA 200 μm		SA 40 μm	
	Camera length, mm (corrected):	Rwp_{no_bkg} (%)	Camera length, mm (corrected)	Rwp_{no_bkg} (%)	Camera length, mm (corrected)	Rwp_{no_bkg} (%)
1360	1322.58(1)	5.05	1324.84(6)	6.01	1315.34(3)	13.39
1080	1039.46(1)	5.70	1036.69(1)	6.96	1034.96(3)	13.36
844	812.249(8)	5.40	808.15(1)	6.53	811.40(6)	13.55
658	618.874(7)	6.11	617.21(2)	7.23	618.37(6)	13.08

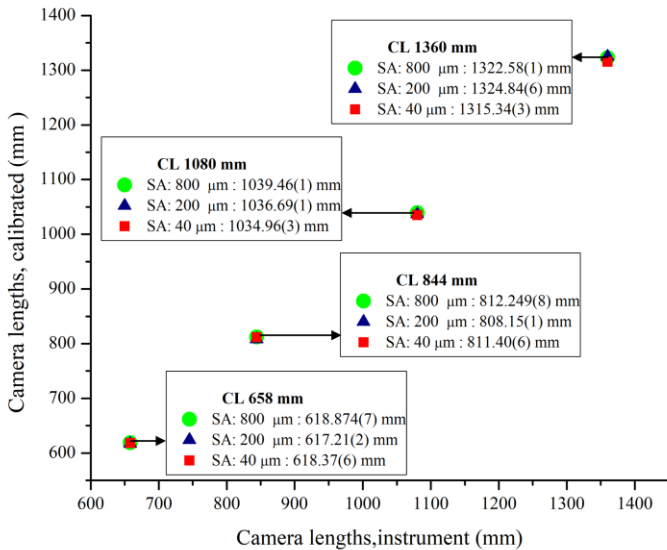


Figure IV- 7 Variation amongst calibrated camera length values from the instrumental nominal values.

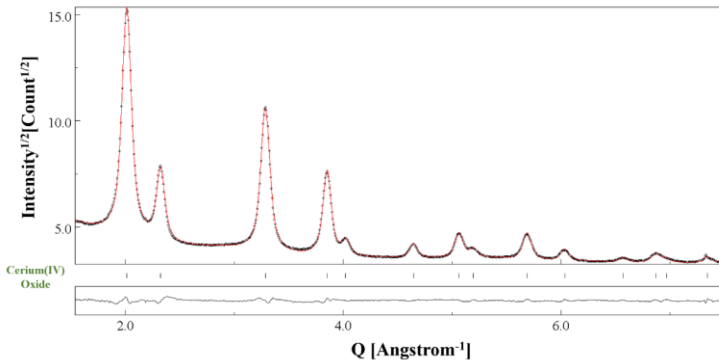


Figure IV- 8 Pattern matching (Le-Bail) fitting of the EPD collected using SA aperture 40 μm – CL 1080 mm combination. Reliability factors are relatively higher for the EPD analyses for the 40 μm SA aperture due to limited number of selected scattering domains. Y-axis: sqrt. (Intensity); X-axis: Q (\AA^{-1})

IV.3.2 Instrumental broadening function

The instrumental broadening function was determined based on the Le-Bail fitting of the EPD patterns. The line profile width (HWHM, ω) and shape, evaluated with respect to the Gaussian fraction (η) of the pseudo-Voigt function, were recorded for all the EPD patterns. The trend of the FWHW (2ω) values was modelled by refining the parameters of the Caglioti function [156]- U, V, and W, using the following equation:

$$2\omega = (W + V \tan \theta + U \tan^2 \theta)^{1/2} \quad (6)$$

At the same, the integral breadth β for a pseudo-Voigt function maybe estimated using the relation [174]:

$$\beta = 2 * \omega * \left(\frac{\sqrt{\pi}}{2\sqrt{\ln 2}} + \left\{ \frac{\pi}{2} - \frac{\sqrt{\pi}}{2\sqrt{\ln 2}} \right\} * \eta \right) \quad (7)$$

During the Rietveld fitting of all the EPD patterns, the case of $\eta > 1$, i.e., ‘flat top super-Lorentzian shape [175] was not allowed and the upper limit of η was set to 1. Using equation 7, the instrumental broadening parameter based on integral breadth was also evaluated for all the EPD patterns. The calculation of the line broadening using the integral breadth has added significance for broadened peaks [235], as encountered in the analysis of EPD.

Table IV-3 summarizes the instrumental broadening functions determined using the twelve EPD patterns. The refinement steps were stopped once there was no improvement in the $R_{wp_no_bkg}$ values. The refined values of the three parameters of the function- U, V, and W must yield a positive value of 2ω . Once these parameters have been determined, the Caglioti equation becomes the function of a single variable: θ . Instead of calculating FWHM at a single θ value, we calculated FWHM at $\theta=0, 0.25, 0.5, 0.75,$ and 1 . These values correspond to Q values from 0 to 8, which are interesting for the EPD pattern of real materials. Thereafter, an average value of the FWHM was calculated, listed in Table IV-4.

Table IV- 3 Caglioti function parameters: W and V; and Gaussian fraction η , determined for different camera length- SA aperture combinations. Please note: The parameter U is zero for all camera length- SA aperture combinations and hence not tabulated.

Camera length, mm (instrument)	SA aperture 800 μm			SA aperture 200 μm			SA aperture 40 μm		
	W	V	η	W	V	η	W	V	η
1360	1.71(3)E-5	0.00224(6)	1	3.05(4)E-5	-0.00141(7)	1	7.30(3)E-5	-0.00434(3)	0.221(3)
1080	6.44(5)E-6	0.00435(1)	1	6.050(2)E-5	0.00120(4)	1	9.24(1)E-5	-0.0046(1)	0.208(5)
844	2.56(2)E-5	0.00399(2)	1	7.6(1)E-5	0.00363(4)	0.713(4)	1.207(1)E-4	-0.0065(2)	0.317(5)
658	4.8(1)E-5	0.0051(1)	1	1.331(5)E-4	0.00736(7)	0.664(3)	2.70(2)E-4	-0.0061(3)	0.362(3)

Table IV- 4 FWHM, $2 * \omega$, determined for different camera length-SA aperture combinations.

Camera length, mm (instrument)	FWHM: $2 * \omega$ ($^\circ$)		
	SA 800 μm	SA 200 μm	SA 40 μm
1360	0.00594	0.00412	0.00558
1080	0.00626	0.00857	0.00683
844	0.00759	0.01035	0.00739
658	0.00955	0.01396	0.01468

Interestingly, for any SA aperture, the instrumental broadening function based on either FWHM or integral breadth was found to depend on the CL. In general, for the smallest camera length of 658 mm, we obtained the largest value of FWHM as 0.01468° . On the other hand, for the largest camera length, the least value of FWHM as 0.00412° was determined. This observation is most likely related to the large detector broadening at smaller camera lengths, a finding consistent with the study in [141]. Zoomed-in diffraction patterns collected with larger camera lengths yield thinner

and better-separated peaks. The same has been shown schematically in Fig IV-9. For the same SA aperture, the focusing conditions of the intermediate lens for a larger camera length produces well-separated diffraction spots in Fig. IV-9 a) in contrast to congested spots in Fig. IV-9 b).

Based on the same, the shorter camera lengths of 844 mm and 658 mm have close FWHM values, just as the same for the larger camera lengths comprising 1360 mm and 1080 mm. Eventually, it is safe to assume that calibration of the electron microscope for the instrumental broadening function must be performed for different SA aperture-CL combinations. The variation in the instrumental broadening value is expected as changing the size of the SA aperture and CL alters the overall lens conditions, in particular, C2 lens current intensity when changing the SA aperture. The variation of the FWHM with respect to the different SA aperture-CL combinations has been shown in Fig. IV-10a) with the help of 3-D plots. A similar trend was observed for the β values, listed in Table IV-5 and plotted along the vertical axis instead of the HWHM, as shown in Fig. IV-10b).

These respective values of HWHM/ β may be used while performing the Rietveld profile fitting of EPD patterns collected using different SA aperture-CL combinations for real materials displaying large anisotropic broadening or texture.

Table IV- 5 Integral breadth, β , determined for different camera length-SA aperture combinations.

Camera length, mm (instrument)	Integral breadth: β (°)		
	SA 800 μm	SA 200 μm	SA 40 μm
1360	0.00933	0.00647	0.00656
1080	0.00983	0.01347	0.00799
844	0.01194	0.01477	0.00906
658	0.01499	0.01955	0.01831

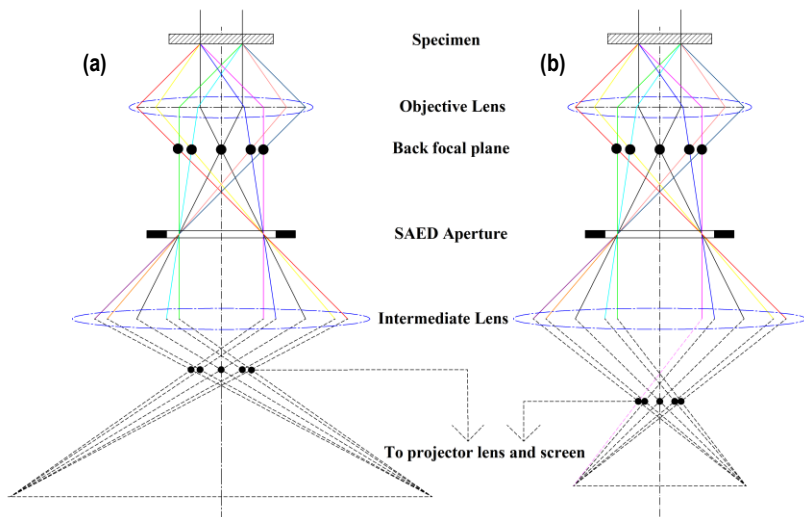
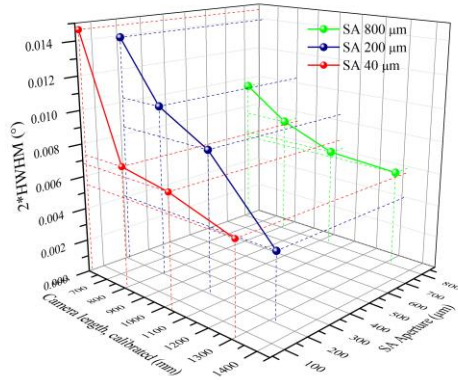


Figure IV- 9 3-D Schematic showing the change in the focusing conditions of the intermediate lens for a larger (a) and smaller (b) camera length, for the same SA aperture. A larger camera length causes a zoomed-in diffraction pattern in (a) as compared to shorter camera length

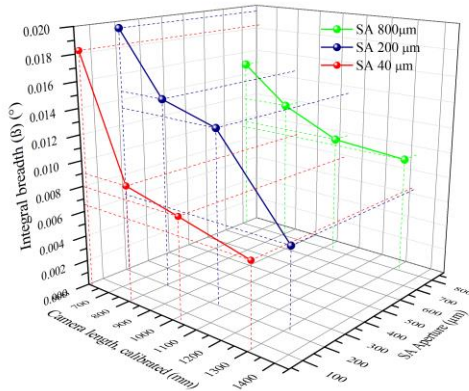
IV.3.3 Microstructure determination from EPD

As mentioned before, once the instrumental broadening was compensated, we determined the microstructure of the specimen following three different analysis modes- pattern matching (Le-Bail fitting), Kinematical approximation, and dynamic two-beam correction (Blackman). Tables IV-6-8) for SA aperture 800 μm , 200 μm , and 40 μm SA aperture, respectively, with different camera length combinations, list the refined microstructural parameters. The reliability factors obtained at the end of the refinement cycles have also been listed

For a selected SA 200 μm -CL 1080 mm combination, Fig. IV-11 shows the EPD profile fitting for the three cases- Fig. a): Le-Bail method; Fig. b): Kinematical approximation; Fig. c): Blackman two-beam correction. For different SA-CL combinations, the crystallite size(s) determined using the Le-Bail fitting was observed to be closer in magnitude to the value 'certified' by the Rietveld fitting of the XRPD. These can be



(a)



(b)

Figure IV- 10 3-D plots showing the trend of FWHM values (a) and integral breadth (b) for different SA aperture- CL combinations.

seen clearly through the crystallite sizes listed in Tables IV- 9-11). The crystallite sizes along two crystallographic directions for the cubic system- [111] and [100] have also been tabulated. For the [100] direction, the crystallite size has been computed corresponding to the (200) planes, since (100) planes are absent, as can be inferred from Fig. IV-6a).

Better values of $R_{wp_no_bkg}$ were obtained using the Le-Bail method. It was clear that the Le-Bail method was able to fit the individual intensities more efficiently as compared to the other two. This is the main reason for less deviation of the average

crystallite size in different crystallographic directions. There was not much difference in the fitting of the profiles (see Fig. IV-11c)) or the measured microstructural parameters (Tables IV-6-8)) when the Blackman two-beam correction model was implemented.

Once we have accounted for the instrumental broadening, the deviation of the total line broadening from the instrumental broadening can be associated with the sample characteristics only: the finite size of the crystallites and the crystal defects [174]. These latter can be associated with dislocations and point defects present even in the standard specimen, and are measured as r.m.s microstrains. For determining the probable shape of the crystallites, the first two harmonic coefficients R_0 and R_1 from equation 4 have been considered in both XRD and ED data refinements. The determined shapes for different sets of data and based on the different modes of the analysis turned out to be different.

As shown in Fig. IV-12a), XRPD data refined using Popa rules yielded a somewhat ellipsoidal shape that would have been spherical in case no anisotropy was present in the sample. The crystallites dimension measured along the $[111]$ direction was 128 Å whereas along the $[100]$ direction a dimension of 119 Å was determined. Le-Bail fitting of the EPD generated approximately the same shapes and sizes: Along the $[111]$ direction a dimension of 129 Å and along the $[100]$ direction a dimension of 108 Å, as shown in IV-12 b). However, a pseudo cubic shape as shown in Figs. IV-12 c-d) were obtained both using the kinematical approach, and also when dynamical two-beam correction was implemented.

Based on the above discussion, it is to be proposed that for the reliability of the microstructural parameters, XRPD-based results should be given preference over the EPD [145]. Rietveld refinement of XRPD data collected from the bulk sample has greater chances of approaching the true 'average' microstructural features since a much larger volume sample is involved in the analysis. On the other hand, as demonstrated previously, the dynamical approach could not converge toward the true sample microstructural features. This aspect has been considered in the paper by Boullay et al. [145], and the implementation of the dynamical correction showed improvement in their results.

The consequences in this scenario are twofold. Firstly, without any bias, analysis of the EPD patterns based on the kinematical approach has yielded satisfactory results reported in other studies [50,159]. Secondly, it is to be noted that although the dynamical two-beam correction is critical in the EPD analyses, dynamical scattering is strongly affected by the state and local thickness of the agglomerates/ aggregates. A small thickness can weaken the effect of dynamical scattering, making the kinematical approach equally reliable [241]. Moreover, the lack of any texture/ preferred orientations also has an overall effect on reducing dynamical scattering [141]. These

Table IV- 6 Microstructural parameters and $R_{wp_{no_bkg}}$ refinements resulting from the size and shape analyses of CeO_2 nanopowders for different camera lengths with 800 μm SA aperture.

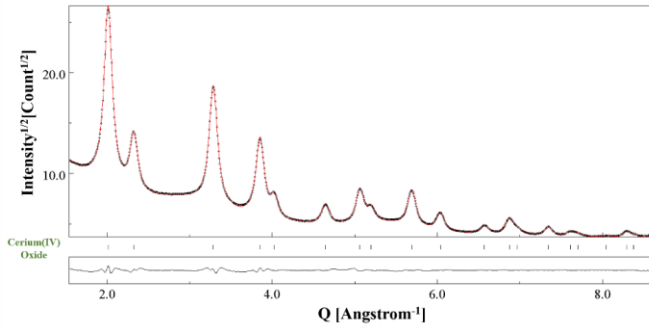
Camera length (mm)/ SA Aperture: 800 μm	EPD PM			EPD Kinematical			EPD Blackman		
	a (\AA)	Average Crystallite size (\AA)	$R_{wp_{no_bkg}}$ (%)	a (\AA)	Average Crystallite size (\AA)	$R_{wp_{no_bkg}}$ (%)	a (\AA)	Average Crystallite size (\AA)	$R_{wp_{no_bkg}}$ (%)
1360	5.41025(6)	112.36(6)	5.07	5.41024(9)	110.8(1)	7.78	5.41022(9)	111.6(1)	7.79
1080	5.41000(5)	112.64(8)	5.02	5.41015(9)	107.8(1)	8.22	5.40999(9)	108.8(1)	8.15
844	5.41014(6)	119.83(7)	5.25	5.4102(1)	114.0(1)	9.32	5.4102(1)	115.02(9)	9.21
658	5.4116(8)	121.0(1)	5.99	5.4115(1)	118.3(2)	8.87	5.4115(1)	118.6(2)	8.89

Table IV- 7 Microstructural parameters and $R_{wp_{no_bkg}}$ refinements resulting from the size and shape analyses of CeO_2 nanopowders for different camera lengths with 200 μm SA aperture.

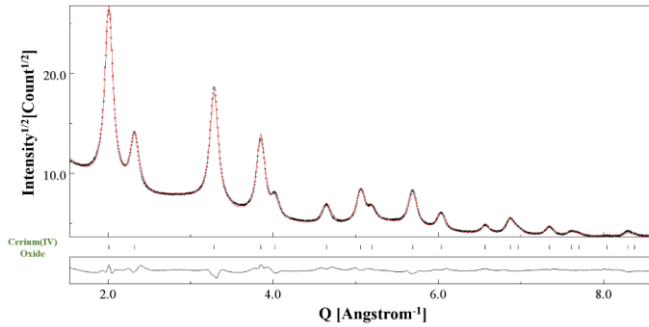
Camera length (mm)/ SA Aperture: 200 μm	EPD PM			EPD Kinematical			EPD Blackman		
	a (\AA)	Average Crystallite size (\AA)	$R_{wp_{no_bkg}}$ (%)	a (\AA)	Average Crystallite size (\AA)	$R_{wp_{no_bkg}}$ (%)	a (\AA)	Average Crystallite size (\AA)	$R_{wp_{no_bkg}}$ (%)
1360	5.4103(2)	114.63(7)	5.80	5.4110(4)	110.01(8)	9.79	5.4110(4)	109.79(8)	9.51
1080	5.41022(8)	121.3(1)	6.96	5.4102(1)	115.22(6)	9.60	5.4102(1)	115.65(7)	9.55
844	5.4102(1)	118.5(1)	7.45	5.4100(1)	112.5(2)	9.86	5.4101(1)	111.34(7)	9.69
658	5.4108(2)	121.18(6)	7.34	5.4110(2)	114.8(1)	10.77	5.4108(2)	115.0(1)	10.81

Table IV- 8 Microstructural parameters and $R_{wp_{no_bkg}}$ refinements resulting from the size and shape analyses of CeO_2 nanopowders for different camera lengths with 40 μm SA aperture.

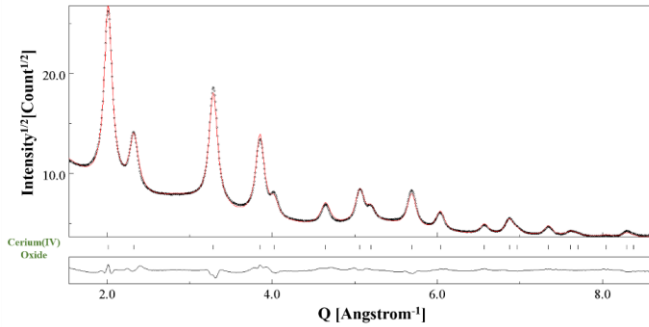
Camera length (mm)/SA Aperture: 40 μm	EPD PM			EPD Kinematical			EPD Blackman		
	a (\AA)	Average Crystallite size (\AA)	$R_{wp_{no_bkg}}$ (%)	a (\AA)	Average Crystallite size (\AA)	$R_{wp_{no_bkg}}$ (%)	a (\AA)	Average Crystallite size (\AA)	$R_{wp_{no_bkg}}$ (%)
1360	5.4102(1)	121.5(2)	13.51	5.4107(2)	114.9(4)	20.67	5.4106(2)	111.2(3)	20.45
1080	5.4102(1)	123.0(2)	13.40	5.4106(2)	120.0(3)	20.36	5.4106(2)	118.0(2)	20.24
844	5.4115(4)	120.1(2)	13.93	5.4130(7)	110.9(2)	22.57	5.4131(7)	115.9(4)	22.68
658	5.4117(4)	113.6(3)	12.77	5.4120(8)	108.3(6)	20.46	5.4116(8)	107.6(8)	20.34



(a)



(b)



(c)

Figure IV- 11 Results of the combined analysis of CeO₂ nanopowders for (a) EPD patterns treated using a pattern-matching mode (Le Bail); (b) using kinematical approximation; (c) using kinematical approximation with Blackman two-beam dynamic correction. Please note: The data refer to the SA aperture 200 μm-CL 1080 mm combination. Y axis: sqrt.

Table IV- 9 Crystallite sizes along the directions $[111]$ and $[100]$, and the average value for different CL combinations of SA aperture 800 μm , calculated using pattern matching (Le Bail decomposition), kinematical approximation, and Blackman with a two-beam dynamic correction.

Camera length, mm SA Aperture: 800 μm	EPD PM: Crystallite size (\AA)			EPD Kinematical: Crystallite size (\AA)			EPD Blackman: Crystallite size (\AA)		
	$[111]$	Average	$[100]$	$[111]$	Average	$[100]$	$[111]$	Average	$[100]$
1360	123.47	112.36(6)	95.70	125.5	110.8(1)	88.8	126.1	111.6(1)	89.9
1080	122.28	112.64(8)	98.17	122.8	107.8 (1)	85.4	123.7	108.8(1)	86.7
844	122.61	119.83(7)	115.64	130.9	114.0(1)	88.7	130.85	115.02(9)	91.28
658	135.2	121.0(1)	99.8	137.4	118.3(2)	89.8	138.0	118.6(2)	89.5

Table IV- 10 Crystallite sizes along the directions $[111]$ and $[100]$, and the average value for different CL combinations of SA aperture 200 μm , calculated using pattern matching (Le Bail decomposition), kinematical approximation, and Blackman with a two-beam dynamic correction.

Camera length, mm SA Aperture: 200 μm	EPD PM: Crystallite size (\AA)			EPD Kinematical: Crystallite size (\AA)			EPD Blackman: Crystallite size (\AA)		
	$[111]$	Average	$[100]$	$[111]$	Average	$[100]$	$[111]$	Average	$[100]$
1360	124.10	114.63(7)	100.42	127.26	110.01(8)	84.14	126.29	109.79(8)	85.04
1080	129.6	121.3(1)	108.9	134.75	115.22(6)	85.92	134.46	115.65(7)	87.45
844	133.1	118.5(1)	96.6	131.2	112.5(2)	84.5	135.15	111.34(7)	87.39
658	127.52	121.18(6)	105.25	130.4	114.8(5)	91.4	130.7	115.0(1)	91.5

Table IV- 11 Crystallite sizes along the directions $[111]$ and $[100]$, and the average value for different CL combinations of SA aperture 40 μm , calculated using pattern matching (Le Bail decomposition), kinematical approximation, and Blackman with a two-beam dynamic correction.

Camera length, mm SA Aperture: 40 μm	EPD PM: Crystallite size (\AA)			EPD Kinematical: Crystallite size (\AA)			EPD Blackman: Crystallite size (\AA)		
	$[111]$	Average	$[100]$	$[111]$	Average	$[100]$	$[111]$	Average	$[100]$
1360	127.6	121.5(2)	112.4	135.1	114.9(4)	84.8	129.3	111.2(3)	84.2
1080	127.5	123.0(2)	116.3	134.0	120.0(3)	99.0	131.1	118.0(2)	98.5
844	121.9	120.1(2)	117.4	126.3	110.9(2)	87.9	132.6	115.9(4)	91.9
658	114.8	113.6(3)	111.9	120.4	108.3(6)	90.1	117.4	107.6(8)	88.0

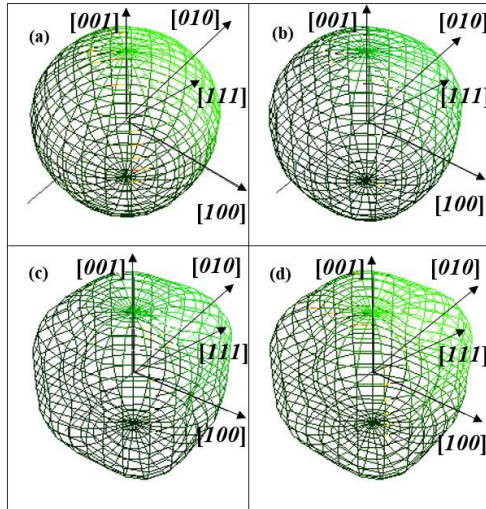


Figure IV- 12 Crystallite shapes modelled based on: (a) XRPD data showing ellipsoidal geometry; (b) ED data following the Le-Bail method depicting similar geometry as in (a); (c) & (d) ED data under kinematical and dynamical two wave approximations displaying irregular pseudo cubic, respectively. Please note: Fig. (b-d) refer to the SA aperture 200 μm -CL 1080 mm combination.

are the possible causes for the similar microstructural features obtained and listed in Tables IV-6-11. Still, the inclusion of the dynamical two-wave correction in the MAUD software is beneficial and its application has been demonstrated in the next chapter.

IV.4 Highlights of the chapter

- In this chapter, the applicability of Rietveld refinement to the electron powder diffraction ring patterns has been demonstrated. The approach was used to calibrate the camera lengths and determine the instrumental broadening function based on the half width at half maximum (HWHM) and integral breadth.
- A standard material- nanocrystalline cerium oxide was used. The reference microstructural features were determined using XRPD, and the line broadening was determined by refining both the crystallite size and the r.m.s. microstrain.
- Concerning the EPD, it was found that the Le-Bail method was better able to match the experimental intensities of the peaks with the calculated ones.

Hence, the Le-Bail method was used for evaluating the instrumental broadening function based on the multiple EPD patterns collected by varying the size of the SA aperture and the camera length. The same method was used for determining the microstructure of the sample using the EPD, once the instrumental broadening function was reliably calculated and fixed.

- The instrumental broadening function was found to vary with the size of the SA aperture and the camera length for which the EPD pattern was collected. Based on the HWHM, the variation was from 0.01468° to 0.00412° and for the integral breadth, the variation was from 0.01955° to 0.00647° . In general, higher values were noted for the shorter camera lengths.
- The chapter highlights the important first step of calibrating the microscope for its instrumental broadening. This is necessary to apply the methodology for microstructure determination using the EPD of complex specimens having multiple phases, as demonstrated in Chapter V.

Chapter V: Rietveld method applied to electron powder diffraction patterns: Application to microstructural analysis

V.1 Introduction

This chapter builds on the previous Chapter IV to demonstrate the application of the developed methodology in the microstructural characterization of nanostructured systems. In Chapter IV we have already established a standard procedure to determine the instrumental effects, with special emphasis on the SA aperture diameters and camera lengths. In this chapter different application cases are considered, to demonstrate the excellent capabilities of the Rietveld refinement of EPD, including the phase determination for multi-phase systems. This is important since although XRPD is the mainstay in the crystallographic studies of nanostructured systems, it still has its cons of being an averaging method. The complementary technique involving microstructural characterization based on TEM jointly with EPD caters to material volumes many orders smaller, and like XRPD the electron diffraction intensities can be modeled to yield the sample structural and microstructural features.

This localized information is crucial in two scenarios. Firstly, when the emphasis is on revealing the alteration layers in the specimens that could be completely overlooked by the bulk characterization tools [158]. Secondly, XRPD-based crystallographic studies could be less reliable if the amount of sample to be characterized is available only in a limited amount, a situation often encountered in environmental monitoring systems [244]. Moreover, the short data acquisition time is of special importance in speeding up the characterization procedure, particularly interesting for metastable structures or kinetics studies. At the same time, under quasi-kinematical conditions structural and microstructural characterization of the nanostructured systems has been achieved through TEM-assisted precession techniques [89]. These include different techniques, such as electron diffraction tomography [90,91], automated crystal orientation and phase mapping [93], orientation mapping [92], and zone-axis precession electron diffraction [94].

V.2 Material sample description

The different materials discussed below, some of them multi-phase systems, feature specific characteristics to be tackled with the proposed methodology. These include nanocrystalline (nc) yttrium oxide (Y_2O_3), silicon (Si), titanium dioxide (TiO_2), and disc brake wear debris, featuring several phases. To illustrate the limits of the proposed approach concerning material characteristics, the EPD of a hematite sample featuring

relatively coarser crystallites obtained from the heat treatment of natural goethite was also studied.

nc- Y_2O_3 has a large-scale application as a refractory material as it displays high thermal stability up to approximately 2327 °C, chemical stability, and corrosion resistance [245,246]. It is also used in thermal barrier coatings [247], optoelectronics [248], as a solid-state laser material [249], and for ceramic processing (zirconia stabilization) [250]. Pure Y_2O_3 has been shown to exist in mainly two stable polymorphs: cubic and hexagonal. A metastable polymorph, having a monoclinic structure, has been also reported [251]. nc- Y_2O_3 has been studied extensively through the Rietveld refinement of XRPD in coordination with the imaging inputs from the TEM [252,253,246]. In this work, we have evaluated the microstructure of the nc- Y_2O_3 sample based on both XRPD and EPD-based Rietveld fitting. The results obtained, especially the crystallite sizes, were in agreement with one another. Additionally, this analysis further validated the instrumental broadening function determined using the different CeO_2 sample, demonstrated in the previous chapter.

nc-Si has widespread usage as a semiconductor material in optoelectronics instruments, such as photodetectors and photovoltaic cells [254,255]. nc-Si possesses a direct bandgap that can emit light efficiently with a quantum yield of more than 60 % [255], with an energy that can be varied from the near-infrared to the blue end of the visible spectrum [256,257]. Thus, nc-Si has contributed immensely to the growth of high-performance optoelectronic devices as the potentially critical issue of the dependence of electromagnetic wavelength emission on the size of the nanocrystals has been substantially managed [258,259]. In this regard, Raman spectroscopy which has been used extensively for particle size elucidation in the range of 5-30 nm has limited scope below the size of 5 nm due to excessive broadening of the Raman peaks by small particles [260–262]. In this context, high-resolution TEM images, possibly in coordination with electron diffraction, is an alternate and valuable choice for microstructural characterization.

nc- TiO_2 exists in three different physical forms- anatase (tetragonal, space group: I41/amd), rutile (tetragonal, space group: P42/mnm), and brookite (orthorhombic, space group: Pbca) [263], and all three are used in a variety of applications. Anatase exhibits properties suitable for light harvesting applications in photocatalysis and photon–electron transfer [264,265]. Rutile finds application as a white pigment for different types of coatings, plastic and paper [266,267]. Brookite has been demonstrated to possess superior theoretically predicted static dielectric constant than anatase and rutile [268,269]. It has been shown that during the synthesis process, the thermal treatments can lead to the formation of a mixture of the three polymorphs [270,271]. Thus, it is essential that before any particular application, the constituents of the synthesized nanopowder along with the respective phase compositions must be

evaluated. For this, the Rietveld refinement of the TiO₂ EPD is a valuable approach [272,273].

Since the emphasis of this thesis work is also on the possible characterization routes for environmental pollutants, a relevant sample was studied. This was a complex and heterogenous PM sample emitted from the dynamometer-based study of the disc brakes [208]. A disc brake converts the kinetic energy of a vehicle into heat energy through friction to stop a vehicle within the minimum possible distance. Two brake pads, typically made of friction materials with a complex composition, are pressed against a rotating cast-iron disc causing the unwanted emission of large quantities of PM, along with the primary function of reducing the velocity of the vehicle. These emitted PM constitute a broad size range of particles (10–0.1 μm) and large heterogeneity in terms of organic and inorganic constituents, including elements like Sb, Cu, and Fe [217,274]. Under extreme working conditions, the disc-pad coupling is subjected to complex thermo-mechanical-chemical interactions, leading even to the formation of phases such as iron oxides [223]. Many studies have applied the technique to determine the phase composition of these PM based on the fingerprinting of the SAED with inputs from spectroscopy for the elemental composition [275,276]. We have applied the developed approach to such complex wear debris to determine the phase fraction of the major constituents and their respective microstructure.

The last sample studied in this chapter served to demonstrate the limitations of the EPD in elucidating the microstructure of materials displaying coarse grain sizes. The sample considered for this purpose was hematite nanopowder obtained from the heat treatment of natural goethite [277]. Hematite, also referred to as “red ochre” in the archaeological literature, was traditionally used during the prehistoric ages for various utilitarian purposes, including primitive cave paintings. Hematite carried cultural importance because of its red colour and the deliberate using fire to convert goethite into hematite has been found in different ancient civilizations [278,279]. Many papers have reported the structural changes noted in goethite during artificial heating, ultimately changing to hematite phase [280,281,277]. The sample studied had crystallite dimensions in excess of 100 nm, at least along certain crystallographic directions. Still, the application of Rietveld refinement to the EPD of this sample gave interesting results in terms of the material characteristics.

V.3 Rietveld method: Key points

Throughout the analyses in this chapter, the instrumental broadening for different SA aperture-CL combinations was compensated as required. In the case of some samples, there was also the contribution of the supporting carbon film present on the TEM grid in the form of diffused scattering. Hence, the diffraction pattern from the

naked TEM grid was also analyzed using MAUD and compensated during the fitting of the nanostructured materials.

A key aspect of the Rietveld fitting procedure is deciding the terminating point of the refinement cycles. This is crucial since the software may permit the setting to 'refine' multiple parameters at the same time, with no substantial improvement in the results. Thus, a close inspection of the weighted sum of squares (WSS) was done at subsequent refinement stages. The goal for all the analyzed materials was to have a minimum possible value for WSS with the least number of refined parameters. However, since it has been proposed that profile and difference plots are also essential visual mediums to decide the level of the fitting achieved [282], they were not discarded either and verified for their compliance with the WSS. All diffraction patterns have been analyzed under two-beam dynamical diffraction approximation.

Concerning the number of parameters that are refined at any particular stage, it is important to highlight that too many of them may simply lead to overprocessing of the experimental data [167]. These in turn may yield results that are difficult to interpret. The issue of selecting the parameters that are refined at different stages is especially true for the microstructural parameters, wherein we may unnecessarily refine anisotropic crystallite size(s) and microstrain (s). Thus, for all the materials discussed in this Chapter, the results obtained from the anisotropic size-strain model were compared with the isotropic size-strain model.

The large surface area to volume ratio of the nanoparticles has a significant impact on their properties, including their physical shape. Indeed, the size and shape of the nanoparticles depend on the kinetics of the processes involved [283], and progress through the stages of nucleation, growth, and ripening [284]. However, it has been demonstrated that for the smallest dimensions, an isotropic shape could be the preferred one. Gardner et al. [285] noted for gold nanoparticles the existence of gold nanospheres and spheres in the size range of 2-20 nm. Thereafter, growth in a particular direction led to the formation of nano rod-like structures due to the preferential selection of crystal facets. Kahn et al. [286] synthesized nanocrystalline ZnO and noticed the formation of isotropic nanoparticles in the size range of 3-6 nm, and thereafter the formation of nanorods with lengths up to 120 nm. Chaudret [287] demonstrated for nanoparticles of different materials that the isotropic spherical shape initially formed could be transformed to regular anisotropic shapes (cubes, rods, wires) by altering the surface chemistry using different ligands.

Additionally, the dislocations in nanoparticles are also affected by the nearby surfaces, which impose a force, thereby causing the ejection of the dislocations towards the nanoparticle surface, discussed in detail by Ashby et al. [288]. This renders the defects to be unstable in nanoparticles below a critical size, and such nanoparticles have been

termed “self-healing”[288]. For instance, Ulvestad and Yau [289] demonstrated that palladium nanoparticles in the size range of 200-400 nm had the unique capability to self-heal the crystallographic defects, yielding improved properties.

All samples but hematite nano-powder studied in this Chapter displayed crystallite size in the size range of 30–200 Å. For such small sizes, it can be expected that the above explanation concerning the existence of isotropic crystallite size and negligible microstrain is applicable. Similar simplification of the microstructural parameters based on the Rietveld refinement can be noted in the literature [273,290].

V.4 Results and discussion

V.4.1 nc- Yttrium oxide

Fig. V-1 shows the TEM data collected from the analyzed nc-Y₂O₃ sample. Fig. V-1a) shows a cluster of particles collected at low magnification, from which the diffraction pattern shown in Fig. V-1b) was collected. The diffraction pattern was collected with the largest SA aperture of 800 μm diameter so that the graininess problem could be minimized. The high magnification image shown in Fig V-1c) clearly shows individual crystallites separated by boundaries. The numbered crystallites display size in the range of 52.2 to 256.2 Å, as evaluated using the ImageJ software. The crystallite numbered ‘3’ that is shown in Fig V-1e) was used to calculate the interplanar spacing for the (222) type of planes based on its FFT shown in Fig. V-1d). The value of the interplanar spacing determined was 3.04 Å, which agreed with the value obtained from the Y₂O₃ crystallographic reference card (COD ID: 1513300).

Fig. V-2a) shows the Rietveld fitting of the nc- Y₂O₃ EPD data shown in Fig. V-1. In this and all subsequent figures showing the Rietveld fitting, the relevant calculated intensities Y_{calc} (red dots) and the experimental intensities Y_{exp} (black dots), and the residual curves have been plotted. The microstructural characteristics determined are listed in Table V-1. To avoid any changes in the structure factor calculations, none of the structural parameters, whether atomic positions or occupancies were refined at any stage of the analysis.

The EPD analyzed using the anisotropic Popa model yielded an approximate isotropic crystallite size and shape, with negligible r.m.s. microstrain. Even when the analysis was performed with the isotropic size-strain model, the r.m.s. microstrain was determined as 1.94(5)E-4. Thus, it could be safely assumed that reliable results could be achieved under the isotropic size-strain model without refining the microstrain parameter and setting it to zero.

In this analysis, a major point of interest is the average value of crystallite size estimated at the final refinement step: 191.7(2) Å. This confirms that the Rietveld refinement of the EPD approach has the capability to satisfactorily determine crystallite

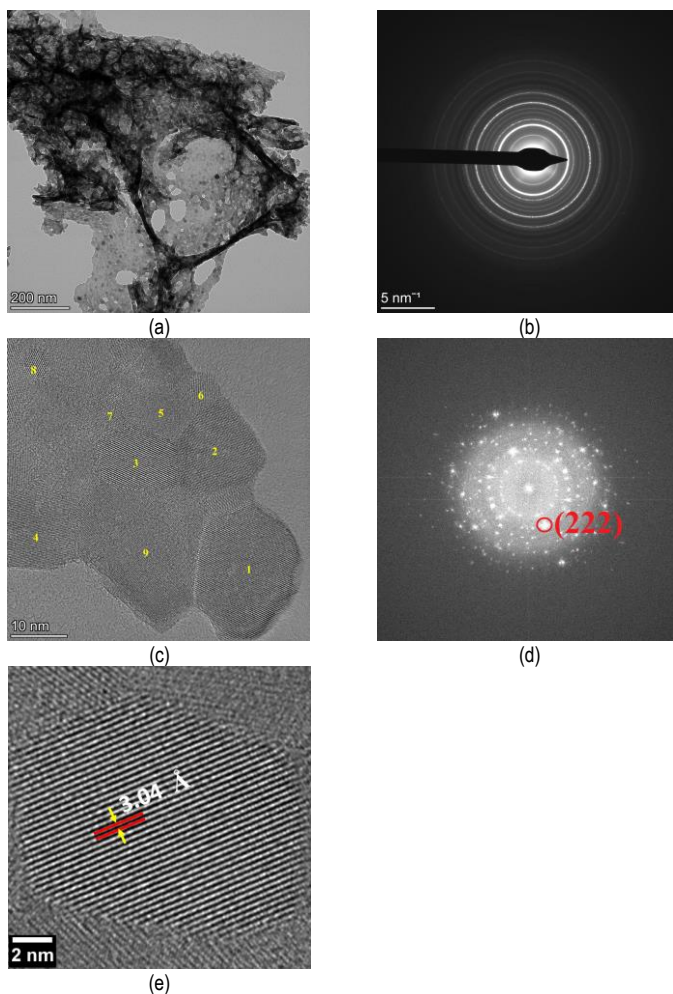
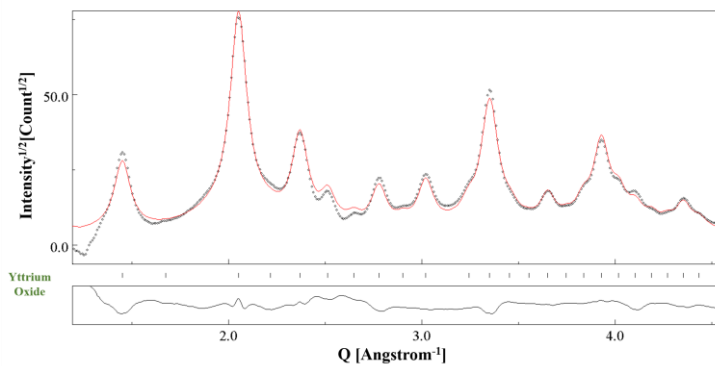
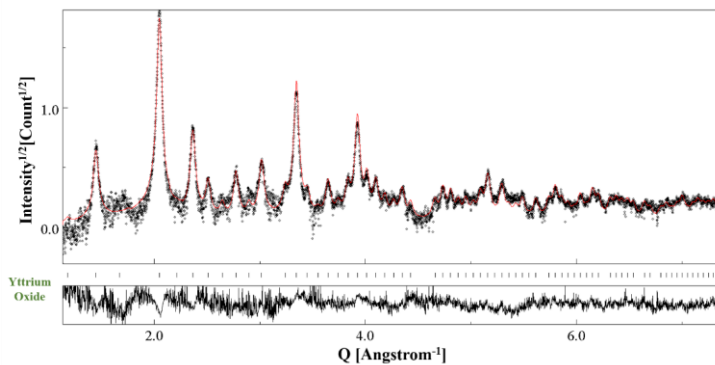


Figure V- 1 Bright-field image of an nc-Y₂O₃ cluster and (b) SAED data from the field of view. (c) Individual crystallites in a high-magnification image, with (d) its FFT. (e) An enlarged area of the crystallite marked '3' in panel (c), used to determine the interplanar spacing of the (222) planes as 3.04 Å

sizes up to 200 Å approx. In previous studies, different research groups have already shown the possibility to determine crystallite sizes for different materials of a smaller size range, such as 90 Å [227], 110 Å [159], and 80 Å [145].



(a)



(b)

Figure V- 2 Result of Rietveld refinement of nc-Y₂O₃ for EPD (a) and XRPD (b) Note: Background has been subtracted for better visualization of smaller peaks and differences. The microstructural parameters determined for each case have been listed in Table V-1.

Rietveld refinement of the XRPD data yielded an average crystallite size of 199(1) Å, along with negligible r.m.s. microstrains. The profile fitting for this is shown in Fig. V-2 b).

Table V- 1 Cell parameters, crystallite sizes, and reliability factors resulting from the analysis of nc-Y₂O₃ following EPD and XRPD in Fig. V-2

Method	a (Å)	Crystallite size, average (Å)	Rwp _{no.bkg} (%)
EPD	10.6070(4)	191.7(2)	11.90
XRPD	10.6198(6)	199(1)	28.64

V.4.2 Nanocrystalline Silicon (nc-Si)

Two different samples of nc-Si were studied to show the difference in their microstructure through their EPD-based Rietveld refinement. The crystallite size distribution of the two samples is shown using their dark field images in Fig. V-3 a-b), determined from the (111) ring of their selected area electron diffraction patterns in Fig V-3 c-d) for Samples A and B, respectively. It is possible to see a clear difference in the morphology of the crystallites and their respective size distribution.

Fig. V-4 shows the Rietveld profile fitting of the EPD pattern of Sample A. A similar fitting could be obtained for Sample B. The results obtained at the final stage of the refinement cycles are listed in Table V-4. We prefer subtracting the background so that the difference between the observed and calculated intensities is clearly visible. Unlike the observation made for the previous sample, i.e., nc-Y₂O₃, a satisfactory Rietveld fitting could not be obtained using the simple isotropic size-strain model. Thus, the results with Popa anisotropic model were checked. It turned out that different sets of planes yielded different crystallite sizes.

The major difference in the crystallite sizes was obtained along the directions [111] and [400], listed in Table V-4. Still, the r.m.s. microstrain contributions determined were negligible. Indeed, the r.ms. microstrain for Sample A was 8.018(1) E-5 similar values were obtained for Sample B, thus having a negligible effect on the profile fitting. The mean value of the crystallite size calculated for Sample B turned out to be smaller, which was in agreement with the direct image information (See Fig. V-3)). Using Image J software, a homogeneous distribution of the crystallite size could be obtained, which ranged from 5 to 12 nm for sample A. For sample B, it was observed that the size distribution was relatively less homogeneous: a coarse size distribution between 5 and 10 nm and a finer fraction that was lesser than 4 nm. In this regard, the important role of the EDP analysis is the possibility of determining the crystallite size, even if the direct image cannot be interpreted in a straightforward manner. Pseudo cubic shapes of the crystallites for the two samples were obtained, as shown in Table V-4. It is

important to emphasize that the refined shapes maybe actually different from the original ones, symmetrized by the Laue point group [243,291].

As mentioned in the previous chapter, there are limitations involved with the kinematical approximation-based Rietveld refinement of EPD. For Sample A, Fig. V-4 b) shows the Rietveld fitting of the EPD under the kinematical approximation. The relevant R_{wp, no_bkg} determined was 15.24 %. The profile fitting in Fig V-4a), performed under Blackman two-beam dynamical correction yields microstructural parameters with better accuracy.

It is worth to further explore this issue of dynamical diffraction. Table V-2 lists the

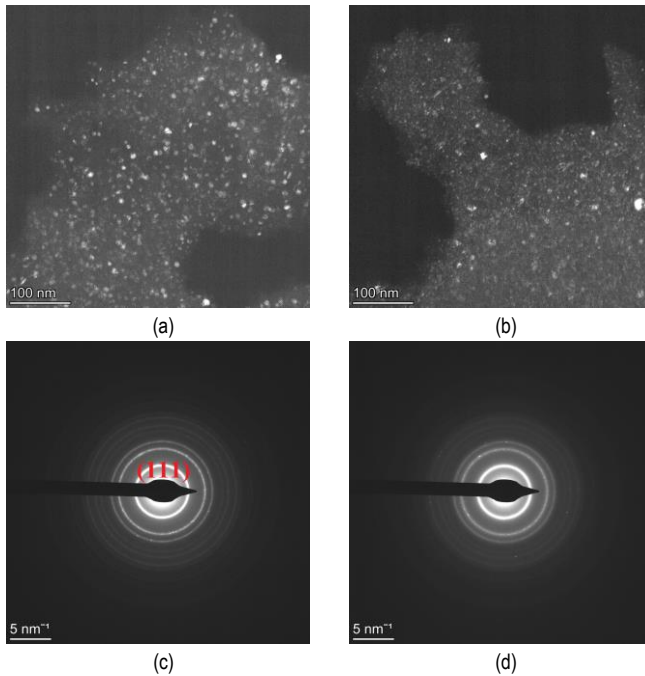
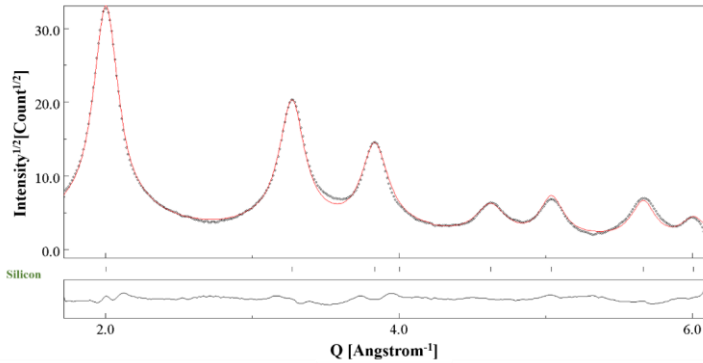
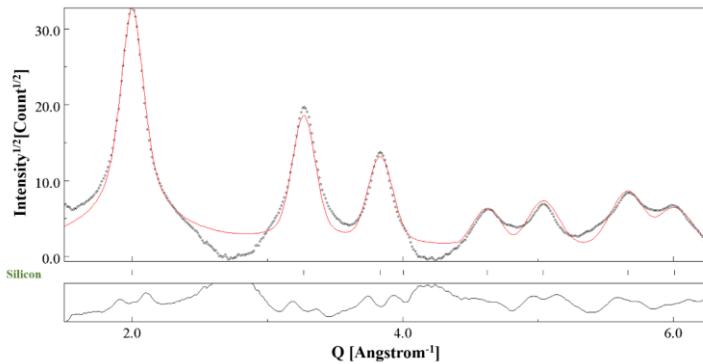


Figure V- 3 TEM results of nc-Si Samples A and B- Dark field images (a and b) formed with the (1 1 1) reflection of the SAED (c and d), respectively. The dark field image (a) shows a homogeneous grain size distribution with dimensions ranging between 5 and 12 nm. The dark field image (b) highlights the presence of coarser grains ranging in size from 5 to 10 nm and finer grains smaller than 4 nm.



(a)



(b)

Figure V- 4 Result of Rietveld refinements of nc-Si Sample A under two-beam dynamical correction (a) and kinematical approximation (b). It is clear that the kinematical approximation fails to match the calculated and experimental profiles causing an erroneous microstructure determination. The difference plot between the experimental and calculated intensities is shown in the lower part of the figures. Note: Background has been subtracted for better visualization of smaller peaks and differences. Dot line: Experimental intensity profile; red line: calculated profile.

calculated values of kinematical and dynamical structure factors magnitude for different planes of nc-Si, along with their ratios. These values have been determined for a constant value of the lattice parameter, with the Debye-Waller factor set to zero.

The values of the structure factor for the kinematical and dynamical models show large variations, depending on the calculated thickness over which the diffraction is taking place. The change in the ratios for different sets of planes indicates the presence of dynamical diffraction [50].

Table V- 2 Kinematical and dynamical structure factors for different planes of nc-Si. The different values of the ratios highlight the presence of dynamical diffraction occurring in the sample.

Plane	F_{DYN} (Å)	F_{KIN} (Å)	Ratio _F
111	4.9414	68.5557	13.8736
220	4.3672	53.6636	12.2880
311	3.7495	43.0188	11.4733
400	2.2856	24.1062	10.5471
331	2.8620	30.9450	10.8124
422	3.4544	38.7193	11.2086
511	2.4356	25.8339	10.6067
333	1.4481	14.9156	10.3002
440	2.2627	23.8454	10.5384

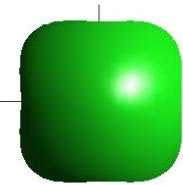

Table V- 3 Kinematical and dynamical structure factors for different planes of nc-CeO₂. Less variations in the absolute values and identical values of the ratios highlight the absence of dynamical diffraction occurring in the sample.

Plane	F_{DYN} (Å)	F_{KIN} (Å)	Ratio _F
111	205.3658	161.3599	1.2727
200	123.1879	96.7966	1.2726
220	253.3199	199.0318	1.2728
311	245.2147	192.6646	1.2728
222	92.95398	73.0415	1.2726
400	140.0245	110.0249	1.2727
331	194.2348	152.6153	1.2727
420	123.9484	97.3942	1.2726

In contrast, Table V-3 lists the same set of values for selected planes of nc-CeO₂ studied in the previous chapter IV. The values of the structure factor for the kinematical

and dynamical models show less variation, and the ratio is seen to be constant. This signifies that we are under kinematical diffraction conditions. A further point of interest originates from this: Although the average crystallite size of CeO₂ (124.9(4)) is larger than that of Si (60.5(2)), still dynamical diffraction is more prominent in Si. This highlights that although smaller crystallite size is a favourable condition for diminishing chances of dynamical diffraction, it doesn't guarantee that reducing the crystallite size will altogether eliminate it.

Table V- 4 Cell parameters, crystallite sizes, reliability factors, and shape refinements resulting from the Rietveld refinement of nc-Si.

Sample	a (Å)	Crystallite size, average (Å)	Anisotropic Crystallite size (Å)	Rwp _{no. bkg} (%)	Shape
A	5.4334(1)	60.5(2)	[111]: 70.4 [400]: 45.6	8.18	
B	5.4435(8)	30.1(1)	[111]: 37.4 [400]: 19.0	11.22	

However, a consequence of dynamical scattering in the EPD data is its impact on the Debye-Waller factor [292]. The former causes a relatively high value of the latter, as also reported by Zuo et al.[141]. At the final refinement cycle for Sample A, the value of the Debye-Waller factor determined was 0.0543(5)(Å)².

V.4.3 Nanocrystalline titanium dioxide (nc- TiO₂)

The theme of this analysis was to study a commercial nc-TiO₂ for the weight percentages of its different polymorphs. Fig. V-5a) shows the bright field image at low magnification of a cluster of particles, and the SAED pattern shown in Fig. V-5b) was obtained from its field of view. Fig. V-5c) shows a bright field image at a high

magnification image of different agglomerates with overlapping crystallites that feature mostly spherical morphology.

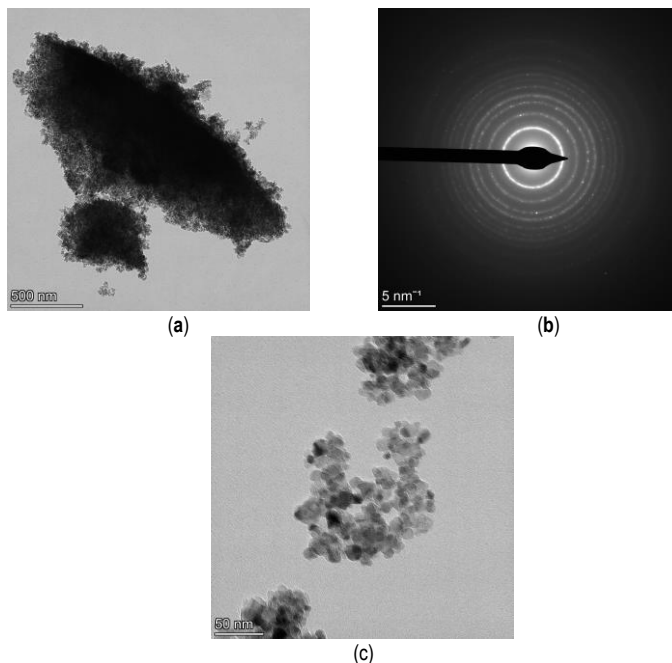


Figure V- 5 Bright-field image of nc-TiO₂ (a) and SAED (b) from the field of view. In (c) agglomerates are shown at a high magnification

The Rietveld fitting of the EPD pattern in Fig. V-5b) is shown in Fig. V-6, which confirms that two polymorphs of titanium oxide are present in the specimen: anatase and brookite. Anatase has a tetragonal crystal structure, with a unit cell whose parameters are listed in Table V-5. Brookite, on the other hand, has an orthorhombic crystal structure, with three different lattice parameters (Table V-5). Based on the Popa model, these three lattice parameters can be refined separately along with the corresponding six anisotropic r.ms. microstrain values.

For the correct weight quantification of anatase and brookite, different combinations of the microstructural parameters that can be refined, have been analyzed, as shown in Table V-6. No significant improvements in the results were seen when the number of refined parameters was increased, in comparison with the simplest refinement strategy (Case 1), with only one lattice parameter of the anatase phase refined and

both anatase and brookite attributed to having isotropic crystallite size with no microstrain.

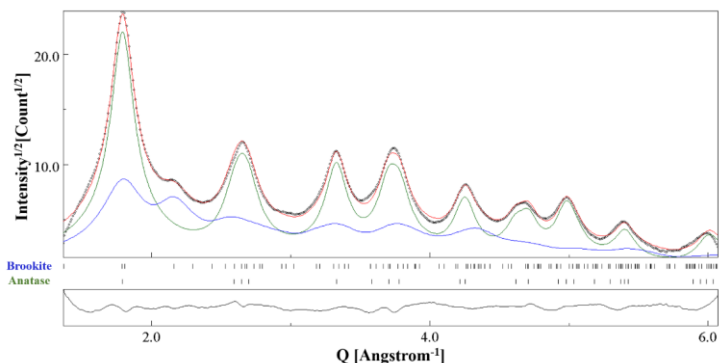


Figure V- 6 Result of Rietveld refinement of nc-TiO₂ SAED shown in Fig. V-5 b). Note: Background has been subtracted for better visualization of smaller peaks and differences. $Rwp_{no_bkg} = 17.77\%$. Dot line: Experimental intensity profile; red line: calculated profile; green line: anatase phase; blue line: brookite phase

Table V- 5 Cell parameters, crystallite sizes, and phase compositions for the nc-TiO₂, as evaluated from the Rietveld refinement.

Phase	Lattice parameters (Å°)	Crystallite size (Å)	Phase composition (wt.%)
Anatase (Tetragonal)	a= 3.7761(3) c= 9.4917	52.1(2)	50-70
Brookite (Orthorhombic)	a= 9.184 b= 5.479 c= 5.158	26.1(1)	30-50

This indicates that although the Rietveld algorithm may allow refining many parameters at the same time, the quality of the data would suggest containing the refinement to those parameters that are statistically significant [167]. A reasonable trade-off in the results can be obtained by considering the simplest model, since it could provide a very close measure of the average crystallite size without the need of refining many parameters.

As expected, the weight fraction for the two phases was found to be dependent on the selected Size-Strain model of the microstructure. However, this variation for the brookite phase was indeed large as shown in Table V-6, for different possible

refinement cases. Attributing the anisotropic model to brookite may yield a relatively lesser and hence more realistic weight percentage for brookite (say 35 wt %).

Table V- 6 Different microstructural parameters refined for nc-TiO₂ based on the size-strain model adopted and their effects on the results

Case	Refined microstructural parameters	WSS	Rwp _{no_bkg}	Total number of refined parameters	Brookite weight %	Average crystallite size of phases
1	Anatase: Isotropic crystallite; one lattice parameter (a), and (c) determined in its relative ratio. Brookite: Isotropic crystallite size	20984	17.77	20	50	Anatase: 52.1(2) Brookite: 26.1(1)
2	Anatase: Isotropic crystallite; one lattice parameter (a) and (c) determined in its relative ratio; strain refined Brookite: Isotropic crystallite size; strain refined	20987	17.73	22	47	Anatase: 52.7(1) Brookite: 23.6(9)
3	Anatase: Anisotropic crystallite; one lattice parameter (a) and (c) determined in its relative ratio. Brookite: Isotropic crystallite size	20941	17.26	23	44	Anatase: 51.6(1) Brookite: 23.3(7)
4	Anatase: Anisotropic crystallite; one lattice parameter (a) and (c) determined in its relative ratio. Brookite: Anisotropic crystallite size	20560	18.08	25	35	Anatase: 49.63(5) Brookite: 24(1)
5	Anatase: Anisotropic crystallite; one lattice parameter (a) and (c) determined in its relative ratio. Brookite: Anisotropic crystallite size; one lattice parameter (a).	20514	17.67	26	36	Anatase: 50.0(2) Brookite: 21.4(4)
6	Anatase: Anisotropic crystallite; one lattice parameter (a) and (c) determined in its relative ratio; Microstrain refined Brookite: Anisotropic crystallite size; one lattice parameter (a); microstrain refined	20500	18.04	36	35	Anatase: 49.6(1) Brookite: 24(1)

However, in this case 4, we obtained the anisotropic crystallite size determined using (210) planes as 43 Å while that calculated using (133) planes was 6 Å, which is unrealistic for a material having a small average crystallite size in the range of 20-27 Å. Based on different weight percentages obtained for the two phases by selecting different size-strain models, it can be best proposed that the weight percentage of brookite lies in the range of 30-50 %.

V.4.4 Particulate matter from a disc brake

Fig. V-7 shows the bright field image (a) of the collected disc brake wear debris and the corresponding dark field image (b). The first ring of the diffraction pattern in Fig. V-7b) was selected for forming the dark field image. The brighter spots along the diffraction pattern along with the dark field image suggest a non-homogeneous distribution of the crystallite size.

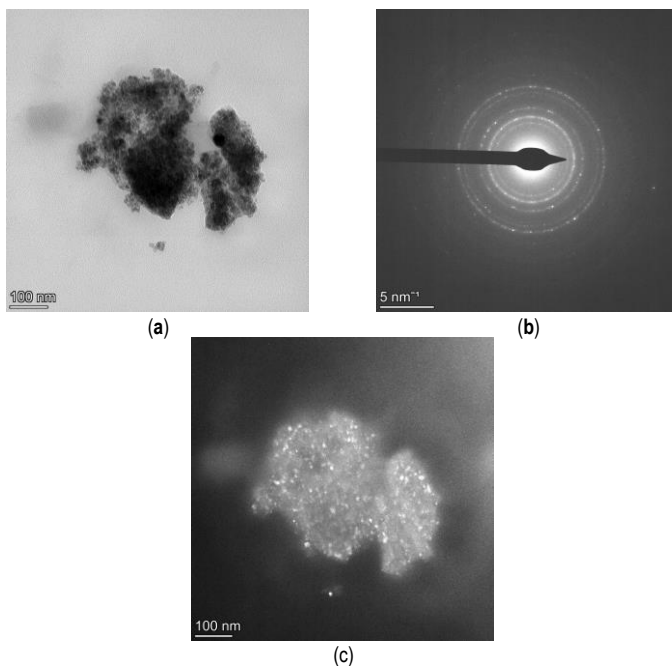


Figure V- 7 Bright-field image of wear debris (a) and SAED (b) from the field of view. The dark field image (c) was formed by selecting the first ring of the SAED. Analysis of the dark field images yielded an average crystallite size of 110 Å.

Fig. V-8 shows the Rietveld fitting of the disc brake wear debris diffraction pattern shown in Fig. V-7b). It was interesting to note that two iron oxides- magnetite and maghemite were found in the specimen. The diffraction profile peaks of these two oxides clearly display some overlapping. The main results of the Rietveld fitting have been listed in Table V-7, including the microstructural parameters and the phase compositions. The reliability factor had a relatively higher value: $Rwp_{no_bkg} = 23.07$ %. This can be attributed to some poor statistics of the diffraction pattern, having been

collected with a SA aperture of a smaller dimension. The microstructural parameters obtained using the Popa model were compared with the isotropic size-strain model. Indeed, the isotropic model yielded better values of the reliability fitting factor. The crystallite size of magnetite was calculated as 83.0(9) Å, which although relatively larger than the crystallite size of maghemite displayed negligible anisotropy both in terms of size and microstrain. As for the TiO₂ sample, the weight percentages of magnetite and maghemite were found to vary with the different size-strain models adopted. It could be estimated that for the magnetite phase, the weight percentage is in the range of 30-40 %.

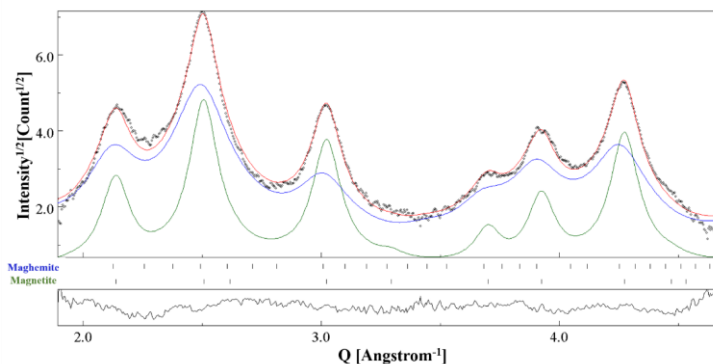


Figure V- 8 Result of Rietveld refinement (a) of wear debris SAED shown in Fig. V-7 b). Note: Background has been subtracted for better visualization of smaller peaks and differences. $R_{wp, no_bkg} = 23.07\%$. Dot line: Experimental intensity profile; red line: calculated profile; green line: Fe₃O₄-magnetite phase; blue line: Fe₂O₃-maghemite phase.

It is important to further explore the possibility of the existence of both maghemite and hematite in the disc brake wear debris. It has been proposed that Magnetite (Fe₃O₄) is mainly produced in the wear debris and then released through the tribo-oxidation wear mechanism of the cast-iron disc, in which the deformed and highly reactive tiny worn-out Fe particles react with the surrounding oxygen [293,294].

Table V- 7 parameters, crystallite sizes, and quantifications of the phases obtained from the analysis of disc brake wear debris

Phase	Lattice parameter (Å)	Crystallite size (Å)	Phase composition (wt.%)
Maghemite	8.352(3)	32.5(7)	60-70
Magnetite	8.316(1)	83.0(9)	30-40

However, it has been found that Fe_2O_3 is also a constituent of the emitted PM. Verma et al. [244] detected the presence of Fe_2O_3 as hematite ($\alpha\text{-Fe}_2\text{O}_3$, rhombohedral), whereas Kukutschová et al. [275] found that the disc brake wear debris constituted maghemite ($\gamma\text{-Fe}_2\text{O}_3$, cubic), and other oxides. Although $\gamma\text{-Fe}_2\text{O}_3$ (maghemite) has been proposed to be only a metastable phase, with the phase transformation to $\alpha\text{-Fe}_2\text{O}_3$ (hematite) occurring above 300°C , the nanocrystalline state of the wear debris particles can give the possibility of $\gamma\text{-Fe}_2\text{O}_3$ becoming thermodynamically stable [295,296]. This is the most probable reason for the detection of $\gamma\text{-Fe}_2\text{O}_3$ in the wear debris studied.

V.4.5 Hematite from heat treatment of natural Goethite

The sample studied in this section was hematite ($\alpha\text{-Fe}_2\text{O}_3$), which was obtained upon heat treatment at 600°C of a natural goethite (FeOOH) sample. The phase transformation occurs through the release of the structural water [297]. Fig.V-9a) shows the bright field image of a cluster of particles at a low magnification from which the SAED pattern in Fig. V-9b) was collected. The diffraction pattern depicts the presence of brighter spots along with the non-continuous rings. As better visible through the high magnification image (Fig. V-9c)), the crystallite sizes are indeed significantly larger than those studied earlier in this chapter. Thus, the point of focus was to determine the upper limit of crystallite size, which could be analyzed with reasonable accuracy through the Rietveld-based fitting of the EPD.

Fig. V-10 shows the Rietveld fitting of the hematite EPD pattern shown in Fig. V-9b). The profile fitting clearly indicates that the complete transformation of the goethite phase to hematite has not yet happened. As also observed by Cavallo et al. [297], the complete recrystallization yielding the hematite phase occurred in the sample that was heat-treated at a higher temperature of 800°C .

As can be noted from Fig. V-10, the peak intensities of the observed and the calculated profiles do not match satisfactorily. The refined values of the r.m.s. microstrain determined for both phases were not negligible in this sample, which demonstrated anisotropic broadening. The lack of accuracy in the microstructural parameters determined from the profile fitting, in this case, is due to two main reasons.

Firstly, since there exists an inverse relationship between the crystallite size and the broadening caused by it, in general, the line profile analysis has more sensitivity towards smaller crystallite dimensions. Lutterotti et al. observed in the analysis of synchrotron diffraction images that collected the diffraction pattern became insensitive for crystallite sizes that were larger than 200 nm [164]. As was observed for our sample as well, there were no apparent changes in the fitting (i.e., the broadening didn't vary

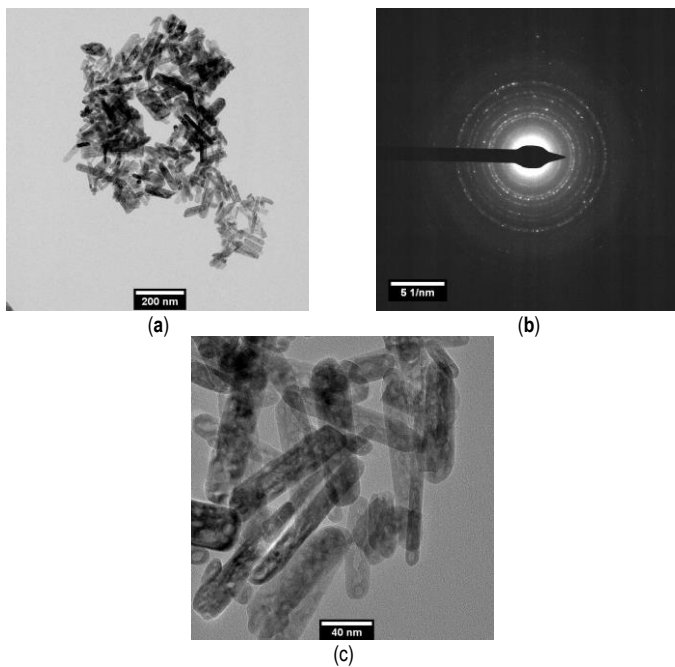


Figure V- 9 (a) Bright-field image of hematite-goethite and SAED pattern (b) collected from (a). Crystallites at high magnification are shown in (c)

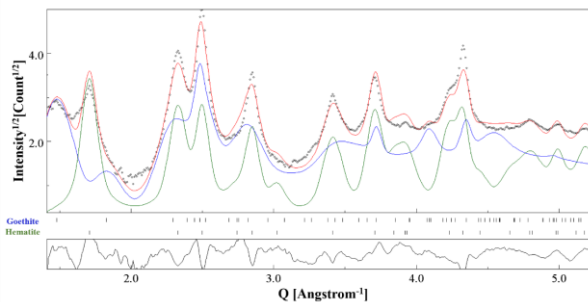


Figure V- 10 Result of Rietveld refinement of the goethite-hematite SAED shown in Fig. V-9 b). Note: Background has been subtracted for better visualization of smaller peaks and differences. Dot line: Experimental intensity profile; red line: calculated profile; green line: hematite; blue line: goethite

much) even if the crystallite sizes were on purpose varied abruptly. Secondly, there is also the role of instrumental broadening. The diffraction pattern shown in Fig. V-9b) was collected with SA aperture 40 μm - CL 658 mm combination. As can be seen from Table IV-4 (Chapter IV), for this combination the instrumental broadening function in terms of FWHM was determined as 0.01468° . In Table V-9, we have highlighted the physical broadening caused by different set of planes of hematite and goethite, compared with that of silicon (Sample A, refer to Section V.4.2).

As can be seen, the physical broadening for silicon is many orders higher than that of the other two. According to Schwartz and Cohen [298], if the overall line broadening is 20 % greater than the instrumental broadening, then it gives an upper limit of about 1000 \AA of the effective domain size that can be determined. However, in our case, the instrumental broadening of the TEM is itself greater than the broadening determined by most planes of hematite, and much greater than those of goethite. To further clarify, in Fig. V-11, the hindrance in accurate determination physical broadening due to large instrumental broadening is demonstrated.

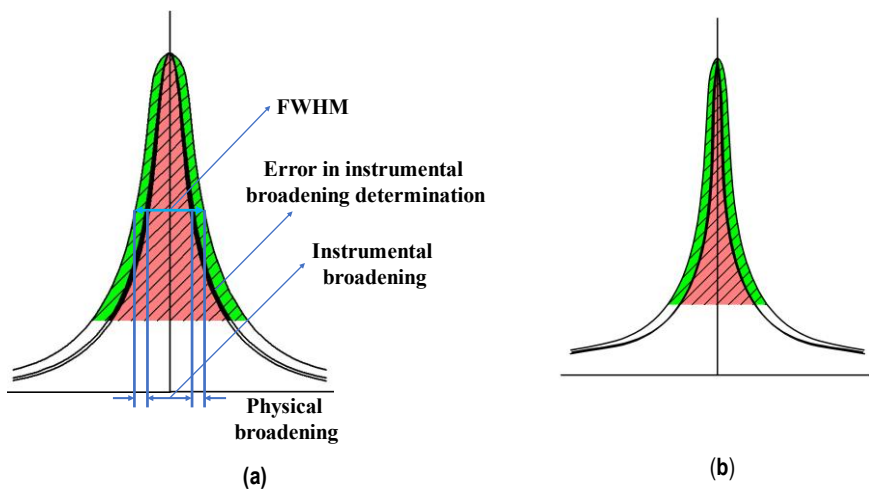


Figure V- 11 Schematic representation of large instrumental broadening compared to physical broadening due to microstructure.

In both Fig. V-11 a-b), the green zone indicates the physical broadening caused by the sample microstructure, red zone pertains to instrumental broadening, and the black zone refers to the error in the accurate instrumental broadening determination.

In both the figures, the FWHM corresponding to the physical broadening has been schematically kept constant, but in Fig. V-11 a), the instrumental broadening has a large magnitude and a dominant share of the overall FWHM. In contrast, in Fig. V-11 b), although the physical broadening is still small as in Fig. V-11 a), but still contributes substantially to the overall FWHM as the instrumental broadening is small. Thus, during any refinement cycle, the fitting profile will have accountable contribution of sample broadening towards the overall FWHM. The worst case would arise in Fig. V-11 a) if the sample broadening is so small as compared to the instrumental broadening that it gets masked by the error (black zone) in the instrumental broadening.

The case at hand is the one shown in Fig. V-11a). Thus, such an analysis based on Rietveld refinement of EPD lacks the general sensitivity to detect even large differences in the crystallite sizes, forming the limitation of the proposed approach. Therefore, the microstructural parameters determined and phase fractions evaluated in Table V-8 are prone to significant errors.

Table V- 8 Cell parameters, crystallite sizes, and phase quantifications refinements obtained from the analysis of the goethite-hematite SAED.

Phase	Lattice parameters (Å)	Crystallite size (Å)	Phase composition (wt.%)
Hematite	5.425(2)	300	60
Goethite	a=4.682(2) b=10.134 c=3.073	1930	40

Table V- 9 Physical broadening in terms of FWHM determined for different sets of planes of nc- silicon, hematite, and goethite.

Silicon		Hematite		Goethite	
Plane	FWHM (°)	Plane	FWHM (°)	Plane	FWHM (°)
(111)	0.02302	(110)	0.01391	(040)	0.00128
(220)	0.02525	(211)	0.01759	(060)	0.00147
(311)	0.02830	($\bar{1}$ 10)	0.00854	(112)	0.00852
(400)	0.03557	(210)	0.00987		
(331)	0.02456	(200)	0.01824		

V.5 Highlights of the chapter

- It has been demonstrated in this chapter that it is feasible to study the microstructure of different nanostructured systems within the specified

crystallite size limits through Rietveld refinement of their EPD. This sort of methodology can support the results from bulk characterization tools like XRPD.

- A close match could be obtained between the refined microstructural parameters obtained through EPD and XRPD for nc-Y₂O₃. This validated the possibility of elucidating the microstructure of other nanostructured systems relying solely on EPD.
- The methodology applied to the unary phase samples: nc Si, and binary phase sample: nc-TiO₂. The advantage of analyzing the EPD patterns with two-beam dynamical correction was highlighted. The effect of increasing the number of refined parameters on the profile fitting was studied. It was often seen that the simple isotropic size-strain model has the capability to elucidate the microstructure satisfactorily.
- The methodology was applied to the complex and heterogeneous disc brake wear debris, including the phase determination of its constituents. Still, an analysis of this type requires further strengthening with the integration of analytical information. This is the topic addressed in the next Chapter 6.
- Coarse crystallites (for instance, those greater than 100 nm) may render the determination of microstructural parameters difficult as these features get masked by the large instrumental broadening function.

Chapter VI: Combined electron powder diffraction and energy dispersive spectroscopy study

VI.1 Introduction

With the continuous growth in synthesis techniques [299,300] and endeavours to solve the unknown structures [31,301], materials characterization has increasingly become challenging. The nanocrystalline state readily offers to manipulate the microstructure and structure, further strengthening the need to innovate the existing characterization tools. It has to be noted that in most cases for a complete quantitative characterization, imaging, spectroscopy, and diffraction techniques should be employed all together, whenever possible. In this regard, transmission electron microscopy is a robust characterization tool that offers to perform all three operations from the same region of interest.

As mentioned in the earlier chapters, XRPD extensively while EPD partially has been used for crystallographic-based studies of nanostructured systems, both having their own strengths and weaknesses. Most importantly, both techniques possess capabilities to encode the material features, that can be modelled to yield a complete description of the structure. However, there are problems associated with the lower limit of detection and quantification of a minor phase or impurity in a multi-phase system relying solely on diffraction techniques [302,303].

Additionally, since amorphous and poorly ordered phases lack periodicity, they generate diffused profiles thereby limiting their accurate quantification. Not only from the point of quantification, but even phase identification can also become cumbersome in the case of the characterization of unknown materials. The preliminary phase identification using dedicated search-match software packages can be very slow and even inaccurate if multiple unknown phases are present in the material, causing broad and overlapped peaks. Moreover, the sensitivity of the diffraction methods to the presence of different elements in the same crystal structure could be limited since it depends on the atomic scattering factor, which could be similar for the different elements. In such cases, information from the corresponding analytical techniques, e.g., XRF and EDXS, have capabilities to aid the characterization process. Furthermore, the elemental composition information can also be extremely useful for obtaining an accurate fitting of the diffraction data during a full pattern fitting procedure. This has a direct positive consequence on the results of the microstructural and structural parameters determined at the end of the refinement.

On the other hand, the spectroscopy analytical methods can also be supported by the diffraction methods to complement the missing or incomplete information. The detection of the light elements, or in general those elements that fall outside the sensitive analytical range can be indirectly ascertained by detecting the presence of the corresponding element-bearing phases. In this perspective, XRD being amongst the robust characterization tools for crystallographic-based studies- phase identification, structural, microstructural, and texture analysis, has been coupled with its analytical counterpart, XRF. Bortolotti et al. [304], for ceramics, and Secchi et al. [305], for different minerals, demonstrated using a Rietveld-like approach, wherein both XRD and XRF data for multiphase systems were modelled separately, that the approach could counter shortcomings of each of the individual methods. The methodology has been implemented in MAUD by extending the Rietveld-like fitting to the XRF data starting with the phases that were identified by XRD.

Based on the same motivation to further gain the advantages from the combined diffraction-spectroscopy analysis, this chapter aims to supplement the Rietveld fitting of the SAED patterns with the simultaneous fitting of the EDXS data. The term combined "SAED-EDXS" analysis generally means analyzing each set of data separately and using the information gathered from one technique to support the other. However, as a further step, the results presented in this chapter are based on merging the datasets in one common Rietveld fitting to better use specific features provided by individual methods.

VI.2 Material: Nanocrystalline cobalt iron oxide

A cobalt-iron oxide (CoFe_2O_4) nano powder: Purity: > 99.5%, Size: 30 nm (quoted), produced by Nanografi Nano Technology [306] was studied in the as-received condition.

Ferrites are used extensively because of their notable properties, such as high dc electrical resistivity, large permeability at high frequency, and high saturation magnetization [307]. Ferrites find large-scale applications in the fields of electronics, high-frequency data storage, electrode material in solid oxide fuel cells, magnetic fluids, and Li-ion batteries [308–312]. The choice of this material stems from the fact that it is a mixed oxide, featuring a wide coverage on the EDXS spectrum, and at the same time, its crystal structure being cubic is relatively simple. The latter has significance in this proposed methodology which is still in the developing stage. The combined analysis involves the simultaneous refinements of the diffraction and spectroscopy data, and in this regard the cubic structure with a single lattice parameters and simplified site occupancies is beneficial.

A small amount of the CoFe_2O_4 nano powder was dispersed in ethanol through ultrasonic mixing for 10 min. Thereafter, 30 μL of the solution was deposited onto an

Au TEM grid (300 mesh) having a supporting carbon film. A low background single tilt holder was used for the analysis. The EDXS spectrum was collected with an acquisition time of 60 s.

VI.3 Results and discussion

Fig. VI-1 shows the TEM data collected on the CoFe_2O_4 nanopowder. Fig. VI-1 a) is a BF image collected at low magnification, from which the SAED pattern in Fig. VI-1 b) was obtained. Fig. VI-1 c) is a high magnification image, showing overlapped crystallites that display a broad size distribution. The EDXS spectrum shown in Fig. VI-2 was collected from the field of view of the BF image in Fig. VI-1 a), just like the SAED pattern.

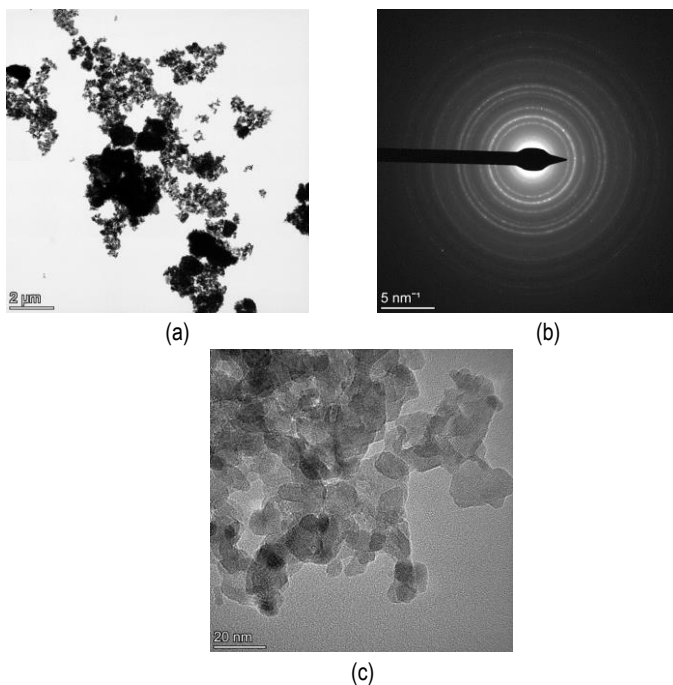


Figure VI- 1 (a) Bright-field image of nanocrystalline CoFe_2O_4 and SAED pattern (b) collected from the field of view in (a). Crystallites at high magnification are shown in (c)

Table VI-1 lists the elemental composition obtained from the EDXS spectrum. Although the abundant elements are O, Co, and Fe, traces of Na, Mg, Ca, Ti, and Mn suggest that there are impurities present in the specimen. These elements could be present as substitutional impurities at the atomic sites, or altogether in the form of a separate phase. Au and C were not quantified as their presence in the spectrum are due to the TEM grid and the supporting film, respectively.

The Rietveld refinement of the electron diffraction pattern was performed following the procedure described in Chapter IV and Appendix A1. To counter the graininess issue in the EPD pattern and to gather material characteristics from a larger area of the specimen, the diffraction pattern shown in Fig. VI-1 b) was collected using the largest SA aperture of 800 μm available on the microscope. The instrumental effects were compensated with the values determined in Chapter IV for different SA aperture-CL combinations. The contribution of the supporting carbon film in the form of two diffused halos was compensated as described in Appendix A1.

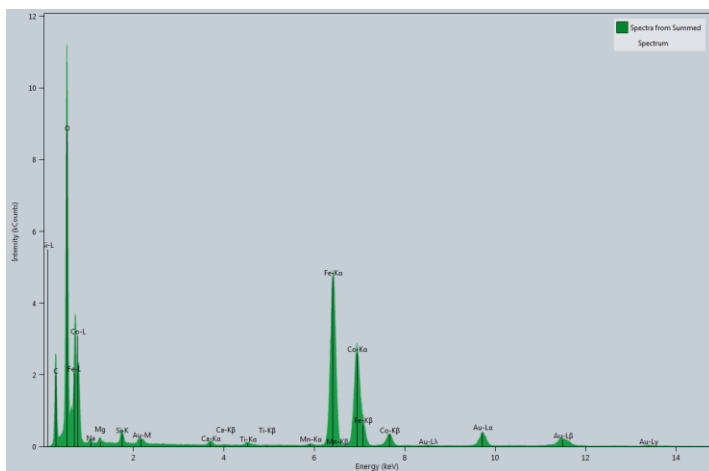


Figure VI- 2 EDXS spectrum collected from the nanocrystalline clusters shown in Fig. VI-1 a). Na, Mg, Ca, Ti, and Mn are the impurity elements. Au and C signals originate from the TEM grid.

Fig. VI-3 shows the Rietveld refinement of the EPD pattern in Fig. VI-1b) This fitting is based solely on the EPD, with no contributions from the EDXS, i.e., it is not a part of the combined analysis. Additionally, the atomic occupancies of the elements- O, Fe, and Co were not refined for this fitting. Still, based on the visual inspection as well as on the reliability factor ($R_{wp_{no_bkg}} = 15.77\%$; $R_{wp} = 4.00\%$), it can be easily deduced that the fitting is reasonably good.

However, as shown using the EDXS spectrum, there are several elements present in the nanopowder, nevertheless in low concentrations (Table VI-1). We clearly see from the fitting of the EPD pattern that all the peaks match with the CoFe_2O_4 phase. This gives an indication that the minority elements are present in the form of substitutional impurities, or in the case that some minor phase(s) are present, their quantity is well below the detection limit and sensitivity of the EPD pattern.

Table VI-1 Quantification of the elements shown in the EDXS spectrum in Fig. VI-2. Please note: C, Au, and Si have not been quantified

Element	Wt %
O	32.2
Na	0.4
Mg	0.5
Ca	0.5
Ti	0.5
Mn	0.7
Fe	40.7
Co	24.5

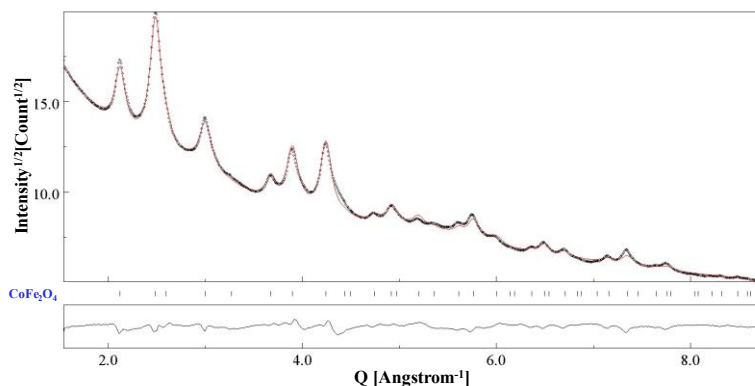


Figure VI-3 Rietveld fitting of the nc- CoFe_2O_4 SAED pattern shown in Fig. VI-1 b). The EPD pattern lacks the sensitivity to detect the impurity elements as a reasonable good fitting ($R_{wp_{no_bkg}} = 15.77\%$) could be obtained even when the impurity elements were not included in the crystal structure.

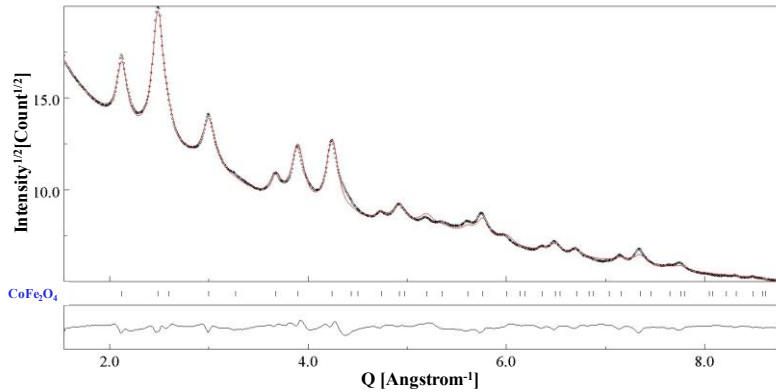
Fig. VI-4 shows the combined EPD-EDXS Rietveld fitting of the CoFe_2O_4 nanopowder. The procedure for implementing the EDXS fitting using MAUD has been explained in Appendix A2. For the EPD data, as done in the conventional Rietveld refinement computation, the crystal structure of the CoFe_2O_4 phase has been used and the additional elements that are not directly detected by the SAED pattern are inserted as substitutional atoms with partial site occupancy. Na, Mg, Ca, Ti, and Mn were interpreted as substitutional impurities. Since a standard EPD-only Rietveld fitting did not possess the sensitivity to refine the occupancy parameters of these parameters, a combined SAED-EDXS Rietveld fitting model was adopted. The setting of the occupancy factors as refinable parameters in the combined analysis allowed us to fit the SAED diffractogram and the EDXS spectrum with the same sample model, and yield both crystallographic and spectroscopic data. The least squares Rietveld algorithm was then used to fit each of the simulated EPD and EDXS patterns against their experimental counterpart, which minimizes the combined fitness function.

A major limitation of the current analysis lies in the wavelength of the incident radiation considered in the EDXS data modelling. The current version of MAUD can model the X-rays emitted due to fluorescence based on the instrumentations described by Lutterotti et al. [200]. The measurements described by the Authors involved using a common X-ray source for both diffraction and fluorescence. Additionally, the experimental apparatus described by the Authors operated in air, limiting the lower detectability limit to silicon. Unlike a common X-ray “source” for the combined XRD-XRF analysis as proposed by Lutterotti et al. [200], in the SAED-EDXS analysis, the incoming radiation is “electron”. In simple terms, the modelling is possible for the X-ray spectrum generated by the incident “X-ray” beam, but not by the “electron” beam. This has been clarified in Fig. VI-5. The incident X-ray corresponding to the Mo source is diffracted essentially under kinematical conditions (VI-5a). Hence, the emitted fluorescent X-ray spectrum can be modelled. However, for the electron beam accelerated at 200 KV, dynamical conditions are unavoidable and under the most favourable scenario, a two-beam dynamical diffraction condition can be assumed (Fig. VI-5 b).

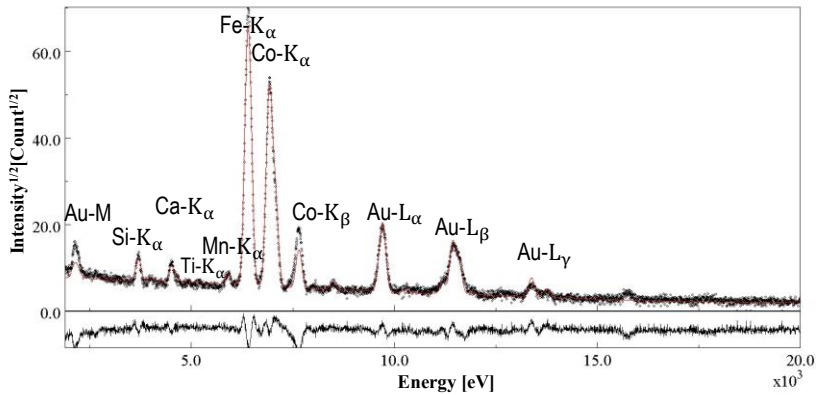
In our opinion, some inputs from Monte-Carlo simulations would be beneficial to model the generation of the X-rays at different penetration depths of the specimens, using simulation software, such as CASINO [313] and WinXRAY [314]. Even these Monte-Carlo simulations have mainly been used for predicting the trajectories of the electrons and the corresponding X-ray generation in low-voltage SEM-EDXS analysis [315,316].

Thus, for the analysis presented in this chapter, we need to depend on the modelling of the EDXS spectrum as done for the XRF spectrum by Bortolotti et al.[304] based on the model of Ebel [317]. This is inherently wrong as the Ebel model has been

described for the X-ray tube and not for the electron microscope. Nevertheless, MAUD has come a long way since its inception with the incorporation of different types of



(a)



(b)

Figure VI- 4 Combined Rietveld fitting of SAED-EDXS data of nc-CoFe₂O₄. The microstructural parameters determined from the fitting are listed in Table VI-2 and the weight fractions of the elements determined from the crystallography are listed in Table VI-3.

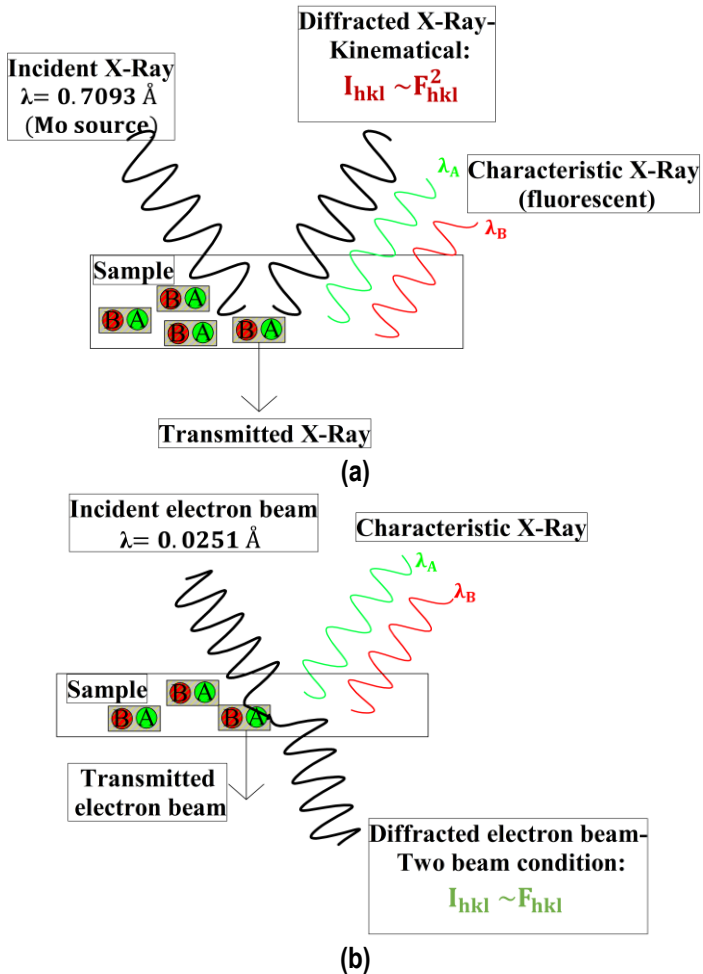


Figure VI- 5 The problem in modeling EDXS: Currently it is possible to fluorescent X-rays produced under kinematical diffraction conditions (a), and not the X-rays produced by a high energy electron beam under dynamical diffraction conditions (b).

radiations, and currently, it is in the development phase as far as a correct modelling of the EDXS spectrum is concerned. Hence a value of 0.5 Å considered as the wavelength of the X-ray instrument (in MAUD we need to define a separate instrument

for spectroscopic analysis) although fundamentally wrong, paved the path for the implementation of the combined SAED-EDXS analysis. The value of the wavelength chosen was based on trial and error.

Moreover, not all the photons generated inside the sample and propagating in the direction of the detector will actually reach the detector. The radiation is attenuated due to the absorption of the emitted X-ray photons by the material itself. The attenuation effect may be expressed using Beer's Law: $I \sim I_o * \exp(-\mu * L)$. In this expression, μ is the absorption coefficient, which is a material constant and L is the absorption path length. The absorption path length is a function of the depth at which the photons are generated and depends on the position of the detector, as shown in Fig. VI-6 [150]. To minimize L , the specimen should be as thin as possible, and the value of the angle ψ should be as large as possible. From the analytical point of view, the sample can be termed as thin only if the absorption on the measured number of photons is negligible.

Additionally, absorption is closely related to fluorescence since a major cause of X-ray absorption is fluorescence. An example of this could be the fluorescence of the Si K α X-rays from the EDXS detector, giving rise to the escape peak. Hence, the Si K α peak in Fig. VI-4b) has not been quantified. Absorption effects become dominant if in a specimen there is a small amount of one element, the X-rays of which are absorbed by the presence of a relatively large amount of another element [60].

Table VI-2 lists the microstructural parameters obtained from the combined SAED - EDXS analysis. The r.m.s. microstrain parameters were negligible, however, some anisotropy in terms of crystallite size along different crystallographic directions was noted based on the Popa model. The major difference in the crystallite size was observed along the [111] and [400] directions. An average crystallite size of 75.8(3) Å was determined at the final refinement stage.

Table VI-3 lists the elemental composition determined from the crystallography of the phases. In spite of the limitations of the present analysis highlighted before, a good match for the composition of certain elements- O, Mn, and Fe could be obtained between the results obtained from the EDXS spectrum and those obtained from the crystallography of the phase. The major discerning factor was the composition of Co, which was obtained as 15.9 wt % based on crystallography, in contrast to the 24.9 wt % as determined from the EDXS. The probable reason is the inaccurate fitting of the Co-K β peak in the combined SAED-EDXS analysis (see Fig. VI-5). We have also added a column highlighting the nominal weight percentages of the elements in the absence of impurities. With increase in the concentration of the substitutional atoms, large variations in these results would be apparent.

As mentioned before, currently we cannot model the X-ray lines below Si. Thus, Na and Mg have been left from the quantification based on the crystallography of the phase, since their peaks cannot be modelled. Moreover, the quantification of Ca as listed in Table VI-3 id 9.8 wt %. This is most probably because electrons are more efficient to excite lighter elements, i.e., electron induced emission factors are definitely different from X-ray induced emission factors, so we overestimating Ca, and Ti. With so many limitations, the whole exercise may seem pointless. However, we beg to disagree.

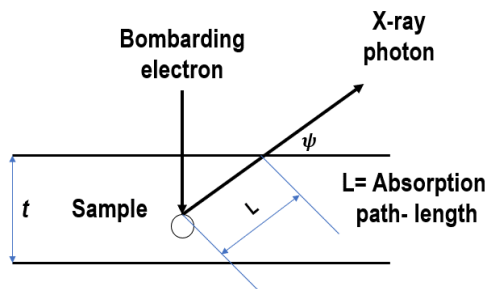
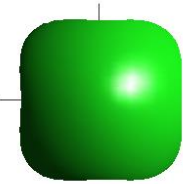


Figure VI- 6 Relation of sample thickness to absorption path length in an idealistic, plan-parallel thin TEM sample [150].

Table VI-2 Microstructural parameters determined from the combined SAED-EDXS fitting. Anisotropic crystallite sizes were obtained for the nc-CoFe₂O₄ sample, however the r.m.s. microstrain parameters were negligible.

Sample	a (Å)	Crystallite size, average (Å)	Anisotropic Crystallite size (Å)	Rwp _{no. bkg} (%)	Shape
CoFe ₂ O ₄	8.3753 (8)	75.8(3)	[111]: 84.9 [400]: 62.2	15.67	

Firstly, the indexing of the EDXS spectrum could be supported as we have indexed the raw EDXS data using crystallographic information. Secondly, once the modelling problem is solved, a comparative study between the elemental composition determined from the microscope with that from Rietveld fitting would be possible. Thirdly, the microstructural data of the phase could also improve if the relevant substitutional elements are accounted for.

Table VI-3 Elemental composition determined from the crystallography of the phase through combined analysis and directly from the TEM-EDXS, and the nominal composition of the pure CoFe_2O_4

Element	Wt % (Crystallography)	Wt % (EDXS)	Wt % (Nominal)
O	28.6	32.2	27.3
Na	-	0.4	
Mg	-	0.5	
Ca	9.8	0.5	
Ti	3.3	0.5	
Mn	0.5	0.7	
Fe	40.3	40.7	47.6
Co	17.3	24.5	25.1

VI.4 Highlights of the chapter

- A nanocrystalline CoFe_2O_4 specimen has been used for the development of a methodology to combine SAED with EDXS for a robust characterization of nanocrystalline systems.
- It was noted through the EDXS spectrum that impurities in the form of Na, Mg, Ca, Ti, and Mn were present. However, the standalone Rietveld refinement of the SAED pattern could not detect the presence of these impurity elements.
- To enhance the robustness of the characterization methodology, EDXS data was coupled with SAED in a combined Rietveld-like fitting. The requirement for fitting also the EDXS spectrum, permitted to refine the partial occupancies of the constituting elements.
- The quantitative EDXS from the electron microscope was compared with the ones obtained from the crystallography of the phases. However, any reliable judgments cannot be made because of unsatisfactory modelling of the EDXS spectrum. The methodology is still at the nascent stage and requires further development.

Chapter VII: Final comments and scope for further development

This PhD thesis deals with the development of TEM-based methodologies for the characterization of nanostructured materials. The same was implemented using an intra-combination of techniques, i.e., imaging-diffraction-spectroscopy, and inter-combination, i.e., with XRPD. A novel sample preparation technique suitable for particulate matter of environmental concern was also developed.

VII.1 Accomplishments of the project

In this section, the major observations made during the entire project work have been highlighted.

The Rietveld refinement of the CeO₂ SAED pattern was applied to determine the instrumental broadening function of TEM. Intricacies of the procedure concerning the collection of the diffraction pattern were also demonstrated. It could be safely concluded that the calibration procedure called for the determination of the instrumental effects using multiple SAED diffraction patterns collected with different SA aperture- camera length combinations. Hence, a total of twelve SAED patterns collected using three SA apertures- 800, 200, and 40 μm , and four camera lengths- 1360, 1080, 844, and 658 mm were judiciously collected and calibrated. This calibration procedure was perhaps the most important initial step of the project, as this indirectly yielded a suitable step-by-step procedure for analyzing electron diffraction patterns using *MAUD*. The combined XRPD- EPD methodology was also established as firstly the microstructure of the nanocrystalline CeO₂ specimen was determined using Rietveld fitting of the XRPD data, and these microstructural parameters were kept constant during the determination of the instrumental broadening function. The camera length calibration could be termed equally critical. Since microstructure analysis is the single most important studied parameter, camera length has a special significance concerning the accurate determination of the lattice parameters. These constitute the results and critical discussions presented in Chapter IV.

The sample preparation in TEM analysis is critical and many times cumbersome. It was our deliberate intention to extend the used methodologies to different nanostructured systems. The overall goal of the project work would have been rather incomplete had we not studied some samples of environmental concern. The emissions from disc brake systems, constituting a non-exhaust source of pollution, were suitable in this regard. The choice of the chosen disc brake wear debris is of extra importance since the European Commission has passed new regulations (Euro 7 standards) recently, concerning also the non-exhaust form of emissions from road

vehicles [318]. The particulate matter from simulation-based studies involving pin-on-disc and brake dynamometer setups were collected on substrates, such as aluminum foils and polycarbonate films. However, the first and foremost step was the development of a suitable sample preparation protocol for a complete extraction without disturbing the pristine features of the particles from these substrates for obtaining reliable microscopy results, to which the methodology could be applied. The developed sample preparation methodology is compliant with obtaining the morphology of the particles, analytical information from the EDXS technique, and structural/microstructural information from the diffraction patterns. Different results based on the sample preparation methodology were presented in Chapter III.

Having established a standard methodology for the Rietveld refinement of the SAED patterns for a single-phase (standard) nanocrystalline CeO_2 and with the instrumental broadening functions known, the possibility of extending the technique to real single and dual-phase systems for their microstructural characterization, and phase identification and subsequent quantitative determination, could be accomplished. These included nanocrystalline Si single-phase material having immense usage in optoelectronics, using which the advantages of two-beam dynamical correction were demonstrated. A two-phase nanocrystalline TiO_2 sample, comprising anatase and brookite phases, for which the phase quantification could be performed and the simplification strategies helpful during the Rietveld refinement of such nanostructured systems were demonstrated. Possibly the most interesting sample was the disc brake wear debris collected during the brake dynamometer tests. It was found that it was a dual-phase mixture composed of maghemite, and another oxide, magnetite, raising some environmental concerns in recent years for its potentially harmful health effects. The phase quantification of this complex mixture, along with its microstructure, could be determined. Such an analysis has a possible application for studying samples from real environmental monitoring stations, with a particular focus on the ultrafine and nanometric fractions of airborne PM, which are raising increasing interest. This analysis carried extra importance since a very less amount of material is collected during the tests and the application of a bulk technique like XRPD yields unsatisfactory results for any reliable quantifications.

It was equally important to propose the limitation of the usage of SAED patterns in the study of nanostructured systems. For fulfilling this important criterion, a sample of archaeological interest has been selected. This is a mixture of goethite and hematite, two natural pigments, being hematite also obtained from controlled heating of goethite. Along certain crystallographic directions, this particular sample had crystallite sizes in excess of 100 nm. The Rietveld refinement of the SAED pattern yielded unsatisfactory results since the large instrumental broadening of the TEM coupled with smaller broadening caused by the large crystallites lead to unsatisfactory, and unreliable results. All these results were presented in Chapter V.

Wherever it was possible, we tried to compare the information as obtained from direct images with the indirect information obtained from the diffraction route. This was highlighted in the case of the CeO₂ sample, wherein a crystallite size of 128 Å was obtained from TEM BF imaging, 135 Å from DF imaging, 124.9 (4) Å from XRPD data, and 121.3 Å from EPD data (SA 200 µm- CL 1080 mm combination). Similar comparisons were made for nanocrystalline Si, Y₂O₃, and disc brake wear debris. In this regard, the important contribution of EPD lies in the fact that especially for agglomerated systems, the TEM images may not inherently support such analysis.

For a nanocrystalline Y₂O₃ sample the results from XRPD and EPD data were compared with each other and it was concluded that for samples with crystallite sizes up to 200 Å with negligible preferred orientations, i.e., samples with random distribution of crystallites, EPD had similar potentials as XRPD to elucidate the microstructure of nanostructured systems.

Thereafter, it was noted that there exist flaws in the characterization of nanostructured systems, relying only on EPD data. This could be clearly observed for a complex system like the disc brake wear debris, wherein the minor phases present were beyond the detection limits of the diffraction route, and EPD could confirm the presence of only the dominant oxide phases. The elemental composition of the other phases could be easily seen in the EDXS spectrum. Hence a methodology, although having limitations since it is still at the nascent stage, aiming to combine SAED-EDXS data in a combined Rietveld fitting was adopted. A CoFe₂O₄ ferrite of engineering importance having impurities in the form of Na, Mg, Ca, Ti, and Mn was chosen for this purpose. The Rietveld fitting of the SAED pattern, as expected, failed to note the presence of these elements that are present most probably in the form of substitutional impurities. On the other hand, based on the combined SAED-EDXS fitting, the impurity elements could be included in the crystallography and the partial occupancies of all the comprising elements could be refined. However, the model used for the purpose of the fitting is not suitable for EDXS and the methodology needs a lot of probing before it can be extended to complex systems like the wear debris from disc brakes.

Finally, the schematic below in Fig. VII-1 summarizes the possible quantitative characterization route for nanostructured materials using TEM, implemented to the maximum extent possible in this thesis work.

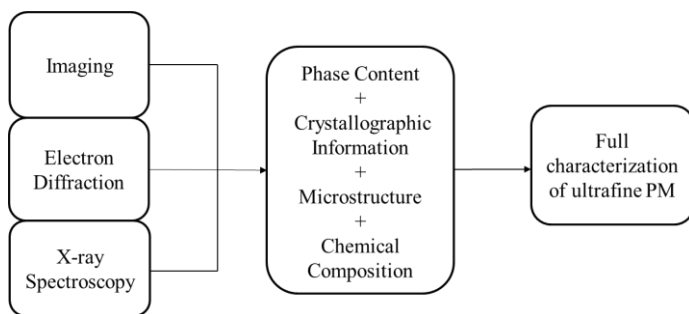


Figure VII-1 Schematic showing the different methodologies and their combined application attempted in the thesis for characterization of nanostructured materials and particulate matter

VII.2 Limitations of the proposed methodologies

In the words of William and Carter, since their usage, only around 1000 mm³ of material has been studied using TEMs [60]. Hence the instrument is definitely not a sampling tool. So, the results obtained from the methodologies presented in this work having been explored in a localized region of a specimen, need to be verified with the bulk sample characteristics. Dependence on TEM to fulfill this criterion is painstaking considering the time and resources required for multiple sample preparation and subsequent analyses.

For the above-described problem, effective and efficient sampling could provide a solution. The other reasonable and judicious method is to club other bulk techniques, such as XRD, ND, Raman spectroscopy, etc, wherever possible. For instance, the phase quantification of multi-phase systems carried out based on SAED is confined to smaller volumes even if the largest SA aperture (in our case 800 μm) is used and the results could be skewed in favor of one phase over the other. Similarly, the lattice parameters determined through the Rietveld refinement depend heavily on the accurate determination of the correct camera length, which can show large deviations. Moreover, all the methodologies present in this thesis work pertain to nanostructured materials that yield ring SAED patterns. A primary requirement for attaining robust microstructural characterization from these patterns is that they should display sufficient diffraction intensities. The latter is possible if and only if the diffraction patterns are collected from a region of a specimen that has a necessary number of diffracting crystallites. A SAED pattern collected from a tiny region of specimen, say with a SA aperture below 10 μm, will produce a spotty SAED with largely discontinuous rings, limiting the scope of the methodology.

TEM specimens should fulfill the inherent criterion of being electron transparent. Although EDXS information may be obtained even from relatively thicker regions of the specimen, since SAED patterns have been the most intriguing part of this thesis work, they suffer from this relatable limitation encountered from the thicker regions, which could be anyway interesting from the view of microstructural characterization. On the same lines of thickness/ size of the particles/crystallites, it was encountered during the microstructural determination of the goethite/hematite sample that SAED patterns having been collected from the coarse region of the sample could not be analyzed satisfactorily with the proposed approach since they caused very less broadening as compared to the large instrumental broadening. However, the proposed methodology works satisfactorily for randomly oriented crystallites up to the size of 200 Å.

VII.3 Further development

As highlighted in Chapter VI, the development of a combined SAED-EDXS methodology in the pursuit of extracting crystallographic data from SAED and spectroscopic information from EDXS was envisioned. This procedure was in line with the works of the cited papers [200,304], which demonstrated the procedure of combined XRD-XRF analysis. However, the modeling and data treatment of EDXS data is inherently different from XRF, for the simple reason that the physical principle involved in the interaction of high energy electron beam with the matter is different from the interaction of X-rays. In fact, the EDX spectrum has undesirable contributions of absorption and fluorescence of radiations that are linked to one another. On these lines, MAUD is being currently updated from the view of the correct modelling of the EDX spectrum. It is to be proposed that the Monte-Carlo simulations of the electron trajectories and the corresponding EDX spectrum could be helpful in this regard.

The methodology has to be made robust firstly for a single-phase material with some possible substitutional impurities. In this light, we suppose that the choice of the CoFe_2O_4 sample with a reasonable number of substitutional atoms was decent. Once we can substantially claim that the methodology works for a simple system, we can extend it to complex materials, such as the wear debris obtained from the disc brakes.

Finally, the methodology should also be extended to textured nanocrystalline samples, featuring eventually large intensity variations along the Debye rings. Many texture models, such as E WIMV, Harmonic functions, Standard Functions, etc., are already available in MAUD. It would be interesting to compare the results obtained from a sample with a random distribution of grains, with the results when the sample is subjected to some mechanical process, inducing texture.

Appendix A1

We have demonstrated in this chapter the step-by-step procedure to perform microstructural analysis of electron powder diffraction patterns using Materials analysis using diffraction (MAUD) software. All the datafiles and MAUD analysis files can be downloaded as a zipped file at <http://maud.radiographema.eu/static/tutorial/EPD.zip>

The latest version of MAUD can be downloaded from <http://maud.radiographema.eu/> and saved to a local directory. In the windows operating system, we have to use MAUD.bat file for running MAUD. It would be a good idea to see video tutorials at: <http://www.youtube.com/user/MaudRietveldProgram> for some elementary analysis.

When we run MAUD for the first time (batch file), the window shown in Fig. A1-1 is opened. On the top left side, we see the “Datafiles”, “Phases” and “Samples” tabs. Above these, in the taskbar, we have “Floppy disk” for saving the analysis (it is a good practice to save the analysis at different stages), “Eye” for editing an object that has been selected (datafiles, phases, etc.), “Light bulb” for selecting different refinable parameters, “Calculator” for computing the diffraction patterns, “Hammer/ Machine” for initiating the refinement cycle.

A1.1 Setting up the Instrument:

MAUD can be used for diffraction data of neutrons, x-rays, electrons. For every dataset, we first need to define the instrument. In our case, we define our TEM instrument as follows:

Datasets → DataFileSet_x → Edit Object (in the menu taskbar) / press “Eye”. In the General tab of the next window, select “Edit” under Instrument. The window shown in Fig. A1-2 will open.

- Here, we can give the name of our instrument. In our case, it is Thermofisher Scientific- TALOS F200 S.
- Make sure that we choose “none cal” for the intensity calibration option for the current analysis.
- We can set the value of the incident intensity to 0.001 initially. This value will be refined at a later stage.
- Under the “Angular Calibration” drop-down menu, we have to select “Flat Image Transmission”. Under the options tab, we have to set the detector distance as 1080 mm. This was the camera length as obtained directly from the TEM instrument, which needs to be refined later. The detector distance is an essential parameter for the conversion of coordinates of the 2D image to 2θ values. Later, we can also convert the 2θ values to d-spacing or Q-values. For now, we need not change the remaining parameters, such as center x and center y (in the integration tab) and their errors.

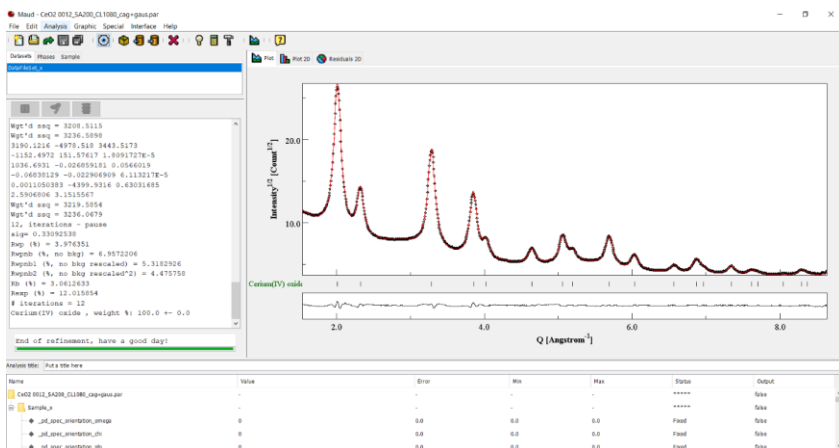


Figure A1-1 Main MAUD window on a computer running on Windows 10. When the program is started the plot is blank. Here, data for the CeO₂ standard have been entered and refined. The superposed image (top right) shows the window “DataFileSet” with options for modifying the selected Dataset.

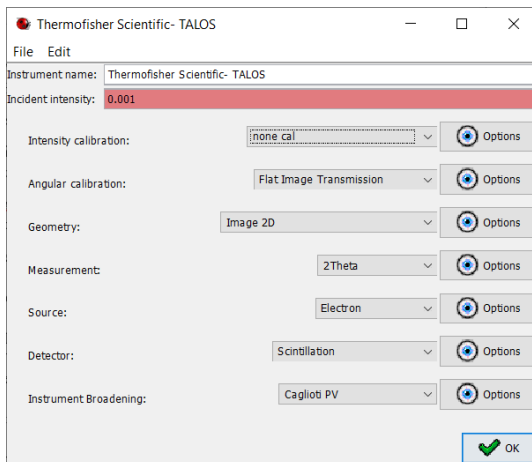


Figure A1-2 “Diffraction Instrument” window with general setup for transmission electron diffraction images.

- Under the “Geometry” tab, we choose “Image 2D”.
- For “Measurement”, we select “2Theta”.

- For “Source” we have to select “Electron”. We can click on “Options” and change the default wavelength to 0.0251 (Å), as we had collected the TEM data at 200 kV. The “Dynamical correction (Blackman)” should be checked, while “Crystallite value for thickness” unchecked.
- In the “Instrument Broadening” tab, we should set the default parameters that are compatible with electron diffraction. If we click the “Options” button that is next to the “Caglioti PV” model (Caglioti et al., 1958), we will see the additional tabs. Here, we should remove the asymmetry parameters/or set them to zero. We repeat the same for all the parameters under the “HWHM” and “Gaussianity” tabs. Next, we can close the Instrument editing window.

A1.2 Entering 2D image data

- The ImageJ plugin has been embedded in MAUD. Thus, an image in .tif format can be directly opened in MAUD and the resulting data files can be saved as .esg files, which are ASCII files. These contain a list of radial positions or diffraction angles and the experimental intensities corresponding to these. However, if the diffraction data is in a format that is not readily recognized by ImageJ, it needs to be converted to a regular .tif file, preserving the original intensities. To perform the image integration in MAUD using the ImageJ plugin, we proceed as follows: Datasets→ Edit (eye button) → Datafiles → From images (Fig. A1-3). A small window showing the typical ImageJ toolbar will be displayed.
- Using the ImageJ menu “File→Open” we can load the diffraction image CeO2 0012_SA200_CL1080.tif. It is advised to work with the raw file, which is already in the 16-bit format and without the magnification scale bar.
- We can set the proper brightness/contrast of the image. From the menu select: “Image→Adjust→Brightness/Contrast”, and press the “Auto” button as many times until we can see clearly also weaker diffraction circles. Thereafter, we can close this window.
- We need to specify the pixel size for the detector. Select “Image→Properties”. A new window will open. Here, change the “Unit of length” to mm and set “Pixel width” and “Pixel height” to 0.014 mm (14 μm/pixel) and press “Ok”. These values refer to the pixel size of the CCD on which diffraction patterns were collected.
- The latest version of MAUD facilitates removing the beam stopper shadow that masks a portion of the diffraction rings. For this, select the “Polygon selections” option from the Image J taskbar and select the entire area of the beam stopper. Then, select Process → Math→ Set →Value to -1. Click on Ok. Thus, there will be no contribution from the selected portion of the image. This operation has been shown in Fig. A1-4.

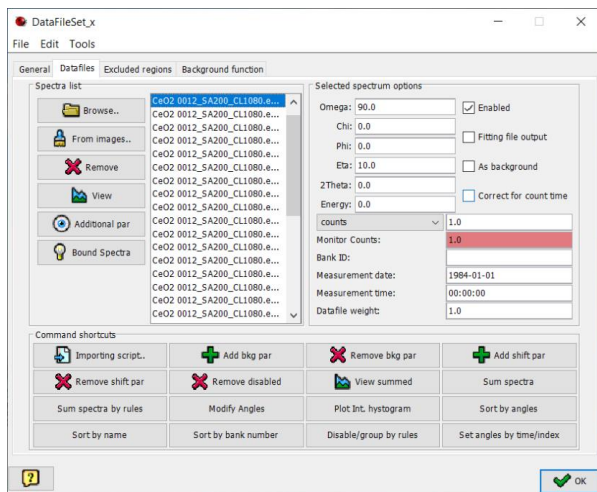


Figure A1-3 “Datafiles” in Dataset options window for CeO₂ standard. Initially, there is no data in this window. In the view shown here, they have been loaded selecting “From images”. Superposed on the right, we see all the individual diffractograms formed by selecting all the .esg files and pressing “View”.

- Now we proceed to integrate the image by selecting: “Plugins→Maud plugins→Multi spectra from normal transmission/reflection image”. The diffraction image appears as shown in Figure A1-5. Also, another window “Choose the integration lines” will appear showing a list of parameters. For this sample, the Sample-Detector distance was 1080 mm. We need to adjust the “Center X (unit: mm)” and “Center Y (unit: mm)” causing the tracker circle (in red) to move towards the center (X = 29.43 and Y = 28.43). We should also adjust the tracker radius so that it coincides with the first ring. Then we update the plot by pressing “Update” and the changes made would be visible. We can set the “Number of Spectra” to 36, i.e. the image will be integrated with 10° sectors. The angle Omega (ω) should be set to 90°. This will serve to bring the normal to the sample into the pole figure center. We can leave the rest of the entries to 0. However, we should be sure that “Reflection image” and “2-Theta angles calibrated” buttons are unchecked since we are working with a transmission image.
- When we press on “OK”, the integration will start and the software will ask the location to save the ASCII files. We can choose the directory (better not the MAUD directory) and give a name such as CeO₂ 0012_SA200_CL1080.esg.

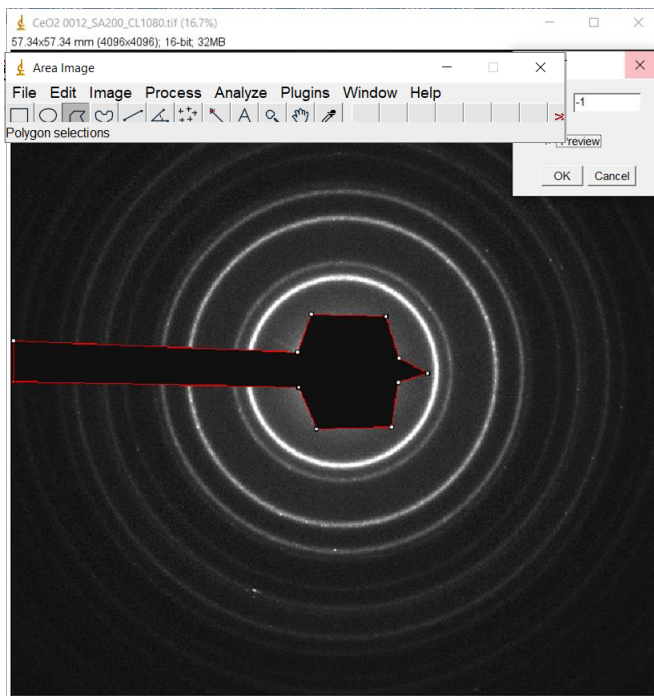


Figure A1-4 The area of the diffraction pattern of CeO₂ masked by the beam stopper is selected (red boundary lines) using “Polygon selections” from the ImageJ menu window shown on the top left. The intensity values for the selected region are set to -1, shown on the top right.

- At this point, we can close the diffraction image and ImageJ windows. In the MAUD dataset editing window, the .esg files would now be listed in the “Spectra list” panel, shown in Fig. A1-3. We can see all the individual diffractograms by selecting all of them (Ctrl+A) and then clicking “View”. However, first, we should delete the diffractograms numbers 17 and 18 (note that the numbering of diffractograms starts from 0), falling in the region of the beam stopper. Thus, 34 individual diffractograms shown in Fig. A1-3 can be obtained. If we now close the dataset window, a summation of all the patterns would be visible in the main MAUD window plot panel (Figure A1-1).

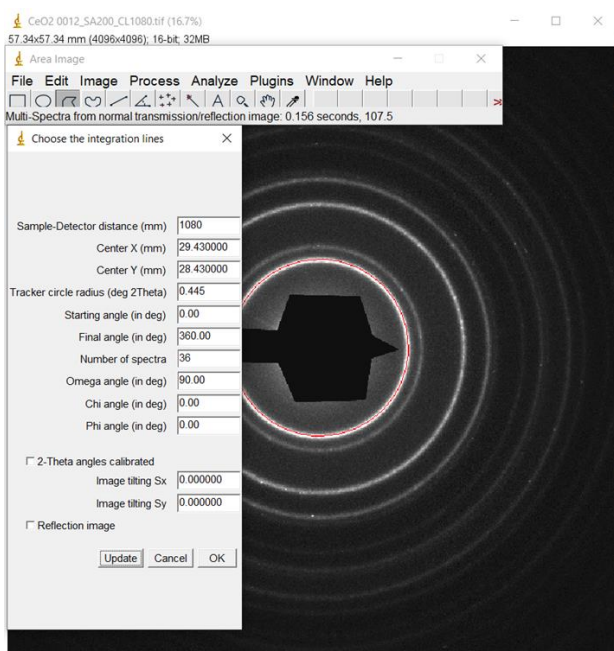


Figure A1-5 ImageJ setup for CeO₂ diffraction image processing to generate a set of patterns by azimuthal integration of the 2D image. The red circle is used for aligning the image in the center.

A1.3 Refinement range and background

We can restrict the range for the refinement. This can be done by selecting the “General” tab of the dataset editing window (Fig. A1-1, inset) and changing “Min in data units” and “Max in data units” values. Units for those are the same as the actual diffraction data. Thus, 2θ in degrees for this case.

Next, we should set the background. For selecting the background model, switch to “Background function” tab following: Datasets → DataFileSet_x → Eye button → Background function. By default, a polynomial background is used in MAUD. We need to add 5 parameters to approximate the background by a 4th order polynomial. We have to click “Add parameter” or “Remove parameter” buttons to set the number of parameters to 5.

We also need to account for the sharp increase in the background at low $2\theta/Q$ values. At the same time, the contribution of the carbon film needs to be accounted for. We proceed as follows: Background function tab → Background Peaks → add term. We

have to add three terms, one corresponding to the direct beam, and two for the Halos from the carbon film. For the direct beam, we can give initial values as follows- Height: 10; position: 0; HWHM: 0.5; Eta:1. We can set to refine these parameters, except for the position value.

Initial values for the Halos 1: Height: 1; position: 0.6666; HWHM: 0.0889; Eta: 0.3699.

Initial values for the Halos 2: Height: 1; position: 1.2124; HWHM: 0.1053; Eta: 0.5878.

We can refine the Height parameter but others should be kept fixed.

Please refer to Section A1-8, wherein we have demonstrated the procedure to obtain these values.

A1.4 Phase and initial parameters adjustment

The “Phases” tab in the main MAUD window (A1-1) contains the crystallographic and microstructural data of all the phases present in the sample. These are lattice parameters, space group, atomic positions, occupancy, crystallite size, microstrains, texture, etc. The basic sample features can be entered through “crystallographic information files” (.cif). These files can be downloaded from different databases, such as the ICSD (ICDD) or the COD (<http://www.crystallography.net>). Some examples of phases are also available in the MAUD file “structures.mdb”. To import a structure from a .cif file we have to press the “Cylinder with arrow out” button on the taskbar or select the “Edit→Load object from CIF...” menu. However, in our case, we need to import sample characteristics from the profile fitting of CeO₂ XRD data. So, we proceed as follows: Phases → Load object from CIF→XRD file (CeO2_00_XRD_cal.par) → Cerium oxide →select and choose. Following these steps, all structural and microstructural parameters obtained from the XRPD analysis would be taken as input for the EPD analysis. We have to be careful and not load the CeO₂.cif file downloaded from the COD.

After entering all the above information, pressing the “Calculator” button on the main page (Figure A1-1) shows diffraction patterns based on the instrumental and phase parameters provided by the user and compares them with the experimental data. This can be viewed with the “Plot” tab (selected by default) above the pattern in MAUD main window. Here, an average of all patterns from a dataset is shown. Otherwise, with the “Plot 2D” tab a stack of all individual 34 patterns can be displayed. In the 2D representation, model patterns are at the top and experimental patterns are at the bottom.

For diffraction data, we can choose different scales for representing the intensity values. The square root scale intensity representation is useful, as smaller peaks could also be visible. This can be selected or changed in the “Graphic→Plot options” menu. The calculated intensity values are different from the experimental values. So, we should adjust the scale factor (beam intensity in MAUD). This can be performed “live” by selecting the parameter list below the plot, i.e., the lowermost portion of the main MAUD window (Figure A1-1). In the parameter list, we should enlarge the tree-table

and scroll to reach the parameter “_pd_proc_intensity_incident”. It is present in the instrument in the dataset. We can make the “Value” column of the tree- table sufficiently large by changing its border length. We have to click on the value of the entity that we want to edit (one click). Then, in the text field, we can assign the value by which we want to increase or decrease the selected entity. The change in the value is performed by pressing the corresponding arrows. The changes hence made would be directly visible in the plot. We can set the initial value to 2.052E-5. After making the suitable adjustments, we should exit the editing mode by clicking anywhere in the tree table, except on a value.

We would notice disagreement between the peak positions of the experimental and calculated profiles. This is because the camera length of 1080 mm that we entered before is not the calibrated value. To approach the calibrated value, proceed as follows in the tree table: Thermofischer Scientific- Talos→ Flat Image Transmission→pd_instr_dist_spec/detc. We can bring this value down to 1039 mm. Also, we set it to refined.

At this stage, we can set to refined background parameters “_riet_par_background_pol0 to _pol4”. Then we go ahead with one refinement cycle by pressing the hammer/machine icon. The least-square minimization will start, visible on the left side of the main MAUD window. We can increase the number of cycles by using the “slider”. Usually, 5-7 refinements should be sufficient. If the refinement cycle is successful, we will notice that the experimental and calculated intensities show less difference than before.

A1.5 Refine instrument parameters

In the next refinement cycle, we account for the centering and tilting errors. Under the “Flat Image Transmission” option, set all the remaining parameters to be refined, except for “inst_ang_calibration_ratio_pixels”. Then we go for the next refinement cycle by pressing the “Hammer/Machine” icon. This will adjust the reflection positions. We should save the analysis as a MAUD parameter file in the .par format. (e.g. name it CeO2 0012Ceta_ SA200_CL1080_02_cent+tilt.par) . We should proceed using the menu item: “File→Save analysis as...”. This parameter file contains all essential information about the sample features, phases, and instrument. It can be used as the starting analysis file for other diffraction images.

Finally, we proceed to refine the instrument broadening parameters (W, V, and U) in the “Caglioti PV” model. In MAUD, the designation is as follows: W= _riet_par_caglioti_value0; V= _riet_par_caglioti_value1; U= _riet_par_caglioti_value2. Caglioti parameters essentially describe instrument broadening, with respect to peak width, shape, and asymmetry. These parameters also explain the Gaussian plus Lorentzian mixing (Caglioti *et al.*, 1958). These instrument peak shape and width parameters are essential if we want to study the line broadening analysis of real samples to determine their microstructure.

Caglioti parameters are very sensitive to changes in their values and a strict order needs to be followed to obtain the desired results. We describe the procedure for transmission electron image data where the 2θ range is limited.

It is advisable to start with non-zero values. So, set the first FWHM parameter “_riet_par_caglioti_value0” to 1E-5, manually by using the parameter tree list at the bottom of the main window. We can set the second FWHM parameter to 0.001. Set both these parameters to be refined. There should be no need to use the third parameter, as we are not dealing with a large 2θ range. If we want to see an enlarged view of any particular peak, we should select an area around that peak by pressing the “right” click and dragging. Then, to zoom out and see the full pattern view, we have to double click on the plot. Otherwise, we can also right-click on the plot and select “reset scale”. Next, we go for a refinement cycle.

If we look at the plot window, we would notice that the peak intensities fit rather poorly. So, we can do an intensity-independent Le-Bail fitting for each pattern. We proceed as follows: Cerium oxide → edit (eye button) → Advanced models → Texture → choose arbitrary texture. Click on Ok.

Next, we can fix all the parameters related to the intensity or scale factors, as these are not needed with the Le-Bail fitting. So, set “_pd_processing_intensity_incident” as fixed. Perform another refinement cycle.

Next, we can refine the first gaussian term “_riet_par_gaussian_value0”. It is advisable to start with a non-zero value. So, manually set the value to 0.1 before going for the refinement cycle. Once the refinement cycle is completed, check the refined value of this term. If the value goes above 1, we will encounter an error. In this case, manually set the value to 1 and put the status as fixed.

On some occasions after a refinement cycle, we may encounter an error as “Cholesky negative diagonal” on the MAUD output panel. This means that some of the parameters that the software was trying to refine were ill-conditioned to be refined with the given set of conditions. Such parameters can be viewed in the MAUD output file (with the .lst extension). Alternatively, such refined parameters would have the value “-1” in the “Error” column of the tree structure. We may rectify the problem by putting suitable correct values for such parameters, or altogether, refraining from refining them.

A1.6 Saving the results

At the last refinement stage, the calculated peaks should fit the experimental peaks adequately. This should be checked both in the “Plot” as well as “Plot2D” displays. We must save this file. To export this instrument setting for use in the refinement cycle of other samples, proceed as follows: DataFileSet_x → Edit (eye button) → General tab → Store button, in the “Instrument” panel. Following these steps, we can save the instrument settings for a particular SA aperture-CL combination as a separate file in our directory (e.g., with name, Thermofischer_Talos_SA200_CL1080.mdb).

Using the CeO₂ standard, we have now obtained the refined values of relevant instrument parameters. While applying them to diffraction patterns from other samples measured under identical conditions, we should set all Caglioti parameters as “fixed”. We should also set the camera length as “fixed”, as using the standard CeO₂ material, it has now been calibrated.

A1.7 Two-stage calibration: Microstructural parameters of CeO₂ from EPD

We should start the analysis again with a blank MAUD window, so start by double-clicking on the .bat file. We need to load the instrument file that we had saved at the last step in section S6. We proceed as follows: Data_File_Set_x → Edit (eye button) → General tab → Import → CeO₂_Calibration.mdb → Choose instrument → Ok
In this file, we should make sure that camera length and Caglioti parameters have been set to “Fixed”.

We do not need to import the electron diffraction image again as we already have the ASCII files in the .esg format. So we can directly proceed as follows: Data_File_Set_x → Edit (eye button) → Datafiles tab → Browse and locate the CeO₂ 0012_SA200_CL1080.esg file previously stored. Another way to load the .esg file is to drag and drop it in the blank region in the Data_File_Set_x window. We can remove the diffractograms number 17 and 18. Then click on “OK” to obtain the 1D plot in the MAUD main window.

Next, we have to load the phase. This time we will not be importing the phase information from the XRD analysis, as we want to determine the microstructure using EPD. So, we switch to the “Phases” tab and drag and drop the CeO₂.cif file in the blank space just below it. Alternatively, we can load this file following the procedure explained in section S5. Press on the “Calculator” icon and we will see the calculated and experimental data together.

Here we should proceed with the setting of the correct background and detector tilting and centering as explained previously. We should also add the contribution of the carbon film towards the background. Ideally, we should not need to change the errors due to the detector tilting and image center, and these should be taken from the calibration file and fixed. It will be a good idea to save the analysis at this stage. We may save as CeO₂ 0012 Ceta_SA200_CL1080_04_two_stage.par. Once these steps have been completed, we can go for a refinement cycle.

Now, we are ready for the refinement of the microstructural parameters. We can proceed in the following fashion: Phases tab → Edit (eye button) → General tab → Cell parameters → Right-click (on the value 5.4116) → Set to refined. Do not close this window yet. We can also refine the crystallite size and microstrains at this step. So, we can proceed as follows: Switch to Microstructure tab → Size-Strain model → Change from Isotropic to Popa rules → Click on options. The window shown in Fig. S6 will pop up. We should not change any other entity in the microstructure tab. In the

Popa model window, set to refined the `_riet_par_anisocryst_size0`. Since we already know that the crystallite size is around 125 Å, we can set the default 1000 Å to a lower value. For now, do not refine the `_riet_par_anisocryst_size1`. However, set to refined the two R.m.s. microstrain terms. Click on “OK”. Alternatively, we can perform these steps from the tree structure.

Now we can go for the next refinement cycle. We would notice the changes in the lattice parameter, the crystallite size (size 0), and microstrain values. We should save the file at this point.

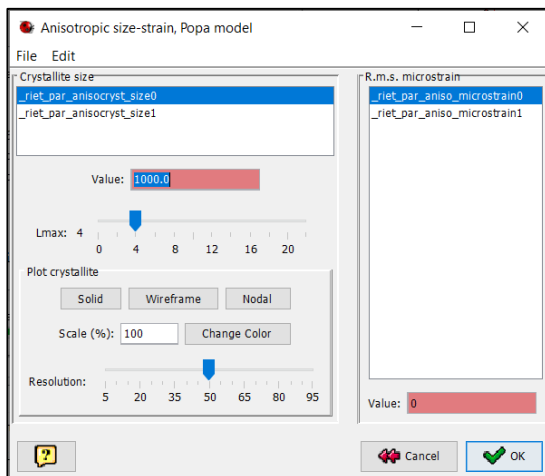


Figure A1-6 ImageJ setup for image processing to generate diffraction patterns by azimuthal integration of the 2D image. The red circle is used for aligning the image in the center.

At this stage, if we want to go for Kinematical approximation, we proceed in the following manner: Again, go to the Popa model window as explained before and this time, also set to refined the `_riet_par_anisocryst_size1` parameter. However, it is a good idea to start with a non-zero value. So set a value in between 1/2 to 1/3 of the refined `_riet_par_anisocryst_size0` value. Click on OK and go for another refinement cycle. We would notice that the intensities fit poorly. To get better results, we can define an overall thermal factor following the steps: Phases → Structure → right-click on the “Bisofactor” value of Ce1 (see Fig. A1-7.) → refined. Since we want the same B factor for both Ce and O, we proceed with refining the B factor of O as follows: Switch to O tab → right-click on the “Bisofactor” value → select equal to. The window superposed in Fig. A1-7 pops up. In this window, locate for Ce1 `_atom_site_B_iso_or_equiv` and select it. Then click on “Set bound” and close this

window. Also, close the Cerium Oxide phase window. Go for another refinement cycle. At this step, the analysis under kinematical approximation is completed. We can save this file as CeO2 0012 Ceta_SA200_CL1080_07_two_stage_kin.par

For performing the Le-Bail fitting/Pattern matching, we can proceed as follows: Load the file CeO2 0012 Ceta_SA200_CL1080_07_two_stage_kin.par. We should fix the scale/intensity factors: “_pd_processing_intensity_incident” on the tree structure. We should also fix the overall B-factor refined earlier. So, set to fixed “_atom_site_B_iso_or_equiv” for the Ce1 atom site. Then we should set the texture to arbitrary texture as follows: Cerium oxide→edit (eye button) → Advanced models → Texture → choose arbitrary texture. Click on Ok. Perform another refinement cycle. These would yield the microstructural parameters with Le-Bail fitting.

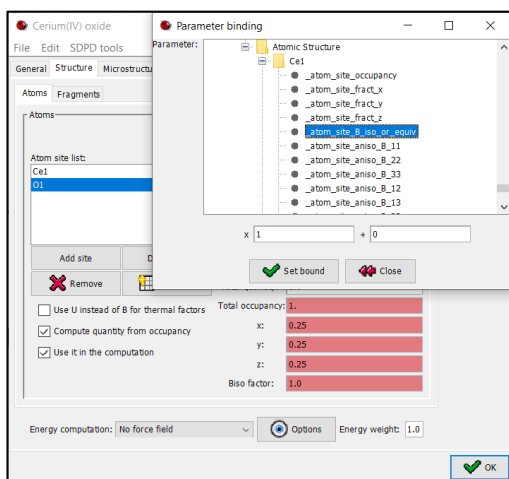


Figure A1-7 Setting an equivalent Biso factor for Ce and O.

For obtaining the results with Blackman two-beam correction, we should load the file obtained after refining only `_riet_par_anisocryst_size0` crystallite size R.M.S microstrain values. In MAUD, the dynamical correction can be activated in the “Dynamical scattering correction” option under the “Microstructure” tab, with the possibility of using the same anisotropic crystallite size for the line broadening analysis. In the “Grain size (Angstrom)” enter the obtained refined value of `_riet_par_anisocryst_size0` and set it to refined. Click on OK. If we now press on “Calculator”, we would notice that the experimental and calculated data do not match at all. So, locate the “_pd_processing_intensity_incident” on the tree structure and increase its value till a match is observed. Then, go for a refinement cycle. Finally, refine the `_riet_par_anisocryst_size1` and an overall Biso factor, as done for the

Kinematical case. We can save the file as CeO₂ 0012 Ceta_SA200_CL1080_06_two_stage_dyn.par.

A1.8 Procedure to determine amorphous carbon halo contribution

- Load the instrumental setup used as done previously.
- Load the Cu_Grid 0010 Ceta_SA_200um-CL_1080mm.tiff.

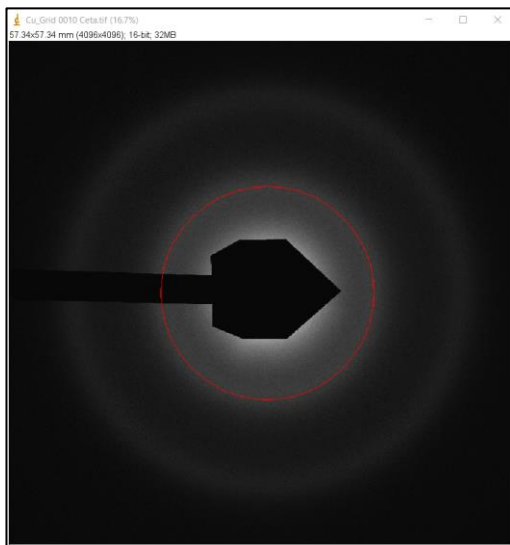


Figure A1-8 ImageJ setup for Cu grid diffraction image processing to generate a set of patterns by azimuthal integration of the 2D image. The red circle is used for aligning the image in the center.

- Treat the pattern using the ImageJ plugin as demonstrated previously. Figure S8 shows the electron diffraction image with the shadow of the sample holder removed. After performing the integration, we should save the ASCII files as done for the CeO₂ sample. The resulting set of diffractograms is shown in Fig. A1-9. These are summed up to obtain the 1-D pattern.
- We should add the background peak contribution for the strong signal at 0 Q, as demonstrated in Section A1-3.
- Open the “Background peaks” section under “Background function”. Click on “add term” and set the initial parameters for the first Halos as follows:

Height: 10; position: 0.66; HWHM: 0.07; Eta: 0.26. Set all these values to be refined.

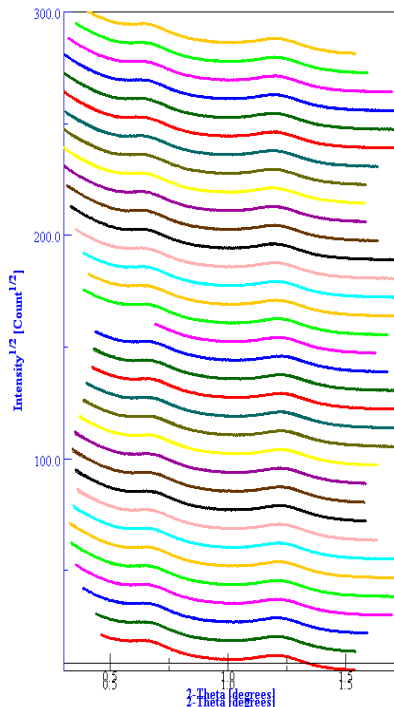


Figure A1-9 The resulting set of patterns from the azimuthal integration of the diffraction pattern of the Cu grid shown in Fig. A1-8

- We repeat the same step for the second Halos and set the Initial values as follows: Height: 10; position: 1.22; HWHM: 0.10; Eta: 0.75. Set all these values to be refined.
- Then free the scale parameters and background parameters. Run the refinement cycle by pressing on the "Hammer/Machine" icon.
- Collect the refined values of the background contribution from the two Halos. We use these for the background evaluation when we have CeO₂ sample on the Cu-grid.

Appendix A2

A2.1 Saving the EDXS data in the .mca format

The absolute intensity v/s energy of the X-rays file (.txt format) firstly needs to be extracted from the TEM software. The intensity values then need to be entered in the following calibration file and saved in the.mca format.

```
<<PMCA SPECTRUM>>
TAG - multi_element
DESCRIPTION - Multi-Element Fluorescence with XR-100CR
GAIN - 2
THRESHOLD - 99999
LIVE_MODE - 0
PRESET_TIME - 0
LIVE_TIME - 0.000000
REAL_TIME - 0.000000
START_TIME - 10/14/2009 10:27:59
SERIAL_NUMBER - 0
<<CALIBRATION>>
LABEL - keV
0 0
222.03 5.9
<<DATA>>
..... (Intensity values to be entered here)

<<END>>
<<DPP CONFIGURATION>>
COM Port: USB
Rise: 9.6uS
Top: 0.4uS
Fast Threshold: 15
PUR Enable: PUROn
RTD ON/OFF: RTDOff
RTD Ratio: 164.1%
RTD Slow Thresh: 3% FS
AutoBaseline: Off
BLR: BLR:ON DN:16 UP:4
Acquisition Mode: MCA
MCS Timebase: 10mS/channel
MCA Channels: 1024
Slow Threshold: 1.07% FS
Buffer Select: Buffer A
```

Gate Input (TTL): GateOff
Preset: 5 min
Coarse Gain: 38.18x
Fine Gain: 1.0466
Input Polarity: Positive
Input Offset: 0.922V
Pole Zero: OFF
Det Rst Lockout: 410uS
TEC: 213.0K
HV: 279.8V
Preamp Power: 8.5V
Analog Out: Decimated Input
Offset: 0mV
Aux: ICR
Audio: Off
<<DPP CONFIGURATION END>>
<<DPP STATUS>>
Device Type: DP5
Serial Number: 5214
Firmware: 5.07
FPGA: 5.04
Fast Count: 1439845
Slow Count: 1297604
Accumulation Time: 300
Dead Time: 9.88%
HV Volt: -280V
TEC Temp: 216K
Board Temp: 31°C
<<DPP STATUS END>>

A2.2 Setting up the EDXS Instrument:

It is important to highlight the procedure for importing the EDXS data in the MAUD software for performing the combined Rietveld refinement.

Press on the 'create and add a new object to the visible list (Cube)' in the menu task bar. We can rename it by double clicking on the 'DataFileSet_x' and giving a suitable name like EDXS.

Then we define our TEM-EDXS instrument as follows:

Datasets → EDXS → Edit Object (in the menu taskbar) / press "Eye." In the General tab of the next window, change the instrument Type to "XRF Instrument." Ideally, we

should have a separate setting for the EDXS, however the software is still at the development stage from the perspective of EDXS. Now, we have to select “Edit” under Instrument. The window shown in Fig. A2-1 will open.

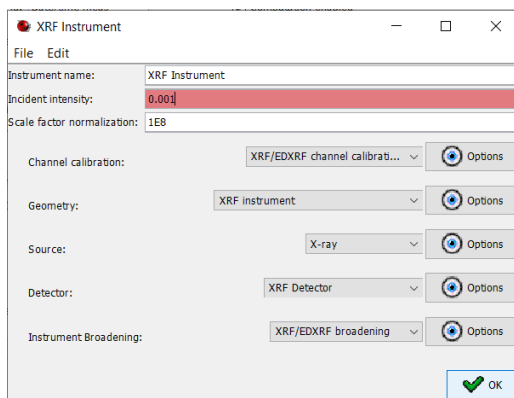


Figure A2-1 “XRF Instrument” window with general setup for the instrument.

We can choose the Incident intensity as 0.001.

Select the Channel calibration as “XRF/EDXS channel calibration”. Under options we have “Zero channel (eV) and Gain (eV/channel)” that will be refined later.

We should select the Geometry of the instrument as “XRF instrument”. Again, the software is still in the development stage.

We should select the Source as “X-ray.” The point of flaw in the current analysis is the wavelength of the X-ray chosen under the Options. In this analysis, the wavelength was arbitrarily chosen as 0.5 Å.

Under the Detector tab, choose “XRF Detector”. Under the Options tab, we have to define the characteristics of the detector. Under “Semiconductor composition” add Si as an element and set the quantity to 1, as shown in Fig. A2-2. It can be refined later. Under “Filters and windows,” Select →add object. We should add two objects in this manner. Select one object and go to Object options. Here, we add Si and Au under Material composition. Give a small value (like 2.5 E-5) to the fluorescence probability. Later we can set it to refined. The unnecessary contributions coming from the detector and the TEM grid can be compensated in this manner and their role in the crystallographic analysis can be nullified.

Thereafter, for the other Object, set the material composition as Be under material composition. We can give a very small thickness like 1E-10.

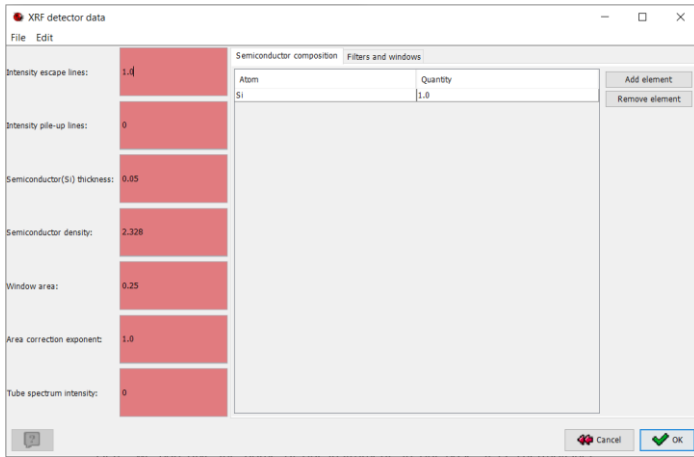


Figure A2-2 Window for setting the detector information.

References

1. Gleiter, H. Nanocrystalline Materials. *Progress in Materials Science* **1989**, *33*, 223–315, doi:10.1016/0079-6425(89)90001-7.
2. Suryanarayana, C.; Koch, C.C. Chapter 12 Nanostructured Materials. In *Pergamon Materials Series*; Suryanarayana, C., Ed.; Non-equilibrium Processing of Materials; Pergamon, 1999; Vol. 2, pp. 313–344.
3. Commissioner, O. of the Considering Whether an FDA-Regulated Product Involves the Application of Nanotechnology Available online: <https://www.fda.gov/regulatory-information/search-fda-guidance-documents/considering-whether-fda-regulated-product-involves-application-nanotechnology> (accessed on 15 July 2022).
4. Thomas, L.; Gert, R.; Douglas, G.; Luigi, C.; Francois, R.; Peter, G.; Christoph, K. Requirements on Measurements for the Implementation of the European Commission Definition of the Term "Nanomaterial." **2012**.
5. Siegel, R.W. Nanostructured Materials -Mind over Matter-. *Nanostructured Materials* **1994**, *4*, 121–138, doi:10.1016/0965-9773(94)90134-1.
6. Gleiter, H. Nanostructured Materials: Basic Concepts and Microstructure. *Acta Materialia* **2000**, *48*, 1–29, doi:10.1016/S1359-6454(99)00285-2.
7. Suryanarayana, C. Nanocrystalline Materials. *International Materials Reviews* **1995**, *40*, 41–64, doi:10.1179/imr.1995.40.2.41.
8. Lu, K. Nanocrystalline Metals Crystallized from Amorphous Solids: Nanocrystallization, Structure, and Properties. *Materials Science and Engineering: R: Reports* **1996**, *16*, 161–221, doi:10.1016/0927-796X(95)00187-5.
9. Schafner, E.; Zehetbauer, M. Characterization of Nanostructured Materials by X-Ray Line Profile Analysis. *Rev. Adv. Mater. Sci* **2005**, *10*, 28–33.
10. Divinski, S.; Rösner, H.; Wilde, G. Chapter 1 - Functional Nanostructured Materials – Microstructure, Thermodynamic Stability and Atomic Mobility. In *Frontiers of Nanoscience*; Wilde, G., Ed.; Nanostructured Materials; Elsevier, 2009; Vol. 1, pp. 1–50.
11. Kumar, K.S.; Van Swygenhoven, H.; Suresh, S. Mechanical Behavior of Nanocrystalline Metals and Alloys11The Golden Jubilee Issue—Selected Topics in Materials Science and Engineering: Past, Present and Future, Edited by S. Suresh. *Acta Materialia* **2003**, *51*, 5743–5774, doi:10.1016/j.actamat.2003.08.032.
12. Vepřek, S. The Search for Novel, Superhard Materials. *Journal of Vacuum Science & Technology A* **1999**, *17*, 2401–2420, doi:10.1116/1.581977.
13. Niederhofer, A.; Bolom, T.; Nesladek, P.; Moto, K.; Eggs, C.; Patil, D.S.; Vepřek, S. The Role of Percolation Threshold for the Control of the Hardness and Thermal Stability of Super- and Ultrahard Nanocomposites. *Surface and Coatings Technology* **2001**, *146–147*, 183–188, doi:10.1016/S0257-8972(01)01469-4.
14. Lu, Y.; Liaw, P.K. The Mechanical Properties of Nanostructured Materials. *JOM* **2001**, *53*, 31–35, doi:10.1007/s11837-001-0177-6.
15. Latysh, V.; Krallics, Gy.; Alexandrov, I.; Fodor, A. Application of Bulk Nanostructured Materials in Medicine. *Current Applied Physics* **2006**, *6*, 262–266, doi:10.1016/j.cap.2005.07.053.
16. Zhu, Y.T.; Lowe, T.C.; Langdon, T.G. Performance and Applications of Nanostructured Materials Produced by Severe Plastic Deformation. *Scripta Materialia* **2004**, *51*, 825–830, doi:10.1016/j.scriptamat.2004.05.006.

17. Höppel, H.-W.; Mughrabi, H.; Vinogradov, A. Fatigue Properties of Bulk Nanostructured Materials. In *Bulk Nanostructured Materials*; John Wiley & Sons, Ltd, 2009; pp. 481–500 ISBN 978-3-527-62689-2.
18. Wang, Y.; Chen, M.; Zhou, F.; Ma, E. High Tensile Ductility in a Nanostructured Metal. *Nature* **2002**, *419*, 912–915, doi:10.1038/nature01133.
19. Champion, Y.; Langlois, C.; Guérin-Mailly, S.; Langlois, P.; Bonnentien, J.-L.; Hÿtch, M.J. Near-Perfect Elastoplasticity in Pure Nanocrystalline Copper. *Science* **2003**, *300*, 310–311, doi:10.1126/science.1081042.
20. He, G.; Eckert, J.; Löser, W.; Schultz, L. Novel Ti-Base Nanostructure–Dendrite Composite with Enhanced Plasticity. *Nature Mater* **2003**, *2*, 33–37, doi:10.1038/nmat792.
21. Valiev, R.Z.; Islamgaliev, R.K.; Semenova, I.P. Superplasticity in Nanostructured Materials: New Challenges. *Materials Science and Engineering: A* **2007**, *463*, 2–7, doi:10.1016/j.msea.2006.08.121.
22. Edalati, K.; Horita, Z.; Valiev, R.Z. Transition from Poor Ductility to Room-Temperature Superplasticity in a Nanostructured Aluminum Alloy. *Sci Rep* **2018**, *8*, 6740, doi:10.1038/s41598-018-25140-1.
23. Schaefer, H.-E.; Wurschum, R.; Gessmann, T.; Stöckl, G.; Scharwaechter, P.; Frank, W.; Valiev, R.Z.; Fecht, H.-J.; Moelle, C. Diffusion and Free Volumes in Nanocrystalline Pd. *Nanostructured Materials* **1995**, *6*, 869–872, doi:10.1016/0965-9773(95)00197-2.
24. Kolobov, Yu.R.; Grabovetskaya, G.P.; Ratochka, I.V.; Ivanov, K.V. Diffusion — Induced Creep of Polycrystalline and Nanostructured Metals. *Nanostructured Materials* **1999**, *12*, 1127–1130, doi:10.1016/S0965-9773(99)00311-6.
25. Hall, E.O. The Deformation and Ageing of Mild Steel: III Discussion of Results. *Proc. Phys. Soc. B* **1951**, *64*, 747, doi:10.1088/0370-1301/64/9/303.
26. Padmanabhan, K.A.; Dinda, G.P.; Hahn, H.; Gleiter, H. Inverse Hall–Petch Effect and Grain Boundary Sliding Controlled Flow in Nanocrystalline Materials. *Materials Science and Engineering: A* **2007**, *452–453*, 462–468, doi:10.1016/j.msea.2006.10.084.
27. Padmanabhan, K.A.; Sripathi, S.; Hahn, H.; Gleiter, H. Inverse Hall–Petch Effect in Quasi- and Nanocrystalline Materials. *Materials Letters* **2014**, *133*, 151–154, doi:10.1016/j.matlet.2014.06.153.
28. Kushwaha, A.K.; John, M.; Misra, M.; Menezes, P.L. Nanocrystalline Materials: Synthesis, Characterization, Properties, and Applications. *Crystals* **2021**, *11*, 1317, doi:10.3390/cryst11111317.
29. Rao, C.N.R.; Biswas, K. Characterization of Nanomaterials by Physical Methods. *Annual Review of Analytical Chemistry* **2009**, *2*, 435–462, doi:10.1146/annurev-anchem-060908-155236.
30. Moghri Moazzen, M.A.; Borghei, S.M.; Taleshi, F. Change in the Morphology of ZnO Nanoparticles upon Changing the Reactant Concentration. *Appl Nanosci* **2013**, *3*, 295–302, doi:10.1007/s13204-012-0147-z.
31. Sanyal, M.K.; Datta, A.; Hazra, S. Morphology of Nanostructured Materials. *Pure and Applied Chemistry* **2002**, *74*, 1553–1570, doi:10.1351/pac200274091553.
32. Chapter 1 - Basic Properties and Measuring Methods of Nanoparticles. In *Nanoparticle Technology Handbook (Third Edition)*; Naito, M., Yokoyama, T., Hosokawa, K., Nogi, K., Eds.; Elsevier, 2018; pp. 3–47 ISBN 978-0-444-64110-6.
33. Goldstein, J.I.; Newbury, D.E.; Echlin, P.; Joy, D.C.; Lyman, C.E.; Lifshin, E.; Sawyer, L.; Michael, J.R. The SEM and Its Modes of Operation. In *Scanning Electron Microscopy and X-ray Microanalysis: Third Edition*; Goldstein, J.I., Newbury, D.E., Echlin, P., Joy, D.C., Lyman,

- C.E., Lifshin, E., Sawyer, L., Michael, J.R., Eds.; Springer US: Boston, MA, 2003; pp. 21–60 ISBN 978-1-4615-0215-9.
34. Chen, J.; Wang, F.; Huang, K.; Liu, Y.; Liu, S. Preparation of Fe₃O₄ Nanoparticles with Adjustable Morphology. *Journal of Alloys and Compounds* **2009**, *475*, 898–902, doi:10.1016/j.jallcom.2008.08.064.
 35. Biswas, A.K.; Islam, M.R.; Choudhury, Z.S.; Mostafa, A.; Kadir, M.F. Nanotechnology Based Approaches in Cancer Therapeutics. *Adv. Nat. Sci.: Nanosci. Nanotechnol.* **2014**, *5*, 043001, doi:10.1088/2043-6262/5/4/043001.
 36. Rizvi, S.A.A.; Saleh, A.M. Applications of Nanoparticle Systems in Drug Delivery Technology. *Saudi Pharm J* **2018**, *26*, 64–70, doi:10.1016/j.jsps.2017.10.012.
 37. Siddiqui, M.R.H.; Al-Wassil, A.I.; Al-Otaibi, A.M.; Mahfouz, R.M. Effects of Precursor on the Morphology and Size of ZrO₂ Nanoparticles, Synthesized by Sol-Gel Method in Non-Aqueous Medium. *Materials Research* **2012**, *15*, 986–989.
 38. Li, J.; Yan, R.; Xiao, B.; Liang, D.T.; Du, L. Development of Nano-NiO/Al₂O₃ Catalyst to Be Used for Tar Removal in Biomass Gasification. *Environ. Sci. Technol.* **2008**, *42*, 6224–6229, doi:10.1021/es800138r.
 39. Yang, L.; Zhu, Z.; Yu, X.-Y.; Rodek, E.; Saraf, L.; Thevuthasan, T.; Cowin, J.P. In Situ SEM and ToF-SIMS Analysis of IgG Conjugated Gold Nanoparticles at Aqueous Surfaces. *Surface and Interface Analysis* **2014**, *46*, 224–228, doi:10.1002/sia.5252.
 40. Goodhew, P.J.; Humphreys, J.; Beanland, R. *Electron Microscopy and Analysis*; CRC press, 2000;
 41. Wahlström, J.; Olander, L.; Olofsson, U. Size, Shape, and Elemental Composition of Airborne Wear Particles from Disc Brake Materials. *Tribol Lett* **2010**, *38*, 15–24, doi:10.1007/s11249-009-9564-x.
 42. Weidenthaler, C. Pitfalls in the Characterization of Nanoporous and Nanosized Materials. *Nanoscale* **2011**, *3*, 792–810, doi:10.1039/C0NR00561D.
 43. Pyrz, W.D.; Buttrey, D.J. Particle Size Determination Using TEM: A Discussion of Image Acquisition and Analysis for the Novice Microscopist. *Langmuir* **2008**, *24*, 11350–11360, doi:10.1021/la801367j.
 44. Zhong, Y.; Ping, D.; Song, X.; Yin, F. Determination of Grain Size by XRD Profile Analysis and TEM Counting in Nano-Structured Cu. *Journal of Alloys and Compounds* **2009**, *476*, 113–117, doi:10.1016/j.jallcom.2008.08.075.
 45. Bescond, A.; Yon, J.; Ouf, F.X.; Ferry, D.; Delhaye, D.; Gaffié, D.; Coppalle, A.; Rozé, C. Automated Determination of Aggregate Primary Particle Size Distribution by TEM Image Analysis: Application to Soot. *Aerosol Science and Technology* **2014**, *48*, 831–841, doi:10.1080/02786826.2014.932896.
 46. Mast, J.; Verleysen, E.; Hodoroaba, V.-D.; Kaegi, R. Chapter 2.1.2 - Characterization of Nanomaterials by Transmission Electron Microscopy: Measurement Procedures. In *Characterization of Nanoparticles*; Hodoroaba, V.-D., Unger, W.E.S., Shard, A.G., Eds.; Micro and Nano Technologies; Elsevier, 2020; pp. 29–48 ISBN 978-0-12-814182-3.
 47. Tanaka, N. *Scanning Transmission Electron Microscopy of Nanomaterials: Basics of Imaging and Analysis*; World Scientific, 2014;
 48. Albrecht, W.; Bals, S. Fast Electron Tomography for Nanomaterials. *J. Phys. Chem. C* **2020**, *124*, 27276–27286, doi:10.1021/acs.jpcc.0c08939.
 49. Dampare, J.; Zondode, M.; Liou, S.-C.; Ozturk, B.; Yu, H.; Lan, Y. EELS Investigations of Carbon-Rich Boron Carbide Nanomaterials. *Microscopy and Microanalysis* **2018**, *24*, 1756–1757, doi:10.1017/S1431927618009261.

50. Weirich, T.E.; Winterer, M.; Seifried, S.; Mayer, J. Structure of Nanocrystalline Anatase Solved and Refined from Electron Powder Data. *Acta Cryst A* **2002**, *58*, 308–315, doi:10.1107/S0108767302005007.
51. Sun, S.; Li, Z.; Chang, X. Synthesis and Structural Characterization of Tungsten Disulfide Nanomaterials. *Materials Letters* **2011**, *65*, 3164–3166, doi:10.1016/j.matlet.2011.06.118.
52. Ding, Y.; Wang, Z.L. Structure Analysis of Nanowires and Nanobelts by Transmission Electron Microscopy. *J. Phys. Chem. B* **2004**, *108*, 12280–12291, doi:10.1021/jp048163n.
53. Kim, B.; Hochella, M.F. Chapter 4 - Analytical Transmission Electron Microscopy and Scanning Transmission Electron Microscopy Techniques for the Characterization of Nanomaterial Composition, Phase and Crystallinity. In *Frontiers of Nanoscience*; Baalousha, M., Lead, J.R., Eds.; Characterization of Nanomaterials in Complex Environmental and Biological Media; Elsevier, 2015; Vol. 8, pp. 123–152.
54. Nayak, P.K.; Grinblat, J.; Levi, M.; Aurbach, D. Electrochemical and Structural Characterization of Carbon Coated Li_{1.2}Mn_{0.56}Ni_{0.16}Co_{0.08}O₂ and Li_{1.2}Mn_{0.6}Ni_{0.20}O₂ as Cathode Materials for Li-Ion Batteries. *Electrochimica Acta* **2014**, *137*, 546–556, doi:10.1016/j.electacta.2014.06.055.
55. Tian, M.; Mahjouri-Samani, M.; Eres, G.; Sachan, R.; Yoon, M.; Chisholm, M.F.; Wang, K.; Puzos, A.A.; Rouleau, C.M.; Geoghegan, D.B.; et al. Structure and Formation Mechanism of Black TiO₂ Nanoparticles. *ACS Nano* **2015**, *9*, 10482–10488, doi:10.1021/acsnano.5b04712.
56. Jayashree, P.; Sinha, A.; Gialanella, S.; Straffellini, G. Dry Sliding Behavior and Particulate Emissions of a SiC-Graphite Composite Friction Material Paired with HVOF-Coated Counterface. *Atmosphere* **2022**, *13*, 296, doi:10.3390/atmos13020296.
57. El-Nahhal, I.M.; Salem, J.K.; Kuhn, S.; Hammad, T.; Hempelmann, R.; Al Bhai, S. Synthesis & Characterization of Silica Coated and Functionalized Silica Coated Zinc Oxide Nanomaterials. *Powder Technology* **2016**, *287*, 439–446, doi:10.1016/j.powtec.2015.09.042.
58. Greene, D.; Serrano-Garcia, R.; Govan, J.; Gun'ko, Y.K. Synthesis Characterization and Photocatalytic Studies of Cobalt Ferrite-Silica-Titania Nanocomposites. *Nanomaterials* **2014**, *4*, 331–343, doi:10.3390/nano4020331.
59. Pennycook, S.J.; Lupini, A.R.; Varela, M.; Borisevich, A.; Peng, Y.; Oxley, M.P.; Van Benthem, K.; Chisholm, M.F. Scanning Transmission Electron Microscopy for Nanostructure Characterization. In *Scanning Microscopy for Nanotechnology: Techniques and Applications*; Zhou, W., Wang, Z.L., Eds.; Springer: New York, NY, 2007; pp. 152–191 ISBN 978-0-387-39620-0.
60. Williams, D.B.; Carter, C.B. *Transmission Electron Microscopy: A Textbook for Materials Science*; 2nd ed.; Springer US, 2009; ISBN 978-0-387-76500-6.
61. Pennycook, S.J.; Nellist, P.D. *Scanning Transmission Electron Microscopy: Imaging and Analysis*; Springer Science & Business Media, 2011; ISBN 978-1-4419-7200-2.
62. Tata, B.V.R.; Raj, B. Confocal Laser Scanning Microscopy: Applications in Material Science and Technology. *Bull Mater Sci* **1998**, *21*, 263–278, doi:10.1007/BF02744951.
63. Paddock, S.W. Confocal Laser Scanning Microscopy. *BioTechniques* **1999**, *27*, 992–1004, doi:10.2144/99275ov01.
64. Zhang, L.W.; Monteiro-Riviere, N.A. Use of Confocal Microscopy for Nanoparticle Drug Delivery through Skin. *JBO* **2012**, *18*, 061214, doi:10.1117/1.JBO.18.6.061214.

65. Germann, J.A.; Davis, L.M. Three-Dimensional Tracking of a Single Fluorescent Nanoparticle Using Four-Focus Excitation in a Confocal Microscope. *Opt. Express, OE* **2014**, *22*, 5641–5650, doi:10.1364/OE.22.005641.
66. Donev, E.U.; Lopez, R.; Feldman, L.C.; Haglund, R.F.Jr. Confocal Raman Microscopy across the Metal–Insulator Transition of Single Vanadium Dioxide Nanoparticles. *Nano Lett.* **2009**, *9*, 702–706, doi:10.1021/nl8031839.
67. Samori, P. *Scanning Probe Microscopies beyond Imaging: Manipulation of Molecules and Nanostructures*; John Wiley & Sons, 2006;
68. Rao, A.; Schoenenberger, M.; Gnecco, E.; Glatzel, T.; Meyer, E.; Brändlin, D.; Scandella, L. Characterization of Nanoparticles Using Atomic Force Microscopy. *J. Phys.: Conf. Ser.* **2007**, *61*, 971, doi:10.1088/1742-6596/61/1/192.
69. Grobely, J.; DelRio, F.W.; Pradeep, N.; Kim, D.-I.; Hackley, V.A.; Cook, R.F. Size Measurement of Nanoparticles Using Atomic Force Microscopy. In *Characterization of Nanoparticles Intended for Drug Delivery*; McNeil, S.E., Ed.; Methods in Molecular Biology; Humana Press: Totowa, NJ, 2011; pp. 71–82 ISBN 978-1-60327-198-1.
70. Walton, A.S.; Lauritsen, J.V.; Topsøe, H.; Besenbacher, F. MoS₂ Nanoparticle Morphologies in Hydrodesulfurization Catalysis Studied by Scanning Tunneling Microscopy. *Journal of Catalysis* **2013**, *308*, 306–318, doi:10.1016/j.jcat.2013.08.017.
71. Ohara, S. Nanostructure and Function (Characterization of Local Nanostructure). *Nanoparticle Technology Handbook* **2007**, 269–270.
72. Stevie, F.A.; Donley, C.L. Introduction to X-Ray Photoelectron Spectroscopy. *Journal of Vacuum Science & Technology A* **2020**, *38*, 063204, doi:10.1116/6.0000412.
73. Zhang, F.; Wang, P.; Koberstein, J.; Khalid, S.; Chan, S.-W. Cerium Oxidation State in Ceria Nanoparticles Studied with X-Ray Photoelectron Spectroscopy and Absorption near Edge Spectroscopy. *Surface Science* **2004**, *563*, 74–82, doi:10.1016/j.susc.2004.05.138.
74. Alwin, E.; Nowicki, W.; Wojcieszak, R.; Zieliński, M.; Pietrowski, M. Elucidating the Structure of the Graphitic Carbon Nitride Nanomaterials via X-Ray Photoelectron Spectroscopy and X-Ray Powder Diffraction Techniques. *Dalton Trans.* **2020**, *49*, 12805–12813, doi:10.1039/D0DT02325F.
75. Aoki, T. Photoluminescence Spectroscopy. In *Characterization of Materials*; John Wiley & Sons, Ltd, 2012; pp. 1–12 ISBN 978-0-471-26696-9.
76. Peng, X.; Wickham, J.; Alivisatos, A.P. Kinetics of II-VI and III-V Colloidal Semiconductor Nanocrystal Growth: “Focusing” of Size Distributions. *J. Am. Chem. Soc.* **1998**, *120*, 5343–5344, doi:10.1021/ja9805425.
77. Vafaee, M.; Ghamsari, M.S. Preparation and Characterization of ZnO Nanoparticles by a Novel Sol–Gel Route. *Materials Letters* **2007**, *61*, 3265–3268, doi:10.1016/j.matlet.2006.11.089.
78. Liqiang, J.; Xiaojun, S.; Baifu, X.; Baiqi, W.; Weimin, C.; Honggang, F. The Preparation and Characterization of La Doped TiO₂ Nanoparticles and Their Photocatalytic Activity. *Journal of Solid State Chemistry* **2004**, *177*, 3375–3382, doi:10.1016/j.jssc.2004.05.064.
79. Chen, H.S.; Chiu, J.J.; Perng, T.P. On the Photoluminescence of Si Nanoparticles. *Materials Physics and Mechanics* **2001**, *4*, 62–66.
80. Shipp, D.W.; Sinjab, F.; Notingher, I. Raman Spectroscopy: Techniques and Applications in the Life Sciences. *Adv. Opt. Photon., AOP* **2017**, *9*, 315–428, doi:10.1364/AOP.9.000315.
81. Ferraro, J.R.; Nakamoto, K.; Brown, C.W. *Introductory Raman Spectroscopy* (Academic Press, San Diego). **1994**.

82. Dresselhaus, M.S.; Eklund, P.C. Phonons in Carbon Nanotubes. *Advances in Physics* **2000**, *49*, 705–814, doi:10.1080/000187300413184.
83. Viera, G.; Huet, S.; Boufendi, L. Crystal Size and Temperature Measurements in Nanostructured Silicon Using Raman Spectroscopy. *Journal of Applied Physics* **2001**, *90*, 4175–4183, doi:10.1063/1.1398601.
84. Choi, H.C.; Jung, Y.M.; Kim, S.B. Size Effects in the Raman Spectra of TiO₂ Nanoparticles. *Vibrational Spectroscopy* **2005**, *37*, 33–38, doi:10.1016/j.vibspec.2004.05.006.
85. Gao, J.; Gu, H.; Xu, B. Multifunctional Magnetic Nanoparticles: Design, Synthesis, and Biomedical Applications. *Acc. Chem. Res.* **2009**, *42*, 1097–1107, doi:10.1021/ar9000026.
86. Gosens, I.; Post, J.A.; de la Fonteyne, L.J.; Jansen, E.H.; Geus, J.W.; Cassee, F.R.; de Jong, W.H. Impact of Agglomeration State of Nano- and Submicron Sized Gold Particles on Pulmonary Inflammation. *Part Fibre Toxicol* **2010**, *7*, 37, doi:10.1186/1743-8977-7-37.
87. Vainshtein, B.K. CHAPTER I - Diffraction Methods in Structure Analysis. In *Structure Analysis by Electron Diffraction*; Vainshtein, B.K., Ed.; Pergamon, 1964; pp. 1–26 ISBN 978-0-08-010241-2.
88. Fultz, B.; Howe, J. Diffraction and the X-Ray Powder Diffractometer. In *Transmission Electron Microscopy and Diffractometry of Materials*; Fultz, B., Howe, J., Eds.; Graduate Texts in Physics; Springer: Berlin, Heidelberg, 2013; pp. 1–57 ISBN 978-3-642-29761-8.
89. Vincent, R.; Midgley, P.A. Double Conical Beam-Rocking System for Measurement of Integrated Electron Diffraction Intensities. *Ultramicroscopy* **1994**, *53*, 271–282, doi:10.1016/0304-3991(94)90039-6.
90. Kolb, U.; Gorelik, T.; Kübel, C.; Otten, M.T.; Hubert, D. Towards Automated Diffraction Tomography: Part I—Data Acquisition. *Ultramicroscopy* **2007**, *107*, 507–513, doi:10.1016/j.ultramic.2006.10.007.
91. Gemmi, M.; La Placa, M.G.I.; Galanis, A.S.; Rauch, E.F.; Nicolopoulos, S. Fast Electron Diffraction Tomography. *J Appl Cryst* **2015**, *48*, 718–727, doi:10.1107/S1600576715004604.
92. Portillo, J.; Rauch, E.F.; Nicolopoulos, S.; Gemmi, M.; Bultreys, D. Precession Electron Diffraction Assisted Orientation Mapping in the Transmission Electron Microscope. *Materials Science Forum* **2010**, *644*, 1–7, doi:10.4028/www.scientific.net/MSF.644.1.
93. Rauch, E.F.; Véron, M. Automated Crystal Orientation and Phase Mapping in TEM. *Materials Characterization* **2014**, *98*, 1–9, doi:10.1016/j.matchar.2014.08.010.
94. Morozov, V.A.; Bertha, A.; Meert, K.W.; Van Rompaey, S.; Batuk, D.; Martinez, G.T.; Van Aert, S.; Smet, P.F.; Raskina, M.V.; Poelman, D.; et al. Incommensurate Modulation and Luminescence in the CaGd₂(1-x)Eu_{2x}(MoO₄)₄(1-y)(WO₄)_{4y} (0 ≤ x ≤ 1, 0 ≤ y ≤ 1) Red Phosphors. *Chem. Mater.* **2013**, *25*, 4387–4395, doi:10.1021/cm402729r.
95. Cullity, B.D.; Stock, S.R. *Elements of X-Ray Diffraction, Third Edition*; Prentice-Hall: New York, 2001;
96. Zou, X. What Is Electron Crystallography? In *Proceedings of the Electron Crystallography*; Weirich, T.E., Lábár, J.L., Zou, X., Eds.; Springer Netherlands: Dordrecht, 2006; pp. 3–16.
97. Shull, C.G.; Wollan, E.O. X-Ray, Electron, and Neutron Diffraction. *Science* **1948**, *108*, 69–75.
98. Balzar, D. X-Ray Diffraction Line Broadening: Modeling and Applications to High-T_c Superconductors. *J Res Natl Inst Stand Technol* **1993**, *98*, 321–353, doi:10.6028/jres.098.026.

99. Delhez, R.; de Keijser, Th.H.; Mittemeijer, E.J. Determination of Crystallite Size and Lattice Distortions through X-Ray Diffraction Line Profile Analysis. *Z. Anal. Chem.* **1982**, *312*, 1–16, doi:10.1007/BF00482725.
100. Stokes, A.R. A Numerical Fourier-Analysis Method for the Correction of Widths and Shapes of Lines on X-Ray Powder Photographs. *Proc. Phys. Soc.* **1948**, *61*, 382, doi:10.1088/0959-5309/61/4/311.
101. Wagner, C.N.J.; Aqua, E.N. Analysis of the Broadening of Powder Pattern Peaks from Cold-Worked Face-Centered and Body-Centered Cubic Metals. *Advances in X-Ray Analysis* **1963**, *7*, 46–65, doi:10.1154/S037603080002408.
102. Wilson, A.J.C. On Variance as a Measure of Line Broadening in Diffractometry General Theory and Small Particle Size. *Proc. Phys. Soc.* **1962**, *80*, 286, doi:10.1088/0370-1328/80/1/333.
103. de Keijser, T.H.; Langford, J.I.; Mittemeijer, E.J.; Vogels, A.B.P. Use of the Voigt Function in a Single-Line Method for the Analysis of X-Ray Diffraction Line Broadening. *J Appl Cryst* **1982**, *15*, 308–314, doi:10.1107/S0021889882012035.
104. Scherrer, P. Nachr Ges Wiss Goettingen. *Math. Phys.* **1918**, *2*, 98–100.
105. Patterson, A.L. The Scherrer Formula for X-Ray Particle Size Determination. *Phys. Rev.* **1939**, *56*, 978–982, doi:10.1103/PhysRev.56.978.
106. Langford, J.I.; Wilson, A.J.C. Scherrer after Sixty Years: A Survey and Some New Results in the Determination of Crystallite Size. *J Appl Cryst* **1978**, *11*, 102–113, doi:10.1107/S0021889878012844.
107. Uvarov, V.; Popov, I. Metrological Characterization of X-Ray Diffraction Methods for Determination of Crystallite Size in Nano-Scale Materials. *Materials Characterization* **2007**, *58*, 883–891, doi:10.1016/j.matchar.2006.09.002.
108. He, K.; Chen, N.; Wang, C.; Wei, L.; Chen, J. Method for Determining Crystal Grain Size by X-Ray Diffraction. *Crystal Research and Technology* **2018**, *53*, 1700157, doi:https://doi.org/10.1002/crat.201700157.
109. Guinier, A. *X-Ray Diffraction in Crystals, Imperfect Crystals, and Amorphous Bodies*; Courier Corporation, 1994; ISBN 978-0-486-68011-8.
110. Stokes, A.R.; Wilson, A.J.C. The Diffraction of X Rays by Distorted Crystal Aggregates - I. *Proc. Phys. Soc.* **1944**, *56*, 174, doi:10.1088/0959-5309/56/3/303.
111. Bertaut, F. Etude Aux Rayons-x de La Repartition Des Dimensions Des Cristallites Dans Une Poudre Cristalline. *COMPTE RENDUS HEBDOMADAIRES DES SEANCES DE L ACADEMIE DES SCIENCES* **1949**, *228*, 492–494.
112. Warren, B.E.; Averbach, B.L. The Effect of Cold-Work Distortion on X-Ray Patterns. *Journal of Applied Physics* **1950**, *21*, 595–599, doi:10.1063/1.1699713.
113. Williamson, G.K.; Hall, W.H. X-Ray Line Broadening from Filed Aluminium and Wolfram. *Acta Metallurgica* **1953**, *1*, 22–31, doi:10.1016/0001-6160(53)90006-6.
114. Rietveld, H.M. Line Profiles of Neutron Powder-Diffraction Peaks for Structure Refinement. *Acta Cryst* **1967**, *22*, 151–152, doi:10.1107/S0365110X67000234.
115. Pawley, G.S. Unit-Cell Refinement from Powder Diffraction Scans. *J Appl Cryst* **1981**, *14*, 357–361, doi:10.1107/S0021889881009618.
116. Toraya, H. Whole-Powder-Pattern Fitting without Reference to a Structural Model: Application to X-Ray Powder Diffraction Data. *J Appl Cryst* **1986**, *19*, 440–447, doi:10.1107/S0021889886088982.
117. De Broglie, L. Recherches Sur La Théorie Des Quanta, Paris, 1924 (Thèse de Physique). *Ann. de Physique* **1925**, *3*, 10–22.

118. Knoll, M.; Ruska, E. Das Elektronenmikroskop. *Z. Physik* **1932**, *78*, 318–339, doi:10.1007/BF01342199.
119. History of Electron Microscopy, 1931-2000 Available online: https://authors.library.caltech.edu/5456/1/hrst.mit.edu/hrs/materials/public/ElectronMicroscope/EM_HistOverview.htm (accessed on 10 October 2022).
120. Scherzer, O. Über einige Fehler von Elektronenlinsen. *Z. Physik* **1936**, *101*, 593–603, doi:10.1007/BF01349606.
121. Heidenreich, R.D. Electron Microscope and Diffraction Study of Metal Crystal Textures by Means of Thin Sections. *Journal of Applied Physics* **1949**, *20*, 993–1010, doi:10.1063/1.1698264.
122. Hirsch, P.B.; Home, R.W.; Whelan, M.J. LXVIII. Direct Observations of the Arrangement and Motion of Dislocations in Aluminium. *The Philosophical Magazine: A Journal of Theoretical Experimental and Applied Physics* **1956**, *1*, 677–684, doi:10.1080/14786435608244003.
123. Bollmann, W. Interference Effects in the Electron Microscopy of Thin Crystal Foils. *Phys. Rev.* **1956**, *103*, 1588–1589, doi:10.1103/PhysRev.103.1588.
124. Vainshtein, B.K. Kinematic Theory of Intensities in Electron Diffraction Patterns. Part 2. Patterns from Textures and Polycrystalline Aggregates. *Soviet Physics—Crystallography* **1956**, *1*, 117–122.
125. Andrusenko, I.; Gemmi, M. 3D Electron Diffraction for Structure Determination of Small-Molecule Nanocrystals: A Possible Breakthrough for the Pharmaceutical Industry. *WIREs Nanomedicine and Nanobiotechnology* **2022**, *14*, e1810, doi:10.1002/wnan.1810.
126. Zhukhlistov, A.P.; Zvyagin, B.B. Crystal Structure of Lizardite 1T from Electron Diffractometry Data. *Crystallography Reports* **1998**, *43*, doi:10.1134/1.170880.
127. Menter, J.W.; Bowden, F.P. The Direct Study by Electron Microscopy of Crystal Lattices and Their Imperfections. *Proceedings of the Royal Society of London. Series A. Mathematical and Physical Sciences* **1956**, *236*, 119–135, doi:10.1098/rspa.1956.0117.
128. Komoda, T. Observation of Lattice Planes of 2.35 Å Spacing with an Electron Microscope. *Jpn. J. Appl. Phys.* **1964**, *3*, 122, doi:10.1143/JJAP.3.122.
129. Heidenreich, R.D.; Hess, W.M.; Ban, L.L. A Test Object and Criteria for High Resolution Electron Microscopy. *J Appl Cryst* **1968**, *1*, 1–19, doi:10.1107/S0021889868004930.
130. von Ardenne, M. Das Elektronen-Rastermikroskop. *Z. Physik* **1938**, *109*, 553–572, doi:10.1007/BF01341584.
131. Crewe, A.V.; Wall, J.; Langmore, J. Visibility of Single Atoms. *Science* **1970**, *168*, 1338–1340, doi:10.1126/science.168.3937.1338.
132. Cliff, G.; Lorimer, G.W. The Quantitative Analysis of Thin Specimens. *Journal of Microscopy* **1975**, *103*, 203–207, doi:10.1111/j.1365-2818.1975.tb03895.x.
133. Lorimer, G.W.; Cliff, G. Analytical Electron Microscopy of Minerals. Pp. 506Å519 in: *Electron Microscopy in Mineralogy* (HR Wenk, Editor) 1976.
134. Haider, M.; Rose, H.; Uhlemann, S.; Kabius, B.; Urban, K. Towards 0.1 Nm Resolution with the First Spherically Corrected Transmission Electron Microscope. *Journal of Electron Microscopy* **1998**, *47*, 395–405, doi:10.1093/oxfordjournals.jmicro.a023610.
135. Kolb, U.; Mugnaioli, E.; Gorelik, T.E. Automated Electron Diffraction Tomography – a New Tool for Nano Crystal Structure Analysis. *Crystal Research and Technology* **2011**, *46*, 542–554, doi:10.1002/crat.201100036.

136. Gemmi, M.; Mugnaioli, E.; Gorelik, T.E.; Kolb, U.; Palatinus, L.; Boullay, P.; Hovmöller, S.; Abrahams, J.P. 3D Electron Diffraction: The Nanocrystallography Revolution. *ACS Cent. Sci.* **2019**, *5*, 1315–1329, doi:10.1021/acscentsci.9b00394.
137. Plana-Ruiz, S.; Krysiak, Y.; Portillo, J.; Alig, E.; Estradé, S.; Peiró, F.; Kolb, U. Fast-ADT: A Fast and Automated Electron Diffraction Tomography Setup for Structure Determination and Refinement. *Ultramicroscopy* **2020**, *211*, 112951, doi:10.1016/j.ultramic.2020.112951.
138. Kodjikian, S.; Klein, H. Low-Dose Electron Diffraction Tomography (LD-EDT). *Ultramicroscopy* **2019**, *200*, 12–19, doi:10.1016/j.ultramic.2019.02.010.
139. Krumeich, F. Introduction into Transmission and Scanning Transmission Electron Microscopy. *Laboratory of Inorganic Chemistry* **2018**.
140. Humphreys, C.J. The Scattering of Fast Electrons by Crystals. *Rep. Prog. Phys.* **1979**, *42*, 1825, doi:10.1088/0034-4885/42/11/002.
141. Zuo, J.-M.; Lábár, J.L.; Zhang, J.; Gorelik, T.E.; Kolb, U. Electron Powder Diffraction. In *Electron powder diffraction*; International Union of Crystallography, 2019; Vol. H, ch. 2.4, pp. 102–117.
142. Cowley, J.M.; Goodman, P.; Vainshtein, B.K.; Zvyagin, B.B.; Dorset, D.L. Electron Diffraction and Electron Microscopy in Structure Determination. In *International Tables for Crystallography Volume B: Reciprocal space*; Shmueli, U., Ed.; International Tables for Crystallography; Springer Netherlands: Dordrecht, 2001; pp. 276–345 ISBN 978-1-4020-5407-5.
143. Cowley, J.M.; Moodie, A.F. The Scattering of Electrons by Atoms and Crystals. I. A New Theoretical Approach. *Acta Crystallographica* **1957**, *10*, 609–619, doi:10.1107/S0365110X57002194.
144. Blackman, M.; Thomson, G.P. On the Intensities of Electron Diffraction Rings. *Proceedings of the Royal Society of London. Series A. Mathematical and Physical Sciences* **1939**, *173*, 68–82, doi:10.1098/rspa.1939.0129.
145. Boullay, P.; Lutterotti, L.; Chateigner, D.; Sicard, L. Fast Microstructure and Phase Analyses of Nanopowders Using Combined Analysis of Transmission Electron Microscopy Scattering Patterns. *Acta Cryst A* **2014**, *70*, 448–456, doi:10.1107/S2053273314009930.
146. Spence, J.C.H.; Zuo, J.M. The Geometry of CBED Patterns. In *Electron Microdiffraction*; Spence, J.C.H., Zuo, J.M., Eds.; Springer US: Boston, MA, 1992; pp. 7–28 ISBN 978-1-4899-2353-0.
147. Vainshtein, B.K. *Structure Analysis by Electron Diffraction.*; Oxford: Pergamon Press, 1964;
148. Palatinus, L.; Jacob, D.; Cuvillier, P.; Klementová, M.; Sinkler, W.; Marks, L.D. Structure Refinement from Precession Electron Diffraction Data. *Acta Cryst A* **2013**, *69*, 171–188, doi:10.1107/S010876731204946X.
149. Shindo, D.; Oikawa, T. Energy Dispersive X-Ray Spectroscopy. In *Analytical Electron Microscopy for Materials Science*; Shindo, D., Oikawa, T., Eds.; Springer Japan: Tokyo, 2002; pp. 81–102 ISBN 978-4-431-66988-3.
150. Lábár, J.L. Phase Identification by Combining Local Composition from EDX with Information from Diffraction Database. In *Proceedings of the Electron Crystallography*; Weirich, T.E., Lábár, J.L., Zou, X., Eds.; Springer Netherlands: Dordrecht, 2006; pp. 207–218.
151. *The Rietveld Method*; International Union of Crystallography Monographs on Crystallography; Oxford University Press: Oxford, New York, 1995; ISBN 978-0-19-855912-2.
152. Dinnebier, R.; Müller, M. Modern Rietveld Refinement, a Practical Guide. In *Modern Diffraction Methods*; John Wiley & Sons, Ltd, 2012; pp. 27–60 ISBN 978-3-527-64988-4.

153. Scardi, P.; Leoni, M. Whole Powder Pattern Modelling: Theory and Applications. In *Diffraction Analysis of the Microstructure of Materials*; Mittemeijer, E.J., Scardi, P., Eds.; Springer Series in Materials Science; Springer: Berlin, Heidelberg, 2004; pp. 51–91 ISBN 978-3-662-06723-9.
154. Langford, J.I.; Louër, D. Powder Diffraction. *Rep. Prog. Phys.* **1996**, *59*, 131, doi:10.1088/0034-4885/59/2/002.
155. Peterson, V.K. Lattice Parameter Measurement Using Le Bail versus Structural (Rietveld) Refinement: A Caution for Complex, Low Symmetry Systems. *Powder Diffraction* **2005**, *20*, 14–17, doi:10.1154/1.1810156.
156. Caglioti, G.; Paoletti, A.; Ricci, F.P. Choice of Collimators for a Crystal Spectrometer for Neutron Diffraction. *Nuclear Instruments* **1958**, *3*, 223–228, doi:10.1016/0369-643X(58)90029-X.
157. Rietveld, H.M. A Profile Refinement Method for Nuclear and Magnetic Structures. *J Appl Crystallogr* **1969**, *2*, 65–71, doi:10.1107/S0021889869006558.
158. Serafini, A.; Lutterotti, L.; Gross, S.; Gialanella, S. Characterization of Nanograined Powder Samples Using the Rietveld Method Applied to Electron Diffraction Ring Patterns. *Powder Diffraction* **2017**, *32*, S63–S68, doi:10.1017/S0885715617000343.
159. Kim, J.-G.; Seo, J.-W.; Cheon, J.-W.; Kim, Y.-J. Rietveld Analysis of Nano-Crystalline MnFe₂O₄ with Electron Powder Diffraction. *Bulletin of the Korean Chemical Society* **2009**, *30*, 183–187, doi:10.5012/bkcs.2009.30.1.183.
160. Song, K.; Kim, Y.-J.; Kim, Y.-I.; Kim, J.-G. Application of Theta-Scan Precession Electron Diffraction to Structure Analysis of Hydroxyapatite Nanopowder. *Journal of Electron Microscopy* **2012**, *61*, 9–15, doi:10.1093/jmicro/df078.
161. Gjønnes, K.; Cheng, Y.; Berg, B.S.; Hansen, V. Corrections for Multiple Scattering in Integrated Electron Diffraction Intensities. Application to Determination of Structure Factors in the [001] Projection of Al₂Fe. *Acta Cryst A* **1998**, *54*, 102–119, doi:10.1107/S0108767397009963.
162. Weirich, T.E.; Zou, X.D.; Ramlau, R.; Simon, A.; Cascarano, G.L.; Giacomazzo, C.; Hovmöller, S. Structures of Nanometre-Size Crystals Determined from Selected-Area Electron Diffraction Data. *Acta Cryst A* **2000**, *56*, 29–35, doi:10.1107/S0108767399009605.
163. Wagner, P.; Terasaki, O.; Ritsch, S.; Nery, J.G.; Zones, S.I.; Davis, M.E.; Hiraga, K. Electron Diffraction Structure Solution of a Nanocrystalline Zeolite at Atomic Resolution. *J. Phys. Chem. B* **1999**, *103*, 8245–8250, doi:10.1021/jp991389j.
164. Lutterotti, L.; Vasin, R.; Wenk, H.-R. Rietveld Texture Analysis from Synchrotron Diffraction Images. I. Calibration and Basic Analysis. *Powder Diffraction* **2014**, *29*, 76–84, doi:10.1017/S0885715613001346.
165. Sinha, A.; Bortolotti, M.; Ischia, G.; Lutterotti, L.; Gialanella, S. Electron Diffraction Characterization of Nanocrystalline Materials Using a Rietveld-Based Approach. Part I. Methodology. *J Appl Cryst* **2022**, *55*, 953–965, doi:10.1107/S1600576722006367.
166. Rodríguez-Carvajal, J. Recent Advances in Magnetic Structure Determination by Neutron Powder Diffraction. *Physica B: Condensed Matter* **1993**, *192*, 55–69, doi:10.1016/0921-4526(93)90108-I.
167. McCusker, L.B.; Von Dreele, R.B.; Cox, D.E.; Louër, D.; Scardi, P. Rietveld Refinement Guidelines. *J Appl Cryst* **1999**, *32*, 36–50, doi:10.1107/S0021889898009856.
168. Thompson, P.; Cox, D.E.; Hastings, J.B. Rietveld Refinement of Debye–Scherrer Synchrotron X-Ray Data from Al₂O₃. *J Appl Cryst* **1987**, *20*, 79–83, doi:10.1107/S0021889887087090.

169. Gemmi, M.; Voltolini, M.; Ferretti, A.M.; Ponti, A. Quantitative Texture Analysis from Powder-like Electron Diffraction Data. *J Appl Cryst* **2011**, *44*, 454–461, doi:10.1107/S0021889811012106.
170. Li, X.-Z. QPCED2.0: A Computer Program for the Processing and Quantification of Polycrystalline Electron Diffraction Patterns. *J Appl Cryst* **2012**, *45*, 862–868, doi:10.1107/S0021889812027173.
171. Weirich, Th.E.; Winterer, M.; Seifried, S.; Hahn, H.; Fuess, H. Rietveld Analysis of Electron Powder Diffraction Data from Nanocrystalline Anatase, TiO₂. *Ultramicroscopy* **2000**, *81*, 263–270, doi:10.1016/S0304-3991(99)00189-8.
172. Warren, B.E. X-Ray Studies of Deformed Metals. *Progress in Metal Physics* **1959**, *8*, 147–202, doi:10.1016/0502-8205(59)90015-2.
173. Dasgupta, P. On Use of Pseudo-Voigt Profiles in Diffraction Line Broadening Analysis. *FIZIKA A-ZAGREB* **2000**, *9*, 61–66.
174. de Keijser, T.; Mittemeijer, E.J.; Rozendaal, H.C.F. The Determination of Crystallite-Size and Lattice-Strain Parameters in Conjunction with the Profile-Refinement Method for the Determination of Crystal Structures. *J Appl Cryst* **1983**, *16*, 309–316, doi:10.1107/S0021889883010493.
175. Wertheim, G.K.; Butler, M.A.; West, K.W.; Buchanan, D.N.E. Determination of the Gaussian and Lorentzian Content of Experimental Line Shapes. *Review of Scientific Instruments* **1974**, *45*, 1369–1371, doi:10.1063/1.1686503.
176. The Principles of Diffraction Analysis. In *Industrial Applications of X-Ray Diffraction*; CRC Press, 1999 ISBN 978-0-429-17771-2.
177. Smith, D.K.; Johnson, G.G.; Scheible, A.; Wims, A.M.; Johnson, J.L.; Ullmann, G. Quantitative X-Ray Powder Diffraction Method Using the Full Diffraction Pattern. *Powder Diffraction* **1987**, *2*, 73–77, doi:10.1017/S0885715600012409.
178. Toraya, H.; Tsusaka, S. Quantitative Phase Analysis Using the Whole-Powder-Pattern Decomposition Method. I. Solution from Knowledge of Chemical Compositions. *J Appl Cryst* **1995**, *28*, 392–399, doi:10.1107/S0021889894014986.
179. Cressey, G.; Schofield, P.F. Rapid Whole-Pattern Profile-Stripping Method for the Quantification of Multiphase Samples. *Powder Diffraction* **1996**, *11*, 35–39, doi:10.1017/S0885715600008885.
180. Lábár, J.L.; Adamik, M. ProcessDiffraction VI.2: New Possibilities in Manipulating Electron Diffraction Ring Patterns. *Microscopy and Microanalysis* **2001**, *7*, 372–373, doi:10.1017/S1431927600027938.
181. Moeck, P.; Rouvimov, S. Precession Electron Diffraction and Its Advantages for Structural Fingerprinting in the Transmission Electron Microscope. *Zeitschrift für Kristallographie* **2010**, *225*, 110–124, doi:10.1524/zkri.2010.1162.
182. Crystallography Open Database Available online: <http://www.crystallography.net/cod/> (accessed on 14 November 2022).
183. American Mineralogist Crystal Structure Database Available online: <http://ruff.geo.arizona.edu/AMS/amcsd.php> (accessed on 14 November 2022).
184. PDF-2 – ICDD.
185. PDF-4+ – ICDD.
186. *International Tables for Crystallography, Volume C*;
187. Peng, L.-M.; Ren, G.; Dudarev, S.L.; Whelan, M.J. Robust Parameterization of Elastic and Absorptive Electron Atomic Scattering Factors. *Acta Cryst A* **1996**, *52*, 257–276, doi:10.1107/S0108767395014371.

188. Lábár, J.; Adamik, M.; Barna B., P.; Czigány, Z.; Fogarassy, Z.; Horváth, Z.E.; Geszti, O.; Misják, F.; Radnóczy, G.; Sáfrán, G.; et al. Electron Diffraction Based Analysis of Phase Fractions and Texture in Nanocrystalline Thin Films, Part III: Application Examples. *MICROSCOPY AND MICROANALYSIS* **2012**, *18*, 406–420.
189. Le Bail, A.; Duroy, H.; Fourquet, J.L. Ab-Initio Structure Determination of LiSbWO₆ by X-Ray Powder Diffraction. *Materials Research Bulletin* **1988**, *23*, 447–452, doi:10.1016/0025-5408(88)90019-0.
190. Toby, B.H. Estimating Observed Structure Factors without a Structure. **2019**.
191. Whole Pattern Fitting: II. LeBail Method Available online: <http://pd.chem.ucl.ac.uk/pdnn/solve1/lebaill.htm> (accessed on 31 January 2023).
192. Maud – Materials Analysis Using Diffraction.
193. Xu, P.G.; Tomota, Y.; Arakaki, Y.; Harjo, S.; Sueyoshi, H. Evaluation of Austenite Volume Fraction in TRIP Steel Sheets Using Neutron Diffraction. *Materials Characterization* **2017**, *127*, 104–110, doi:10.1016/j.matchar.2017.02.028.
194. Saville, A.I.; Creuziger, A.; Mitchell, E.B.; Vogel, S.C.; Benzing, J.T.; Klemm-Toole, J.; Clarke, K.D.; Clarke, A.J. MAUD Rietveld Refinement Software for Neutron Diffraction Texture Studies of Single- and Dual-Phase Materials. *Integr Mater Manuf Innov* **2021**, *10*, 461–487, doi:10.1007/s40192-021-00224-5.
195. Xie, Y.; Lutterotti, L.; Wenk, H.R.; Kovacs, F. Texture Analysis of Ancient Coins with TOF Neutron Diffraction. *Journal of Materials Science* **2004**, *39*, 3329–3337, doi:10.1023/B:JMSC.0000026933.28906.19.
196. Wenk, H.-R.; Lutterotti, L.; Vogel, S.C. Rietveld Texture Analysis from TOF Neutron Diffraction Data. *Powder Diffraction* **2010**, *25*, 283–296, doi:10.1154/1.3479004.
197. Lutterotti, L.; Matthies, S.; Chateigner, D.; Ferrari, S.; Ricote, J. Rietveld Texture and Stress Analysis of Thin Films by X-Ray Diffraction. In Proceedings of the Materials Science Forum; Transtec Publications; 1999, 2002; Vol. 408, pp. 1603–1608.
198. Lutterotti, L. Total Pattern Fitting for the Combined Size–Strain–Stress–Texture Determination in Thin Film Diffraction. *Nuclear Instruments and Methods in Physics Research Section B: Beam Interactions with Materials and Atoms* **2010**, *268*, 334–340, doi:10.1016/j.nimb.2009.09.053.
199. Wenk, H.-R.; Lutterotti, L.; Kaercher, P.; Kanitpanyacharoen, W.; Miyagi, L.; Vasin, R. Rietveld Texture Analysis from Synchrotron Diffraction Images. II. Complex Multiphase Materials and Diamond Anvil Cell Experiments. *Powder Diffraction* **2014**, *29*, 220–232, doi:10.1017/S0885715614000360.
200. Lutterotti, L.; Dell'Amore, F.; Angelucci, D.E.; Carrer, F.; Gialanella, S. Combined X-Ray Diffraction and Fluorescence Analysis in the Cultural Heritage Field. *Microchemical Journal* **2016**, *126*, 423–430, doi:10.1016/j.microc.2015.12.031.
201. Minor, A. Introduction to Focused Ion Beams: Instrumentation, Theory, Techniques and Practice By Lucille A. Giannuzzi and Fred A. Stevie Springer, New York, 2005 ISBN 038723116-1; Hard Cover; 347 Pages, \$79.95. *Scanning* **2005**, *27*, 56–56, doi:10.1002/sca.4950270109.
202. Ayache, J.; Beauquier, L.; Boumendil, J.; Ehret, G.; Laub, D. *Sample Preparation Handbook for Transmission Electron Microscopy*; Springer: New York, NY, 2010; ISBN 978-1-4419-5974-4.
203. Capannelli, G.; Castello, E.; Comite, A.; Costa, C.; Mamolini, G. Electron Microscopy Characterization of Airborne Micro- and Nanoparticulate Matter. *J Electron Microscop (Tokyo)* **2011**, *60*, 117–131, doi:10.1093/jmicro/df001.

204. Marvanová, S.; Kulich, P.; Skoupý, R.; Hubatka, F.; Ciganek, M.; Bendl, J.; Hovorka, J.; Machala, M. Size-Segregated Urban Aerosol Characterization by Electron Microscopy and Dynamic Light Scattering and Influence of Sample Preparation. *Atmospheric Environment* **2018**, *178*, 181–190, doi:10.1016/j.atmosenv.2018.02.004.
205. Sielicki, P.; Janik, H.; Guzman, A.; Namieśnik, J. The Progress in Electron Microscopy Studies of Particulate Matters to Be Used as a Standard Monitoring Method for Air Dust Pollution. *Critical Reviews in Analytical Chemistry* **2011**, *41*, 314–334, doi:10.1080/10408347.2011.607076.
206. Jones, T.; Moreno, T.; BéruBé, K.; Richards, R. The Physicochemical Characterisation of Microscopic Airborne Particles in South Wales: A Review of the Locations and Methodologies. *Science of The Total Environment* **2006**, *360*, 43–59, doi:10.1016/j.scitotenv.2005.08.055.
207. Sinha, A.; Ischia, G.; Straffelini, G.; Gialanella, S. A New Sample Preparation Protocol for SEM and TEM Particulate Matter Analysis. *Ultramicroscopy* **2021**, *230*, 113365, doi:10.1016/j.ultramic.2021.113365.
208. Candeo, S.; Nogueira, A.P.; Leonardi, M.; Straffelini, G. A Study of Friction, Wear and Particulate Emissions during the Bedding Stage of a Cu-Free Friction Material. *Wear* **2021**, *486–487*, 204095, doi:10.1016/j.wear.2021.204095.
209. Michen, B.; Geers, C.; Vanhecke, D.; Endes, C.; Rothen-Rutishauser, B.; Balog, S.; Petri-Fink, A. Avoiding Drying-Artifacts in Transmission Electron Microscopy: Characterizing the Size and Colloidal State of Nanoparticles. *Sci Rep* **2015**, *5*, 9793, doi:10.1038/srep09793.
210. Forman, H.J.; Finch, C.E. A Critical Review of Assays for Hazardous Components of Air Pollution. *Free Radical Biology and Medicine* **2018**, *117*, 202–217, doi:10.1016/j.freeradbiomed.2018.01.030.
211. World Health Organization. Regional Office for Europe *Health Effects of Particulate Matter: Policy Implications for Countries in Eastern Europe, Caucasus and Central Asia*; World Health Organization. Regional Office for Europe, 2013; ISBN 978-92-890-0001-7.
212. Hughes, L.S.; Cass, G.R.; Gone, J.; Ames, M.; Olmze, I. Physical and Chemical Characterization of Atmospheric Ultrafine Particles in the Los Angeles Area. *Environmental Science and Technology* **1998**, *32*, 1153–1161, doi:10.1021/es970280r.
213. Ja, S.; J, S.; Hh, S. Fine Particulate Air Pollution and Mortality in 20 U.S. Cities. *N Engl J Med* **2001**, *344*, 1253–1254, doi:10.1056/nejm200104193441614.
214. Ghio, A.J. Disruption of Iron Homeostasis and Lung Disease. *Biochimica et Biophysica Acta (BBA) - General Subjects* **2009**, *1790*, 731–739, doi:10.1016/j.bbagen.2008.11.004.
215. Almetwally, A.A.; Bin-Jumah, M.; Allam, A.A. Ambient Air Pollution and Its Influence on Human Health and Welfare: An Overview. *Environ Sci Pollut Res* **2020**, *27*, 24815–24830, doi:10.1007/s11356-020-09042-2.
216. Copper-Free Brake Initiative Available online: <https://www.epa.gov/npdes/copper-free-brake-initiative> (accessed on 8 September 2020).
217. Straffelini, G.; Ciudin, R.; Ciotti, A.; Gialanella, S. Present Knowledge and Perspectives on the Role of Copper in Brake Materials and Related Environmental Issues: A Critical Assessment. *Environmental Pollution* **2015**, *207*, 211–219, doi:10.1016/j.envpol.2015.09.024.
218. European Union Emission Inventory Report 1990–2018 — European Environment Agency Available online: <https://www.eea.europa.eu/publications/european-union-emission-inventory-report-1990-2018> (accessed on 30 October 2020).

219. Mathissen, M.; Grochowicz, J.; Schmidt, C.; Vogt, R.; Farwick zum Hagen, F.H.; Grabiec, T.; Steven, H.; Grigoratos, T. A Novel Real-World Braking Cycle for Studying Brake Wear Particle Emissions. *Wear* **2018**, *414–415*, 219–226, doi:10.1016/j.wear.2018.07.020.
220. Farwick zum Hagen, F.H.; Mathissen, M.; Grabiec, T.; Hennicke, T.; Rettig, M.; Grochowicz, J.; Vogt, R.; Benter, T. On-Road Vehicle Measurements of Brake Wear Particle Emissions. *Atmospheric Environment* **2019**, *217*, 116943, doi:10.1016/j.atmosenv.2019.116943.
221. Verma, P.C.; Ciudin, R.; Bonfanti, A.; Aswath, P.; Straffelini, G.; Gialanella, S. Role of the Friction Layer in the High-Temperature Pin-on-Disc Study of a Brake Material. *Wear* **2016**, *346–347*, 56–65, doi:10.1016/j.wear.2015.11.004.
222. Menapace, C.; Leonardi, M.; Perricone, G.; Bortolotti, M.; Straffelini, G.; Gialanella, S. Pin-on-Disc Study of Brake Friction Materials with Ball-Milled Nanostructured Components. *Materials & Design* **2017**, *115*, 287–298, doi:10.1016/j.matdes.2016.11.065.
223. Perricone, G.; Matějka, V.; Alemani, M.; Valota, G.; Bonfanti, A.; Ciotti, A.; Olofsson, U.; Söderberg, A.; Wahlström, J.; Nosko, O.; et al. A Concept for Reducing PM10 Emissions for Car Brakes by 50%. *Wear* **2018**, *396–397*, 135–145, doi:10.1016/j.wear.2017.06.018.
224. Sinha, A.; Ischia, G.; Menapace, C.; Gialanella, S. Experimental Characterization Protocols for Wear Products from Disc Brake Materials. *Atmosphere* **2020**, *11*, 1102, doi:10.3390/atmos11101102.
225. Stratton, W.G.; Buckett, M.I.; McKernan, S. Procedure for TEM Measurement of Nanoparticles. *Microscopy and Microanalysis* **2013**, *19*, 1098–1099, doi:10.1017/S1431927613007484.
226. Schlieper, G.; Aretz, A.; Verberckmoes, S.C.; Krüger, T.; Behets, G.J.; Ghadimi, R.; Weirich, T.E.; Rohmann, D.; Langer, S.; Tordoir, J.H.; et al. Ultrastructural Analysis of Vascular Calcifications in Uremia. *JASN* **2010**, *21*, 689–696, doi:10.1681/ASN.2009080829.
227. Horstmann, M.; Meyer, G. Messung der elastischen Elektronenbeugungsintensitäten polykristalliner Aluminium-Schichten. *Acta Cryst* **1962**, *15*, 271–281, doi:10.1107/S0365110X62000638.
228. Luo, Z.; Vasquez, Y.; Bondi, J.F.; Schaak, R.E. Pawley and Rietveld Refinements Using Electron Diffraction from L12-Type Intermetallic Au3Fe1-x Nanocrystals during Their in-Situ Order-Disorder Transition. *Ultramicroscopy* **2011**, *111*, 1295–1304, doi:10.1016/j.ultramic.2011.04.003.
229. Scardi, P.; Lutterotti, L.; Maistrelli, P. Experimental Determination of the Instrumental Broadening in the Bragg-Brentano Geometry. *Powder Diffraction* **1994**, *9*, 180–186, doi:10.1017/S0885715600019187.
230. Ida, T.; Toraya, H. Deconvolution of the Instrumental Functions in Powder X-Ray Diffractometry. *J Appl Cryst* **2002**, *35*, 58–68, doi:10.1107/S0021889801018945.
231. Chateigner, D. Quantitative Microstructure Analysis. In *Combined Analysis*; John Wiley & Sons, Ltd London: ISTE-Wiley., 2013; pp. 191–220 ISBN 978-1-118-62250-6.
232. Balzar, D. Voigt-Function Model in Diffraction Line-Broadening Analysis. *International union of crystallography monographs on crystallography* **1999**, *10*, 94–126.
233. Scardi, P.; Leoni, M.; Delhez, R. Line Broadening Analysis Using Integral Breadth Methods: A Critical Review. *J Appl Cryst* **2004**, *37*, 381–390, doi:10.1107/S0021889804004583.
234. Taupin, D. Automatic Peak Determination in X-Ray Powder Patterns. *J Appl Cryst* **1973**, *6*, 266–273, doi:10.1107/S0021889873008666.
235. Scardi, P.; Leoni, M. Line Profile Analysis: Pattern Modelling versus Profile Fitting. *J Appl Cryst* **2006**, *39*, 24–31, doi:10.1107/S0021889805032978.

236. Soleimanian, V.; Aghdaee, S.R. Comparison Methods of Variance and Line Profile Analysis for the Evaluation of Microstructures of Materials. *Powder Diffraction* **2008**, *23*, 41–51, doi:10.1154/1.2888763.
237. Young, R.A.; Wiles, D.B. Profile Shape Functions in Rietveld Refinements. *J Appl Cryst* **1982**, *15*, 430–438, doi:10.1107/S002188988201231X.
238. Jagodzinski, H. H. P. Klug Und L. E. Alexander: X-Ray Diffraction Procedures for Polycrystalline and Amorphous Materials, 2. Auflage. John Wiley & Sons, New York-Sydney-Toronto 1974, 966 Seiten, Preis: £ 18.55. *Berichte der Bunsengesellschaft für physikalische Chemie* **1975**, *79*, 553–553, doi:10.1002/bbpc.19750790622.
239. Ischia, G.; Wenk, H.-R.; Lutterotti, L.; Berberich, F. Quantitative Rietveld Texture Analysis of Zirconium from Single Synchrotron Diffraction Images. *J Appl Cryst* **2005**, *38*, 377–380, doi:10.1107/S0021889805006059.
240. Andrews, K.W.; Dyson, D.J.; Keown, S.R. *Interpretation of Electron Diffraction Patterns*; Springer, 1971; Vol. 202:.
241. Li, X.Z. PCED2.0—A Computer Program for the Simulation of Polycrystalline Electron Diffraction Pattern. *Ultramicroscopy* **2010**, *110*, 297–304, doi:10.1016/j.ultramic.2009.12.009.
242. McCaffrey, J.P.; Baribeau, J.-M. A Transmission Electron Microscope (TEM) Calibration Standard Sample for All Magnification, Camera Constant, and Image/Diffraction Pattern Rotation Calibrations. *Microscopy Research and Technique* **1995**, *32*, 449–454, doi:10.1002/jemt.1070320507.
243. Popa, N.C. The (Hkl) Dependence of Diffraction-Line Broadening Caused by Strain and Size for All Laue Groups in Rietveld Refinement. *J Appl Cryst* **1998**, *31*, 176–180, doi:10.1107/S0021889897009795.
244. Verma, P.C.; Alemani, M.; Gialanella, S.; Lutterotti, L.; Olofsson, U.; Straffelini, G. Wear Debris from Brake System Materials: A Multi-Analytical Characterization Approach. *Tribology International* **2016**, *94*, 249–259, doi:10.1016/j.triboint.2015.08.011.
245. Hajizadeh-Oghaz, M.; Razavi, R.S.; Barekat, M.; Naderi, M.; Malekzadeh, S.; Rezazadeh, M. Synthesis and Characterization of Y2O3 Nanoparticles by Sol–Gel Process for Transparent Ceramics Applications. *J Sol-Gel Sci Technol* **2016**, *78*, 682–691, doi:10.1007/s10971-016-3986-3.
246. B.r., V.K.; Dasgupta, A.; Ghosh, C.; Sinha, S.K. Analysis of Structural Transformation in Nanocrystalline Y2O3 during High Energy Ball Milling. *Journal of Alloys and Compounds* **2022**, *900*, 163550, doi:10.1016/j.jallcom.2021.163550.
247. Miller, R.A. Thermal Barrier Coatings for Aircraft Engines: History and Directions. *JTST* **1997**, *6*, 35–42, doi:10.1007/BF02646310.
248. Badehian, H.A.; Salehi, H.; Ghoohestani, M. First-Principles Study of Elastic, Structural, Electronic, Thermodynamical, and Optical Properties of Yttria (Y2O3) Ceramic in Cubic Phase. *Journal of the American Ceramic Society* **2013**, *96*, 1832–1840, doi:10.1111/jace.12259.
249. Lu, J.; Takaichi, K.; Uematsu, T.; Shirakawa, A.; Musha, M.; Ueda, K.; Yagi, H.; Yanagitani, T.; Kaminskii, A.A. Yb3+:Y2O3 Ceramics – a Novel Solid-State Laser Material. *Jpn. J. Appl. Phys.* **2002**, *41*, L1373, doi:10.1143/JJAP.41.L1373.
250. Majumdar, D.; Chatterjee, D. X-ray Photoelectron Spectroscopic Studies on Yttria, Zirconia, and Yttria-stabilized Zirconia. *Journal of Applied Physics* **1991**, *70*, 988–992, doi:10.1063/1.349611.

251. Husson, E.; Proust, C.; Gillet, P.; Itié, J.P. Phase Transitions in Yttrium Oxide at High Pressure Studied by Raman Spectroscopy. *Materials Research Bulletin* **1999**, *34*, 2085–2092, doi:10.1016/S0025-5408(99)00205-6.
252. Gajović, A.; Tomašić, N.; Djerdj, I.; Su, D.S.; Furić, K. Influence of Mechanochemical Processing to Luminescence Properties in Y2O3 Powder. *Journal of Alloys and Compounds* **2008**, *456*, 313–319, doi:10.1016/j.jallcom.2007.02.083.
253. Ning, K.; Wang, J.; Luo, D.; Dong, Z.L.; Kong, L.B.; Tang, D.Y. Low-Level Sintering Aids for Highly Transparent Yb:Y2O3 Ceramics. *Journal of Alloys and Compounds* **2017**, *695*, 1414–1419, doi:10.1016/j.jallcom.2016.10.267.
254. Kocevski, V.; Eriksson, O.; Rusz, J. Transition between Direct and Indirect Band Gap in Silicon Nanocrystals. *Phys. Rev. B* **2013**, *87*, 245401, doi:10.1103/PhysRevB.87.245401.
255. Ni, Z.; Zhou, S.; Zhao, S.; Peng, W.; Yang, D.; Pi, X. Silicon Nanocrystals: Unfading Silicon Materials for Optoelectronics. *Materials Science and Engineering: R: Reports* **2019**, *138*, 85–117, doi:10.1016/j.mser.2019.06.001.
256. Hessel, C.M.; Reid, D.; Panthani, M.G.; Rasch, M.R.; Goodfellow, B.W.; Wei, J.; Fujii, H.; Akhavan, V.; Korgel, B.A. Synthesis of Ligand-Stabilized Silicon Nanocrystals with Size-Dependent Photoluminescence Spanning Visible to Near-Infrared Wavelengths. *Chem. Mater.* **2012**, *24*, 393–401, doi:10.1021/cm2032866.
257. Dasog, M.; De los Reyes, G.B.; Titova, L.V.; Hegmann, F.A.; Veinot, J.G.C. Size vs Surface: Tuning the Photoluminescence of Freestanding Silicon Nanocrystals Across the Visible Spectrum via Surface Groups. *ACS Nano* **2014**, *8*, 9636–9648, doi:10.1021/nn504109a.
258. Greben, M.; Khoroshyy, P.; Liu, X.; Pi, X.; Valenta, J. Fully Radiative Relaxation of Silicon Nanocrystals in Colloidal Ensemble Revealed by Advanced Treatment of Decay Kinetics. *Journal of Applied Physics* **2017**, *122*, 034304, doi:10.1063/1.4993584.
259. Su, Y.; Wang, C.; Hong, Z.; Sun, W. Thermal Disproportionation for the Synthesis of Silicon Nanocrystals and Their Photoluminescent Properties. *Frontiers in Chemistry* **2021**, *9*.
260. Richter, H.; Wang, Z.P.; Ley, L. The One Phonon Raman Spectrum in Microcrystalline Silicon. *Solid State Communications* **1981**, *39*, 625–629, doi:10.1016/0038-1098(81)90337-9.
261. Meier, C.; Lüttjohann, S.; Kravets, V.G.; Nienhaus, H.; Lorke, A.; Wiggers, H. Raman Properties of Silicon Nanoparticles. *Physica E: Low-dimensional Systems and Nanostructures* **2006**, *32*, 155–158, doi:10.1016/j.physe.2005.12.030.
262. Köthemann, R.; Weber, N.; Lindner, J.K.N.; Meier, C. High-Precision Determination of Silicon Nanocrystals: Optical Spectroscopy versus Electron Microscopy. *Semicond. Sci. Technol.* **2019**, *34*, 095009, doi:10.1088/1361-6641/ab3536.
263. Leal, J.H.; Cantu, Y.; Gonzalez, D.F.; Parsons, J.G. Brookite and Anatase Nanomaterial Polymorphs of TiO2 Synthesized from TiCl3. *Inorganic Chemistry Communications* **2017**, *84*, 28–32, doi:10.1016/j.inoche.2017.07.014.
264. Lee, S.; Drwiega, J.; Wu, C.-Y.; Mazyck, D.; Sigmund, W.M. Anatase TiO2 Nanoparticle Coating on Barium Ferrite Using Titanium Bis-Ammonium Lactato Dihydroxide and Its Use as a Magnetic Photocatalyst. *Chem. Mater.* **2004**, *16*, 1160–1164, doi:10.1021/cm0351902.
265. Leyva-Porras, C.; Toxqui-Teran, A.; Vega-Becerra, O.; Miki-Yoshida, M.; Rojas-Villalobos, M.; García-Guaderrama, M.; Aguilar-Martínez, J.A. Low-Temperature Synthesis and Characterization of Anatase TiO2 Nanoparticles by an Acid Assisted Sol–Gel Method. *Journal of Alloys and Compounds* **2015**, *647*, 627–636, doi:10.1016/j.jallcom.2015.06.041.

266. McNeil, L.E.; French, R.H. Multiple Scattering from Rutile TiO₂ Particles. *Acta Materialia* **2000**, *48*, 4571–4576, doi:10.1016/S1359-6454(00)00243-3.
267. Dhage, S.R.; Choube, V.D.; Samuel, V.; Ravi, V. Synthesis of Nanocrystalline TiO₂ at 100 °C. *Materials Letters* **2004**, *58*, 2310–2313, doi:10.1016/j.matlet.2004.02.021.
268. Hu, W.; Li, L.; Li, G.; Tang, C.; Sun, L. High-Quality Brookite TiO₂ Flowers: Synthesis, Characterization, and Dielectric Performance. *Crystal Growth & Design* **2009**, *9*, 3676–3682, doi:10.1021/cg9004032.
269. Pourjafari, D.; Reyes-Coronado, D.; Vega-Poot, A.; Escalante, R.; Kirkconnell-Reyes, D.; García-Rodríguez, R.; Anta, J.A.; Oskam, G. Brookite-Based Dye-Sensitized Solar Cells: Influence of Morphology and Surface Chemistry on Cell Performance. *J. Phys. Chem. C* **2018**, *122*, 14277–14288, doi:10.1021/acs.jpcc.8b02384.
270. Yu, H.; Yu, J.; Cheng, B.; Zhou, M. Effects of Hydrothermal Post-Treatment on Microstructures and Morphology of Titanate Nanoribbons. *Journal of Solid State Chemistry* **2006**, *179*, 349–354, doi:10.1016/j.jssc.2005.10.024.
271. Luca, V. Comparison of Size-Dependent Structural and Electronic Properties of Anatase and Rutile Nanoparticles. *J. Phys. Chem. C* **2009**, *113*, 6367–6380, doi:10.1021/jp808358v.
272. Tonejc, A.M.; Djerdj, I.; Tonejc, A. An Analysis of Evolution of Grain Size-Lattice Parameters Dependence in Nanocrystalline TiO₂ Anatase. *Materials Science and Engineering: C* **2002**, *19*, 85–89, doi:10.1016/S0928-4931(01)00447-7.
273. Djerdj, I.; Tonejc, A.M. Structural Investigations of Nanocrystalline TiO₂ Samples. *Journal of Alloys and Compounds* **2006**, *413*, 159–174, doi:10.1016/j.jallcom.2005.02.105.
274. Grigoratos, T.; Martini, G. Brake Wear Particle Emissions: A Review. *Environ Sci Pollut Res* **2015**, *22*, 2491–2504, doi:10.1007/s11356-014-3696-8.
275. Kukutschová, J.; Moravec, P.; Tomášek, V.; Matějka, V.; Smolík, J.; Schwarz, J.; Seidlerová, J.; Šafařová, K.; Filip, P. On Airborne Nano/Micro-Sized Wear Particles Released from Low-Metallic Automotive Brakes. *Environmental Pollution* **2011**, *159*, 998–1006, doi:10.1016/j.envpol.2010.11.036.
276. Alemani, M.; Nosko, O.; Metinoz, I.; Olofsson, U. A Study on Emission of Airborne Wear Particles from Car Brake Friction Pairs. *SAE International Journal of Materials and Manufacturing* **2016**, *9*, 147–157.
277. Cavallo, G.; Ischia, G.; Zorzini, R.; Gialanella, S. Experimental Analysis on Natural Heated Goethite from Ponte Di Veja (Mt Lessini, NE Italy). *Journal of Archaeological Science: Reports* **2021**, *36*, 102871, doi:10.1016/j.jasrep.2021.102871.
278. Pomiés, M.-P.; Menu, M.; Vignaud, C. Red Palaeolithic Pigments: Natural Hematite or Heated Goethite*. *Archaeometry* **1999**, *41*, 275–285, doi:10.1111/j.1475-4754.1999.tb00983.x.
279. Salomon, H.; Vignaud, C.; Lahlii, S.; Menguy, N. Solutrean and Magdalenian Ferruginous Rocks Heat-Treatment: Accidental and/or Deliberate Action? *Journal of Archaeological Science* **2015**, *55*, 100–112, doi:10.1016/j.jas.2014.12.024.
280. Löffler, L.; Mader, W. Anisotropic X-Ray Peak Broadening and Twin Formation in Hematite Derived from Natural and Synthetic Goethite. *Journal of the European Ceramic Society* **2006**, *26*, 131–139, doi:10.1016/j.jeurceramsoc.2004.09.032.
281. Gialanella, S.; Belli, R.; Dalmeri, G.; Lonardelli, I.; Mattarelli, M.; Montagna, M.; Toniutti, L. Artificial or Natural Origin of Hematite-Based Red Pigments in Archaeological Contexts: The Case of Riparo Dalmeri (Trento, Italy). *Archaeometry* **2011**, *53*, 950–962, doi:10.1111/j.1475-4754.2011.00594.x.

282. Tsubota, M.; Kitagawa, J. A Necessary Criterion for Obtaining Accurate Lattice Parameters by Rietveld Method. *Sci Rep* **2017**, *7*, 15381, doi:10.1038/s41598-017-15766-y.
283. Monge, M.; Kahn, M.L.; Maisonnat, A.; Chaudret, B. Room-Temperature Organometallic Synthesis of Soluble and Crystalline ZnO Nanoparticles of Controlled Size and Shape. *Angewandte Chemie International Edition* **2003**, *42*, 5321–5324, doi:10.1002/anie.200351949.
284. Metal Oxide Chemistry and Synthesis: From Solution to Solid State | Wiley Available online: <https://www.wiley.com/en-us/Metal+Oxide+Chemistry+and+Synthesis%3A+From+Solution+to+Solid+State-p-9780471970569> (accessed on 27 April 2022).
285. Gardner, D.F.; Evans, J.S.; Smalyukh, I.I. Towards Reconfigurable Optical Metamaterials: Colloidal Nanoparticle Self-Assembly and Self-Alignment in Liquid Crystals. *Molecular Crystals and Liquid Crystals* **2011**, *545*, 3/[1227]-21/[1245], doi:10.1080/15421406.2011.571966.
286. Kahn, M.L.; Monge, M.; Collière, V.; Senocq, F.; Maisonnat, A.; Chaudret, B. Size- and Shape-Control of Crystalline Zinc Oxide Nanoparticles: A New Organometallic Synthetic Method. *Advanced Functional Materials* **2005**, *15*, 458–468, doi:10.1002/adfm.200400113.
287. Chaudret, B. Organometallic Approach to Nanoparticles Synthesis and Self-Organization. *Comptes Rendus Physique* **2005**, *6*, 117–131, doi:10.1016/j.crhy.2004.11.008.
288. Ashby, M.F.; Ferreira, P.J.; Schodek, D.L. Chapter 6 - Nanomaterials: Classes and Fundamentals. In *Nanomaterials, Nanotechnologies and Design*; Ashby, M.F., Ferreira, P.J., Schodek, D.L., Eds.; Butterworth-Heinemann: Boston, 2009; pp. 177–197 ISBN 978-0-7506-8149-0.
289. Ulvestad, A.; Yau, A. The Self-Healing of Defects Induced by the Hydriding Phase Transformation in Palladium Nanoparticles. *Nat Commun* **2017**, *8*, 1376, doi:10.1038/s41467-017-01548-7.
290. Mi, J.-L.; Clausen, C.; Bremholm, M.; Lock, N.; Jensen, K.M.Ø.; Christensen, M.; Iversen, B.B. Rapid Hydrothermal Preparation of Rutile TiO₂ Nanoparticles by Simultaneous Transformation of Primary Brookite and Anatase: An in Situ Synchrotron PXRD Study. *Crystal Growth & Design* **2012**, *12*, 6092–6097, doi:10.1021/cg301230w.
291. Balzar, D.; Popa, N.C. Crystallite Size and Residual Strain/Stress Modeling in Rietveld Refinement. In *Diffraction Analysis of the Microstructure of Materials*; Mittemeijer, E.J., Scardi, P., Eds.; Springer Series in Materials Science; Springer: Berlin, Heidelberg, 2004; pp. 125–145 ISBN 978-3-662-06723-9.
292. Trueblood, K.N.; Bürgi, H.-B.; Burzlaff, H.; Dunitz, J.D.; Gramaccioli, C.M.; Schulz, H.H.; Shmueli, U.; Abrahams, S.C. Atomic Displacement Parameter Nomenclature. Report of a Subcommittee on Atomic Displacement Parameter Nomenclature. *Acta Cryst A* **1996**, *52*, 770–781, doi:10.1107/S0108767396005697.
293. Stott, F.H. The Role of Oxidation in the Wear of Alloys. *Tribology International* **1998**, *31*, 61–71, doi:10.1016/S0301-679X(98)00008-5.
294. Straffelini, G.; Trabucco, D.; Molinari, A. Oxidative Wear of Heat-Treated Steels. *Wear* **2001**, *250*, 485–491, doi:10.1016/S0043-1648(01)00661-5.
295. Schimanke, G.; Martin, M. In Situ XRD Study of the Phase Transition of Nanocrystalline Maghemite (γ -Fe₂O₃) to Hematite (α -Fe₂O₃). *Solid State Ionics* **2000**, *136–137*, 1235–1240, doi:10.1016/S0167-2738(00)00593-2.
296. Cornell, R.M.; Schwertmann, U. *The Iron Oxides: Structure, Properties, Reactions, Occurrences and Uses*; John Wiley & Sons, 2003; ISBN 978-3-527-30274-1.

297. Cavallo, G.; Ischia, G.; Zorzin, R.; Gialanella, S. Experimental Analysis on Natural Heated Goethite from Ponte Di Veja (Mt Lessini, NE Italy). *Journal of Archaeological Science: Reports* **2021**, *36*, 102871, doi:10.1016/j.jasrep.2021.102871.
298. Schwartz, L.H.; Cohen, J.B. *Diffraction from Materials*; Springer Science & Business Media, 2013;
299. Shiju, N.R.; Gulians, V.V. Recent Developments in Catalysis Using Nanostructured Materials. *Applied Catalysis A: General* **2009**, *356*, 1–17, doi:10.1016/j.apcata.2008.11.034.
300. Kopp Alves, A.; Bergmann, C.P.; Berutti, F.A. Introduction. In *Novel Synthesis and Characterization of Nanostructured Materials*; Kopp Alves, A., Bergmann, C.P., Berutti, F.A., Eds.; Engineering Materials; Springer: Berlin, Heidelberg, 2013; pp. 1–9 ISBN 978-3-642-41275-2.
301. Das, P.P.; Mugnaioli, E.; Nicolopoulos, S.; Tossi, C.; Gemmi, M.; Galanis, A.; Borodi, G.; Pop, M.M. Crystal Structures of Two Important Pharmaceuticals Solved by 3D Precession Electron Diffraction Tomography. *Org. Process Res. Dev.* **2018**, *22*, 1365–1372, doi:10.1021/acs.oprd.8b00149.
302. Holder, C.F.; Schaak, R.E. Tutorial on Powder X-Ray Diffraction for Characterizing Nanoscale Materials. *ACS Nano* **2019**, *13*, 7359–7365, doi:10.1021/acsnano.9b05157.
303. Khan, H.; Yerramilli, A.S.; D'Oliveira, A.; Alford, T.L.; Boffito, D.C.; Patience, G.S. Experimental Methods in Chemical Engineering: X-Ray Diffraction Spectroscopy—XRD. *The Canadian Journal of Chemical Engineering* **2020**, *98*, 1255–1266, doi:10.1002/cjce.23747.
304. Bortolotti, M.; Lutterotti, L.; Pepponi, G. Combining XRD and XRF Analysis in One Rietveld-like Fitting. *Powder Diffraction* **2017**, *32*, S225–S230, doi:10.1017/S0885715617000276.
305. Secchi, M.; Zanatta, M.; Borovin, E.; Bortolotti, M.; Kumar, A.; Giarola, M.; Sanson, A.; Orberger, B.; Daldosso, N.; Gialanella, S.; et al. Mineralogical Investigations Using XRD, XRF, and Raman Spectroscopy in a Combined Approach. *Journal of Raman Spectroscopy* **2018**, *49*, 1023–1030, doi:10.1002/jrs.5386.
306. Cobalt Iron Oxide (CoFe₂O₄) Nanopowder/Nanoparticles, Purity: 99.5+%, Size: 30 Nm Available online: <https://nanografi.com/nanoparticles/cobalt-iron-oxide-cofe2o4-nanopowder-nanoparticles-purity-99-5-size-30-nm/> (accessed on 11 January 2023).
307. Zubair, A.; Ahmad, Z.; Mahmood, A.; Cheong, W.-C.; Ali, I.; Khan, M.A.; Chughtai, A.H.; Ashiq, M.N. Structural, Morphological and Magnetic Properties of Eu-Doped CoFe₂O₄ Nano-Ferrites. *Results in Physics* **2017**, *7*, 3203–3208, doi:10.1016/j.rinp.2017.08.035.
308. Rafferty, A.; Prescott, T.; Brabazon, D. Sintering Behaviour of Cobalt Ferrite Ceramic. *Ceramics International* **2008**, *34*, 15–21, doi:10.1016/j.ceramint.2006.07.012.
309. Mohaideen, K.K.; Joy, P.A. Enhancement in the Magnetostriction of Sintered Cobalt Ferrite by Making Self-Composites from Nanocrystalline and Bulk Powders. *ACS Appl. Mater. Interfaces* **2012**, *4*, 6421–6425, doi:10.1021/am302053q.
310. Andreu, I.; Natividad, E.; Ravagli, C.; Castro, M.; Baldi, G. Heating Ability of Cobalt Ferrite Nanoparticles Showing Dynamic and Interaction Effects. *RSC Adv.* **2014**, *4*, 28968–28977, doi:10.1039/C4RA02586E.
311. Amiri, S.; Shokrollahi, H. The Role of Cobalt Ferrite Magnetic Nanoparticles in Medical Science. *Materials Science and Engineering: C* **2013**, *33*, 1–8, doi:10.1016/j.msec.2012.09.003.
312. Gunjakar, J.L.; More, A.M.; Shinde, V.R.; Lokhande, C.D. Synthesis of Nanocrystalline Nickel Ferrite (NiFe₂O₄) Thin Films Using Low Temperature Modified Chemical

Method. *Journal of Alloys and Compounds* **2008**, 465, 468–473, doi:10.1016/j.jallcom.2007.10.130.

313. Casino Available online: <https://www.gegi.usherbrooke.ca/casino/What.html> (accessed on 23 November 2022).

314. Win X-Ray - What Is Win X-Ray? Available online: <https://montecarlotooling.mcgill.ca/software/winray/winray.html> (accessed on 23 November 2022).

315. Gauvin, R.; Lifshin, E.; Demers, H.; Horny, P.; Campbell, H. Win X-Ray: A New Monte Carlo Program That Computes X-Ray Spectra Obtained with a Scanning Electron Microscope. *Microscopy and Microanalysis* **2006**, 12, 49–64, doi:10.1017/S143192760600089.

316. Choël, M.; Deboudt, K.; Flament, P. Evaluation of Quantitative Procedures for X-Ray Microanalysis of Environmental Particles. *Microscopy Research and Technique* **2007**, 70, 996–1002, doi:10.1002/jemt.20510.

317. Ebel, H. X-ray tube spectra. *X-Ray Spectrometry* **1999**, 28, 255–266, doi:10.1002/(SICI)1097-4539(199907/08)28:4<255::AID-XRS347>3.0.CO;2-Y.

318. Commission Proposes New Euro 7 Standards Available online: https://ec.europa.eu/commission/presscorner/detail/en/ip_22_6495 (accessed on 2 April 2023).

Publications

- **Sinha, A.**; Ischia, G.; Menapace, C.; Gialanella, S. Experimental Characterization Protocols for Wear Products from Disc Brake Materials. *Atmosphere* 2020, 11, 1102. <https://doi.org/10.3390/atmos11101102>
- **Sinha, A.**; Ischia, G.; Straffelini, G.; Gialanella, S. A New Sample Preparation Protocol for SEM and TEM Particulate Matter Analysis. *Ultramicroscopy* 2021, 230, 113365. doi:10.1016/j.ultramic.2021.113365
- Lyu, Y.; **Sinha, A.**; Olofsson, U.; Gialanella, S.; Wahlström, J. Characterization of Ultrafine Particles from Hardfacing Coated Brake Rotors. *Friction* 2022, doi:10.1007/s40544-021-0585-2.
- Jayashree, P.; **Sinha, A.**; Gialanella, S.; Straffelini, G. Dry Sliding Behavior and Particulate Emissions of a SiC-graphite Composite Friction Material Paired with HVOF-Coated Counterface. *Atmosphere* 2022, 13, 296. <https://doi.org/10.3390/atmos13020296>
- **Sinha, A.**; Bortolotti, M.; Ischia, G.; Lutterotti, L.; Gialanella, S. Electron Diffraction Characterization of Nanocrystalline Materials Using a Rietveld-Based Approach. Part I. Methodology. *J Appl Cryst* 2022, 55, 953–965, doi:10.1107/S1600576722006367.

- **Sinha, A.**; Ischia, G.; Lutterotti, L.; Gialanella, S. Electron Diffraction Characterization of Nanocrystalline Materials Using a Rietveld-Based Approach. Part II. Application to microstructural analysis. *Accepted* in J Appl Cryst 2022.
- **Sinha, A.**; Candeo, S.; Straffelini, G.; Gialanella, S. TEM characterization of particulate matter emissions from the bedding stage of a Cu-free brake friction material. *Tribology International*, 2023 (*In Press*).

Conferences, Workshops, and Schools attended

- Ultrafine grained nanostructured materials (UFGNSM) conference 2021, Tehran, Iran- Presented a paper on “SEM and TEM based characterization of particulate matter from disc-brake wear”.
- Attended ECOPADS winter school- “From linear to circular thinking”, from 2nd -6th December, 2019, Trento, Italy.
- Attended online summer school- “Electric and Magnetic Field-assisted Processing of Inorganic Materials”, from 14th -16th September, 2020.
- Attended workshop- “Combined Analysis Using Ray Scattering”, from July 4th – 8th, 2022, Caen, France.

Acknowledgment

Reaching 'almost' the end, I am grateful to many people who have contributed to this journey.

I would like to express my deepest regards to my thesis supervisor Prof. Stefano Gialanella for allotting me this interesting topic. From all the online meetings we had during the COVID times when he kept me motivated, to the offline meetings, which always exceeded the scheduled hours, I am thankful for his patience during discussions. His diverse knowledge of the materials engineering field and more than that his humility, are the qualities I aspire to acquire one day. I also thank him for letting me work at my own pace- I suppose, sometimes that is what a PhD student needs the most.

I am equally thankful to my second thesis supervisor, Prof. Luca Lutterotti. It has to start with the fact that he developed the *MAUD* software, on which almost all the major results presented in the thesis are based. I am deeply indebted to him for clarifying so many doubts, whenever I barged into his office unannounced. I thank him for his amicable nature and readiness to have multiple discussions on topics related to materials engineering, in particular those related to diffraction.

I also thank Prof. Giovanni Straffelini and Prof. Cinzia Menapace for their helpful discussions related to the disc brake wear debris results presented in the thesis.

To my trainer of TEM- Dr. Gloria Ischia, I am thankful and express my deepest apologies for the many mistakes that I made in the lab during the training sessions. I am also thankful to her for teaching me the sample preparation techniques. I am thankful to Dr. Lorena Maines for helping me with the SEM analysis of some samples, and Dr. Mauro Bortolotti for the XRD analysis. I also thank Dr. Angela Berloffa with whom I shared the office space for some time for trying to teach me the Italian language, and who was always ready to provide any help in the labs.

I thank all the professors under whom I attended the theory courses- It would be a long list if I named them all.

I got to meet some really talented fellow PhD students, from whom I got to learn directly or indirectly- Mara, Ana, Stefano, Hossein, Davide, Alberto, Andrea, Ricardo, Michele, Rafaella, Domenico, Chiara, Fahim, Abhishek, and Neeraj. I am deeply indebted to Priya and Sunil for helping selflessly during the initial phases of my PhD. I am thankful to my friend Minakshi who has listened to every stupid topic I had to discuss over the last thirteen years. To the flatmates I had in the last three years- Elisa, Martina, Greta, and Claudia: a big thanks for being so generous and maintaining a peaceful environment in the flat.

Lastly, I am thankful to my family members in India- my mother, Mrs. Anjani Srivastava; my sister, Dr. Shraddha; and my brother, Mr. Anshu Sinha. It was actually my brother who persuaded me take on this journey. It has been tough staying away from all of them, but their kindness has kept me going.

Ankur Sinha.